High resolution magnetic field measurements in high-mass star-forming regions

Dissertation

zur

Erlangung des Doktorgrades (Dr. rer. nat.)

der

Mathematisch-Naturwissenschaftlichen Fakultät

der

Rheinischen Friedrich-Wilhelms-Universität Bonn

vorgelegt von

Gabriele Surcis

aus

Chiavari (GE), Italien

Bonn (June 2011)

Angefertigt mit Genehmigung der Mathematisch-Naturwissenschaftlichen Fakultät
der Rheinischen Friedrich-Wilhelms-Universität Bonn

1. Gutachter: Dr. Wouter Vlemmings
2. Gutachter: Prof. Dr. Frank Bertoldi

Tag der Promotion: September 12, 2011

Diese Dissertation ist auf dem Hochschulschriftenserver der ULB Bonn unter
http://hss.ulb.uni-bonn.de/diss_online
elektronisch publiziert. Das Erscheinungsjahr ist 2011.

to my wife...

Abstract

A number of different formation scenarios have been proposed to explain the formation of stars with masses larger than about 8 $M_{\odot}$. These include formation through the merger of less massive stars (*Coalescence model*) or through the accretion of unbound gas from the molecular cloud (*Competitive accretion model*). In the third scenario, *Core accretion model*, massive stars form through gravitational collapse, which involves disc-assisted accretion to overcome radiation pressure. This scenario is similar to the favored picture of low-mass star formation, in which magnetic fields are thought to slow the collapse, to transfer the angular momentum and to power the bipolar outflows. Moreover, during the formation of low-mass stars the gravitational collapse of molecular clouds proceeds preferentially along the magnetic field lines, giving rise to large rotating disc or torus structures orthogonal to the magnetic field. Consequently, the molecular bipolar outflows, which originate from the protostar, are driven parallel to the magnetic field. Although the magnetic fields play such an important and crucial role in the formation of low-mass stars, its role in the formation of high-mass stars is still under debate.

The debate is due to the several unanswered questions about the role of the magnetic fields in high-mass star formation. The difficulties in answering these questions is due to their fast evolution (of order of hundreds thousands years). As a result of this, the massive star-forming regions are rare and typically found at fairly large distance. Moreover the massive star-forming regions consist of a large number of protostars that make the identification of individual massive protostar very complex. Consequently it is very difficult to observe and measure the magnetic fields during the protostellar phase of high-mass stars. Current observations of magnetic fields in massive star-forming regions are often limited to low density regions and/or envelopes at scales of several thousands astronomical units. Linear polarization observations of dust also only provide information on the magnetic field in the plane of the sky, so these observations have been yet unable to probe the strength and the full structure of the magnetic field close to the protostars

and around protostellar discs.

The probes of magnetic fields in the high density regions close to the massive protostars currently available are masers. Their bright and narrow spectral line emissions are ideal for measuring the Zeeman-splitting as well as for determining the orientation of the magnetic field in 3-dimension. So far the most investigated sources have been H_2O and OH masers that revealed ordered magnetic fields and field strengths between 10 and 600 mG and few mG, respectively. Even though CH_3OH is the most abundant maser species in the massive star formation, the very first 6.7-GHz CH_3OH maser linear and circular polarization observations have only recently been made. This maser emission can significantly improve the understanding of the role of the magnetic fields in massive star-forming regions.

The aim of this Ph.D. thesis is to investigate the role of magnetic fields in massive star-forming regions at milliarcsecond resolution by observing the polarization emission of H_2O and in particular 6.7-GHz CH_3OH masers. Six massive star-forming regions were studied using European VLBI Network observations at 6.7-GHz and one using the MERLIN telescope. Furthermore two of them (W75N and NGC7538) were also observed at 22-GHz in order to determine the magnetic fields using the H_2O maser emission. These observations allowed us to observe magnetic fields with hourglass morphology, magnetic fields along outflows and on the surfaces of torus and disc and in some cases also to determine the strength of the field. Moreover several important characteristics of masers were also determined.

Contents

INTRODUCTION

Chapter 1

Star formation: low-mass stars vs high-mass stars

Stars with a mass lower than about eight solar masses are defined as low-mass stars and stars with a mass greater than about eight solar masses are called high-mass stars. The choice of the mass as one of the main parameters in the classification of stars comes from its influence on their formation, their subsequent evolution and even their death. The greater the mass is, the faster the star forms and evolves. This is the reason why high-mass stars are more rare and often more distant than low-mass stars. The rarity of high-mass stars makes their study observationally more difficult and more challenging, in particular in understanding the role of magnetic fields. Before advancing in the study of the magnetic field in massive star-forming regions, it is important to summarise how low-mass stars form and what the role of the magnetic field is in their formation. A brief description on low-mass star formation can be read in Sect. 1.1. Sect. 1.2 is focused on the three models of massive star formation and on the most recent theoretical and observational results about the magnetic fields.

1.1 Low-mass star formation

The general processes that govern low-mass star formation are nowadays thought to be fairly well understood and only few questions remain unanswered. The largely accepted model says that low-mass stars are formed from gravitationally bound cores that are created by the fragmentation of cold molecular clouds ($\sim$ $10 - 20$ K). The molecular clouds are the densest part of the interstellar medium (ISM) with average gas number (molecular hydrogen dominated) $n_{\mathrm{H_2}}$ of 20 cm^{-3} (Giant Molecular Cloud, GMC; Larson 2003). The low temperature and the high density

of the clumps (10^3 cm^{-3} < n_{H_2} < 10^5 cm^{-3}, Larson 2003) within the molecular clouds make the collapse of prestellar cloud cores possible. At these conditions the self-gravity should be important and should dominate over thermal pressure by a large factor, except in the smallest clumps ($n_{H_2} \approx 10^5$ cm^{-3}), implying that the molecular cloud can collapse rapidly and efficiently into stars. Nevertheless the observations reveal that typically only a few percent of their mass is turned into stars, i.e. the collapse is slower and less efficient than expected. So there must be additional effects that support the gravity and prevent the collapse such as the ISM magnetic fields and the internal random motions (better known as "turbulence"). The charged species within a molecular cloud, electrons and ions (mostly protons), gyrate rapidly around the magnetic field lines and collide with the neutral particles. The collisions help to counteract the gravity. Moreover, since the molecular clouds are significantly magnetized, the turbulence is predominantly wavelike, consisting basically of magnetohydrodynamics (MHD) waves such as Alfvén waves, which involve only transverse and non-compressional motions. The MHD turbulence waves provide a source of pressure that can supplement the thermal pressure and help to support molecular clouds against gravity. Nevertheless, these waves cannot support the collapse for a long time because of the rapid wave dissipation due to the shocks produced from the motions along the magnetic field lines. Even the magnetic fields, which still have important consequences for star formation, cannot balance the gravity for long because of the loss of magnetic flux due to the *ambipolar diffusion*, i.e. the decoupling of neutrals from plasma, that is however still debated. If the fractional ionization of the gas becomes very low (one part per million) the neutrals gradually drift across the magnetic field lines in response to gravity. Because of the *magnetic flux freezing* the electrons and the ions are still tied to the magnetic field but they are not able to stop the collapse that proceeds fast. The gas now tends to accumulate along the magnetic field, i.e. in the direction where it meets the least resistance, and meanwhile the cross-field drift also distorts the magnetic field towards the centre of the core. This distortion occurs through the collisional drag exerted on the gyrating electrons and ions by the inflowing neutral gas. The collapse accelerates as ambipolar diffusion continues to remove magnetic flux from the collapsing region. As the central density grows, the magnetic field continues to squeeze until the field lines diverge nearly radially from the centre, producing a hourglass morphology, and the gas form an elongated structure. The timescale of the ambipolar diffusion is estimated to be about 10^7 yr, which is one order of magnitude longer than the free-fall time.

The matter in the molecular cloud is rotating during the formation of the prestellar core, and

consequently this rotation must strongly influence the later stages of the collapse if angular momentum is conserved. The angular momentum of a typical prestellar cloud is orders of magnitude more than can be contained in a single star and this implies that some loss and redistribution of it are necessary. There are three processes thought to contribute to this: magnetic braking, formation of a disc and jets, and formation of multiple stellar systems and planets. The *magnetic braking* phenomenon must operate from the earliest times, as gas condenses along field lines and begins to form the equatorial pinch described above. So any spin-up during the collapse twists the magnetic field, which is anchored to the more rarefied medium, and increases the local magnetic tension. This tension in turn creates a braking torque on the element that counteracts the spin-up and lowers the specific angular momentum. The angular momentum flows into the surrounding medium, i.e. the twist imposed by the rotating cloud propagates along the field lines through the associated magnetic tension. As density rises, the matter and the magnetic field decouple because of the drop in fractional ionization. Consequently, the matter inside some volume of the equatorial region conserves angular momentum and spins up as it approaches the central protostar creating a *rotating disc*. The angular momentum is thus redistributed to the disc that sooner or later will transfer it to the star. Therefore, some process that removes the angular momentum from the disc is necessary, but the exact process is still unclear. An outward transport of angular momentum can occur if the disc is viscous or if some mechanism creates an effective viscosity in the disc, as supposed in most of the models of accretion discs in other astrophysical objects. Part of the angular momentum can be removed through the *formation of jets*. The winds of the inner part of the disc create, along the magnetic field lines, collimated high-velocity jets with a bipolar morphology. These contain both individual knots with bow-shock morphology, which are the observational tracer of the jets, and more diffuse emission between these knots. These jets are also able to stir up and drag forward molecular outflows that both have lower velocities and are more extended than the central jets. The residual angular momentum can be distributed to the *planets* that might form from the disc matter.

Since the difference between angular momentum of the molecular cloud and the angular momentum of low-mass stars is very large, an additional possibility is that the collapse of a prestellar cloud core produces a *binary* or *multiple system*. Thus, much of the initial angular momentum goes into the orbital motions of the stars in such a system. This scenario would be consistent with the observed fact that about two-third of all stars are in binary systems while about one-third are single.

Summarising, low-mass stars form through the formation of an accretion disc around the central protostar, and jets/bipolar outflows are launched from the protostar. See Larson (2003), Stahler & Palla (2005), and McKee & Ostriker (2007) for more details.

1.2 High-mass star formation

Despite the fundamental importance of massive stars in the evolution of the Universe, the early evolutionary stages of their formation have in the last decade been intensively investigated, both observationally and theoretically. This is due to the difficulties that astrophysicists have encountered in observing them, in fact they are distant, rare, evolve quickly and the evolutionary phases are short-lived. These complications are also reflected on the theoretical models. However, the new generation of telescopes, satellites and computers have made, and will make possible to obtain important pieces of the whole puzzle that will be sooner or later resolved. The first pieces are collected in two main reviews on the high-mass star formation. These are the review of Beuther et al. (2007) and the review of Zinnecker & Yorke (2007) that have been extensively taken into account in this section.

1.2.1 Models

Massive star formation occurs in the densest ($n_{\rm H_2} > 10^5$ cm^{-3}), compact (radii$<$ 1 pc) clumps of giant molecular clouds (sizes from 20 to 100 pc and masses between 10^4 and 10^6 M$_\odot$) that are usually located at a distance larger than 300 pc. One of the major conceptual problems in massive star formation comes from the radiation pressure. This is due to the short Kelvin-Helmhotz time of massive protostars, i.e. the protostars reach the main sequence while they are still forming from their parent clouds. In principle, the radiation pressure could be strong enough to halt any flow of gas onto the protostars and consequently we should not observe stars with masses of the order of tens of solar masses. However, since such massive stars are observed there must exist some process that overcomes this problem and enable the massive stars to form. In the last year the idea that the high-mass protostars are a scaled-up version of the low-mass stars (*Core accretion model*), with some changes due to the high masses and energies, has become the most popular in the scientific community, even if two more models are still in vogue: the *Competitive accretion model* and the *Coalescence model*. These three models are described below.

Core accretion model

The basic premise of the Core accretion model is that massive stars form in the same way as low-mass stars, i.e. by a top-down fragmentation process in which a molecular cloud breaks up into smaller and smaller pieces under the combined influence of turbulence, magnetic fields, and self-gravity. Here the cores are massive and determine the mass reservoir available to form the star. Moreover, like in the low-mass protostars, the collapse of such cores produces accretion discs and outflows. The outflows are often observed towards massive star-forming regions and contrary to their smaller counterpart they are often not collimated. If this model is correct it must overcome three important issues: a model for the origin and structure of the massive cores, a method to allow accretion to occur despite the radiation pressure, and an explanation for why ionization does not stop the accretion.

The first proposed model of massive core formation came from McKee & Tan (2003), who found that the core density and velocity dispersion are power law functions of radius such that at every radius turbulent motions provide enough ram pressure to marginally support the core against collapse. Hence their central idea was that at the high pressures found in massive star-forming regions, massive cores are molecular condensations in turbulence-supported quasi-equilibrium. The formation of turbulent and pressurized clouds permit sufficient material to be available in the cores for the formation of massive stars. Theoretical simulations show that this model does not produce subfragmentation in low-mass stars, as instead reported in some papers (e.g., Dobbs et al. 2005), if the radiative transfer is included in the simulations (Krumholz et al. 2007).

Once a massive protostar reaches about 15 $M_{\odot}$, the pressure exerted by its radiation field begins to have a significant effect on the accretion flow. Yorke & Sonnhalter (2002) found that the isotropic radiation emitted from the central object becomes quickly anisotropic farther from the centre, i.e. the radiative flux close to the equatorial plane can be much smaller than the component parallel to the rotation axis. Because of the beaming of radiation in the polar direction this effect is called *flashlight effect*. This effect is increased if polar cavities blown free by outflows originating close to the stars exist (Krumholz et al. 2005, 2009). This allows higher final masses than 43 $M_{\odot}$ obtained with the flashlight effect. Since observing discs around massive protostars is difficult, the massive outflows become the best observational clues of their existence during the early phases of massive star formation. However, the high far ultraviolet (UV) and extreme UV fluxes associated with high-mass stars will begin to photoevaporate the discs on timescales of about 10^5 yr and it seems to limit the buildup of massive stellar objects.

When a massive star is formed via accretion an increasing number of hydrogen ionizing photons are produced, even while it grows as it becomes hotter and more luminous. This radiation ionizes all the material in the disc and in the immediate vicinity of the accreting massive star producing the so-called *H II regions*. The H II regions associated with individual high-mass protostars are classified into two types: Ultracompact H II (UCH II) regions (diameters 0.01–0.1 pc) and Hypercompact H II (HCH II) regions (< 0.1 pc). Observations shows that the ionized gas is confined near the star for long periods (e.g., Kurtz 2005; Keto 2007), and some observed systems show signs of both accretion and the presence of HCH II region, providing direct evidence that accretion can continue past H II region formation (e.g., Sollins et al. 2005). This means both that the protostellar core is not destroyed by the ionization and that accretion is not halted. Several models have been proposed to explain these observational evidences. Tan & McKee (2003) have suggested that winds, which are often associated with the disc accretion and originate the protostellar jet, confine the HCH II regions. The winds clear the gas along the axis, and the ionizing radiation then illuminates the inner surfaces of the winds instead of the infalling gas permitting the accretion. Therefore, the resulting HCH II region is likely confined in all but the polar directions by the protostellar jet. However, if the disc is ionized out to a radius where the escape speed is about equal to the ionized gas sound speed, then a photo-evaporated flow is set up, reducing accretion to the star.

Competitive accretion model

The main differences between the Core accretion model and the Competitive accretion model are in how and when the mass is gathered to form the massive star. In the Competitive accretion model massive protostars are "seeded" by low-mass protostars which compete with the other protostars to draw in matter from the entire molecular cloud. In this scenario the subfragmentation process that is avoided in the Core accretion model is crucial. The fragmentation produces clusters of lower mass stars, with masses between 0.001 $M_\odot$ and 0.5 $M_\odot$ (Bonnell et al. 2004; Bate & Bonnel 2005), that are born in a dense molecular clump and immediately begin accreting gas to which they were not initially bound. This is the fundamental difference between the two models; in the Core accretion model the reservoir is the core itself and the accretion proceeds via a disc while here the reservoir of matter is the entire cloud and the accretion is spherical (i.e., Bondi–Hoyle accretion). The gravitational potential of each star attracts the gas from its own accretion dominion, i.e. the region from which the gas can be gathered. These domain becomes larger and larger with the growth of the "seed". Since the gravitational potentials of the individual stars form a larger scale

potential that funnels gas down to the centre of the cluster, the stars immersed in the centre of a protostellar cluster accrete much more mass than those located farther. Therefore, stars near the centre of the clump are immersed in the highest density, lowest velocity dispersion gas, and consequently accrete most rapidly (Bonnell et al. 2001). The gas that accretes onto the protostar must be free to move under the same gravitational acceleration as the stars, otherwise the accretion would be limited and massive stars would not be formed (Bonnell 2008). Because the total gas reservoir is limited, the protostars eventually compete for cloud gas, especially after the accretion domains start to overlap, the name of the model takes is origin from this aspect.

Several observational evidences can be predicted from this model. The steep nonlinear mass dependence of the accretion rate (Bondi–Hyle rate) onto a gravitating point mass naturally gives a steep, power low Initial Mass Function (IMF), i.e. the mass distribution function of massive stars at birth, close to the observed IMF in young clusters. The central location of the most massive stars in the clusters in which they form (e.g., Hillenbrand & Hartmann 1998) and the unusually high frequency of close companions in binary or multiple systems (e.g., Stahler et al. 2000), whose companions are themselves often massive stars, are direct consequences of the Competitive accretion model (Bonnell 2008).

This model, however, has two main difficulties. First, the Bondi-Hoyle accretion is disrupted by the radiative pressure when the mass reach a value about 10 $M_{\odot}$ (Edgar & Clarke 2004) and consequently stars with higher masses cannot be formed. Second, the model is effective only if the virial parameter is much less than observed (Beuther et al. 2007). Bonnell et al. (2007) argue that both difficulties can be resolved if the clump in which the massive stars are forming is undergoing global gravitational collapse. Recent simulations with higher spatial and mass resolution have shown that circumstellar discs, which are actually circumbinary discs, and consequently molecular outflows should also be a common outcome of competitive accretion, especially around more massive stars (Bonnell 2008; Dale & Bonnell 2008).

Coalescence model

Since the formation of massive stars always occurs at the dense centres of stellar clusters another model was also proposed. Although this model is nowadays considered inadequate to form most of the massive stars, it is still possible in the extreme case of the most massive stars. This model is the Coalescence model where the massive stars form through the merging of lower mass stars (e.g., Bally & Zinnecker 2005). At that time, radiation pressure problem was considered a severe

obstacle to gas accretion and the packing of massive stars in dense clusters was too tight, and so a sufficient large gas reservoir for the core collapse was not available (Zinnecker & Yorke 2007). These two problems have been solved by the models described above and so the coalescence model has gone into the background of massive star formation.

The short descriptions of the three models show that much work is still necessary before having a final model for the formation of the high-mass stars. Very recently, from the observational point of view, great effort have been made and every day more and more pieces of the entire puzzle are put together. Some of the crucial pieces are related to the measurements of the direction and the strength of the magnetic fields around massive protostars.

1.2.2 Magnetic fields

Despite the important role played in the formation of low-mass stars (see Sect. 1.1), the magnetic fields have been detected and included in the theoretical simulations of massive star formation only recently. Since massive stars are fully radiative, they are, with few exceptions (e.g., Donati et al. 2006), not expected to have significant magnetic fields. Consequently it has been thought that the magnetic fields do not have any role in their formation. However, the detection of molecular outflows in massive star-forming regions and their inevitable inclusion in the two main models makes the presence of strong magnetic fields during the formation of high-mass stars unavoidable.

To evaluate the importance of the magnetic fields to cloud structure it is fundamental to compare the mass to magnetic flux ratio (M/Φ) to the critical value of this ratio, which is defined by the condition that the magnetic energy must be equal to the gravitational energy for a cold cloud in magnetostatic equilibrium, that is

$$\lambda = \frac{(M/\Phi)}{(M/\Phi)_{\rm crit}}. \tag{1.1}$$

The critical value $(M/\Phi)_{\rm crit} = c_\Phi/\sqrt{G} \approx 0.12/\sqrt{G}$ (Tomisaka et al. 1988) is taken from numerical models for the collapse of a spherical molecular cloud into a highly flattened structure. When $\lambda < 1$, the magnetic field prevent collapse, but when λ becomes larger than 1, gravity overwhelms the magnetic field. Because $(M/\Phi) \propto N(H_2)/|B|$, measuring column density $N(H_2)$ and magnetic field strength B allows inferring M/Φ. The importance of the magnetic field in star-forming regions can be also estimated by evaluating the ratio between thermal and magnetic energies, that is

$$\beta = \frac{\rm E_T}{\rm E_B} = 2 \cdot \left(\frac{c_{\rm s}}{V_{\rm A}}\right)^2 = 2 \cdot \left(\frac{m_{\rm a}}{m_{\rm s}}\right)^2, \tag{1.2}$$

where c_s is the sound velocity, V_A is the Alfvén velocity, m_a is the Alfvénic Mach number, and m_s is the sonic Mach number. If $\beta < 1$ the magnetic field is dynamically important in the star-forming region. Another useful observational parameter is the scaling of field strength with density, $|B| \propto \rho^{\tau}$. Depending on τ value it is possible to determine if the magnetic field is frozen into the gas ($\tau = 1$ or $\tau = 0$ if the compression of the ISM is perpendicular or parallel to the magnetic field, respectively); if a cloud becomes self-gravitating but the magnetic field is very weak, i.e. an approximately spherical collapse is expected ($\tau = 2/3$); if magnetic fields support clouds and contraction due to ambipolar diffusion in cores $\tau \approx 0.4 - 0.5$ (Crutcher 2005).

Observational information on magnetic fields can be obtained via linear polarization of dust emission and spectral-line emission (e.g., masers through Zeeman effect). Linear polarization of thermal emission from dust grains arises from elongated grains with their short axes aligned generally with the magnetic field. The position angle of maximum emission is perpendicular to the magnetic field projected onto the plane of the sky, so maps of polarized dust emission give the morphology of the magnetic field (Crutcher 2005). Estimation of the magnetic field strength from dust observations can be made by analyzing the small-scale randomness of field lines (Chandrasekhar & Fermi 1953). For instance, from Submillimeter Array (SMA) observations of dust continuum linear polarized emission at 870 μm towards the UCH II region G5.89-0.39 Tang et al. (2009a) measured magnetic field strength between 2 and 3 mG and a morphology of the magnetic field that is disturbed by the expansion of the H II region. Moreover, they measured an increment of λ from 0.1 to 2.5 indicating a supercritical phase near the H II region. Also in the region DR21OH a supercritical magnetic field ($\lambda \approx 2$; $|B| \approx 1.2$ mG) has been measured, with the Berkeley Illinois Maryland Association (BIMA) array. The field shows a helical morphology towards the two high-density cores, which could be produced by the orbital motion of the double core (Crutcher 2005). Very recently Carrasco-González et al. (2010) detected for the first time polarized synchrotron emission arising from the jet of the massive protostar IRAS18162-2048, indicating an helical magnetic field with a strength of about 0.2 mG.

Before this PhD work, only five spectral lines observed in massive star-forming regions have shown Zeeman-splitting (i.e., magnetic field strengths are measurable), these are H I, OH, SiO, CN, and H_2O. The OH, SiO, and H_2O are maser emissions, the latter is described in details in section 2.3. From these five spectral lines it is possible to measure directly the strength of the magnetic field by measuring the separation of the split lines, however for H_2O masers the argument is more complicated and it is described in Chapter 2. Typical values for B are from few mG to

tens mG but the H_2O masers can also show higher magnetic field strength. The CO polarization ($n_{H_2} \sim 100$ cm^{-3}) observations are of great importance in studying the morphology of the magnetic field, especially if the Chandrasekhar-Fermi method can be applied. In the case of DR21OH the CO and dust polarization maps show similar morphology. This means that the magnetic field is similar between the envelope and the core of the massive star-forming region (Crutcher 2005). The CO together with the other tracers are useful to determine the scaling of the magnetic field with the density. To date the relationship between ρ and $|B|$ shows a parameter τ around 0.5 that indicates a dynamical importance of the magnetic field in the formation of massive stars.

The recent observations also provided a stimulating input to the theoretical simulations. In 2007 Banerjee & Pudritz investigated the three-dimensional collapse of magnetized, massive molecular cloud cores at the early stages. They found high accretion rates that allow the formation of massive stars in only 10^4 yr, which is short enough for the massive star to build up before its surrounding disc is photoevaporated. Therefore their model suggests that low-mass and high-mass stars form in the same way, which is also supported by observations (e.g., Chini et al. 2004, 2006). Furthermore they found that angular momentum is efficiently transferred by bars/spiral arms and magnetic torque. They also demonstrated that an early outflow is formed only when magnetic field is taken into account, and that the outflow cavities suggested by Krumholz et al. (2005) are formed very early, much before the central star has even accumulated a solar mass worth of material. Peters et al. (2011) extended the work of Banerjee & Pudritz (2007) further. They have shown that the magnetic field prevents the gas from collapsing into several cores, i.e. reduces the fragmentation of the massive core, and that the magnetic braking near the centre reduces the angular momentum of the collapsing gas further, i.e. more material is transported radially inward onto the protostar. Moreover, they also reported that there are two effects that tend to weaken and broaden the outflow: the gravitational fragmentation of the accretion flow and the thermal pressure if ionized gas is dominant within the H II region. They concluded that the uncollimated outflows from massive stars may be better explained as driven by the ionization feedback because the fast jets launched from the inner disc region should then be highly episodic.

The role of the magnetic fields in massive star formation needs further observational efforts especially in determine their orientations and strengths close to the protostars, i.e. at AU distances from the central future star. The best probes for doing it are the masers and, apart the H_2O masers, the CH_3OH masers might be fundamental to reach this goal. In the next chapter a brief introduction to this astronomical objects is given by mainly focusing on their polarization.

Chapter 2

Maser theory

The acronym maser stands for Microwave Amplification by Stimulated Emission of Radiation and usually indicates the laboratory device developed by J. Gordon, H.Zeiger, and C. Townes in 1955. This device produces coherent electromagnetic waves through an amplification based on one of the effects of the quantum theory: the stimulated emission. A decade after, the first astronomical maser was detected. Here the radiation intensity is amplified in a single pass through a large dense region of molecular gas. Although astronomical masers, or simply masers, are found in many astrophysical environments (e.g. comets, atmospheres of giant stars, supernova remnants, nuclei of external galaxies) they mostly arise in the perturbed vicinity of young stars of both low- and high-mass. In particular, their bright and narrow spectral lines emission is ideal to probe the magnetic fields, both the strength and the orientation, on the smallest scales in star-forming regions. In Sect. 2.1 an essential introduction on the maser theory is provided and the polarization property of the maser radiation, which is fundamental in this thesis work, is treated in Sect. 2.2. Finally, the main characteristics of the water and methanol masers are reported in Sect. 2.3.

2.1 Foundations of Maser Theory

Two main conditions must be satisfied to have maser emission: a non-equilibrium state of a gas and an efficient pumping mechanism. The latter is responsible for the *population inversion* of the energy levels that is fundamental for amplifying the incoming radiation. To understand why let us consider a simple maser cloud composed of molecules having only two energy levels, denoted u (upper) and l (lower), with population densities $n_{\rm u}$ and $n_{\rm l}$ respectively.

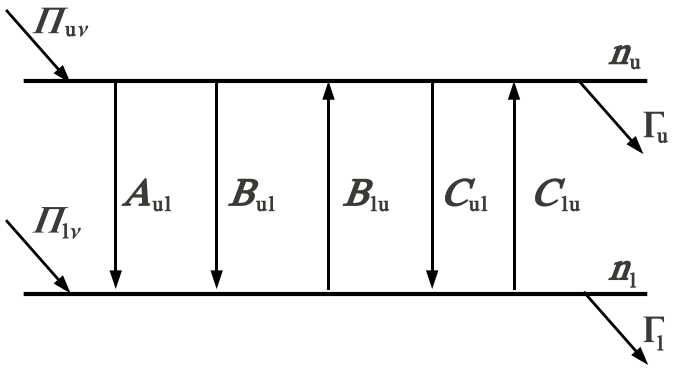

Figure 2.1: Schematic diagram of the upper and lower maser levels with population densities $n_{\rm u}$ and $n_{\rm l}$ respectively. $A_{\rm ul}$, $B_{\rm lu}$, $B_{\rm ul}$ are the Einstein coefficients for spontaneous, absorption, and induced emission respectively. $C_{\rm ul}$ and $C_{\rm lu}$ are the collision rates from the upper to the lower level and viceversa. $\Gamma_{\rm i}$ and $\Pi_{{\rm i}\nu}$ with i=u,l are the decay and pump rates, respectively.

2.1.1 Population inversion

The *equation of radiative transfer* that describes the variation of the specific intensity (I_ν) is

$$\frac{dI_\nu}{ds} = -\kappa_\nu I_\nu + \epsilon_\nu, \tag{2.1}$$

where s is the distance along the ray path and ν the given frequency. The absorption (κ_ν) and emission (ϵ_ν) coefficients are given by:

$$\kappa_\nu = (n_{\rm l}\ B_{\rm lu} - n_{\rm u}\ B_{\rm ul})\ \phi(\nu)\ \frac{h\nu}{4\pi}, \tag{2.2}$$

$$\epsilon_\nu = n_{\rm u}\ A_{\rm ul}\ \phi(\nu)\ \frac{h\nu}{4\pi}, \tag{2.3}$$

where $A_{\rm ul}$, $B_{\rm lu}$, $B_{\rm ul}$ are the Einstein coefficients for spontaneous, absorption, and induced emission respectively, and $\phi(\nu)$ is the line profile function. Eq. 2.1 can also be written as:

$$\frac{dI_\nu}{d\tau_\nu} = -I_\nu + S_\nu, \tag{2.4}$$

where $d\tau_\nu = \kappa_\nu\ ds$ is the *optical depth* element and $S_\nu = \epsilon_\nu/\kappa_\nu$ is the *source function*, which has the same dimensions as the intensity. Substituting Eqs. 2.2 and 2.3 into Eq. 2.1 and assuming that

the two levels have the same degeneracy, i.e. $B_{\rm lu} = B_{\rm ul}$, we have

$$\frac{dI_\nu}{ds} = -(n_{\rm l} - n_{\rm u})\ B_{\rm ul}\ I_\nu\ \phi(\nu)\ \frac{h\nu}{4\pi} + n_{\rm u}\ A_{\rm ul}\ \phi(\nu)\ \frac{h\nu}{4\pi}. \tag{2.5}$$

Since in astronomical masers the radiation must be amplified when it passes through the cloud, it is necessary that $\kappa_\nu < 0$, or from Eq. 2.5 that $n_{\rm l} < n_{\rm u}$. However, in the cold interstellar clouds normally $n_{\rm l} \gg n_{\rm u}$ and this condition is not satisfied. Therefore, the presence of a mechanism that produces a population inversion of the upper and lower levels of the molecules is crucial. This mechanism is called *pumping mechanism* and the source of energy that maintains it is called *pump*.

The population inversion is not possible in a system with only two energy levels but it can occur as a result of particle moving through other levels. To have a more detailed study of the maser effect it is necessary to generalize the description by including the system gains and losses that come from the population exchange with other levels that are not directly responsible of the maser radiation. Thus it is necessary to introduce the *pump rates* $\Pi_{\rm u\nu}$ and $\Pi_{\rm l\nu}$, which are defined as the number of additional molecules brought to the upper and lower level per unit time and unit volume, and the *decay rates* $\Gamma_{\rm u}$ and $\Gamma_{\rm l}$ which are the opposites of the pump rates. Since the frequency distribution of the particles in the other levels, which are unaffected by the maser radiation, follow the Doppler profile, the pump rates in the frequency interval $[\nu, \nu + \Delta\nu]$ are $\Pi_{\rm u\nu} = \Pi_{\rm u}\ \phi(\nu)$ and $\Pi_{\rm l\nu} = \Pi_{\rm l}\ \phi(\nu)$. The level populations also change through inelastic collisions with ambient molecules. This collisions transfer particles from the upper to the lower level and viceversa at rates $C_{\rm ul}$ and $C_{\rm lu}$, respectively. Note that the particles that dominate the *collision rates* may be different from the system particles. The variation of the population densities of the upper and lower levels in steady-state are zero. Then the total rate equations for the two levels are

$$\frac{\partial\ n_{\rm u}}{\partial\ t} = \Pi_{\rm u\nu} - n_{\rm u}\Gamma_{\rm u} - (n_{\rm u} - n_{\rm l})\ B_{\rm ul}\ J_\nu + n_{\rm l}C_{\rm lu} - n_{\rm u}C_{\rm ul} - n_{\rm u}A_{\rm ul} = 0 \tag{2.6}$$

$$\frac{\partial\ n_{\rm l}}{\partial\ t} = \Pi_{\rm l\nu} - n_{\rm l}\Gamma_{\rm l} + (n_{\rm u} - n_{\rm l})\ B_{\rm ul}\ J_\nu - n_{\rm l}C_{\rm lu} + n_{\rm u}C_{\rm ul} + n_{\rm u}A_{\rm ul} = 0 \tag{2.7}$$

The term J_ν is the angle-averaged maser intensity, i.e $J_\nu = I_\nu \frac{\Delta\Omega}{4\pi}$, that is function of ν. The assumption that the two decay rates are equal, i.e. $\Gamma_{\rm u} = \Gamma_{\rm l} = \Gamma$, does not change the physical meaning of the phenomenon. Thus by adding the Eqs. 2.6 and 2.7 the *overall population* of the maser system is

$$n_\nu \equiv n_{\rm u\nu} + n_{\rm l\nu} = n\ \phi(\nu), \tag{2.8}$$

where $n = (\Pi_{\rm u} + \Pi_{\rm l})/\Gamma$. It is important to note that n_ν is distributed according to the thermal profile. Subtracting the Eqs. 2.6 and 2.7 the *population difference* of the maser system is

$$\Delta n_\nu \equiv n_{{\rm u}\nu} - n_{{\rm l}\nu} = \frac{\Pi_{\rm u} - \Pi_{\rm l}}{\Gamma + 2B_{\rm ul}\ J_\nu}\ \phi_\nu = \frac{\Delta\Pi/\Gamma}{1 + 2B_{\rm ul}J_\nu/\Gamma}\ \phi_\nu = \frac{\Delta n_0}{1 + J_\nu/J_{\rm s}}\ \phi_\nu \equiv (n_{\rm u} - n_{\rm l})\phi(\nu). \quad (2.9)$$

Note that Δn_ν can deviate from the profile shape ϕ_ν.

Population inversion require $\Pi_{\rm u} > \Pi_{\rm l}$, i.e. the pump rate for the upper level must exceed that of the lower level. The *pump efficiency* of the inversion process is given by

$$\eta = \frac{\Delta n_0}{n} = \frac{\Pi_{\rm u} - \Pi_{\rm l}}{\Pi_{\rm u} + \Pi_{\rm l}}, \quad (2.10)$$

and it must have a positive value in order to yield the population inversion, necessary for maser action.

Finally, Eq. 2.9 is still valid even if $\Gamma_{\rm u} \neq \Gamma_{\rm l}$ and the two levels have different statistical weights $g_{\rm u}$ and $g_{\rm l}$. In this case $\Delta n_0 = (\Pi_{\rm u}/\Gamma_{\rm u} - \Pi_{\rm l}/\Gamma_{\rm l})$ and $J_{\rm s}^{-1} = g_{\rm u}B_{\rm ul}[(g_{\rm l}\Gamma_{\rm l})^{-1} + (g_{\rm u}\Gamma_{\rm u})^{-1}]$, where now $g_{\rm l}B_{\rm lu} = g_{\rm u}B_{\rm ul}$.

2.1.2 Unsaturated and saturated maser emission

Considering Eqs. 2.9 and 2.2 the maser absorption coefficient can be written as

$$\kappa_\nu = -\frac{\kappa_{0\nu}}{1 + J_\nu/J_{\rm s}}, \quad (2.11)$$

where $\kappa_{0\nu} = \Delta n_0\ g_{\rm u}\ B_{\rm ul}\ h\nu\ \phi(\nu)/4\pi$. We can distinguish two cases:

1. When the stimulated emission rate is negligible with respect to the decay rates, i.e $J_\nu \ll J_{\rm s}$, the population difference Δn_ν is then independent of the maser radiation field and $\kappa_\nu = -\kappa_{0\nu}$. Such maser is called *unsaturated*. The transfer equation Eq. 2.1 becomes

$$\frac{dI_\nu}{ds} = \kappa_{0\nu}\ I_\nu + \epsilon_\nu. \quad (2.12)$$

Integrating Eq. 2.12 the intensity of radiation propagating through the cloud is

$$I_\nu(s') = I_\nu(0)\ e^{\kappa_{0\nu}\ s'} + \frac{\epsilon_\nu}{\kappa_{0\nu}}\left(e^{\kappa_{0\nu}\ s'} - 1\right), \quad (2.13)$$

thus it grows exponentially as it propagates through the cloud. Since $\kappa_{0\nu} \propto \Delta n_0 = \eta\ n$, the intensity of an unsaturated maser responds exponentially to changes in the pumping conditions. Therefore such masers can be expected to display erratic time variability that is difficult to predict. The beaming angle ($\Delta\Omega$) in the unsaturated case is roughly proportional to $|\tau_\nu|^{-1}$, where τ_ν is the optical depth.

2. Exponential amplification of unsaturated maser intensity cannot continue indefinitely because it would eventually lead to infinite energy density for sufficiently long path (s). At some point the maser intensity increases so much that $J_\nu \gg J_\mathrm{s}$, i.e. the pump efficiency of the inversion process approaches unity and the maser *saturates*. Here κ_ν is

$$\kappa_\nu \approx -\kappa_{0\nu}\frac{J_\mathrm{s}}{J_\nu} = -\kappa_{0\nu}\ J_\mathrm{s}\frac{4\pi}{I_\nu\ \Omega} \simeq -\kappa_{0\nu}\ J_\mathrm{s}\frac{4\ s^2}{I_\nu\ r^2}, \tag{2.14}$$

where $J_\nu = I_\nu\Omega/4\ \pi$ and $\Omega \simeq \pi r^2/s^2$. Integrating the transfer equation

$$\frac{dI_\nu}{ds} = \kappa_{0\nu}\ J_\mathrm{s}\frac{4s^2}{r^2} + \epsilon_\nu. \tag{2.15}$$

between s' and s'' the maser intensity becomes

$$I_\nu(s'') = I_\nu(s') + \frac{4}{3}\kappa_{0\nu}\ J_\mathrm{s}\left(\frac{s''^3 - s'^3}{r^2}\right) + \epsilon_\nu(s'' - s'). \tag{2.16}$$

The intensity of radiation propagating through the cloud thus grows linearly with distance. Saturation starts at line centre, where the intensity is the highest, then spreads to the wings with further increase in intensity. In saturated masers the beaming angle is proportional to $|\tau_\nu|^{-2}$.

2.1.3 Line narrowing and rebroadening

The maser radiation is characterized by the narrowing and rebroadening of the line if the maser is in the unsaturated or saturated regime, respectively. Suppose that the maser gain has a Doppler absorption profile

$$\phi(\nu) = \phi_\mathrm{D}(\nu) = \frac{1}{\sqrt{\pi}\ \Delta\nu_\mathrm{D}}\ e^{-\frac{(\nu-\nu_0)^2}{\Delta\nu_\mathrm{D}^2}}, \tag{2.17}$$

where $\Delta\nu_\mathrm{D} = \frac{\nu_0}{c}\sqrt{\frac{2\ k_\mathrm{B}\ T}{m}}$. In this expression ν_0, k_B, c, T, and m are the line centre frequency, the Boltzmann constant, the speed of light, the temperature of the cloud, and the mass of the molecule. Thus $\kappa_{0\nu} = \kappa_0\ \phi(\nu)$ is

$$\kappa_{0\nu} = \kappa_0'\ e^{-\frac{(\nu-\nu_0)^2}{\Delta\nu_\mathrm{D}^2}} = \kappa_0'\ e^{-\frac{\Delta\nu_*^2}{\Delta\nu_\mathrm{D}^2}}, \tag{2.18}$$

where $\kappa_0' = \kappa_0/(\sqrt{\pi}\ \Delta\nu_\mathrm{D})$.

The *unsaturated maser* intensity is given by Eq. 2.13 that, ignoring the final term representing spontaneous emission, becomes

$$I_\nu(s') = I_\nu(0)\ e^{\kappa_{0\nu}\ s'}, \tag{2.19}$$

so that

$$\frac{I_\nu(s')}{I_0(s')} = \frac{I_\nu(0)}{I_0(0)}\ e^{(\kappa_{0\nu}-\kappa'_0)\ s'}. \tag{2.20}$$

The input source is presumably a continuous radiation, for which $I_\nu(0)/I_0(0)$ is close to unity. Then $I_\nu(s')$ falls to $1/e$ of its central value when the condition $(\kappa_{0\nu}-\kappa'_0)\cdot s' = -1$ is satisfied, that is when

$$1 - e^{-\frac{\Delta\nu_*^2}{\Delta\nu_{\rm D}^2}} = \frac{1}{\kappa'_0\ s'}. \tag{2.21}$$

Since the Maclaurin series of $e^x = \sum_{n=0}^{\infty} \frac{x^n}{n!}$, for $n = 1$ Eq. 2.21 is

$$1 - \left(1 - \frac{\Delta\nu_*^2}{\Delta\nu_{\rm D}^2}\right) = \frac{1}{\kappa'_0\ s'}, \tag{2.22}$$

thus

$$\Delta\nu_* = \Delta\nu_{\rm D}\ \frac{1}{\sqrt{\kappa'_0\ s'}}. \tag{2.23}$$

Eq.2.23 describes the *line narrowing* as a function of path length, the longer is the path the narrower is the maser line.

In the case of *line rebroadening* the calculations are longer and more complicated because the positions in the linear maser (z) must be considered. Therefore to understand this process it is better to follow a qualitative argument. The maser line can only narrow by a finite amount before the central portion begins to saturate. In the *saturated regime* the intensity follows Eq. 2.16 and the amplification increases linearly with the path length. At the same time the wings of the line have not reached the saturation regime yet, so they are still growing exponentially. Consequently the line begins to broaden and eventually $\Delta\nu_* = \Delta\nu_{\rm D}$ when the maser is fully saturated. For a quantitative argument see Elitzur (1992).

2.2 Polarization of maser radiation

In 1896 the Dutch physicist Pieter Zeeman showed that in the presence of a magnetic field (B) the spectral lines of atoms (or molecules) are split into several components. This shift is proportional to the magnetic field strength and is known as *Zeeman-splitting* ($\Delta\nu_{\rm Z}$). Since masers are spectral lines, even if they differ from the regular thermal emission because of the stimulated emission process and a range of other properties, they must also show the splitting of their emission line when a magnetic field is present. Hence, investigating the polarization of maser radiation provides valuable information on the elusive magnetic field in massive star-forming regions.

2.2.1 General considerations

The magnitude of the Zeeman effect is three orders of magnitudes larger for paramagnetic molecules (e.g. OH), i.e. the molecules have a magnetic permeability greater or equal to unity, than for non-paramagnetic molecules (e.g., SiO, H_2O, and CH_3OH) for similar magnetic field strength. This is due to the ratio between the Bohr magneton ($\mu_B = e\hbar/2m_e c$) and the nuclear magneton ($\mu_N = e\hbar/2m_n c$) $\mu_B/\mu_N \approx 10^3$, where m_e and m_n are the electron and nucleon masses. Moreover, typically in *paramagnetic molecules* $\Delta\nu_Z$ is larger than $\Delta\nu_D$, i.e the Zeeman components are well separated and resolved, while in non-paramagnetic molecules $\Delta\nu_Z < \Delta\nu_D$, i.e. the Zeeman components overlap. In the former case there are no theoretical ambiguities. The circularly polarized $\sigma^{\pm}$ components (for which $\Delta M_F = \pm 1$) are perpendicular to B and they show a frequency shift $\pm\Delta\nu_Z$ with respect to the maser frequency ν_0. While the linearly polarized π component ($\Delta M_F = 0$) is along B and its centre frequency is exactly ν_0. For an arbitrary θ angle between B and the maser propagation direction, the resultant components are elliptically polarized for $\theta < \frac{\pi}{2}$, and linearly polarized for $\theta = \frac{\pi}{2}$. The observed splitting of the Zeeman components directly gives the full magnetic field $B = B_{||}/\cos\theta$.

In the case of *non-paramagnetic molecules* the relation between the linear polarization angle and the magnetic field direction is more complex. When $\theta < \theta_{crit} \approx 55°$, where θ_{crit} is the so-called Van Vleck angle, the linear polarization vectors are parallel to the magnetic field and when $\theta > \theta_{crit} \approx 55°$ they are perpendicular. This relation is valid only when the Zeeman frequency shift $g\Theta$, where g is the Landé factor and $\Theta = eB/m_e c$, is much larger than the rate of stimulated emission R, which corresponds to the third term in Eqs. 2.6 and 2.7. Otherwise, the relation between polarization angle and magnetic field direction is dependent on the maser intensity. Here the derived B strengths do not depend on the circular polarization fraction but also depend on the maser saturation level, which also influences the frational linear polarization (P_l). Especially for masers that are saturated, simple assumptions with a fixed proportionality between circular polarization and magnetic field strength can lead to B being overestimated by up to a factor of 4. On the other hand, velocity gradients along the maser path can cause the true field strength to be underestimated by a factor of two. Also the blending of maser features in lower angular resolution observations typically causes another factor of two underestimation of B.

In both cases the *Faraday rotation* (Φ), i.e. the rotation of the plane of polarization of polarized emission passing through a magnetic field along the lines of that field, can make a direct connection between the polarization angle and the magnetic field uncertain. Two main Faraday rotations can

affect the polarization of maser radiation: the *external* and the *internal* Faraday rotations. The former is due to the medium and magnetic field between the maser and the observer, which is the sum of the *ambient* and the *foreground* Faraday rotations, and can cause significant vector rotation. The latter comes from the maser itself and can alter the polarization characteristics of individual maser features in a source in different ways, possibly destroying any large scale structure in the linear polarization measurements.

2.2.2 Model of Nedoluha & Watson (1992) for water maser radiation

This section summarises the model developed by Nedoluha & Watson (1992) for the Zeeman effect in H_2O masers. They solved the transfer equations for the polarized radiation of 22-GHz H_2O masers in the presence of a magnetic field which causes a Zeeman-splitting that is much smaller than the spectral line breadth ($\Delta\nu_{\rm Z} < \Delta\nu_{\rm D}$). The calculations were performed for the regime in which $g\Theta \gg R$, $g\Theta \gg \Gamma$, and $g\Theta \gg \Gamma_\nu$, where Γ_ν is the rate for cross-relaxation between the magnetic substates. They derived the following equations of radiative transfer for the *Stokes parameters*[1] per unit angular frequency $I(\omega)$, $Q(\omega)$ and, $V(\omega)$ due to the combined effect of the three strongest hyperfine components $F - F' = 7-6$, $6-5$, and $5-4$

$$\frac{dI(\omega)}{ds} = (A_\omega^{76} + A_\omega^{65} + A_\omega^{54})\ I(\omega) + (B_\omega^{76} + B_\omega^{65} + B_\omega^{54})\ Q(\omega) + (C_\omega^{76} + C_\omega^{65} + C_\omega^{54})\ V(\omega), \quad (2.24)$$

$$\frac{dQ(\omega)}{ds} = (A_\omega^{76} + A_\omega^{65} + A_\omega^{54})\ Q(\omega) + (B_\omega^{76} + B_\omega^{65} + B_\omega^{54})\ I(\omega), \quad (2.25)$$

$$\frac{dV(\omega)}{ds} = (A_\omega^{76} + A_\omega^{65} + A_\omega^{54})\ V(\omega) + (C_\omega^{76} + C_\omega^{65} + C_\omega^{54})\ I(\omega), \quad (2.26)$$

where the $A_\omega^{\rm FF'}$, $B_\omega^{\rm FF'}$, and $C_\omega^{\rm FF'}$ coefficients are determined from the populations of the magnetic substates. Note that here the Stokes component $U(\omega) = 0$ because the calculations are being performed in the regime $g\Theta \gg R$ and the Stokes component $Q(\omega)$ is defined as $Q(\omega) = I_\perp - I_{||}$, i.e. the linear polarization is only perpendicular or parallel to the magnetic field. The overlapping of the hyperfine components, by itself, causes the profile for $V(\omega)$ to be quite asymmetric. These equations are the same of those derived by Deguchi & Watson (1990) who did not include Γ_ν in their calculations. The similarity between the two sets of equations comes from the replacing of Γ by $(\Gamma + \Gamma_\nu)$ in all the calculations of Deguchi & Watson (1990). The solutions of Eqs. 2.24,

[1]The Stokes parameters are a set of values that describe the polarization state of electromagnetic radiation. They are the total intensity I, the linearly polarized intensities $-1 < Q < +1$ (+1 corresponds to polarization angle $\chi = 0°$, -1 to $\chi = 90°$) and $-1 < U < +1$ (+1 to $\chi = +45°$, -1 to $\chi - 45°$), and the circularly polarized intensity $-1 < V < +1$ (+1 to left hand, -1 to right-hand). For purely monochromatic coherent radiation $I^2 = Q^2 + U^2 + V^2$.

2.25, and 2.26 can be scaled with $I_0\Delta\Omega/(\Gamma+\Gamma_\nu)$. That is, the effects of cross-relaxation on the spectral line profiles and fractional polarizations for a maser with a peak intensity I_0' are given exactly by these quantities computed in the absence of cross-relaxation but with peak intensity $I_0 = I_0'\ \Gamma/(\Gamma+\Gamma_\nu)$.

Note that the shapes of $I(\omega)$, $Q(\omega)$, and $V(\omega)$ depend on the product of the brightness temperature T_b of the continuum radiation that is incident onto the masing region ($T_\mathrm{b} = 4\pi^3c^2I(\omega)/k_\mathrm{B}\omega^2$) and the solid angle of the maser beam $\Delta\Omega$, and on the intrinsic linewidth of the maser ΔV_i (or in frequency $\Delta\nu_\mathrm{D}$). From their simulations they found that the measurement of the circular polarization can be surprisingly reliable indicator of $B\cos\theta$ despite the complicating aspects of the radiative transfer.

2.3 Maser Molecules

There exist several molecules that can give rise to astronomical maser emission. The most studied of these are *silicon monoxide* (SiO), *hydroxyl radical* (OH), *water* (H_2O), and *methanol* (CH_3OH). All these maser species are detected in the Milky Way towards massive star-forming regions. Although SiO, OH, and H_2O masers are also detected towards other astronomical environments, e.g. in the envelope of evolved stars, the CH_3OH masers arise only in massive star-forming regions where they are the most abundant of the observed maser species. They are usually found close to the central protostar (100-1000 AU; Bartkiewicz et al. 2006), with H_2O masers found in shocked region at similar distances. Therefore investigating the polarization of CH_3OH and H_2O maser emissions gives the opportunity to obtain information about the magnetic field in the vicinity of the young star and of its potential disc-outflow system. Before introducing the observational technique used in this research and the results obtained, it is crucial to give some more details on the two maser species at the centre of this research: H_2O and CH_3OH masers.

2.3.1 Water maser

The discovery of the astronomical H_2O maser emission was made by Cheung et al. (1969) towards several star-forming regions. The transition detected was the $6_{16} \rightarrow 5_{23}$ rotational transition of the ortho-H_2O, whose frequency is 22.235 GHz ($\lambda = 1.3$ cm), that consists of six hyperfine components. Analyses of interstellar H_2O masers indicate that all 6 hyperfine components contribute to the maser (Walker 1984). The separation between the three strongest hyperfine components ($F - F' = 7-6$, $6-5$, and $5-4$) is 0.45 and 0.58 $\mathrm{km\,s^{-1}}$, respectively. The weakest components

($F - F' = 5-6$, $5-5$, and $6-6$) are separated by more than 2.5 $\mathrm{km\,s^{-1}}$.

The H_2O masers arise in gas with hydrogen number density n_{H_2} between 10^8 to 10^{10} $\mathrm{cm^{-3}}$ (Elitzur et al. 1989) and temperature $300 < T < 1000$ K (Stahler & Palla 2005), showing a velocity width of about 1 $\mathrm{km\,s^{-1}}$ and a high brightness temperature $T_\mathrm{b} > 10^9$ K (e.g., Reid & Moran 1981). The pumping mechanism involves collisions with neutral molecules (de Jong 1973), thought the mechanism is not yet completely understood.

As described in Sect. 2.2 a crucial assumption in the analysis of maser polarization is that the Zeeman frequency shift $g\Theta$ is greater than the decay rate Γ and the cross-relaxation rate Γ_ν, moreover Γ must be greater than the stimulated rate R. The 22-GHz H_2O masers are in this regime, for which the linear polarization direction is determined by the magnetic field, even in the presence of anisotropic pumping. When the effect of anisotropic pumping is not significant, even $g\Theta > \Gamma$ is a sufficient condition (Watson 2002). To dimostrate that the 22-GHz H_2O masers satisfy $g\Theta \gg \Gamma > R$ and $g\Theta \gg \Gamma_\nu$, let consider the stimulated emission rate given by

$$R = (n_\mathrm{l} - n_\mathrm{u})\ B_\mathrm{ul}\ J_\nu. \tag{2.27}$$

Since the well-known relation between the Einstein coefficient B_ul and A_ul is

$$B_\mathrm{ul} = \frac{A_\mathrm{ul}\ c^2}{2\ h\ \nu^3}, \tag{2.28}$$

and since radio frequencies are sufficiently low that the Planck function can be approximated by the classical Rayleigh-Jeans law, that is

$$J_\nu = I_\nu \frac{\Delta\Omega}{4\pi} = \frac{2\ \nu^2\ T_\mathrm{b}\ k_\mathrm{B}}{c^2}\ \frac{\Delta\Omega}{4\pi}, \tag{2.29}$$

Eq. 2.27 becomes

$$R \simeq \frac{A_\mathrm{ul}\ k_\mathrm{B}\ T_\mathrm{b}\ \Delta\Omega}{4\ \pi\ h\ \nu}. \tag{2.30}$$

The A_ul Einstein coefficient for H_2O maser is $A_\mathrm{ul} \approx 2{\cdot}10^{-9}\ \mathrm{s^{-1}}$ and thus $R \approx 0.015\ \mathrm{s^{-1}}$ (considering $T_\mathrm{b} = 10^{10}$ K and $\Delta\Omega = 10^{-2}$ sr). When the maser transition involves collisions the decay rate is given by

$$\Gamma = \frac{0.1\ n_{H_2}}{10^9}, \tag{2.31}$$

Thus for the hydrogen number density range of H_2O maser $0.1\ \mathrm{s^{-1}} < \Gamma < 1\ \mathrm{s^{-1}}$. Detailed calculations of the cross-relaxation rate Γ_ν, which is expected to be considerably larger than Γ, give $\Gamma_\nu \approx 2\ \mathrm{s^{-1}}$ at temperatures of 400 K and $\Gamma_\nu \approx 5\ \mathrm{s^{-1}}$ for $T \sim 1000$ K (Anderson & Watson 1993). Deguchi & Watson (1990) reported that the Zeeman frequency shift is $g\Theta = 10\ \mathrm{s^{-1}}$ for a

magnetic field $B = 1$ mG. Thus the conditions $g\Theta(= 10\ \mathrm{s}^{-1}) \gg \Gamma(= 1\ \mathrm{s}^{-1}) > \mathrm{R}(\approx 0.015\ \mathrm{s}^{-1})$ and $g\Theta(= 10\ \mathrm{s}^{-1}) \gg \Gamma_\nu(= 5\ \mathrm{s}^{-1})$ are satisfied.

The first discovery of interstellar H_2O maser Zeeman-splitting was made by Fiebig & Güsten (1989). Afterward an increasing number of higher spatial resolution circular polarization observations were carried out (e.g., Sarma et al. 2001; Vlemmings et al. 2006a). Being a non-paramagnetic molecules the linear polarization fraction is of the order of few percents ($\lesssim 3\%$) and only when the masers are saturated they can reach higher percentage ($\sim 10\%$, e.g., Vlemmings et al. 2006a). The circular polarization fraction is typically lower ($< 2\%$). The largest magnetic field strength ever measured using the 22-GHz H_2O maser emission has been $\sim$650 mG towards the massive star-forming region Cepheus A HW2 (Vlemmings et al. 2006a).

2.3.2 Methanol maser

CH_3OH masers divide into two categories, known as *class I* and *class II*. Class I masers are pumped collisionally while class II masers are likely pumped radiatively. The class II masers include the 6.7-GHz ($\lambda = 4.5$ cm), which have been observed during this Ph.D. research, and the 12-GHz CH_3OH masers. The 6.7-GHz CH_3OH maser corresponds to the $5_1 - 6_0$ A^+ transition and is likely pumped by a combination of collisions and emission from nearby, warm ($T > 150$ K) dust. The masers themselves occur in gas at much lower temperature ($T < 50$ K) with $n_{\mathrm{H_2}} > 10^6$ cm^{-3} and a high methanol abundance (e.g., Sobolev et al. 1997; Cragg et al. 2005).

Like H_2O masers also the 6.7-GHz CH_3OH masers satisfy the conditions $g\Theta >> \Gamma > R$. Considering an upper limit for the brightness temperature of 10^{12} K (Menten et al. 1992) and $\Delta\Omega = 10^{-2}$ sr, from Eq. 2.30 the stimulated rate is $R < 0.04\ \mathrm{s}^{-1}$ ($A_{\mathrm{ul}} = 0.1532 \cdot 10^{-8}\ \mathrm{s}^{-1}$). The maser decay rate Γ is more difficult to determine. For maser transitions in which infrared pumping is involved, which includes CH_3OH, $\Gamma \sim 1\ \mathrm{s}^{-1}$ (Scappaticci & Watson 1992). However, infrared trapping can reduce this value, although likely not by more than an order of magnitude (Goldreich & Kwan 1974). Alternatively, when the maser transition involves collisions, $\Gamma < 0.1\ \mathrm{s}^{-1}$. However, as the collisional decay rate is smaller than the radiative decay rate, the radiative decay rate determines Γ. Thus $\Gamma = 1\ \mathrm{s}^{-1}$ can be assumed, though other authors have assumed the lower value of $\Gamma = 0.6\ \mathrm{s}^{-1}$ (Minier et al. 2002).

Even with conservative estimates for R and Γ, the CH_3OH masers are in the regime where $\Gamma > R$. However, $g\Theta$ must be sufficiently much larger than R and Γ so that, even in the case of anisotropic pumping, the polarization vectors can be used to determine the magnetic field direction.

For a magnetic field strength of $B \approx 100$ mG it is expected that from the recalculated g Landé factor coefficient $g\Theta \approx 0.1B[\mathrm{mG}] = 10\ \mathrm{s}^{-1}$ (Vlemmings et al. 2011). Nedoluha & Watson (1990) found that, for a ratio $R/\Gamma < 0.1$ and $g\Theta/\Gamma > 10$, the relation between polarization angle and magnetic field direction hold to within $\sim 15°$. This improves quickly to better than $\sim 5°$ when $g\Theta/\Gamma$ becomes larger. The CH_3OH masers are thus in the regime where the polarization vectors directly determine the magnetic field direction within a 5° uncertainty.

Even though CH_3OH is the most abundant of massive star-formation maser species, the first 6.7-GHz CH_3OH maser linear polarization observations have only recently been made (e.g., Vlemmings et al. 2006b; Green et al. 2007; Dodson 2008). Like H_2O, CH_3OH is a non-paramagnetic molecule, and thus any linear polarization is a few percent ($\sim 2-3\%$), while circular polarization is well below 1% (e.g., Vlemmings et al. 2006b; Vlemmings 2008). Still, Vlemmings (2008) detected 6.7-GHz CH_3OH masers Zeeman-splitting for the first time in a sample of 24 massive star-forming regions using the Effelsberg telescope. Recently, Vlemmings et al. (2011) extended this sample up to a total of ~ 100 massive star-forming regions. Since the Zeeman-splitting coefficient for the 6.7-GHz CH_3OH masers is uncertain, it is not possible to estimate the magnetic field strength until careful laboratory measurements of the g Landé factor are made (Vlemmings et al. 2011). The range of Zeeman-splitting ΔV_{Z} measured so far is between $-1.49\ \mathrm{km\,s^{-1}}$ and $+1.36\ \mathrm{km\,s^{-1}}$.

Chapter 3

Instruments, data reduction and analysis

The maser lines occur in the radio range of the electromagnetic spectrum, thus the observations of masers can only be made by using radio-telescopes. Since the aim of this Ph.D. research is to investigate the magnetic field on scales of a few hundred astronomical units in massive star-forming regions at distances of the order of kiloparsec, milli-arcsecond angular resolution observations are needed. Therefore this can only be achieved with radio-interferometry. Three of the most powerful facilities in this respect are the Multi-Telescope Radio Linked Interferometer in England, the Very Long Baseline Array in the USA, and the European VLBI Network, which consists of several antennas located in Europe, Asia, and South-Africa. Beside introducing the polarization in radio-interferometry technique (Sect. 3.1), this chapter also contains a description of the software tools used to calibrate and analyse the data (Sect. 3.2).

3.1 Polarization in radio-interferometry

The *resolving power* of a radio-telescope, and in general for an imaging device, is the ability to separate points of an object which are located at a small angular distance. The minimum *angular resolution* (ϑ), i.e. minimum resolvable distance between distinguishable objects, is given by

$$\sin \vartheta = 1.22 \, \frac{\lambda}{\mathrm{D}}, \tag{3.1}$$

where λ is the wavelength of the radiation and D is the diameter of the radio-telescope aperture, which is approximately the diameter of the antenna dish. Considering a wavelength of 1.3 cm and $D = 100$ m (e.g., the Effelsberg telescope) the angular resolution is $\vartheta \approx 35''$. Hence, for a given

frequency, to improve the angular resolution of the observations it is necessary to increase the diameter of the radio-telescope. However, the engineering limits make impossible to have diameter greater than 300 m (e.g., Arecibo telescope), for which $\vartheta \approx 11''$ at $\lambda = 1.3$ cm. In order to reach angular resolution of the order of milliarcsecond ($0\overset{''}{.}001 \equiv 1$ mas) the radio-interferometry technique has to be used. In this technique the distance (or better known *baseline*) between the telescopes is important, in fact

$$\vartheta\ [''] \approx \frac{\lambda\ [\mathrm{cm}]}{B\ [\mathrm{km}]}, \tag{3.2}$$

where D has been replaced by the baseline B. An angular resolution $\vartheta \sim 0\overset{''}{.}001$ at $\lambda = 1.3$ cm is reached with $B \sim 1000$ km. In order to have a good image with low rms noise it is necessary to increase either the observational time, or the number of antennas, or the sensitivity of the antennas. The detailed theory of radio-interferometry can be read in Thompson (1999), while a summary of the polarization in interferometry is treated in this section (based on Cotton 1999).

Polarization measurements are generally made using a pair of feeds[1] on each interferometer element; usually these are sensitive to orthogonal circular polarizations. There are several effects that can modify or corrupt the polarized signals. These need to be evaluated and the derived corrections must be applied to the data before it can be used. The phase relation of the signals detected by the two feeds of any given interferometer element can be disturbed both by *ionospheric Faraday rotation* and by the *interferometer electronics*. Interferometers using circularly polarized feeds do not directly measure the polarization angle of a source, so observations of a *calibrator of known polarization angle* are necessary.

Since *ionospheric Faraday* rotation is time variable, it can corrupt polarization images from an extended synthesis or produce incorrect polarization angles for snapshot observations. The strong dependence on observing frequency means that it is most troublesome for low frequencies observations (< 2 GHz), especially near maxima in solar activity when the ionosphere is the most active. Since the frequency of the observations made in this Ph.D. research are greater than 2 GHz this effect is not treated further here.

Let consider the instrumental response to a polarized signal. The response of antenna i with orthogonally polarized feeds R and L[2] can be factorized into a number of physically distinct

[1] In a radio-telescope the feed is typically a waveguide horn and transfers the incoming signal to the sensitive radio receiver.

[2] R and L refer to the right circular polarization (RCP) and to the left circular polarization (LCP) receivers, respectively.

components using the *Jones' matrix formalism*:

$$J_{\rm i} = G_{\rm i}\ D_{\rm i}\ P_{\rm i}. \tag{3.3}$$

The first term, $G_{\rm i}$, is usually called the *gain* and is

$$G_{\rm i} = \begin{pmatrix} g_{\rm iR} & 0 \\ 0 & g_{\rm iL} \end{pmatrix}, \tag{3.4}$$

where $g_{\rm iR}$ and $g_{\rm iL}$ are complex gain factors for the two orthogonally polarized signals. This term represents the uncorrected effects of the atmosphere and electronics.

The second term, $D_{\rm i}$, is called *leakage* and models imperfections in the feed polarization response. This term is given by

$$D_{\rm i} = \begin{pmatrix} 1 & d_{\rm iR} \\ -d_{\rm iL} & 1 \end{pmatrix}, \tag{3.5}$$

where $d_{\rm iR}$ and $d_{\rm iL}$ are complex *leakage* terms which represent the fraction of the orthogonally polarized signal *leaking* into a given feed.

The third term includes the effects of the rotation of an altazimuth mounted[3] antenna as seen by the source while the antenna tracks the source. This rotation, known as *parallactic angle*, is given by

$$\psi = \tan^{-1}\left(\frac{\cos(\varsigma)\ \sin(\varrho)}{\sin(\varsigma)\ \cos(\delta) - \cos(\varsigma)\ \sin(\delta)\ \cos(\varrho)}\right), \tag{3.6}$$

where δ is the source declination, ς is the latitude of the antenna, and ϱ is the source hour angle. Antennas with equatorial mounts do not rotate and therefore have a constant parallactic angle ($\psi = 0$). Parallactic angle has an effect on the measured signals which depends on the feed polarization type, for circular feeds it is

$$P_{\rm i} = \begin{pmatrix} e^{-j\psi} & 0 \\ 0 & e^{j\psi} \end{pmatrix}, \tag{3.7}$$

where $j = \sqrt{-1}$.

The interferometer response to polarized radiation is thus given by

$$\iota = (J_{\rm i} \otimes J_{\rm k}^{*})\ S\ s, \tag{3.8}$$

where S is the coordinate transformation from Stokes system to that of the correlations, s is the the true Stokes visibility vector and * indicates the complex conjugate. In the limit of a weakly

[3]An *altazimuth mount* is a simple two-axis mount for supporting and rotating an antenna about two mutually perpendicular axes; one vertical and the other horizontal. Rotation about the vertical axis varies the azimuth (compass bearing) of the pointing direction of the instrument. Rotation about the horizontal axis varies the altitude (angle of elevation) of the pointing direction.

polarized source and nearly perfect feeds the linearized approximation for circularly polarized feeds on baseline $i-k$ is

$$\iota_{\rm RR} = \frac{1}{2}\, g_{\rm iR}\, g^*_{\rm kR}(I+V), \tag{3.9}$$

$$\iota_{\rm RL} = \frac{1}{2}\, g_{\rm iR}\, g^*_{\rm kL}\left[(d_{\rm iR} - d^*_{\rm kL})\; I + e^{-2j\psi}(Q+jU)\right], \tag{3.10}$$

$$\iota_{\rm LR} = \frac{1}{2}\, g_{\rm iL}\, g^*_{\rm kR}\left[(d^*_{\rm kR} - d_{\rm iL})\; I + e^{2j\psi}(Q-jU)\right], \tag{3.11}$$

$$\iota_{\rm LL} = \frac{1}{2}\, g_{\rm iL}\, g^*_{\rm kL}(I-V). \tag{3.12}$$

Eq. 3.10 and 3.11 show that the *instrumental contribution* (the first term in both equations) to the cross polarized interferometer response is unaffected by parallactic angle so it can be evaluated separetely from the effect of the source.

For interferometer with altazimuth mounts (e.g., VLBA, EVN, MERLIN), observations of a calibrator source over a range of parallactic angles can be used to separate the effects of source and instrumental polarization. Polarization calibration consists of several independent steps: determining and correcting instrumental polarization and calibrating the polarization angle. Correlations between parallel and circular feeds are sensitive to total intensity and the source circular polarization. Synchrotron emitting, compact extra-galactic sources are quite weakly circularly polarized, usually less than 0.1%. Calibration using such a source can assume it to have no circular polarization to quite high accuracy. This approximation allows the separation of the calibration of the R and L gains from each other and from the instrumental polarization. Measured interferometer phases are sensitive only to differences in gain phases, so the usual calibration procedure is to arbitrarily set the gain phase of a *reference antenna* to zero independently for the R and L systems of feeds. Since this independent calibration ensures that the $R-L$ phase difference is that of the reference antenna, it is important to use the same reference antenna for both the R and L calibration. This usual calibration technique of independently calibrating R and L systems thus leaves an unknown *phase difference* between them. Moreover in the case of Very Long Baseline Interferometry (VLBI) observations, there is also a $R-L$ *delay offset* between the two systems.

The spurious instrumental contribution to the measured correlations are given by the *D-terms* (Eq. 3.5), and *instrumental polarization calibration* consists of determining these values and applying corrections to the measured correlations by observing a calibrators of known (or unknown) polarization.

The unknown $R-L$ phase difference, which comes from the independent calibration of R

and L systems, produces a rotation of the apparent *polarization angle* of the source. In this case this difference can be corrected by making sufficiently sensitive measurements of a calibrator of known polarization. Note that a constant $R - L$ phase difference will not corrupt the derived image other than to produce the wrong polarization angle; fractional linear polarization is unaffected.

3.2 "Software tools"

This last section of the introduction part of this thesis is focused on three different important "software tools". The first is the data reduction recipe for calibrating the European VLBI Network (EVN) spectral data at 6.7 GHz in full polarization, this is necessary because no observations of this type were made before this thesis work.

The second "tool" is a process that is able to identify maser features in a calibrated image cube. This process is faster than any other identification process used so far. The last "tool" is a code that allows to analyse the polarized maser emission with the model described in Chapter 2.

3.2.1 EVN data reduction procedure in AIPS

All the EVN data were edited and calibrated using the Astronomical Image Processing System (AIPS), which is characterized by independent *tasks* that are regulated by input parameters called *verbs* and *adverbs*.

After loading the FITS data-set, provided by the correlator of the Joint Institute for VLBI in Europe (JIVE), with the task FITLD, the data were inspected with several tasks. The very first calibration must be done on the amplitude and the parallactic angles, both of which are already calibrated by JIVE. The solutions obtained from the calibrators (unpolarized and polarized) are usually provided as separated tables that can be copied and applied on the entire data-set. However, these steps can be done by the tasks APCAL and CLCOR. After applying these first corrections an accurate *flagging* procedure is necessary. The term *flagging* refers to the action of deleting visibilities that vary from the general trend of the most of visibilities (see Thompson 1999). Before the calibration of the polarization, it is crucial to correct the frequency and time dependent phase variations, which are the delay and the phase rate due to the VLBI technique, by *fring-fitting* the visibilities running the task FRING on the calibrators. In spectral mode it is also necessary to determine the bandpass response functions of the antennas and in AIPS this is achieved with the task BPASS, the solutions from the continuum calibrator are thus applied to

the data-set.

The phase and delay corrections obtained by fring-fitting the calibrators can only remove $R-R$ and $L-L$ offsets between different antennas. There is still $R-L$ phase delay offsets. The $R-L$ delay corrections are determined using the procedure VLBACPOL that runs different tasks on a selected subset of the data-set. In this case the calibrator must be the polarized calibrator. The calibration of the polarization continues with the measurements of the $D-terms$. Before doing that, it is important to insert the polarization intensity of the polarized calibrator in the data-set, this can be done by the task SETJY. The $D-terms$ are then determined running the task PCAL. Although this procedure for calibrating the polarization is usually used for the Very Long Baseline Array (VLBA observations), this works perfectly also for the EVN observations. Finally the correction of the polarization angles is made out of AIPS. This is made by rotating all the polarization angles of the masers according to the difference between the polarization angle of the polarized calibrator measured after the whole calibration and that one measured by the National Radio Astronomy Observatory (NRAO). This can be find in their website (http://www.aoc.nrao.edu/ smyers/calibration/).

The last part of the calibration consists of *self-calibrating* the source of interest. In maser observations, especially when the masers are very bright, the self-calibration is done on the channel that shows the brightest maser spot, which can be considered as a point source. Of course before that, it is necessary to check and eventually flag some bad visibilities and determine the delay and the phase rate solutions for the brightest channel in order to refine the fring-fitting calibration. The self-calibration is composed of several interactive cycles of phase and amplitude-phase solutions. This means to produce a model of the spot running the imaging task IMAGR (only the RR image) and then to find the phase (or amplitude-phase) solutions with the task CALIB by varying the time interval on which the solutions must be determined in each cycle. In order to measure the polarization angle of the polarized calibrator (see above) it is also necessary to self-calibrate it. The calibration is thus ended.

Now the different image cubes can be produced with IMAGR. In the subsequent analysis, see below, it is also necessary to produce the polarization intensity and polarization angle image cubes. These are defined in term of Stokes parameters by

$$POLI = \sqrt{Q^2 + U^2}, \tag{3.13}$$

$$POLA = \frac{1}{2}\,\tan^{-1}\,\frac{\mathrm{U}}{\mathrm{Q}}. \tag{3.14}$$

Therefore the Q and U image cubes must be combined together and the task COMB is designed for this purpose.

3.2.2 Maser identification process

To identify the H_2O and CH_3OH maser features in massive star-forming regions, an *identification process* divided into three steps has been used: 1) running the program called "maser finder", which is able to search for maser spots, velocity channel by velocity channel, with a signal-to-noise ratio greater than a given value; 2) fitting the identified maser spots using the AIPS task IMFIT; and 3) identifying a maser feature when three or more maser spots coincided spatially (within a box of 2 by 2 pixels) and each of them appeared in consecutive velocity channels.

In the first part of the process and after evaluating the global noise level of the channel map, the program searches for maser spots in the velocity map, excluding the edges of the channel map. When strong maser spots are found (for instance, with a peak flux density higher than 2 Jy beam^{-1}), the local rms around these strong maser spots (within a predefined box, for instance, 400 by 400 pixels) is estimated, as well as the rms outside the boxes. The program identifies a maser spot when the SNR of the candidate (using the local rms) is greater than a predefined value. A lower limit of 8-sigma has been adopted in this Ph.D. work. The program produces a table with the spatial location and intensity of all the identified maser spots. This procedure is repeated for each velocity channel included in the input file that is used by the program. The program also produces a script for each velocity channel that can be run inside AIPS in order to produce Gaussian fits of all the identified maser spots. After running all the AIPS scripts, a table with all the important parameters (e.g., spatial resolution, velocity, intensity) of each maser spot is produced. Then the output table have been used to search for maser features that fulfill the criteria described above.

3.2.3 Full radiative transfer method code

From the maser theory we know that the fractional linear polarization P_l of the H_2O maser emission depends on the degree of its saturation and the angle (θ) between the maser propagation direction and the magnetic field. Even the relation between the measured polarization angle χ and the magnetic field angle on the sky (ϕ_B) depends on θ, with the linear polarization vector perpendicular to the field for $\theta > \theta_{\rm crit} \sim 55^\circ$ (Sect. 2.2). It is therefore important to evaluate θ for every H_2O and CH_3OH maser that shows linear polarization emission. In order to obtain the best

values for θ, it is necessary to determine the emerging brightness temperature ($T_{\rm b}\Delta\Omega$) and the intrinsic thermal linewidth ($\Delta V_{\rm i}$), which is the full width half-maximum (FWHM) of the Maxwellian distribution of particle velocities (i.e. $\Delta\nu_{\rm D}$ of Sect. 2.1), of the masers with high precision. For the H_2O maser this could be done by fitting the emissions with the *full radiative transfer method* described by Vlemmings et al. (2006a), who successfully used it for H_2O masers in Cepheus A. This radiative transfer method is based on Eqs. 2.24, 2.25, and 2.26 of the model of Nedoluha & Watson (1992), for which the shapes of the total intensity (I), linear polarization ($POLI$), and circular polarization spectra (V) depend on $T_{\rm b}\Delta\Omega$ and $\Delta V_{\rm i}$. Eq. 2.25 is still valid even if $U(\omega) \neq 0$, in fact there $Q(\omega)$ represents the linearly polarized intensity that can be replace with the $POLI$ spectra. Nedoluha & Watson (1992) also found that the emerging brightness temperature scaled linearly with $(\Gamma + \Gamma_\nu)$. Since for the 22-GHz H_2O masers $\Gamma \lesssim 1{\rm s}^{-1}$ and Γ_ν depends on the gas temperature, The value $(\Gamma + \Gamma_\nu) = 1{\rm s}^{-1}$ has been considered, so that the fitted $T_{\rm b}\Delta\Omega$ values can be adjusted by simply scaling according to $(\Gamma+\Gamma_\nu)$. Note that $\Delta V_{\rm i}$ and θ do not need to be adjusted.

We modelled the observed $POLI$ and I maser spectra by gridding the intrinsic thermal linewidth ΔV_i between 0.4 and 3.5 $\rm km\,s^{-1}$, in steps of 0.025 $\rm km\,s^{-1}$, using a least square fitting routine (χ^2-model) with an upper limit of the brightness temperature $T_{\rm b}\Delta\Omega = 10^{11}$ K sr. From these first fits, the angles θ can be obtained by considering the relation between $P_{\rm l}$ and θ (see Vlemmings et al. 2006a for more details). The best values for $T_{\rm b}\Delta\Omega$ and $\Delta V_{\rm i}$ are then included in the full radiative transfer code to produce the I and V models that were used for fitting the total intensity and circular polarized spectra of the H_2O masers extracted from the high-resolution I and V cubes. The magnetic field strength along the line-of-sight is evaluated by using the equation

$$B_{||} = B\ cos\theta = \frac{P_V\ \Delta v_L}{2 \cdot A_{F-F'}}, \tag{3.15}$$

where Δv_L is the FWHM of the total intensity spectrum, the $A_{\rm F-F'}$ coefficient, which depends on $T_{\rm b}\Delta\Omega$, describes the relation between the circular polarization and the magnetic field strength for a transition between a high (F) and low (F') rotational energy level. The circular polarization fraction ($P_{\rm V}$) is obtained from the I and V models. Note that this code can fit the I and $POLI$ spectra only if the spectral velocity resolution $\delta_{\rm v}$ is less than 1.5 $\rm km\,s^{-1}$, and the V spectrum if $\delta_{\rm v} < 0.05$ $\rm km\,s^{-1}$. To measure the Zeeman-splitting when $\delta_{\rm v} \geq 0.05$ $\rm km\,s^{-1}$ the cross-correlation between the RR and LL spectra is used.

Since the 6.7-GHz CH_3OH maser satisfy the condition $g\Theta >> \Gamma > R$ (Sect. 2.3.2) the model for H_2O masers can be adapted to the CH_3OH by replacing the nine $A_\omega^{\rm FF'}$, $B_\omega^{\rm FF'}$, and $C_\omega^{\rm FF'}$ coefficients with the three corresponding coefficients of the CH_3OH maser transition 5_1-6_0 A^+. In this case the

grid of the intrinsic thermal linewidth ΔV_i was between 0.5 and 2.6 km s^{-1}, in steps of 0.05 km s^{-1}.

Another important aspect that must be considered in the analysis of the H_2O and CH_3OH masers is the degree of their saturation, which influences P_l. We are able to estimate it by considering the ratio between maser rate of stimulated emission (R) and the sum of maser decay rate and the cross-relaxation rate ($\Gamma + \Gamma_\nu$). The masers are unsaturated when $R/(\Gamma + \Gamma_\nu) < 1$, in the onset of saturation when $R/(\Gamma + \Gamma_\nu) \geq 1$, and fully saturated when $R/(\Gamma + \Gamma_\nu) \approx 100$ (Vlemmings et al. 2006a). Moreover, when the saturation sets in, the maser lines start to broaden again (Sect. 2.1), and this means that the observed linewidth (Δv_L) becomes as large as ΔV_i or larger depending on the degree of the saturation.

Although the full radiative transfer method is based on a model for general H_2O and CH_3OH masers, it should be noted that, when this model is applied to *saturated masers*, it is impossible to properly disentangle the values of $T_b\Delta\Omega$ and ΔV_i. In this case the method only provides a lower limit for $T_b\Delta\Omega$ and an upper limit for ΔV_i. For high maser brightness temperatures, i.e. greater than 10^9cm^{-3} K sr (Nedoluha & Watson 1992), the cosθ dependence of Eq. 3.15 breaks down thereby introducing a more complex dependence on θ. As a result, the angle θ obtained from the fit is overestimated and, in particular, reaches a value of 90°. Consequently, the values of $T_b\Delta\Omega$, ΔV_i and θ obtained for saturated masers could not be taken into account in the analysis.

RESULTS

Chapter 4

Cepheus A

We present polarization observations of the 6.7-GHz CH_3OH masers around the massive protostar Cepheus A HW2 and its associated disc. The data were taken with the Multi-Element Radio Linked Interferometer Network. The maser polarization is used to determine the full three-dimensional magnetic field structure around Cepheus A HW2. The observations suggest that the masers probe the large scale magnetic field and not isolated pockets of a compressed field. We find that the magnetic field is predominantly aligned along the protostellar outflow and perpendicular to the molecular and dust disc. From the three-dimensional magnetic field orientation and measurements of the magnetic field strength along the line-of-sight, we are able to determine that the high density material, in which the masers occurs, is threaded by a large scale magnetic field of ~ 230 mG. This indicates that the protostellar environment at ~ 1000 AU from Cepheus A HW2 is slightly supercritical and the relation between density and magnetic field is consistent with collapse along the magnetic field lines. Thus, the observations indicate that the magnetic field likely regulates accretion onto the disc. The magnetic field dominates the turbulent energies by approximately a factor of three and is sufficiently strong to be the crucial component stabilizing the massive accretion disc and sustaining the high accretion rates needed during massive star formation.

4.1 The source

Cepheus A is one of the closest regions of active massive star formation at a distance of 700 pc (Moscadelli et al. 2009). Located in the Cepheus OB3 complex, it hosts a powerful extended bipolar molecular outflow that likely originates from HW2, the brightest radio continuum source in the region (Hughes & Wouterloot 1984). HW2 is thought to be a young protostar of spectral type B0.5 with a mass of $\sim$20 $M_\odot$ (Jiménez-Serra et al. 2007). The extended outflow appears to

be driven by a small scale (∼700 AU) thermal radio jet, with ionized gas ejected at a velocity of ∼500 km s^{-1} (Curiel et al. 2006). In addition to the bipolar outflow, Cepheus A HW2 is surrounded by a rotating disc of dust and molecular gas oriented perpendicular to the jet (Jiménez-Serra et al. 2007; Patel et al. 2005; Torrelles et al. 2007). The jet and disc structure supports the picture where massive stars form through disc accretion, similar to low-mass stars. The environment of Cepheus A HW2 however, is significantly more complex than that of typical low-mass protostars. Besides HW2, at least three additional young stellar objects are located within an area of $\sim 500 \times 500$ AU. All these sources seem to be located within or close to the molecular disc (Torrelles et al. 2007; Comito et al. 2007; Jiménez-Serra et al. 2009). The presence of OH, H_2O and CH_3OH masers in or near to the disc of Cepheus A HW2 gives us an unique opportunity to study its magnetic field (Vlemmings et al. 2006a; Bartkiewicz et al. 2005), with recent CH_3OH maser Zeeman-splitting measurements revealing a dynamically important magnetic field with a ~ 8 mG component along the maser line-of-sight (Vlemmings 2008). This value was measured considering a Zeeman-splitting coefficient $\alpha = 0.049$ km s^{-1} G^{-1} that is larger than the most recent one ($\alpha = 0.005$ km s^{-1} G^{-1}, Vlemmings et al. 2011), and consequently $B_{||} = \Delta V_Z/\alpha_Z$ might be one order of magnitude larger. Since α_Z is still uncertain until careful laboratory measurements of g are made, we can conservatively consider $B_{||} > 8$ mG.

4.2 Observations and data reduction

4.2.1 6.7-GHz MERLIN data

The $5_1 - 6_0$ A$^+$ maser transition of CH_3OH at 6.7-GHz was observed on 2006 December 2-4 using 6 of the Multi-Telescope Radio Linked Interferometer (MERLIN[1]) telescopes. Total on source time was ~ 27 hr, which was interleaved with observations of the phase calibrator source 2300+638. The resulting beam-size was 40×30 mas. We used a 250 kHz bandwidth with 256 channels for a total velocity coverage of ~ 11 km s^{-1} centred on the source local standard of rest (LSR) velocity $V_{\rm LSR} = -3$ km s^{-1}. This provided a velocity resolution of 0.044 km s^{-1}. To obtain the linear polarization, the data were correlated with the full Stokes parameters. For calibration purposes, the continuum calibrators were observed with the 16 MHz wide-band mode. Both 3C84 and 3C286 were also observed in the narrow-band spectral line configuration and were used to determine the phase off-set between the wide- and narrow-band setup. Flux and bandpass calibration was done

[1]MERLIN is operated by the University of Manchester as a National Facility of the Science and Technology Facilities Council

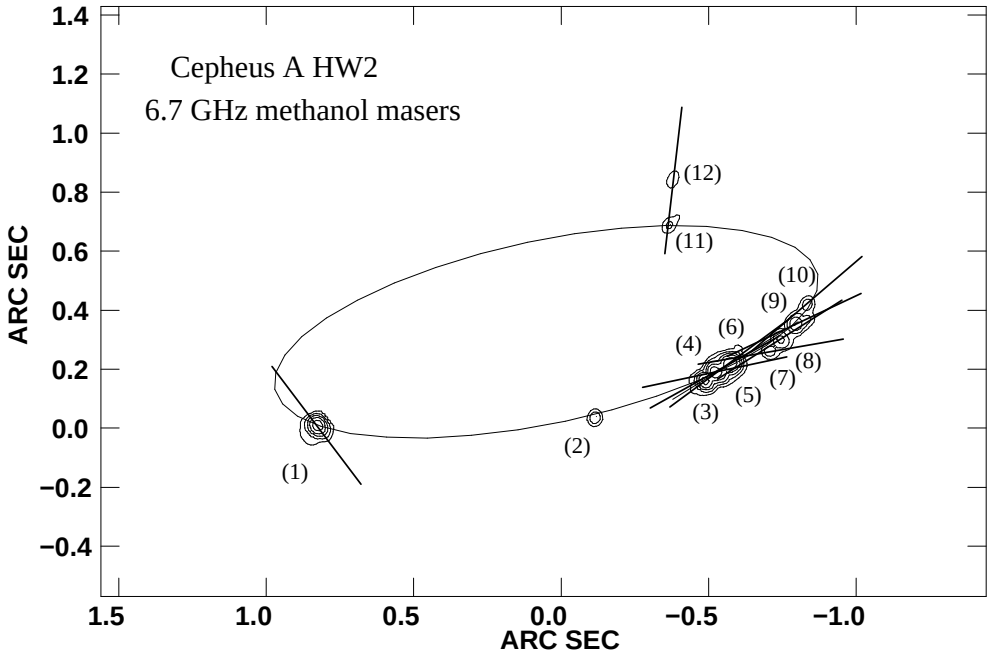

Figure 4.1: Total intensity (I) map of the 6.7-GHz CH_3OH masers around Cepheus A HW2. Contours are drawn at $5, 10, 20, 40$ & 80 Jy beam^{-1}. The labels identify the features presented in Tables 4.1. The vectors indicate the observed polarization angle χ. Also indicated is the best fit ellipse to the CH_3OH maser feature distribution observed with MERLIN.

using the primary flux calibrator 3C286. Instrumental feed polarization was determined using the unpolarized calibrator 3C84 and the polarization angle was calibrated using 3C286. The residual instrumental linear polarization was determined to be less than $< 0.1\%$ from the observations of 3C84 and 2300+638. Self-calibration, in RCP and LCP separately, was performed on the strongest isolated maser feature. After calibration, the antenna contributions were re-weighted according to their sensitivity at 5 GHz and their individual efficiency. Finally, $5\farcs12 \times 5\farcs12$ image cubes were created in Stokes I, Q, and U. The rms noise in the emission free channels was ~ 6 mJy beam^{-1} for Stokes I and ~ 9 mJy beam^{-1} for Stokes Q and U. For the channels with strong maser emission we are limited to a dynamic range of ~ 850 due to residual calibration errors. Because of the dynamic range limit we were unable to determine the circular polarization due to Zeeman-splitting in these observations. The non-detection of the $\sim 0.17\%$ circular polarization observed for the 6.7-GHz CH_3OH masers using the Effelsberg 100-m telescope (Vlemmings 2008) is unsurprising considering the rms noise limits of our circular polarization observations ($1\sigma \sim 0.12\%$).

We modelled the observed linear polarized and total intensity CH_3OH maser spectra with the full radiative transfer method code (see Sect. 3.2.3).

4.3 Results

4.3.1 Maser distribution

The resulting velocity integrated image of the 6.7-GHz CH_3OH maser features around Cepheus A HW2 is shown in Fig. 4.1. No maser emission was detected at < 5 Jy beam^{-1}. The 12 maser features that were identified are shown in Fig. 4.2 and presented in Table 4.1 with position offsets, velocity ($V_{\rm LSR}$), peak flux ($I_{\rm peak}$), fractional linear polarization ($P_{\rm l}$), polarization angle (χ), intrinsic thermal linewidth ($\Delta V_{\rm i}$), emerging brightness temperature ($T_{\rm b}\Delta\Omega$), angle between magnetic field and maser propagation direction (θ), and the magnetic field angle on the sky ($\phi_{\rm B}$).

Table 4.1: All 6.7-GHz CH_3OH maser features detected in Cepheus A HW2 with the MERLIN.

(1) Maser	(2) RA offset (arcsec)	(3) Dec offset (arcsec)	(4) Peak flux Density(I) (Jy/beam)	(5) $V_{\rm lsr}$ (km/s)	(6) $P_{\rm l}$ (%)	(7) χ (°)	(8) $\Delta V_{\rm i}{}^{b}$ (km/s)	(9) $T_{\rm b}\Delta\Omega^{b}$ (log K sr)	(10) θ^{c} (°)	(11) $\phi_{\rm B}$ (°)
1	0.826	0.010	136.1	-4.14	0.15 ± 0.02	37 ± 6	$1.41^{+0.04}_{-0.08}$	$8.08^{+0.58}_{-0.47}$	47^{+27}_{-24}	37 ± 11
2	-0.113	0.038	15,5	-2.78	–	–	–	–	–	–
3	-0.489	0.161	101.5	-1.82	0.40 ± 0.06	-79 ± 2	$1.30^{+0.06}_{-0.11}$	$8.20^{+0.78}_{-0.16}$	68^{+7}_{-45}	11 ± 7
4	-0.528	0.189	131.1	-2.30	1.10 ± 0.08	-65 ± 10	–	–	73^{+11}_{-9}	25 ± 15
5	-0.564	0.212	136.3	-2.60	1.01 ± 0.03	-56 ± 2	$1.46^{+0.07}_{-0.17}$	$8.59^{+0.35}_{-0.08}$	73^{+16}_{-10}	34 ± 7
6	-0.593	0.228	74.8	-2.73	1.88 ± 0.05	-56 ± 4	$1.50^{+0.18}_{-0.08}$	$8.90^{+0.35}_{-0.08}$	77^{+10}_{-7}	34 ± 9
7	-0.710	0.270	15.3	-3.68	1.48 ± 0.07	-80 ± 2	$1.35^{+0.11}_{-0.11}$	$8.78^{+0.43}_{-1.59}$	74^{+15}_{-9}	10 ± 7
8	-0.739	0.308	22.0	-3.65	1.02 ± 0.07	-61 ± 3	–	–	72^{+13}_{-9}	29 ± 8
9	-0.805	0.356	-32.1	3.79	1.04 ± 0.15	-65 ± 1	–	–	72^{+14}_{-9}	25 ± 6
10	-0.830	0.430	16.2	-3.70	0.41 ± 0.02	-49 ± 2	$1.09^{+0.04}_{-0.10}$	$8.20^{+0.50}_{-0.08}$	65^{+23}_{-25}	41 ± 7
11	-0.364	0.687	11.2	-4.66	–	–	–	–	–	–
12	-0.379	0.845	8.8	-4.55	1.65 ± 0.34	-3 ± 4	$1.05^{+0.05}_{-0.14}$	$8.90^{+0.27}_{-0.08}$	72^{+8}_{-10}	87 ± 9

Notes. $^{(a)}$ Position offsets with respect to $\alpha_{2000} = 22^h56^m17.98^s$, $\delta_{2000} = 62°01'49.390"$. $^{(b)}$ The best-fitting results obtained by using a model based on the radiative transfer theory of CH_3OH masers for $\Gamma + \Gamma_\nu = 1$ (Sect 3.2). The errors were determined by analysing the full probability distribution function. $^{(c)}$The angle between the magnetic field and the maser propagation direction is determined by using the observed $P_{\rm l}$ and the fitted emerging brightness temperature. The errors were determined by analysing the full probability distribution function. For those maser features where no radiative transfer fit was possible, including the features without detected linear polarization, we have used the range of brightness temperatures as suggested by the fitted maser features.

The 6.7-GHz CH_3OH maser features make up a nearly perfect elliptical distribution around HW2 and its disc, and the maser distribution observed with MERLIN matches that seen in EVN and Japanese VLBI Network (JVN) observations (Torstensson et al. 2011; Sugiyama et al. 2008a).

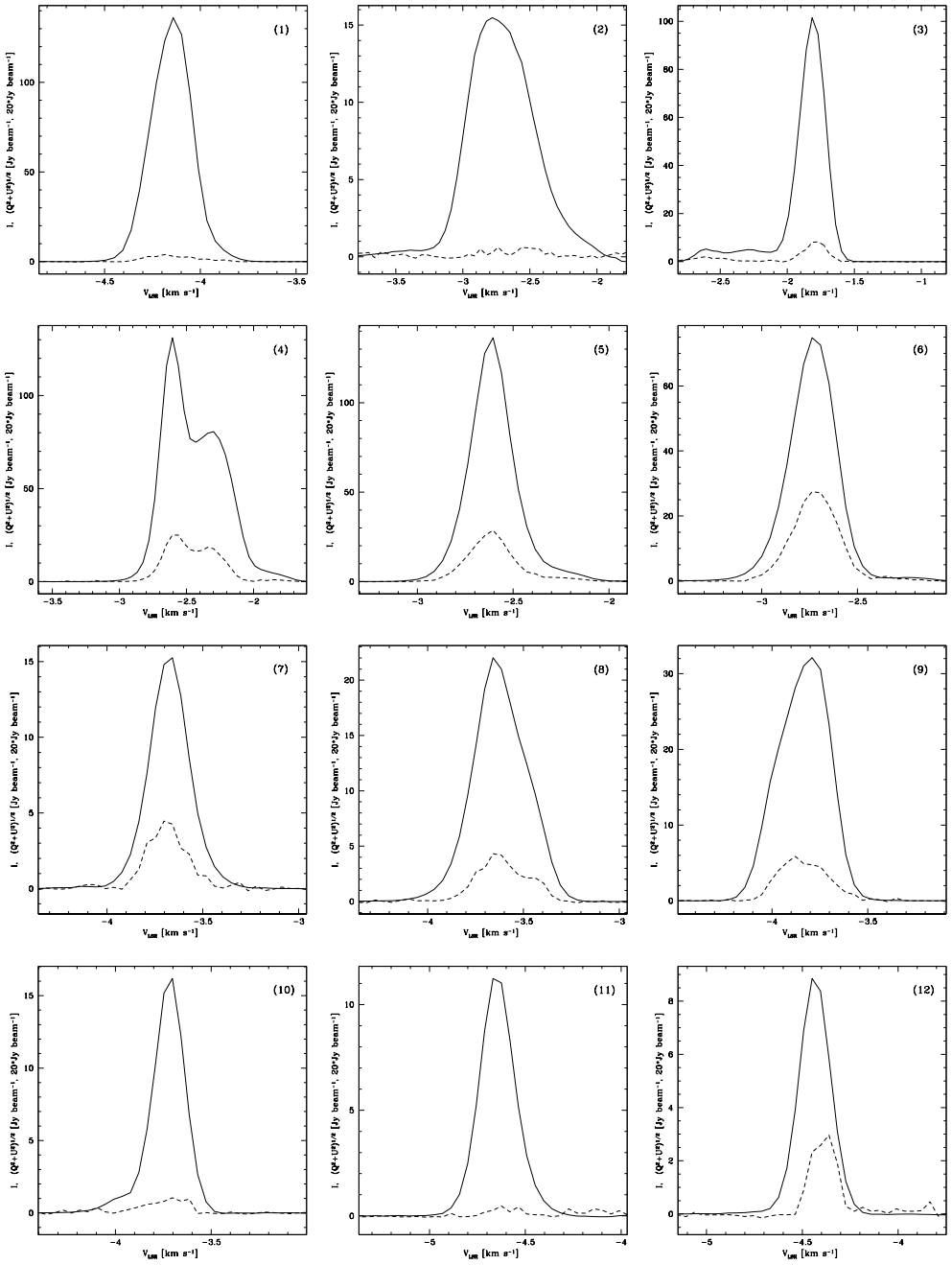

Figure 4.2: Total intensity (I; solid) and linear polarization (dashed) spectra for the 12 CH_3OH maser features detected above a level of 5 Jy beam^{-1} in the MERLIN observations. The linear polarization spectra have been multiplied by a factor 20.

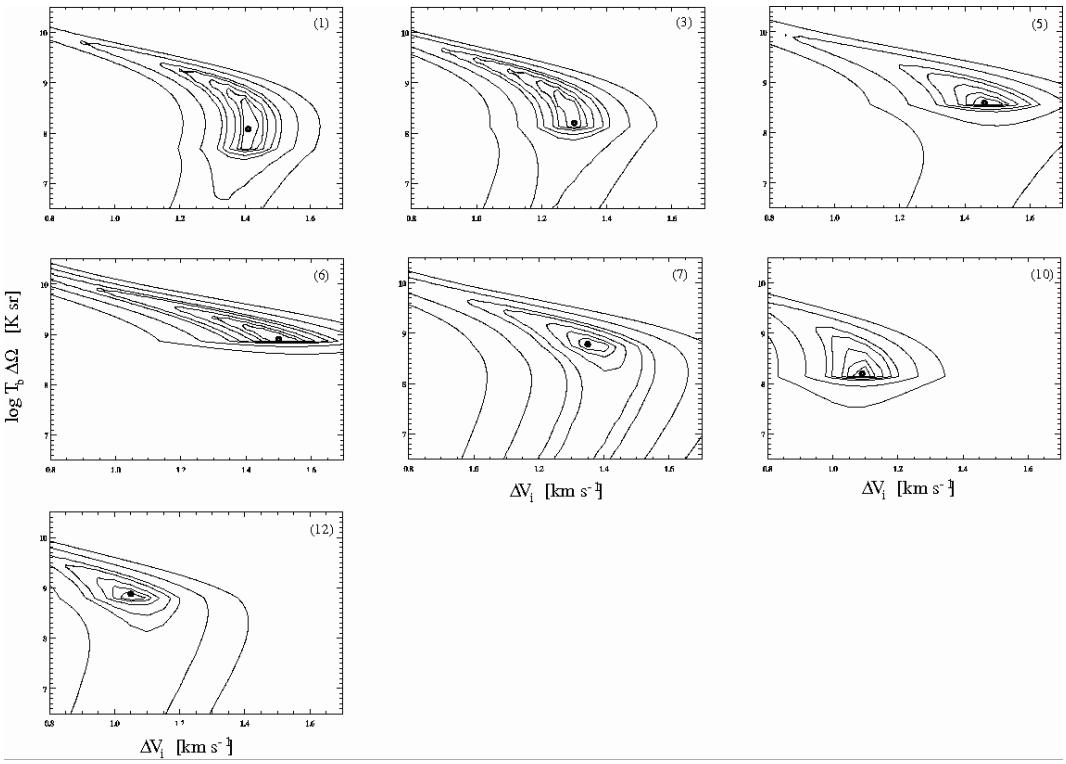

Figure 4.3: Results of the full radiative transfer χ^2-model fits, for those CH_3OH maser features from Fig. 4.2 that do not suffer from blending and for which linear polarization was detected. The fits yield the emerging maser brightness temperature $T_\mathrm{b}\Delta\Omega$ and intrinsic maser linewidth ΔV_i. Contours indicate the significance intervals $\Delta\chi^2 = 0.25, 0.5, 1, 2, 3, 7$, with the thick solid contour indicating the 1σ area.

A least square fit of an ellipse to the MERLIN data indicates that the masers occur in a ring with a radius of ∼650 AU, a thickness of ∼300 AU, a projection angle on the sky of $\varphi = -78°$ and an inclination angle of $i = 71°$. The maser ring appears tilted with respect to the molecular ($r = 580$ AU, $\varphi = -56°$ and $i = 68°$) and dust disc ($r = 330$ AU, $\varphi = -59°$ and $i = 56°$). Observations at high resolution (9×7 mas) with the EVN further indicate that the maser velocities are best fit by infall towards HW2 at $\sim$1.7 $\mathrm{km\,s^{-1}}$ (Torstensson et al. 2011). While the molecular disc rotates with a velocity of $\sim$5 $\mathrm{km\,s^{-1}}$ (Jiménez-Serra et al. 2007), no significant rotation is observed in the maser region.

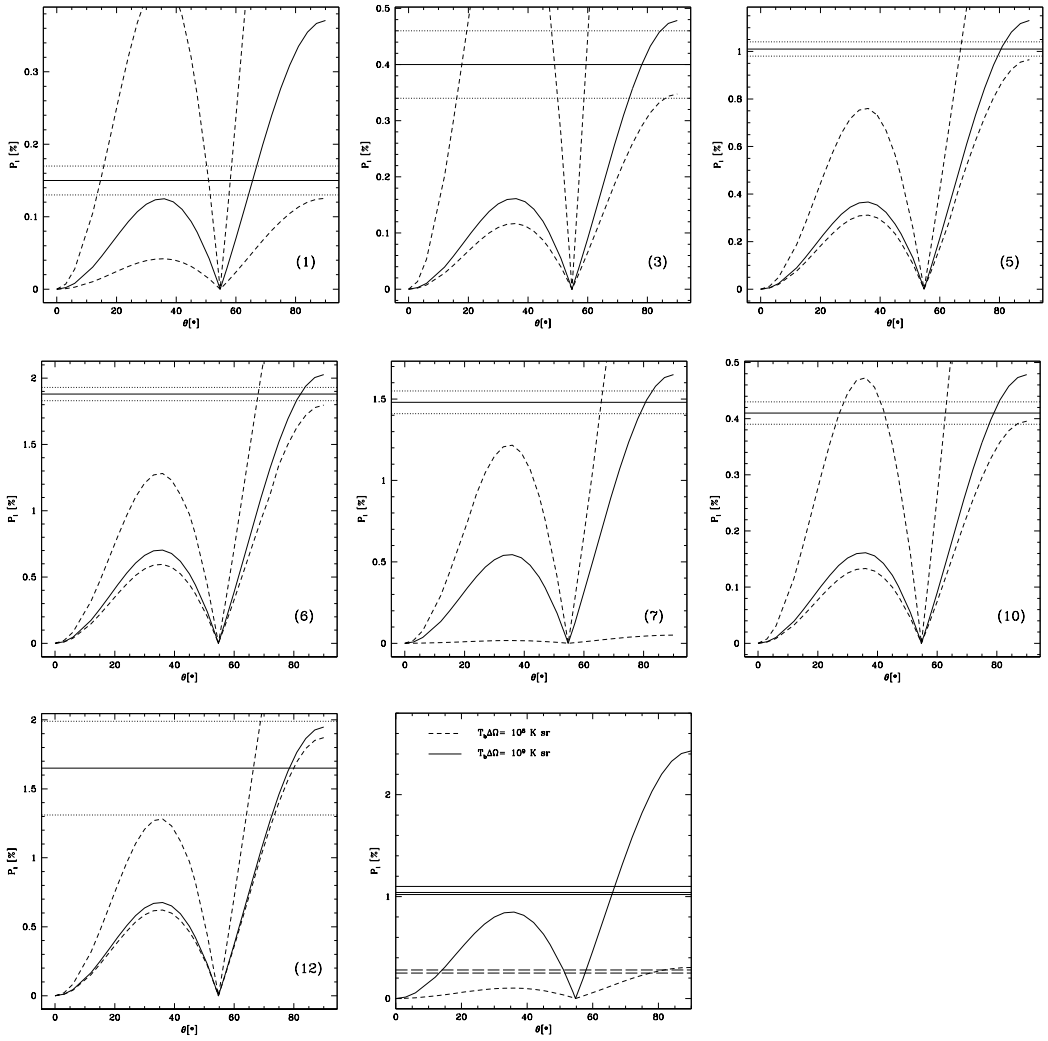

Figure 4.4: The angle θ between the maser propagation direction and the magnetic field vs. the fractional linear polarization P_l. Panels are presented for the 7 CH_3OH maser features for which an accurate fit could be made to the line profiles. The solid curves indicate the best fit emerging brightness temperatures and the dashed curves are the $\pm 1\sigma$ intervals. The horizontal solid and dashed lines are the measured polarization fraction and the corresponding errors. The final panel indicates the remaining 5 maser features with curves for typical emerging brightness temperatures. In this panel, the dashed horizontal lines are the 3σ upper limits for the maser features without measured polarization, as these limits provide strong constraints on θ.

4.3.2 Maser polarization

We used the radiative transfer method adapted to CH_3OH masers described in Sect. 3.2.3 to determine the emerging brightness temperature, $T_b\Delta\Omega$, and the intrinsic thermal linewidth, ΔV_i,

of the observed maser features. As a direct fit requires a regular maser spectrum that does not suffer from blending, we were able to fit to 7 of the maser features around Cepheus A HW2. The results of the fits are shown in Figs. 4.3 and 4.4 and given in Table 4.1. They indicate an emerging brightness temperature in the range 10^8 K sr$< T_\mathrm{b}\Delta\Omega < 10^9$ K sr, implying that the masers are not saturated, as the ratio of stimulated emission rate over decay rate $0.04 < R/(\Gamma + \Gamma_\nu) < 0.4$ (Sect. 2.3.2), and that our assumption for $\Delta\Omega$ in Sect. 2.3.2 is valid. It is worthwhile noting that our model calculations of the $T_\mathrm{b}\Delta\Omega$ assume $(\Gamma + \Gamma_\nu) = 1\ \mathrm{s}^{-1}$. However, the model emerging brightness temperature scale linearly with $(\Gamma + \Gamma_\nu)$ and consequently the saturation level $(R/(\Gamma + \Gamma_\nu))$ does not change. The intrinsic maser thermal linewidth lies in the range $1.0\ \mathrm{km\,s^{-1}} < \Delta V_\mathrm{i} < 1.5\ \mathrm{km\,s^{-1}}$, with a weighted average $\langle \Delta V_\mathrm{i} \rangle = 1.3 \pm 0.2\ \mathrm{km\,s^{-1}}$, which is much larger than the observed linewidth $\Delta v_\mathrm{L} < 0.3\ \mathrm{km\,s^{-1}}$ and shows that rebroadening, as a result of maser saturation, has not occurred yet. As the temperature needed to excite the 6.7-GHz masers is ~ 200 K (Cragg et al. 2005), the thermal linewidth is $\sim 0.7\ \mathrm{km\,s^{-1}}$. The intrinsic thermal linewidth is thus significantly broader due to turbulence in the maser region and we estimate the turbulent linewidth to be $\Delta V_\mathrm{turb} \approx 1.1\ \mathrm{km\,s^{-1}}$.

Using the observed P_l and the fitted emerging brightness temperature we were then able to determine the angle between the magnetic field and the maser propagation direction θ. The quoted errors on θ are the most compact 68% probability interval, determined by analysing the full probability distribution function. For those CH_3OH maser features where no radiative transfer fit was possible, including the features without detected linear polarization, we have used the range of brightness temperatures as suggested by the fitted CH_3OH maser features. The inclination angles θ as well as the angle on the plane of the sky ϕ_B for the CH_3OH maser features are given in Table 4.1. The errors in ϕ_B are determined from the polarization angle χ, with an added uncertainty of 5° as described in Sect. 2.3. As seen in Table 4.1 and shown in Fig. 4.4, θ is constrained to $\theta > \theta_\mathrm{crit}$ at better than 1σ level for the all but three of the CH_3OH maser features. Of those three, the best fit θ for features 3 and 10 are still larger than θ_crit. For the majority of the CH_3OH maser features the magnetic field is thus likely perpendicular to the measured polarization vectors. Only for feature 1, the best fit θ is less than θ_crit, meaning that the magnetic field is more likely parallel to χ.

4.4 Discussion

4.4.1 Methanol maser and the discs of Cepheus A HW2

As noted in Sect. 4.3.1, the 6.7-GHz CH_3OH masers lie in an elliptical distribution around the molecular and dust discs of Cepheus A HW2. The CH_3OH maser features (or simply CH_3OH masers) are found at 650 AU, outside the molecular disc with a radius of 580 AU. The maser distribution also appears $\sim 20^\circ$ tilted with respect to the dust and molecular discs and shows no sign of rotation. This indicates that the CH_3OH masers are not part of the molecular disc itself. The temperature needed to maintain the masing conditions, $T_\mathrm{k} \sim 200$ K (Cragg et al. 2005), is slightly less than the $T = 250 \pm 30$ K found in the outer regions of the molecular disc (Jiménez-Serra et al. 2009). Also, the hydrogen number density in the maser region, $n_{\mathrm{H_2}} \sim 10^9$ cm^{-3} (Cragg et al. 2005) is approximately three orders of magnitude less than that in the disc (Jiménez-Serra et al. 2009). Finally, the masers exhibit signs of infall and their velocity range covers only ~ 3 km s^{-1}, which indicates that it is unlikely that they are part of the Cepheus A HW2 outflow. We thus suggest that the CH_3OH masers, while not associated with the disc directly, probe material that is being accreted onto the disc from the surrounding medium.

4.4.2 Magnetic field in Cepheus A HW2

The magnetic field strength

Dynamic range limits in our MERLIN observations did not enable us to directly determine the magnetic field strength on the individual masers around Cepheus A HW2 and we obtained a 3σ limit of ~ 200 mG (for $\alpha_\mathrm{Z} = 0.005$ km s^{-1} G^{-1}, Vlemmings et al. 2011) for the line-of-sight magnetic field. However, the magnetic field strength in the CH_3OH maser region of Cepheus A was measured using the Effelsberg 100-m telescope (Vlemmings 2008). Through Zeeman-splitting observations, the line-of-sight field strength was determined to be $B_{||} = B\cos(\theta) = 8.1 \pm 0.2$ mG ($\alpha_\mathrm{Z} = 0.049$ km s^{-1} G^{-1}, Vlemmings 2008) that with the new α_Z value is $B_{||} = 81$ mG, which is mostly constant across the full maser spectrum. As this value is a flux averaged magnetic field determined with a single dish telescope, we need to determine the amount of flux recovered and the number of maser features detected in our higher resolution MERLIN observations, to evaluate if the field measurement can be taken to be representative of the observed CH_3OH masers. In Fig. 4.5 we show the comparison between the MERLIN and Effelsberg spectra. It is clear that the shape of the maser spectrum has changed significantly between the two epochs, though all

individual masers found with MERLIN can be identified in the Effelsberg spectrum. The change of the relative flux of the individual masers was noted in Sugiyama et al. (2008b), who monitored Cepheus A with the Yamaguchi 32-m telescope. Comparing our spectra with their Fig. 1, shows that the MERLIN spectrum is remarkably similar to what was observed at August 12 2007, with

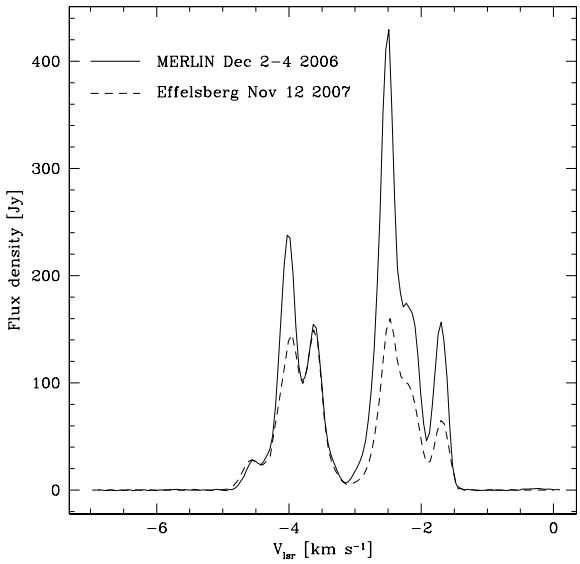

Figure 4.5: Total intensity spectra of the MERLIN observations (solid line) and the Effelsberg observations (dashed line) that were used to determine the magnetic field strength in the 6.7-GHz CH_3OH maser region (Vlemmings 2008).

no more than 10% of the flux resolved out at high angular resolution. The MERLIN observations recover almost all of the single dish maser flux, and all features in the Effelsberg observations can be identified at high angular resolution. We can thus conclude that the Effelsberg magnetic field measurement can be taken as representative for true line-of-sight magnetic field in the maser region.

As discussed in Sect. 4.1, the magnetic field strength is uncertain due to the unknown exact Zeeman-splitting coefficient of the 6.7-GHz CH_3OH maser transition. When we determine the effect of the magnetic field around Cepheus A HW2 we consider $B_{||} = 8$ mG as conservative limit.

Magnetic fiels morphology

The full 3-dimensional magnetic field orientation was inferred using maser radiative transfer models described in Sect. 3.2 and is shown in Fig. 4.6. With the exception of one of the CH_3OH masers that originates from the mid-plane of the molecular disc behind the outflow, the inferred magnetic field in the plane of the sky is perpendicular to the molecular and dust discs with an error weighted

average angle $\phi_{\rm B} = 26° \pm 12°$. Moreover, the error weighted average angle between the magnetic field and the line-of-sight $\theta = 73° \pm 5°$ is consistent with the inclination of the molecular disc and the outflow. The overall magnetic field orientation angle corresponds closely to the magnetic field direction observed in the encompassing dust envelope (Curran & Chrysostomou 2007). The discrepant polarization angle found on the mid-plane CH_3OH maser is either due to the twisting of magnetic field lines towards the disc, or due to Faraday rotation caused by the ionized outflow. While the CH_3OH masers at 6.7-GHz are not significantly affected by interstellar Faraday rotation, an electron density of $\sim$200 cm^{-3} along a short 100 AU path through the ionized outflow with a few mG magnetic field can cause the observed polarization angle of the masers behind the outflow to rotate by more than 10°.

The role of magnetic field

Since we have obtained the angle between the magnetic field and the line-of-sight, we can directly determine the magnetic field strength around the protostellar disc. For $B_{||} = 8 \pm 2$ mG and $\theta = 73° \pm 5°$, the absolute field strength $|B| = 23^{+9}_{-7}$ mG. From this, we can calculate a number of parameters to asses the role of the magnetic field during the massive protostellar collapse. The Alfvénic mach number is given by

$$m_{\rm a} = \frac{\sigma_{\rm turb}\sqrt{3}}{V_{\rm A}}, \tag{4.1}$$

where $\sigma_{\rm turb} = \Delta V_{\rm turb}/\sqrt{8\ln 2}$ and $\Delta V_{\rm turb}$ is the turbulent linewidth. The fits to the radiative transfer models indicate that the intrinsic thermal maser linewidth is much larger than the thermal linewidth expected in the maser region with a typical kinetic temperature $T_{\rm k} \sim 200$ K. Assuming the intrinsic thermal linewidth to be broadened due by turbulent motions, we find that $\Delta V_{\rm turb} \sim 1.1$ km s^{-1}. In the CH_3OH maser region with a hydrogen number density $n_{\rm H_2} \sim 10^9$ cm^{-3}, the Alfvén velocity $V_{\rm A} = |B|/\sqrt{4\pi\rho} = 1.12$ km s^{-1}. The measured infall motions, at 1.7 km s^{-1}, are thus slightly sub-Alfvénic and $m_{\rm a} = 0.7$. At 200 K the sonic mach number $m_{\rm s} = 1.1$, and consequently, the ratio between thermal and magnetic energy

$$\beta = 2\left(\frac{m_{\rm a}}{m_{\rm s}}\right)^2 = 0.8. \tag{4.2}$$

The magnetic field marginally dominates the energies in the high density protostellar environment probed by the masers.

We can also calculate the mass to magnetic flux ratio M/Φ compared to the critical value of this ratio by using Eq. 1.1. The critical value $(M/\Phi)_{\rm crit} = c_\Phi/\sqrt{G} \approx 0.12/\sqrt{G}$ is taken from

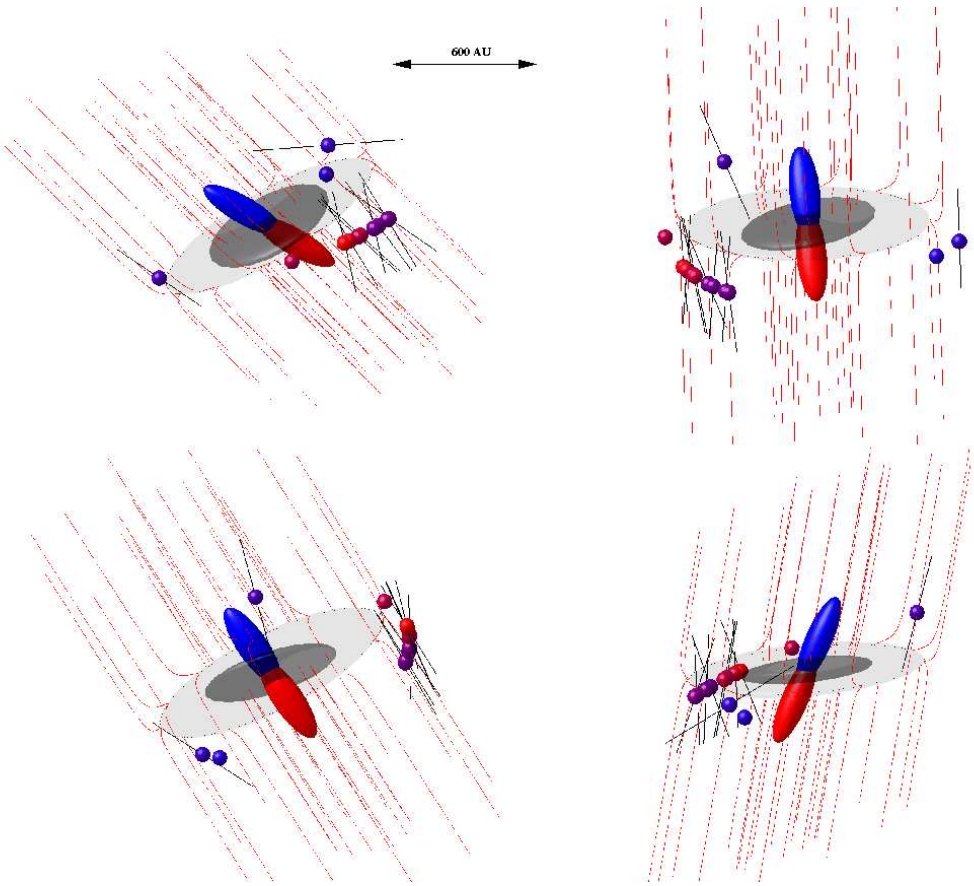

Figure 4.6: The 3-dimensional magnetic field structure around the massive protostar Cepheus A HW2. The top left panel corresponds to a viewing angle close to the observations while the three further panels have different viewing angles. Spheres indicate the masers, with the black vectors indicating the true magnetic field direction. The maser features are color-coded according to their velocity. The molecular disc (Patel et al. 2005) is indicated by the dashed line and light grey structure while the dust disc (Jiménez-Serra et al. 2007; Patel et al. 2005) corresponds to the dark grey ellipse. The blue- and red-shifted lobes of the collimated radio outflow (Curiel et al. 2006) are also shown. The red lines indicate the proposed magnetic field morphology.

numerical models for the collapse of a spherical molecular cloud into a highly flattened structure and defines the critical mass that can be supported against collapse by the magnetic field (Sect. 1.2.2). When $\lambda < 1$, the magnetic field prevents collapse, but when λ becomes larger than 1 gravity overwhelms the magnetic field. In terms of hydrogen column density, λ can be determined from $\lambda = 7.6 \times 10^{-24}\ N(H_2)/|B|$, with the magnetic field in mG. Taking the maser region to be ∼300 AU thick, as determined by our observations, the hydrogen column density along the magnetic field lines is $N(H_2) \approx 5 \times 10^{24}$ cm^{-2}. This yields $\lambda = 1.7^{+0.7}_{-0.5}$, indicating that the region is slightly super-critical, a condition needed for the collapse to proceed. Similar values for λ were found using large-scale Zeeman-splitting observations of an ensemble of molecular clouds (Crutcher 1999). However, as those observations lacked the 3-dimensional magnetic field information, the results were uncertain by of order a factor two, making it impossible to distinguish between sub- and super-critical cloud cores.

We thus suggest that the magnetic field plays a crucial role in regulating the final stages of the formation of the massive protostar Cepheus A HW2, as is commonly expected during low-mass star formation.

4.5 Future perspectives

4.5.1 Cepheus A as a prototype CH_3OH maser source?

Due to their distance and complexity, the relation between the CH_3OH masers and the protostellar environment for most other maser sources is still unknown. However, polarization observations of CH_3OH masers have shown strong and dynamically important magnetic fields in most massive star-forming region traced (Vlemmings 2008; Vlemmings et al. 2011). Furthermore, a recent survey has revealed that ∼30 percent of the CH_3OH maser sources display an elliptical structure (Bartkiewicz et al. 2009). This suggests that the CH_3OH masers of a large fraction of star forming regions are located in an interface between a disc or torus and the infalling material, similar to the inferred origin of the masers around Cepheus A. Our picture of magnetic field regulated infall and accretion towards Cepheus A HW2 thus potentially describes a large number of massive star-forming regions.

4.5.2 Further e-MERLIN observations

With the e-MERLIN upgrade (Garrington et al. 2004), it will soon be possible to map multiple maser transitions simultaneously with the radio-continuum. By observing in full polarization mode, this will allow for a direct comparison between the magnetic field structure determined from the masers and the continuum morphology. Single track observations will allow for mapping of massive star-forming regions at different evolutionary stages down to a continuum sensitivity approaching 3 μJy beam^{-1}. Simultaneously, the sensitivity in a narrow 6.7-GHz maser frequency band will then be sufficient to detect linear polarization for $> 75\%$ of the star-forming regions with CH_3OH masers when assuming the flux analysis of van der Walt (2005). When analyzed in a similar way to the Cepheus A HW2 observations presented here, such observations have the potential to significantly further our understanding of the magnetic field around massive protostars.

4.6 Conclusions

We have demonstrated the power of maser polarization observation, and particularly those using CH_3OH masers, in deducing the full 3-dimensional strength and structure of the magnetic field around massive protostars. The detection of a coherent magnetic field direction in maser features that individually have a size of a few AU, suggests that the masers do not probe isolated pockets of a shock compressed magnetic field. In that case, the polarization direction would be determined by the direction of compression for each maser individually and observing coherent polarization angles would be unlikely. The detection of a large scale magnetic field is further confirmed by the good agreement of the field direction with that determined using dust polarization observations of the entire Cepheus A region. The 3-dimensional magnetic field geometry around Cepheus A HW2 supports the theories in which magnetic fields regulate the infall and outflow close to massive protostars in a similar way as during low-mass star formation, even if the high-mass star-forming regions are considerably more complex. The strong magnetic field that appears to be threading the disc will play a crucial role in maintaining the high accretion rate needed during massive star formation and is potentially essential in maintaining disc stability and creating the conditions to allow for planet formation (Johansen & Klahr 2005; Wardle 2007; Johansen & Levin 2008).

Chapter 5

W75N

The massive star-forming region W75N contains three radio continuum sources (VLA 1, VLA 2, and VLA 3), at three evolutionary stages, and associated masers, while a large-scale molecular bipolar outflow is also present. The observations of H_2O and CH_3OH masers at 22-GHz and 6.7-GHz, respectively, can give information about the gas dynamics and the magnetic fields around VLA 1 and VLA 2. The NRAO Very Long Baseline Array was used to measure the linear polarization and the Zeeman-splitting of the 22-GHz H_2O masers in the star-forming region W75N. Eight of the European VLBI Network antennas were instead used to measure the linear polarization and Zeeman-splitting of the 6.7-GHz CH_3OH masers. We detected 124 H_2O masers, which indicate two different physical environments around VLA 1 and VLA 2, and 10 CH_3OH masers, which arise near the source VLA 1. The linear polarization of both maser species reveals a tightly ordered magnetic field aligned with the large-scale molecular outflow over more than 1300 AU around VLA 1, and an ordered magnetic field around VLA 2, which is not parallel to the outflow. The Zeeman-splitting measured on 20 of the H_2O masers indicates strong magnetic fields around both sources (the averaged values are $|B_{\rm VLA1}| \sim 700\,mG$ and $|B_{\rm VLA2}| \sim 1700\,mG$). We suggest VLA 1 is the powering sources of the bipolar outflow. Moreover, by studying the H_2O maser properties we were also able to determine that the H_2O masers are pumped in C-shocks in both sources.

5.1 The source

W75N is an active high-mass star-forming region in the molecular complex DR21–W75 (Dickel et al. 1978; Persi et al. 2006) at a distance of $1.32^{+0.11}_{-0.09}$ kpc (Rygl et al. 2010). At the resolution of $\sim 1''.5$ three H II regions were identified (Hascick et al. 1981): W75N (A), W75N (B), and W75N (C). At $0''.5$ resolution, Hunter et al. (1994) detected three subregions in W75N (B): Ba, Bb and Bc. At

higher angular resolution ($\sim 0''.1$), Torrelles et al. (1997) resolved the subregions Ba and Bb further (renaming them VLA 1 and VLA 3), and imaged a third weaker and more compact H II region between them, which they named VLA 2 (see Fig. 5.1). A large-scale high-velocity outflow, with an extension greater than 3 pc and a total molecular mass greater than 255 $M_\odot$, was also detected from W75N (B) (e.g., Shepherd et al. 2003). Shepherd et al. (2003) proposed a multi-outflow scenario where VLA 2 may drive the large-scale outflow, and VLA 1 and VLA 3 are the centres of two other small flows. So far, it has been impossible to determine the main powering source of the 3 pc outflow. Several authors have suggested VLA 1 as the powering source (e.g., Torrelles et al. 1997).

Several maser species (H_2O, OH, and CH_3OH) have been detected in W75N (e.g., Torrelles et al. 1997; Baart et al. 1986; Minier et al. 2000), in particular around the two H II regions VLA 1 and VLA 2. The H_2O masers associated with VLA 1 are located along a linear structure parallel to its radio jet with a proper motion of about 2 mas yr^{-1}, while those associated with VLA 2 show a circular distribution, which is expanding with a velocity of about 5 mas yr^{-1} (Torrelles et al. 2003, hereafter T03). Only one H_2O maser is associated with VLA 3 (T03). The CH_3OH masers were detected in a linear structure and off-set from the compact clump at northwest (group A) and south (group B) of VLA 1, respectively (Minier et al. 2000). No CH_3OH masers are associated with VLA 2 (Minier et al. 2000). However, VLA 2 is the place where the most intensive OH flare took place (Alakov et al. 2005; Slysh et al. 2010). Other OH maser emission sites are situated on a ring structure around all three radio sources (Hutawarakorn et al. 2002). Based on the different activity in H_2O and OH masers, Torrelles et al. (1997) suggested that these three sources are at different evolutionary stages, in particular VLA 1 is the "oldest" source of this region and VLA 3 the "youngest" one (driving a radio Herbig-Haro object, Carrasco-González et al. 2010). In this evolutionary scenario, VLA 2 is thus at an intermediate stage. The different evolutionary stages of these three sources is also pointed out by Minh et al. (2010) who observed, with the SMA, several molecules transitions towards the two millimiter cores MM1a and MM1b associated with VLA 2/VLA 3 and VLA 1, respectively. They found that the saturated heavy molecules and methanol show peak emission toward MM1b, and in particular they detected a few tens of transitions from methanol, which is a rapresentative molecule of hot cores. This hot core, which appears in the very early phase ($\sim 10^5$ yr) of star formation, suggests that VLA 1 is the site of the most "recent" star formation in W75N(B). Minh et al. (2010) also derived from sulfur-bearing species a higher rotational temperature ($\sim$240 K) towards MM1a, i.e. VLA 2/VLA 3, than towards

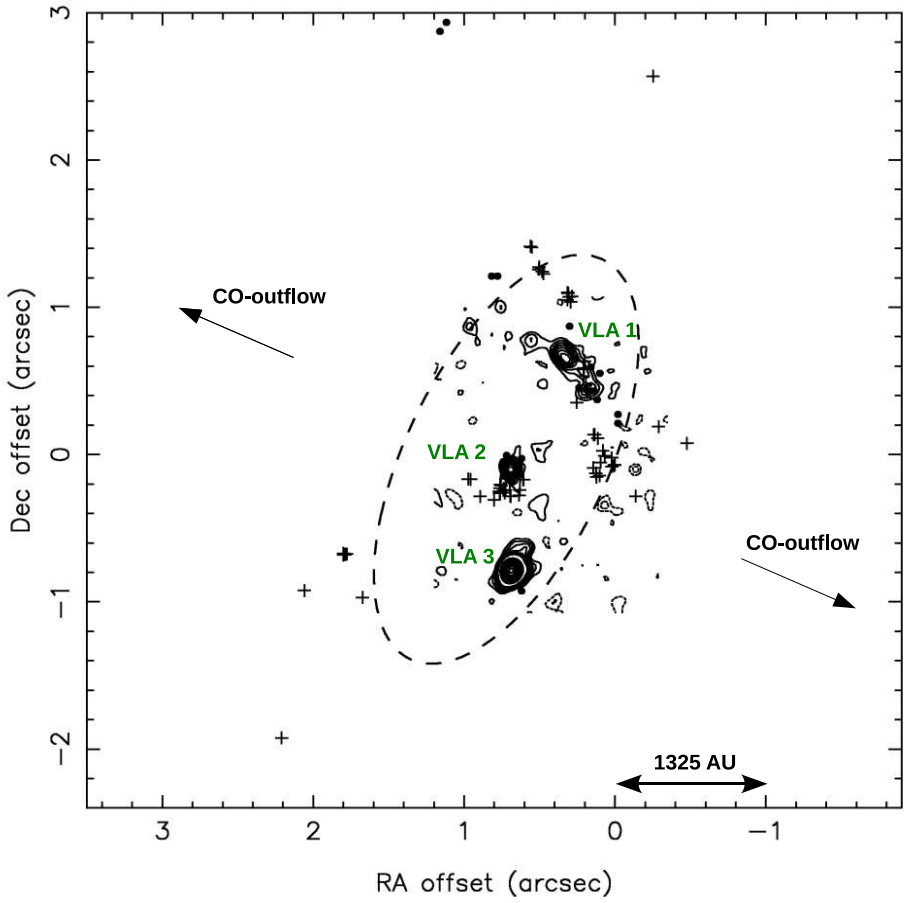

Figure 5.1: Locations of OH masers (crosses, Hutawarakorn et al. 2002) and H_2O masers (filled circles, Torrelles et al. 1997) in W75N(B) relative to the 1.3 cm continuum mapped by Torrelles et al. (1997). The dashed ellipse shows the locus of a ring model fitted to the OH maser position-velocity data (Hutawarakorn et al. 2002). The two arrows indicate the direction of the large-scale molecular bipolar outflow (PA=66°).

MM1b (∼100 K). The observations of magnetic field at small scales might be help to identify which is the most evolved massive protostar among the three radio sources and which is the powering source of the large-scale high-velocity outflow.

In order to determine and investigate the magnetic field of W75N(B), a number of OH maser polarization observations have been made (e.g., Hutawarakorn et al. 2002; Fish & Reid 2007). The magnetic field strength obtained from the OH maser polarization observations was ∼7 mG

(e.g., Hutawarakorn et al. 2002; Slysh et al. 2002). During the OH maser flare near VLA 2, Slysh & Migenes (2006) detected a strong magnetic field of more than 40 mG in several maser spots, which increased in the next observations up to 70 mG (Slysh et al. 2010). Investigating the linear polarization of OH masers (1.6 and 1.7-GHz), Hutawarakorn & Cohen (1996) suggested that the magnetic field is oriented along the outflow. However, OH masers at 1.6 and 1.7-GHz are very susceptible to both internal and external Faraday rotation, making a direct determination of the intrinsic magnetic field structure difficult.

5.2 Observations and analysis

5.2.1 22-GHz VLBA data

We observed the massive star-forming region W75N(B) in the 6_{16}-5_{23} transition of H_2O (rest frequency: 22.23508 GHz) with the NRAO[1] VLBA on November 21, 2005. The observations were made in full polarization spectral mode using 4 overlapped baseband filters of 1 MHz in order to cover a total velocity range of ≈ 50 km s^{-1}. Two correlations were performed. One with 128 channels in order to generate all 4 polarization combinations (RR, LL, RL, LR) with a spectral resolution of 7.8 kHz (0.1 km s^{-1}). The other one with high spectral resolution (512 channels; 1.96 kHz=0.027 km s^{-1}), which only contains the circular polarization combinations (LL, RR), to be able to detect Zeeman-splitting of the H_2O masers across the entire velocity range. Including the overheads, the total observation time was 8 h.

The data were reduced using AIPS following the method of Kemball et al. (1995). The bandpass, the delay, the phase and the polarization calibration were performed on the calibrator J2202+4216, which has been used successfully by Vlemmings et al. (2006a) for H_2O maser polarization observations of Cepheus A. The fringe-fitting and the self-calibration were performed on one of the brightest maser features VLA 1.14 (Table 5.1). All calibration steps were initially performed on the dataset with modest spectral resolution after which the solutions, with the exception of the bandpass solutions that were obtained separately, were copied and applied to the high spectral resolution dataset. Stokes I (rms = 7.3 mJy beam^{-1}), Q (rms = 6.5 mJy beam^{-1}) and U (rms = 6.5 mJy beam^{-1}) data cubes were created using the AIPS task IMAGR (beam-size 2.0 mas $\times$ 0.7 mas) from the modest spectral resolution dataset, while the I and V (rms = 10 mJy beam^{-1}) cubes were imaged from the high spectral resolution dataset and for the same fields. The Q and U cubes were

[1]The National Radio Astronomy Observatory (NRAO) is a facility of the National Science Foundation operated under cooperative agreement by Associated Universities, Inc.

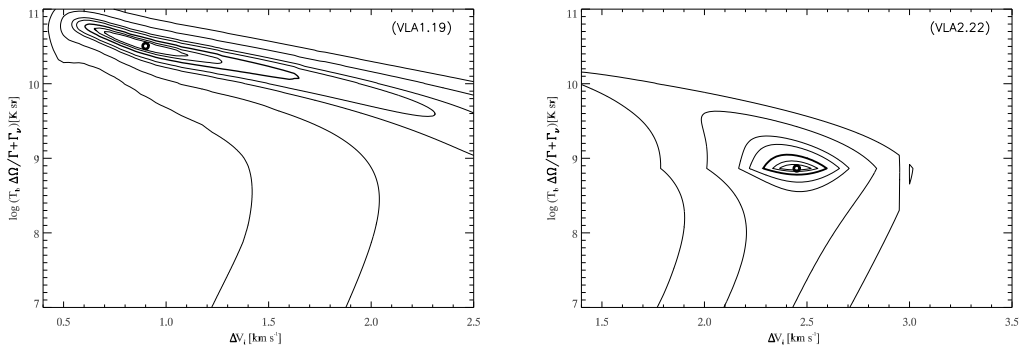

Figure 5.2: Results of the full radiative transfer χ^2-model fits, for the maser that shows the highest linear polarization fraction (VLA1.19) and for the maser that shows the highest $P_{\rm V}$ around VLA2 (VLA2.22). The fits yield the emerging maser brightness temperature $T_{\rm b}\Delta\Omega$ and the intrinsic maser linewidth $\Delta V_{\rm i}$. Contours indicate the significance intervals $\Delta\chi^2$=0.25, 0.5, 1, 2, 3, 7, with the thick solid contours indicating 1σ and 3σ areas.

combined to produce cubes of polarized intensity ($POLI$) and polarization angle ($POLA$). Since these observations were obtained between two Very Large Array (VLA) polarization calibration observations[2], during which the linear polarization angle of J2202+4216 was constant at 13.°5, we were able to estimate the polarization angles with a systemic error of no more than $\sim 2^\circ$.

We identified the H_2O masers by using the identification process and the masers that show linear polarization emission were fitted using the full radiative transfer method code (both described in Sect. 3.2) and based on the models for H_2O masers of Nedoluha & Watson (1992), see Sect. 2.2 for more details. We model the observed linear polarized and total intensity maser spectra by gridding the intrinsic thermal linewidth $\Delta V_{\rm i}$ between 0.4 and 3.5 km s^{-1}, in steps of 0.025 km s^{-1}, using a least square fitting routine (χ^2-model) with an upper limit of the brightness temperature $T_{\rm b}\Delta\Omega = 10^{11}$ K sr. In Fig. 5.2 two examples are shown of the results obtained by fitting the H_2O maser emissions with the full radiative transfer method code. From these first fits, we can then obtain the angles θ by considering the relation between $P_{\rm l}$ and θ. The best values for $T_{\rm b}\Delta\Omega$ and $\Delta V_{\rm i}$ are then included in the full radiative transfer method code to produce the I and V models that were used for fitting the total intensity and circular polarized spectra of the H_2O masers extracted from the high-resolution I and V cubes. Then the magnetic field strength along the line-of-sight has been evaluated using the radiative transfer method code (Sects. 2.2 and

[2]http://www.aoc.nrao.edu/ smyers/calibration/

3.2.3). In Fig. 5.3 the results of the model for three H_2O masers are shown.

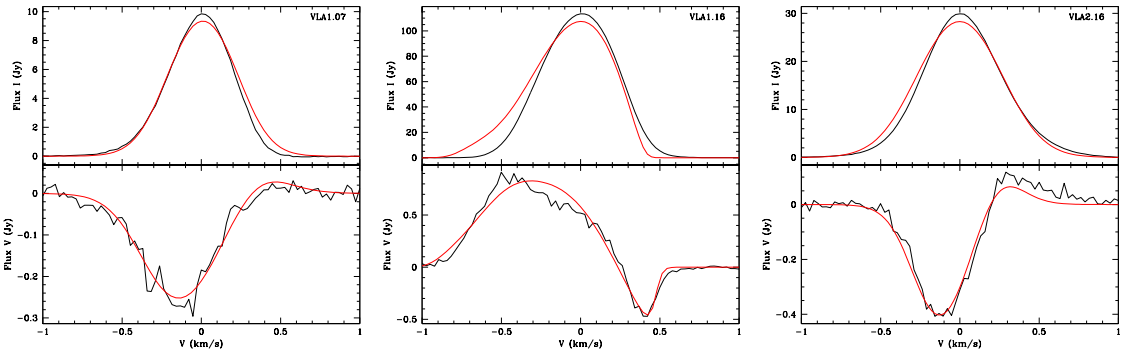

Figure 5.3: Total intensity and circular polarization spectrum for the three maser features VLA1.07, VLA1.16, and VLA2.16. The thick red lines are the best-fit models of I and V emission obtained using the radiative transfer method code (see Sects. 2.2 and 3.2). All maser features were centred to zero velocity.

5.2.2 6.7-GHz EVN data

W75N(B) was observed in full polarization spectral mode at 6668.518 MHz with 8 of the EVN[3] antennas (Jodrell2, Cambridge, Effelsberg, Onsala, Medicina, Torun, Noto, Westerbork) on June 14, 2008. The bandwidth was 2 MHz, providing a velocity coverage of $\sim 100\,\mathrm{km\,s^{-1}}$. The data were correlated twice. First, with modest spectral resolution (512 channels; channel spacing $\sim 0.2\,\mathrm{km\,s^{-1}}$), which enabled us to generate all 4 polarization combinations (RR, LL, RL, LR). The second correlation run with high spectral resolution (1024 channels; channel spacing $\sim 0.1\,\mathrm{km\,s^{-1}}$) only provided the circular polarization combinations (LL, RR). This high spectral resolution data-set was used to attempt the detection of the Zeeman-splitting with a similar RCP-LCP cross-correlation method that was used for the Effelsberg observations by Vlemmings (2008). The observation time was 8 hours, including overheads on the calibrators 3C48, J2007+4029, 3C454.3, and J2202+4216. The last two were also used for polarization calibration.

The data were reduced using AIPS (see Sect. 3.2.1). The initial polarization calibration was performed on J2202+4216. Fringe fitting and self-calibration were performed on the brightest spectral channel, corresponding to the strongest maser feature (~ 90 Jy beam^{-1} at $V_{\mathrm{lsr}} = 7.23\,\mathrm{km\,s^{-1}}$). The observations of the polarization calibrators and the unpolarized calibrator J2007+4029 indi-

[3]The European VLBI Network is a joint facility of European, Chinese, South African and other radio astronomy institutes funded by their national research councils.

cate the remaining polarization leakage after calibration is much less than 1%. Then we imaged the I (rms = 4 mJy beam^{-1}), Q (rms = 6 mJy beam^{-1}), and U (rms = 6 mJy beam^{-1}) cubes (2048 × 2048 mas) of the source W75N(B) using the task IMAGR (beam-size 8.75×6.45 mas). The data cubes were combined to produce cubes of *POLI* and *POLA*. With the exception of the bandpass table, which had to be remade, the calibration solutions were copied from the modest resolution data-set and applied to the high spectral resolution data. From this data-set we produced *RR* (rms = 5 mJy beam^{-1}) and *LL* (rms = 5 mJy beam^{-1}) image cubes.

Our observations were obtained between two VLA polarization calibration observations[2] during which the linear polarization angle of J2202+4216 changed abruptly from −30° to −80°. However, we were able to calibrate the linear polarization angle using 3C454.3, which during our observation had a constant polarization angle of 6.°9 from VLA monitoring[2].

The CH_3OH masers were also identified through the identification process (Sect. 3.2.2). We were unable to determine $T_b\Delta\Omega$ and ΔV_i by using the full radiative transfer method code because of insufficient spectral resolution (Sect. 3.2.3).

The absolute position of the brightest feature (B1 in Table 5.2) was obtained through fringe rate mapping using the AIPS task FRMAP. We determined its position to be $\alpha_{2000} = 20^h38^m36^s.417$, $\delta_{2000} = +42°37'34''.846$ with an absolute position error of about 20 mas. The relative position errors depend on the maser flux of each feature, but are better than 1 mas.

5.3 Results

5.3.1 Maser distribution

In Fig. 5.4 we show the H_2O (blue circles) and CH_3OH masers (red triangles) detected with the VLBA and the EVN and superimposed on the 1.3 cm continuum contour map of VLA 1 and VLA 2 observed by Torrelles et al. (1997).

H_2O maser

We detected 124 22-GHz H_2O maser features towards the massive star-forming region W75N with the VLBA. No H_2O maser emission with a peak flux density less than 80 mJy beam^{-1} is detected. All H_2O maser features are detected around the radio sources VLA 1 (29%, 36/124) and VLA 2 (71%, 88/124).

The H_2O maser features associated with VLA 2, which have local standard of rest velocities

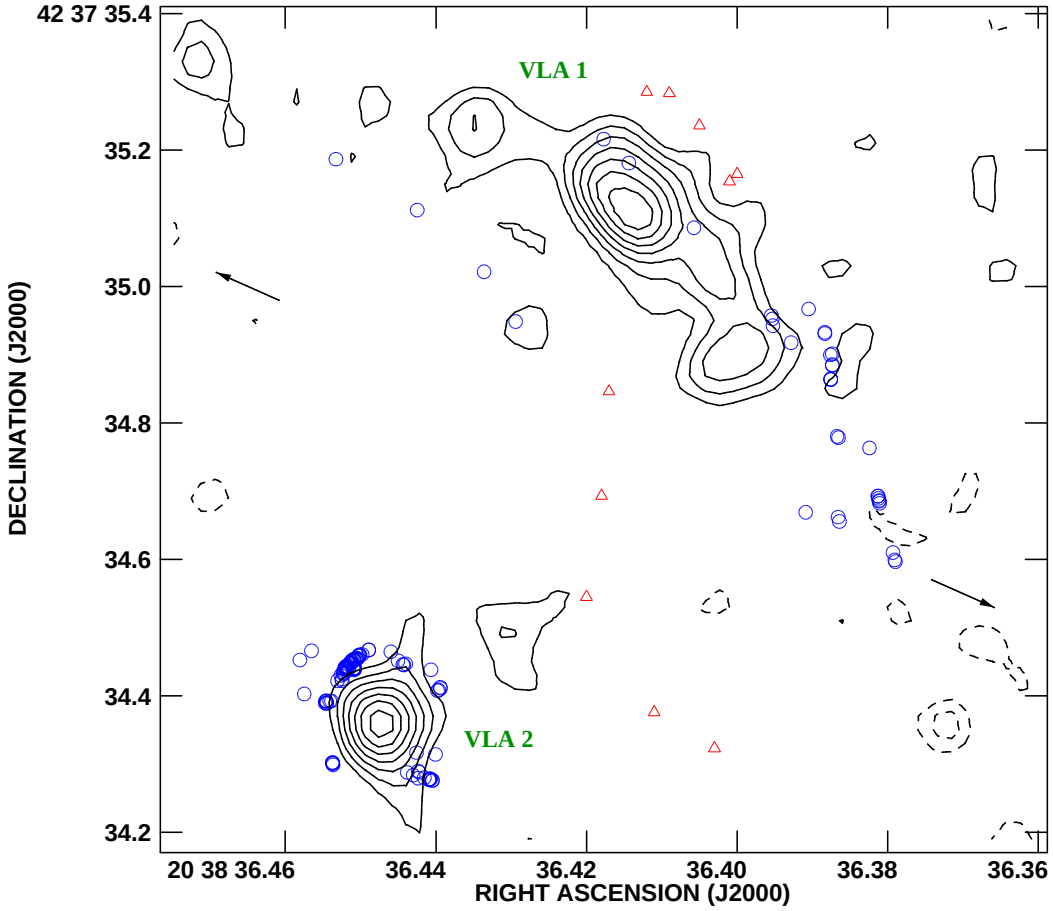

Figure 5.4: Positions of H_2O and CH_3OH maser features superimposed on the 1.3 cm continuum contour map of the VLA1 thermal jet and VLA 2 (Torrelles et al. 1997). Contours are -3, -2, 2, 3, 4, 5, 6, 7, 8 $\times$ 0.16 mJy beam^{-1}. Blue circles indicate the positions of the H_2O maser features detected with the VLBA. Red triangles indicate the position of the CH_3OH masers features detected with the EVN. The two arrows indicate the direction of the large-scale molecular bipolar outflow (PA=66°).

($V_{\rm lsr}$) between -7.7 and 13.7 km s^{-1}, are distributed elliptically around its 1.3 cm continuum peak. In Fig. 5.5 we report two ellipses obtained by fitting the positions of the H_2O maser features detected by T03 (called here ellipse 1) and in the present work (ellipse 2), their parameters are reported in Table 5.3. The major axis of ellipse 2 is 64 mas larger than that of ellipse 1, the minor axes are also in the same ratio. This indicates an expansion velocity of ∼4.8 mas/yr in all directions, corresponding to $\sim$ 30 km s^{-1} (at 1.32 kpc). This value is consistent with the proper motion of the H_2O maser features as reported by T03. Since the expansion velocity is symmetric in

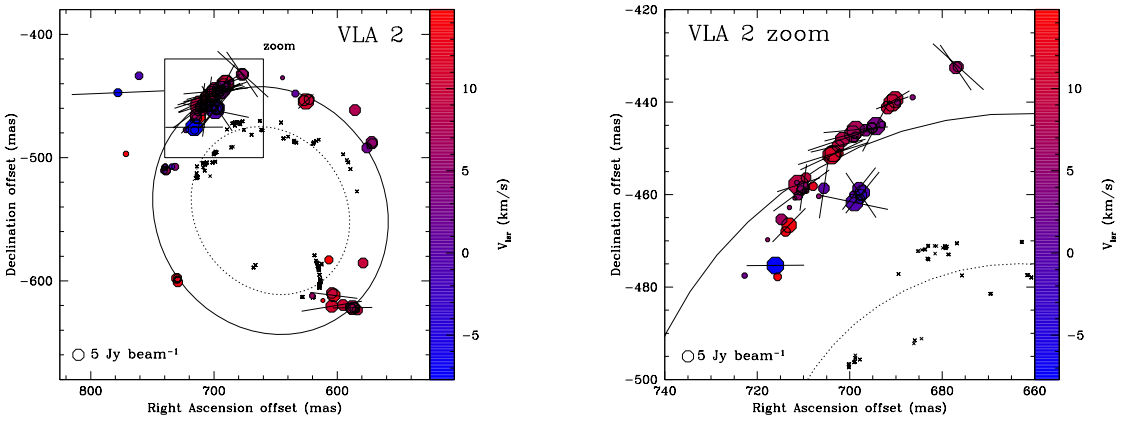

Figure 5.5: Left panel: a close-up view of the H_2O maser features around the radio source VLA 2. Right panel: a zoom-in view of the boxed region of the left panel. The octagonal symbols are the identified H_2O maser features in present work scaled logarithmically according to their peak flux density. The maser LSR radial velocity is indicated by color. A 5 Jy beam^{-1} symbol is plotted for illustration in both panels. The linear polarization vectors, scaled logarithmically according to polarization fraction P_1 (in Table 5.1), are overplotted. Two ellipses are also drawn in both panels. They are the results of the best fit of the H_2O maser features (crosses) detected by T03 (dotted ellipse, ellipse 1; epoch 1999) and of those detected in present work (solid ellipse, ellipse 2; epoch 2005). Their parameters are listed in Table 5.5. The synthesized beam is 2.0 mas × 0.7 mas.

all directions, we aligned the centres of the two ellipses with the position of the 1.3 cm continuum peak obtained from a Gaussian fit. Consequently we were able to overlay all H_2O maser features of the region on the continuum VLA map with an accuracy of approximately 10 mas. In this way we could also compare the positions of the H_2O maser features around VLA 1 at the two different epochs. If we look at the northern H_2O maser features around VLA 2, we see that the masers detected by T03 are better aligned with the ellipse 1 than the masers detected by us with ellipse 2 (Fig. 5.5, right panel), indicating that those features are also moving northeastward. This movement might be due to the formation of a jet (see Fig. 5.4).

The H_2O maser features associated with VLA 1 can be divided into three groups, one composed of the northern features (VLA 1A), one of the features closest to the central protostar (VLA 1B, see Fig. 5.6 left panel) and the third one of the southern features (VLA 1C). The east-northern H_2O maser features of the VLA 1A group did not show emission during the previous observations of epoch 1999 (T03). All VLA 1A features ($V_{\rm lsr} \simeq 19 - 25$ km s^{-1}) are well-aligned with the direction of the thermal radio jet detected by Torrelles et al. (1997) and the CH_3OH masers detected by

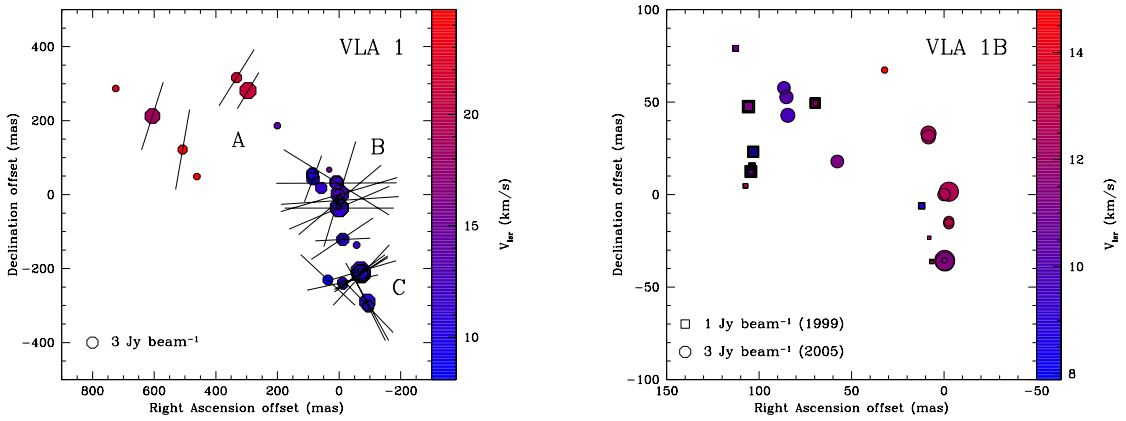

Figure 5.6: Left panel: a close-up view of the H_2O maser features (octagon) around the radio source VLA 1. Right panel: a zoom-in view of the H_2O masers group VLA 1B, here are also reported the H_2O maser features (square) detected by T03. The octagonal and the square symbols are scaled logarithmically according to their peak flux density. The maser LSR radial velocity is indicated by color. The systemic LSR radial velocity of W75N massive star-forming region is 10 km s^{-1} (Shepherd et al. 2003). Symbols for 3 Jy beam^{-1} and for 1 Jy beam^{-1} are shown in the lower left corner of the panels. The linear polarization vectors, scaled logarithmically according to polarization fraction P_1 (in Table 5.1), are overplotted on the left panel. The synthesized beam is 2.0 mas × 0.7 mas.

Minier et al. (2000) and by us (see below). The VLA 1B and VLA 1C groups show a distribution quite similar to that shown on April 2, 1999 (T03). For these two groups T03 reported a proper motion of about ∼2 mas/yr (∼ 12 km s^{-1}). Although we have detected several H_2O masers close to those detected by T03, it is very difficult to estimate the proper motion between the two epochs. In fact, as is shown on the right panel of Fig. 5.6, it is difficult to identify a maser feature that arises in both epochs (1999 and 2005). The LSR radial velocities of VLA 1 are between 9 and 25 km s^{-1}, which are about 3-4 times higher than those of CH_3OH maser features (see below) and greater than the systemic velocity of the whole region (10 km s^{-1}, Shepherd et al. 2003).

CH_3OH maser

We have detected 10 CH_3OH maser features (see Table 5.2), with a minimum signal-to-noise ratio of approximately 80. Figure 5.7 shows a close-up view of the CH_3OH maser features. They can be

Table 5.1: All 22-GHz H_2O maser features in W75N for which linear and/or circular polarization was detected.

(1) Maser	(2) group[a]	(3) RA offset (mas)	(4) Dec offset (mas)	(5) Peak flux Density(I) (Jy/beam)	(6) $V_{\rm lsr}$ (km/s)	(7) $\Delta v_{\rm L}$ (km/s)	(8) $P_{\rm l}$ (%)	(9) χ (°)	(10) $\Delta V_{\rm i}$[b] (km/s)	(11) $T_{\rm b}\Delta\Omega$[b] (log K sr)	(12) $P_{\rm V}$ (x10^{-3})	(13) $B_{||}$ (mG)	(14) θ[c] (°)
VLA 1.01	C	-95.361	-303.062	2.76 ± 0.13	10.7	0.38	2.3 ± 0.4	$+43.8 \pm 8.3$	$1.1^{+0.3}_{-0.3}$	$9.5^{+0.7}_{-0.8}$	–	–	79^{+10}_{-14}
VLA 1.02	C	-94.267	-300.461	3.39 ± 0.09	10.5	0.40	3.2 ± 0.5	$+26.4 \pm 9.4$	$1.1^{+0.3}_{-0.2}$	$9.6^{+0.6}_{-1.1}$	–	–	86^{+2}_{-13}
VLA 1.03	C	-91.698	-289.684	30.78 ± 0.19	11.3	0.39	5.1 ± 0.8	$+29 \pm 1.6$	$0.8^{+0.4}_{-0.3}$	$10.3^{+0.4}_{-0.3}$	7.8	106 ± 18	74^{+10}_{-6}
VLA 1.04	C	-72.037	-217.556	9.77 ± 0.13	10.7	0.46	3.9 ± 0.4	-43.0 ± 1.4	$1.5^{+0.3}_{-0.4}$	$9.7^{+0.3}_{-0.3}$	11.3	-212 ± 51	83^{+5}_{-8}
VLA 1.05	C	-71.532	-214.531	115.41 ± 0.12	10.6	0.44	1.7 ± 0.2	-56.1 ± 6.5	$1.7^{+0.2}_{-0.3}$	$9.3^{+0.5}_{-0.1}$	2.9	-54 ± 9	74^{+16}_{-14}
VLA 1.06	C	-71.321	-213.371	76.79 ± 0.12	10.8	0.46	1.5 ± 0.2	-59.3 ± 6.0	$1.8^{+0.2}_{-0.5}$	$9.4^{+0.6}_{-0.2}$	5.1	-115 ± 18	66^{+11}_{-39}
VLA 1.07	C	-70.479	-210.289	10.16 ± 0.12	11.1	0.45	1.4 ± 0.6	-53.9 ± 11.3	$1.9^{+0.2}_{-0.3}$	$9.2^{+0.6}_{-2.0}$	28.4	599 ± 100	72^{+8}_{-47}
VLA 1.08	C	-69.595	-206.944	158.28 ± 0.20	11.5	0.51	2.6 ± 0.1	-73.5 ± 5.0	$1.8^{+0.2}_{-0.6}$	$9.7^{+0.5}_{-0.1}$	2.8	65 ± 10	69^{+20}_{-5}
VLA 1.09	C	-11.789	-121.338	6.14 ± 0.06	10.4	0.33	1.1 ± 0.5	-87.2 ± 3.2	$1.0^{+0.2}_{-0.1}$	$9.0^{+0.2}_{-2.0}$	–	–	86^{+3}_{-52}
VLA 1.10	C	-11.410	-237.705	2.07 ± 0.20	11.4	0.51	2.5 ± 0.4	-77.9 ± 7.2	$2.0^{+0.2}_{-0.3}$	$9.5^{+0.5}_{-1.5}$	–	–	86^{+4}_{-4}
VLA 1.11	C	-9.768	-119.442	0.39 ± 0.03	10.3	0.51	2.7 ± 0.3	-56.1 ± 14.2	$1.0^{+0.2}_{-0.2}$	$9.5^{+0.6}_{-0.5}$	–	–	83^{+7}_{-9}
VLA 1.12[d]	B	-2.737	-15.713	1.13 ± 0.03	12.8	0.38	19.4 ± 0.7	-86.2 ± 0.7	$0.7^{+0.3}_{-0.1}$	$10.5^{+0.1}_{-0.5}$	–	–	90^{+2}_{-2}
VLA 1.13[d]	B	-2.695	-14.427	0.97 ± 0.03	12.8	0.40	12.4 ± 2.5	-50.0 ± 1.4	$0.8^{+0.2}_{-0.5}$	$10.1^{+0.3}_{-2.5}$	–	–	90^{+10}_{-10}
VLA 1.14[d]	B	-2.695	1.568	80.02 ± 0.07	12.6	0.44	13.5 ± 0.7	-16.9 ± 0.6	$0.6^{+0.2}_{-0.2}$	$10.6^{+0.1}_{-0.4}$	–	–	90^{+5}_{-5}
VLA 1.15[d]	B	-0.589	-36.270	63.25 ± 0.17	11.6	0.49	13.1 ± 1.9	-90.0 ± 3.6	$0.7^{+0.8}_{-0.2}$	$10.7^{+0.1}_{-0.6}$	–	–	90^{+7}_{-7}
VLA 1.16[d]	B	-0.421	-35.545	111.47 ± 0.20	11.4	0.55	12.9 ± 1.2	-66.9 ± 0.6	$0.7^{+0.7}_{-0.2}$	$10.7^{+0.4}_{-0.3}$	11.3	-177 ± 27	90^{+6}_{-6}
VLA 1.17[d]	B	0	0	2.96 ± 0.06	12.7	0.54	22.9 ± 5.1	-73.7 ± 3.3	1.1[e]	$10.4^{+0.6}_{-2.3}$	42.2	809 ± 182	90^{+11}_{-11}
VLA 1.18[d]	B	8.252	31.166	6.17 ± 0.06	12.4	0.52	22.0 ± 5.0	-89.7 ± 1.2	1.0[e]	$10.3^{+0.5}_{-2.3}$	–	–	90^{+12}_{-12}
VLA 1.19[d]	B	8.294	33.016	11.39 ± 0.07	12.6	0.53	25.7 ± 3.5	$+58.2 \pm 7.7$	0.9[e]	$10.5^{+0.4}_{-1.1}$	5.9	-92 ± 30	90^{+6}_{-6}
VLA 1.20	C	36.292	-230.717	1.86 ± 0.02	8.1	0.33	2.7 ± 0.3	$+47.1 \pm 2.9$	$0.9^{+0.2}_{-0.1}$	$9.5^{+0.3}_{-0.3}$	–	–	84^{+3}_{-11}
VLA 1.21[d]	B	57.638	17.914	3.56 ± 0.15	11.2	0.44	–	–	–	–	25.8[f]	-398 ± 102[e]	–
VLA 1.22[d]	B	84.373	42.854	6.71 ± 0.05	9.8	0.43	0.9 ± 0.2	-20.6 ± 6.2	$1.6^{+0.1}_{-0.3}$	$8.9^{+0.6}_{-1.3}$	–	–	78^{+12}_{-33}
VLA 1.23	A	295.388	281.223	39.41 ± 0.05	21.1	0.83	0.6 ± 0.1	-30.6 ± 8.5	–	–	–	–	–
VLA 1.24	A	332.438	316.208	2.00 ± 0.04	21.7	0.68	1.9 ± 0.1	-31.8 ± 8.3	–	–	–	–	–
VLA 1.25	A	507.583	121.956	1.33 ± 0.03	23.8	0.51	3.6 ± 0.3	-9.9 ± 7.6	$1.5^{+0.3}_{-0.4}$	$9.7^{+0.3}_{-1.0}$	–	–	90^{+11}_{-11}
VLA 2.01	-	571.410	-488.743	1.69 ± 0.01	5.2	0.57	–	–	–	–	30.2[f]	567 ± 243[e]	–
VLA 2.02	-	571.957	-487.320	2.82 ± 0.01	5.0	0.58	–	–	–	–	21.5[f]	413 ± 146[e]	–
VLA 2.03	-	587.493	-621.986	12.0 ± 0.05	6.8	0.68	0.5 ± 0.1	-89.5 ± 52.7	$3.0^{+0.2}_{-0.2}$	$8.7^{+0.5}_{-0.1}$	–	–	80^{+10}_{-36}
VLA 2.04	-	602.691	-611.675	6.86 ± 0.06	12.7	0.61	0.8 ± 0.3	$+82.8 \pm 3.8$	–	–	–	–	–
VLA 2.05	-	604.376	-620.571	4.62 ± 0.12	10.9	0.50	1.5 ± 0.4	-80.6 ± 32.0	$1.9^{+0.2}_{-0.3}$	$9.2^{+0.1}_{-2.3}$	–	–	90^{+22}_{-22}
VLA 1.26	A	605.681	212.257	20.73 ± 0.04	18.7	0.53	2.3 ± 0.1	-17.9 ± 2.0	$2.0^{+0.2}_{-0.4}$	$9.4^{+0.3}_{-0.1}$	–	–	85^{+3}_{-12}
VLA 2.06	-	625.258	-454.392	25.44 ± 0.16	11.2	0.69	0.2 ± 0.1	-47.0 ± 16.6	–	–	–	–	–
VLA 2.07	-	676.454	-432.327	1.95 ± 0.08	6.0	0.60	2.0 ± 0.3	$+47.7 \pm 8.7$	$2.3^{+0.2}_{-0.2}$	$9.4^{+0.2}_{-1.9}$	–	–	90^{+15}_{-15}
VLA 2.08	-	677.044	-432.545	4.65 ± 0.01	6.2	0.59	1.1 ± 0.1	$+34.5 \pm 3.1$	$2.5^{+0.2}_{-0.2}$	$9.0^{+0.3}_{-0.1}$	–	–	83^{+8}_{-16}
VLA 2.09	-	690.053	-439.411	30.29 ± 0.06	9.6	0.75	0.4 ± 0.1	-58.7 ± 9.1	$3.3^{+0.1}_{-0.2}$	$8.6^{+0.7}_{-0.1}$	3.9	-158 ± 36	76^{+11}_{-40}
VLA 2.10	-	690.727	-440.163	48.76 ± 0.06	9.7	0.58	0.4 ± 0.1	-69.3 ± 9.0	$2.6^{+0.1}_{-0.2}$	$8.6^{+0.8}_{-0.1}$	6.2	-186 ± 31	72^{+8}_{-44}
VLA 2.11	-	697.169	-459.564	13.99 ± 0.04	-1.1	0.86	1.0 ± 0.3	-39.2 ± 19.2	–	–	–	–	–
VLA 2.12	-	697.421	-460.125	3.25 ± 0.01	-2.9	2.34	1.5 ± 0.6	-34.2 ± 12.1	–	–	–	–	–
VLA 2.13	-	697.884	-458.710	7.16 ± 0.01	0.5	0.69	1.0 ± 0.2	-38.3 ± 7.5	$3.0^{+0.1}_{-0.3}$	$9.0^{+0.6}_{-1.1}$	–	–	82^{+9}_{-13}
VLA 2.14	-	698.600	-445.961	62.39 ± 0.07	7.2	0.63	1.7 ± 0.2	-84.8 ± 1.2	$2.7^{+0.3}_{-0.5}$	$9.3^{+0.7}_{-0.2}$	1.1	-38 ± 13	74^{+15}_{-35}
VLA 2.15	-	698.937	-461.704	49.20 ± 0.05	-0.7	0.87	2.0 ± 0.2	$+78.2 \pm 36.9$	3.4[e]	$9.6^{+0.4}_{-0.3}$	–	–	68^{+3}_{-41}

Table 5.1: (continued)

(1) Maser	(2) group[a]	(3) RA offset (mas)	(4) Dec offset (mas)	(5) Peak flux Density(I) (Jy/beam)	(6) $V_{\rm lsr}$ (km/s)	(7) $\Delta v_{\rm L}$ (km/s)	(8) $P_{\rm l}$ (%)	(9) χ (°)	(10) $\Delta V_{\rm i}$[b] (km/s)	(11) $T_{\rm b}\Delta\Omega$[b] (log K sr)	(12) $P_{\rm V}$ (x10^{-3})	(13) $B_{\rm ||}$ (mG)	(14) θ[c] (°)
VLA 2.16	-	699.316	-446.842	30.98 ± 0.05	6.8	0.58	1.3 ± 0.2	-75.4 ± 1.6	$2.5^{+0.2}_{-0.3}$	$9.1^{+0.7}_{-0.3}$	15.6	470 ± 73	77^{+13}_{-33}
VLA 2.17	-	701.505	-448.017	12.73 ± 0.05	8.3	0.53	2.5 ± 0.5	-71.7 ± 1.7	$2.1^{+0.3}_{-0.3}$	$9.5^{+0.8}_{-0.9}$	16.1	425 ± 76	77^{+13}_{-34}
VLA 2.18	-	702.389	-449.426	4.32 ± 0.03	9.3	0.82	1.2 ± 0.1	-76.9 ± 4.4	–	–	–	–	–
VLA 2.19	-	703.484	-451.126	39.57 ± 0.17	11.6	0.78	2.6 ± 0.3	-72.6 ± 3.7	–	–	–	–	–
VLA 2.20	-	703.863	-451.496	72.56 ± 0.16	11.2	1.09	2.0 ± 0.3	-65.1 ± 3.9	$3.1^{+0.1}_{-0.9}$	$10.2^{+0.3}_{-0.2}$	–	–	61^{+42}_{-42}
VLA 2.21	-	705.505	-458.549	2.48 ± 0.01	0.2	0.53	1.4 ± 0.3	-8.7 ± 5.2	$2.1^{+0.1}_{-0.3}$	$9.2^{+0.2}_{-2.0}$	–	–	90^{+16}_{-16}
VLA 2.22	-	709.968	-458.458	4.02 ± 0.01	5.0	0.56	0.8 ± 0.1	-8.0 ± 4.4	$2.5^{+0.1}_{-0.2}$	$8.9^{+0.5}_{-0.4}$	20.8	957 ± 239	84^{+6}_{-11}
VLA 2.23	-	710.389	-459.141	1.34 ± 0.01	4.9	0.80	2.1 ± 0.1	-53.5 ± 5.5	$3.0^{+0.2}_{-0.1}$	$9.4^{+0.1}_{-0.1}$	–	–	87^{+1}_{-9}
VLA 2.24	-	711.020	-457.901	198.45 ± 0.20	8.7	0.51	0.7 ± 0.1	-72.0 ± 6.2	$2.3^{+0.2}_{-0.3}$	$9.0^{+0.5}_{-0.3}$	6.1	160 ± 24	66^{+11}_{-42}
VLA 2.25	-	713.041	-466.595	16.74 ± 0.02	13.7	0.60	0.8 ± 0.1	-44.5 ± 2.1	$2.6^{+0.2}_{-0.3}$	$8.9^{+0.5}_{-0.1}$	–	–	80^{+10}_{-38}
VLA 2.26	-	716.030	-475.323	53.72 ± 0.06	-7.7	0.68	1.2 ± 0.5	-89.6 ± 61.8	$3.0^{+0.2}_{-0.3}$	$9.1^{+0.5}_{-1.8}$	2.1	79 ± 18	77^{+13}_{-38}
VLA 2.27	-	777.794	-447.278	0.67 ± 0.06	-7.7	0.66	6.1 ± 0.1	-87.7 ± 6.5	$0.7^{+1.8}_{-0.1}$	$10.7^{+0.1}_{-1.7}$	–	–	71^{+13}_{-3}

Notes. [a] The H_2O maser features associated with VLA 1 are divided in three groups according to their positions (see Sect. 5.3.1). [b] The best-fitting results obtained by using a model based on the radiative transfer theory of H_2O masers (Vlemmings et al. 2006a) for $\Gamma + \Gamma_\nu = 1$. The errors were determined by analysing the full probability distribution function. For $T \sim 400$ K ($\Gamma_\nu = 2$) and $T \sim 2500$ K ($\Gamma_\nu = 13$) $T_{\rm b}\Delta\Omega$ has to be adjusted by adding +0.48 and +1.15, respectively (Nedoluha & Watson 1992; Anderson & Watson 1993). [c] The angle between the magnetic field and the maser propagation direction is determined by using the observed $P_{\rm l}$ and the fitted emerging brightness temperature. The errors were determined by analysing the full probability distribution function. [d] Because of the degree of the saturation of these H_2O maser features $T_{\rm b}\Delta\Omega$ is underestimated, $\Delta V_{\rm i}$ and θ are overestimated. [e] The constraint fit did not allow us to evaluate the error bars properly. [f] In the fitting model we include the values for $T_{\rm b}\Delta\Omega$ and $\Delta V_{\rm i}$ of the closest features.

Table 5.2: 6.7-GHz CH_3OH maser features detected in W75N.

(1) Maser	(2) RA[a] (J2000)	(3) Dec[a] (J2000)	(4) Peak Flux Density (I) (Jy/beam)	(5) $S(\nu)$ (Jy)	(6) $V_{\rm lsr}$ (km/s)	(7) $\Delta v_{\rm L}$ (km/s)	(8) $P_{\rm l}$ (%)	(9) χ (°)	(10) $\Delta V_{\rm Z}$[b] (m/s)
A1	20h38m36.412s	42d37m35.285s	15.54 ± 0.09	17.4 ± 0.2	3.54	0.18	2.0 ± 0.4	-22 ± 1	-
A2	20h38m36.409s	42d37m35.283s	48.25 ± 0.17	65.7 ± 0.4	4.07	0.21	4.0 ± 1.2	-20 ± 8	-
A3	20h38m36.405s	42d37m35.236s	67.24 ± 0.21	80.1 ± 0.4	4.60	0.20	4.5 ± 0.3	-9.6 ± 0.3	-
A4	20h38m36.400s	42d37m35.165s	47.58 ± 0.12	60.7 ± 0.3	5.82	0.22	0.9 ± 0.3	-6 ± 6	0.80 ± 0.03
A5	20h38m36.401s	42d37m35.154s	39.39 ± 0.12	50.2 ± 0.3	5.12	0.22	3.5 ± 1.5	-2 ± 12	0.75 ± 0.13
B1	20h38m36.417s	42d37m34.846s	95.38 ± 0.18	107.9 ± 0.3	7.23	0.20	1.5 ± 0.5	-18 ± 9	0.53 ± 0.04
C1	20h38m36.418s	42d37m34.693s	2.33 ± 0.08	2.9 ± 0.2	9.34	0.17	-	-	-
C2	20h38m36.420s	42d37m34.545s	7.02 ± 0.08	7.3 ± 0.2	6.88	0.19	-	-	-
C3	20h38m36.411s	42d37m34.376s	4.11 ± 0.06	4.6 ± 0.1	9.16	0.19	1.3 ± 0.3	-25 ± 4	-
C4	20h38m36.403s	42d37m34.323s	10.83 ± 0.07	10.2 ± 0.12	9.51	0.24	1.4 ± 0.3	-30 ± 21	-

Notes. [a] The CH_3OH maser feature positions were determined after using the task FRMAP on feature B1. [b] The Zeeman-splitting ($\Delta V_{\rm Z}$) was determined from the cross-correlation between the RR and LL spectra.

Table 5.3: Number, epoch, semi-major axis, semi-minor axis, and inclination from the elliptical fit of the H_2O maser features associated with VLA 2 in the two different epochs.

Ellipse	epoch	a (mas)	b (mas)	θ ($^\circ$)	ref.
1	2-Apr.-1999	71.0	61.1	123.5	T03
2	21-Nov.-2005	103.1	92.9	120.5	this work

divided in three groups: A, B and C, following the naming convention adopted by Minier et al. (2000). Using three EVN antennas in May 1997, they detected 12 CH_3OH maser features in W75N(B) divided in two groups: A, which is located at the north-west of VLA 1, and B to the south of VLA 1, with velocities between 3 and 7 km s^{-1}.

As found by Minier et al. (2000), the features A1-A5, with velocities between 3 and 6 km s^{-1},

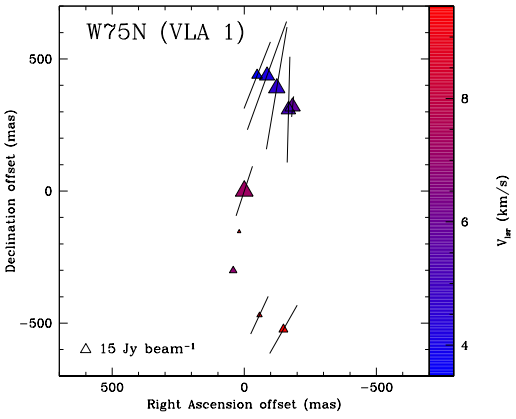

Figure 5.7: A close-up view of the CH_3OH maser features around the radio source VLA 1. The triangles symbols are scaled logarithmically according to their peak flux density. The maser LSR radial velocity is indicated by color. The systemic LSR radial velocity of W75N massive star-forming region is 10 km s^{-1} (Shepherd et al. 2003). A symbol for 15 Jy beam^{-1} is shown in the lower left corner of the panel. The linear polarization vectors, scaled logarithmically according to polarization fraction P_l (in Table 5.2), are also overplotted. The synthesized beam is 8.75 mas × 6.45 mas.

are located along a linear structure. Although the absolute positions in Minier et al. (2000) are uncertain by up to 1 arcsec, we were able to identify 5 features detected previously as A1-A5 (Minier et al. 2000). Their velocities are slightly higher ($+0.04$ km s^{-1}$< \Delta V_{\rm lsr} < +0.16$ km s^{-1}) than those reported by Minier et al. (2000). Only the feature A5 ($V_{\rm lsr}$=5.12 km s^{-1}) has a lower velocity (~ -0.5 km s^{-1}). The feature B1, which is located south-east of the groups A at a distance of about 400 mas (∼530 AU at a distance of 1.32 kpc), has a velocity of 7.23 km s^{-1}. It can be associated with the brightest feature (peak flux = 71.1 Jy) of Minier et al. (2000). Comparing the separations between A1-A5 and B1 in the two epochs, we find a small difference in their relative

positions, implying a separation velocity of 0.93 mas yr^{-1} $\approx$ 5.8 km s^{-1}. Group C, located south of the feature B1, is composed of four CH_3OH maser features undetected in Minier et al. (2000). The features of this group (C1-C4) seem to be along an arc structure with $V_{\rm lsr}$ between 6 and 10 km s^{-1}.

5.3.2 Linear and circular polarization

H_2O maser

Linear polarization was detected in 50 H_2O maser features (Table 5.1). In particular, about 70% of the H_2O maser features associated with VLA 1 show linear polarization emission. The corresponding linear polarization vectors are shown in Figs. 5.5 and 5.6 (left panel). The highest fractional linear polarization was detected in H_2O maser features related to VLA 1 ($P_{\rm l} \sim 26\%$). Eight features associated with VLA 1 have high linear polarizations, $P_{\rm l}$ between 10% and 26%, so that the median value of linear polarizations for the H_2O maser features in VLA 1 is $\sim$7%. In contrast, the maximum $P_{\rm l}$ for the features associated with VLA 2 is 6%, and the median value is much lower at 1.5%. Circular polarization was detected in 20 H_2O maser features, equally distributed between VLA 1 and VLA 2.

The rms weighted linear polarization angles of the H_2O maser features around VLA 1 and VLA 2 are $\langle\chi_1\rangle_{\rm H_2O} \approx -67^\circ\pm40^\circ$ and $\langle\chi_2\rangle_{\rm H_2O} \approx -72^\circ\pm32^\circ$, respectively. Since the H_2O maser features of group VLA 1A show ordered linear polarization vectors, it is worthwhile evaluating its weighted polarization angles, which is $\langle\chi_{\rm 1A}\rangle_{\rm H_2O} = -20^\circ\pm9^\circ$.

We were able to fit 42 features with the full radiative transfer method described in Sects. 2.2.2 and 3.2.3, and the results are given in columns 10 and 11 of Table 5.1, and two examples (i.e., VLA1.19, VLA2.22) are reported in Fig. 5.2. Although the emerging brightness temperatures for VLA 1 and VLA 2 are both in the range $10^8\,{\rm K\,sr} < T_{\rm b}\Delta\Omega < 10^{10}\,{\rm K\,sr}$, their weighted intrinsic maser linewidths are very different. They are $\langle\Delta V_{\rm i}\rangle_{\rm VLA1} = 1.0^{+0.8}_{-0.2}$ km s^{-1} and $\langle\Delta V_{\rm i}\rangle_{\rm VLA2} = 2.5^{+0.6}_{-0.4}$ km s^{-1}, respectively.

Finally, considering the emerging brightness temperature and the observed $P_{\rm l}$ we determined θ for those H_2O maser features which we were able to fit for $\Delta V_{\rm i}$ and $T_{\rm b}\Delta\Omega$. The results are given in column 14 of Table 5.1 with the errors determined by analyzing the full probability distribution functions. Eight of the H_2O maser features around the radio source VLA 1 (from VLA1.12 to VLA1.19, which are the closest features to the protostar) show values for θ equal to 90°. This suggests that, from the theory of the Zeeman effect, we are observing perpendicular to

the magnetic field. Consequently, we should not be able to detect circular polarization from these features. However, since we detected circular polarization in three of them (VLA1.16, VLA1.17, and VLA1.19) the measurements of θ must be affected by the degree of their saturation, as discussed in Sect. 2.2.2. By excluding these 8 features, we evaluated $\langle\theta\rangle_{\rm VLA1} = 83°\pm7°$ and $\langle\theta\rangle_{\rm VLA2} = 85°\pm6°$, which imply that the magnetic fields are close to the plane of the sky.

In column 13 of Table 5.1 we report the magnetic field strength along the line-of-sight obtained by fitting the high-resolution spectra of I and V (see Sect. 5.2.1). The H_2O maser features VLA1.21, VLA2.01, and VLA2.02 do not show any linear polarization emission, but they do show circular polarization emission. Consequently we could not get $T_{\rm b}\Delta\Omega$ and $\Delta V_{\rm i}$ as done for the other features that showed linear polarization emission, and to measure the magnetic field strength, we used the $T_{\rm b}\Delta\Omega$ and $\Delta V_{\rm i}$ values of the closest masers. In Table 5.1 the circular polarization fraction is also reported (column 12).

CH_3OH maser

Linear polarization was detected in 8 of 10 CH_3OH maser features given in Table 5.2. The highest fractional linear polarization ($P_{\rm l} \sim 2-5\%$) was detected in group A. The linear polarization fraction of the features in group B and C is slightly lower ($P_{\rm l} \sim 1-2\%$). No dependence of

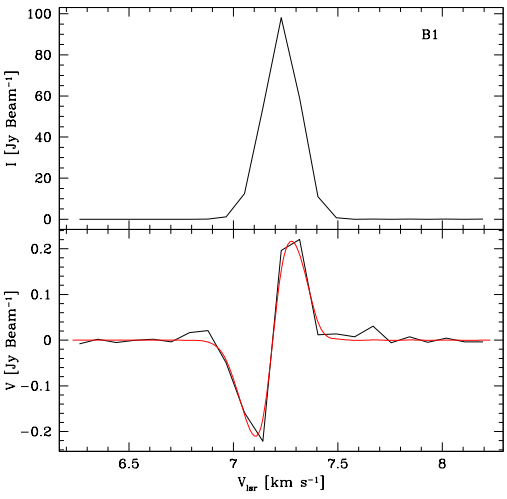

Figure 5.8: Total intensity and circular polarization spectrum for the brightest CH_3OH maser feature of W75N(B). The thick red line in the bottom panel is best fit total power derivative of a Gaussian fit of I spectrum to the circular polarization spectrum.

$P_{\rm l}$ on maser brightness is found. The weighted polarization angle of CH_3OH maser vectors is $\langle\chi\rangle_{\rm CH_3OH} = -17° \pm 10°$. Zeeman-splitting was detected in 3 of 10 maser features (A4, A5 and

B1) and it is reported in column 9 of Table 5.2. Fig. 5.8 shows the total intensity and the circular polarization spectrum for the brightest feature. Since the Zeeman-splitting coefficient (α_Z) for 6.7-GHz CH_3OH maser is still uncertain we cannot give here any value for the magnetic field strength until careful laboratory measurements of g are made.

5.4 Discussion

The H_2O maser features (or simply H_2O masers) detected are related to two different radio continuum sources of W75N(B), VLA 1 and VLA 2, which are thought to be in two different evolutionary stages, while the CH_3OH maser features (or simply CH_3OH masers) are related only to VLA 1. No H_2O and CH_3OH masers are related to VLA 3. In the next sections, we discuss the nature of the masers, their polarization and finally the type of shocks that give rise to the H_2O masers and how these shocks are related to the CH_3OH masers.

5.4.1 H_2O maser properties

As suggested by the difference between their intrinsic thermal linewidths, which is 1.5 $\mathrm{km\,s^{-1}}$, the H_2O masers around VLA 1 and VLA 2 appear to arise under two different physical conditions. Using

$$\Delta V_\mathrm{i} \approx 0.5 \times (T/100)^{\frac{1}{2}}, \tag{5.1}$$

we estimate the gas temperatures in the H_2O masing regions around VLA 1 and VLA 2, and find them to be $T_{\mathrm{VLA\,1}} \sim 400$ K and $T_{\mathrm{VLA\,2}} \sim 2500$ K, respectively. The intrinsic thermal linewidths of the VLA 2 H_2O masers are quite similar to each other, while the three groups of H_2O masers around VLA 1 show a difference in their ΔV_i. In particular, we find that the H_2O maser groups VLA 1A and C have similar intrinsic thermal linewidths ($\langle \Delta V_\mathrm{i} \rangle = 1.0$ $\mathrm{km\,s^{-1}}$) while the group VLA 1B has lower values ($\langle \Delta V_\mathrm{i} \rangle = 0.7$ $\mathrm{km\,s^{-1}}$). This can come from the degree of their saturation that we can evaluate by considering Eq. 2.30.

Since in the radiative transfer method code we used $(\Gamma + \Gamma_\nu) = 1$ $\mathrm{s^{-1}}$, before using Eq. 2.30, we have to adjust the $T_\mathrm{b}\Delta\Omega$ values according to the gas temperature as describe in Sect. 3.2.3. At a temperature of $\sim$400 K, for which $\Gamma + \Gamma_\nu = 3$ $\mathrm{s^{-1}}$ (Nedoluha & Watson 1992), the weighted emerging brightness temperature of VLA 1B is $\langle T_\mathrm{b}\Delta\Omega \rangle > 10^{11}$ K sr, which is close to the limit of full saturation, and for VLA 1A and C is $\langle T_\mathrm{b}\Delta\Omega \rangle = 10^{10}$ K sr. From Eq. 2.30 the masers of VLA 1A and VLA 1C are thus completely unsaturated ($R/(\Gamma+\Gamma_\nu) = 0.5$, Sect. 3.2.3), while VLA 1B masers

are saturated ($R/(\Gamma+\Gamma_\nu) > 5$), even if the real degree of their saturation is unknown because of underestimating $T_\mathrm{b}\Delta\Omega$. The average observed linewidth (Δv_L) of VLA 1B group, which is about 0.5 $\mathrm{km\,s^{-1}}$, gives us another indication of the saturation state of their H_2O masers. As reported in Sect. 3.2.3, the intrinsic thermal linewidths for the saturated masers are overestimated so Δv_L might be larger or at least equal to ΔV_i implying that the maser lines are rebroadened as expected in the saturated maser lines (Sect. 2.1). As the VLA 1B masers are saturated, they have not been taken into account in our conclusions. For the other H_2O masers associated with VLA 1, we observed linewidths well below their intrinsic thermal linewidth, and this confirms that these masers are unsaturated. The H_2O masers associated with VLA 2 are unsaturated; in fact, for $T \sim 2500$ K ($\Gamma+\Gamma_\nu = 14\ \mathrm{s^{-1}}$, Anderson & Watson 1993), we get ratios of $R/(\Gamma+\Gamma_\nu) < 0.5$.

From the measurements of the maser flux densities ($S(\nu)$) and feature angular sizes (Σ) we can estimate the brightness temperature by the equation:

$$\frac{T_\mathrm{b}}{[\mathrm{K}]} = \frac{S(\nu)}{[\mathrm{Jy}]} \cdot \left(\frac{\Sigma^2}{[\mathrm{mas}^2]}\right)^{-1} \cdot \xi\ , \tag{5.2}$$

where for the H_2O masers $\xi = \xi_{H_2O} = 1.24 \times 10^9\,\mathrm{mas^2\,Jy^{-1}\,K}$ is a constant factor which includes all constant values, such as the Boltzmann constant, the wavelength, and the proportionality factor obtained for a Gaussian shape by Burns et al. (1979). Comparing T_b with the emerging brightness temperatures obtained from the model, we can easily estimate $\Delta\Omega$. The Gaussian fit of the H_2O masers gives a size of 0.4 mas for the masers related to VLA 1, which indicates that they are unresolved, while a size of 0.5 for the masers associated with VLA 2, which indicates that they are marginally resolved. The brightness temperatures of the brightest masers in both groups are $T_\mathrm{b,VLA1.08} > 1.23 \times 10^{12}$ K and $T_\mathrm{b,VLA2.24} \approx 10^{12}$ K, for which we find $\Delta\Omega_\mathrm{VLA1.08} < 10^{-2}$ sr and $\Delta\Omega_\mathrm{VLA2.24} \approx 10^{-2}$ sr for $T = 400$ K and 2500 K, respectively. Considering all the features in Table 5.1, the maser beaming of the two groups are $\Delta\Omega_\mathrm{VLA\,1} \lesssim 10^{-2}$ sr ($\Gamma+\Gamma_\nu = 2\,\mathrm{s^{-1}}$) and $\Delta\Omega_\mathrm{VLA\,2} \approx 10^{-2}$ sr ($\Gamma+\Gamma_\nu = 14\,\mathrm{s^{-1}}$). In a tubular geometry $\Delta\Omega \approx (d/l)^2$, where d and l are the transverse size and length of the tube respectively. Assuming d approximately the size of the maser features, the maser lengths are all in the range $10^{12}\,\mathrm{cm} \lesssim l \lesssim 10^{14}\,\mathrm{cm}$.

5.4.2 Magnetic field in W75N(B)

Here we discuss first the strength of the magnetic field that is measured considering the circular polarization emission of the H_2O maser, then we focus our attention on its orientation that is instead obtained considering both maser species.

Magnetic field strength

The magnetic field strength along the line-of-sight was determined from circular polarization measurements for 20 H_2O masers. We detected significant ($\geq 3\sigma$) magnetic fields toward 10 masers in VLA 1 and 7 masers in VLA 2. The detected fields along the line-of-sight ($B_{||}$) range from -400 mG to $+600$ mG for the H_2O masers around VLA 1 and from -200 mG to 1000 mG for those associated with VLA 2 (see Table 5.1). The wide range obtained for $B_{||}^{VLA1}$ and $B_{||}^{VLA2}$ is not anomalous, and a similar range was reported for Cepheus A (Vlemmings et al. 2006a). The changing in the sign indicates the reversal of the magnetic field (negative towards the observer, positive away from the observer) as already observed in other sources (e.g., Vlemmings et al. 2006a). Since the θ values are close to 90°, i.e. close to the plane of the sky, a slight difference in these angles can produce an inversion of the sign of the magnetic fields. In the case of VLA 1, the positive and negative magnetic field strengths measured for VLA 1B and VLA 1C groups indicate a twisted magnetic field, which is not the case for VLA 2. Apart from the H_2O masers VLA2.01 and VLA2.02, which are located on the right edge of the ellipse 2 and show positive values, the other masers in the upper left part of the ellipse 2 (from VLA2.09 to VLA2.26) present a clear separation between positive and negative magnetic field strengths (see Fig. 5.5 and Table 5.1).

Based on these detections the absolute weighted magnetic field strengths along the line-of-sight, where the weights are $w_{\rm i} = 1/e_{\rm i}^2$ and $e_{\rm i}$ is the error of the i-th measurement, are $\langle|B_{||}^{\rm VLA1}|\rangle = (81 \pm 62)$ mG and $\langle|B_{||}^{\rm VLA2}|\rangle = (145 \pm 110)$ mG. In the case of VLA 1, it is more correct to determine $\langle|B_{||}|\rangle$ for only the unsaturated masers; i.e., $\langle|B_{||}^{VLA1}|\rangle = (74 \pm 50)$ mG. The large errors are due to the large scatter of the magnetic field strength values, which depend on the projection effects, on the density of each H_2O maser region, and on the local velocities of shocks. Because of this scatter it is difficult to evaluate the true strength of the full magnetic fields of the entire region and we can estimate them only roughly. Since $\langle\theta\rangle_{\rm VLA1} = 83^{\circ}{}^{+7^{\circ}}_{-15^{\circ}}$ and $\langle\theta\rangle_{\rm VLA2} = 85^{\circ}{}^{+6^{\circ}}_{-36^{\circ}}$ the absolute weighted magnetic field strengths are $|B_{\rm VLA1}| = \langle|B_{||}^{\rm VLA1}|\rangle / cos\langle\theta\rangle_{\rm VLA1} \sim 700$ mG and $|B_{\rm VLA2}| \sim 1700$ mG, respectively. Such high values are also found by Vlemmings et al. (2006a) in Cepheus A. As their shock velocity is 10 km s^{-1}, measuring a magnetic field of 600 mG, these authors explain this high value with the presence of a nearby magnetic dynamo. Hence our large unexpected values of B might be due either to the presence of a magnetic dynamo or to the presence of very high-velocity shocks that strongly compress the gas, and consequently increase the magnetic field strength from 70 mG (pre-shock OH region, Slysh et al. 2010) to > 1 Gauss (H_2O maser region). For the last hypothesis we refer the reader to Sect. 5.4.3.

With regard to the orientation of the magnetic field, it is worthwhile discussing the influence of the Faraday rotation in our observations.

Faraday rotation

The measurements of the linear polarization angle (χ) might be disturbed by the foreground, ambient, and internal Faraday rotation, which are given by

$$\Phi[^\circ] = 1.35 \times 10^{-15}\, D\,[\mathrm{cm}]\, n_\mathrm{e}\,[\mathrm{cm}^{-3}]\, B_{||}\,[\mathrm{mG}]\, \nu^{-2}\,[\mathrm{GHz}], \tag{5.3}$$

where D is the length of the path over which the Faraday rotation occurs, n_e and $B_{||}$ are respectively the average electron density and the magnetic field along this path and ν the frequency. For the foreground Faraday rotation (i.e. the rotation due to the medium between the source and the observer) ϕ_f is 0.°4 at 22-GHz and 5° at 6.7-GHz, assuming the interstellar electron density and the magnetic field are $n_\mathrm{e} \approx 0.012$ cm^{-3} and $B_{||} \approx 2$ μG (Sun et al. 2008), respectively.

All masers are not in the same plane, but they arise in clouds at different depths. This depth is impossible to determine from our observations, so in order to estimate the ambient Faraday rotation (i.e. the rotation due to the ambient medium where masers arise), we assume the maximum projected separation as upper limit of D among masers close to each other with the highest velocity difference, which is $D_\mathrm{max}^{\mathrm{H_2O}} \sim 10^{15}$ cm and $D_\mathrm{max}^{\mathrm{CH_3OH}} \sim 10^{14}$ cm for the H_2O and CH_3OH masers, respectively. For the electron density, we assume the value reported by Fish & Reid (2006), $n_\mathrm{e} \approx 300$ cm^{-3}, which can produce a rotation of 90° along the path amplification of OH maser around H II regions. Considering a typical magnetic field strength $B_{||} = 10$ mG (from OH masers, Fish et al. 2005), the ambient Faraday rotation is $\phi_\mathrm{a}^{\mathrm{H_2O}} < 8^\circ$ and $\phi_\mathrm{a}^{\mathrm{CH_3OH}} < 9^\circ$ for the H_2O and CH_3OH masers, respectively.

In the case of the internal Faraday rotation (ϕ_i) $B_{||}$ in Eq. 5.3 is the magnetic field strength measured from the circular polarization emission of each maser. Since we are not able to measure the magnetic field strength from the CH_3OH maser polarized emission as explained in Sect. 5.3.2, we can estimate ϕ_i only for the H_2O masers. The internal Faraday rotation, which can destroy the linear polarization (Fish & Reid 2006), depends on the type of shock that pumps the H_2O masers. They can either be a dissociative jump shock (J-shock) or a nondissociative continuous shock (C-shock). In the case of a C-shock, the intrinsic Faraday rotation at 22-GHz can be considered negligible because the ionization state of the gas is controlled by cosmic-ray ionization, which generates electron-molecular ion pairs at a rate of 10^{-17}s^{-1} (Kaufam & Neufeld 1996), while

we have to roughly estimate its contribution for a J-shock. In this case, the electron density is $n_{\rm e} = \chi_{\rm e}\, n_{\rm H_2}$, where $\chi_{\rm e}$ is the ionization fraction ($\chi_{\rm e} = 10^{-5} - 10^{-4}$; Kylafis & Norman 1987) and $n_{\rm H_2}$ the number density of the H_2O masers. In the most conservative situation, for which $n_{\rm e} \sim 10^4\,{\rm cm}^{-3}$, we determine an internal Faraday rotation of tens of degrees, enough to destroy the linear polarization in some cases. This means that either the electron density must be much lower or, more likely, the internal Faraday rotation must be negligible, and consequently the shock must be a C-shock.

Magnetic field orientation

Suppose that in both sources there are C-shocks (see Sect 5.4.3), this means that the Faraday rotation is $\phi_{\rm tot}^{\rm H_2O} = \phi_{\rm f} + \phi_{\rm a} + \phi_{\rm i} < 9^\circ$ and $\phi_{\rm tot}^{\rm CH_3OH} < 14^\circ$. Since the H_2O masers associated with VLA 1 and VLA 2 indicate that there are two different magnetic fields around the two sources, it is worthwhile discussing them separately. All H_2O masers show $\theta > \theta_{\rm crit} \sim 55^\circ$; i.e., the magnetic field direction is perpendicular to the linear polarization vectors and close to the plane of the sky.

The H_2O maser group VLA 1A shows an orientation NE-SW of the magnetic field of $\varphi_{\rm B}^{\rm VLA\,1A} = 70^\circ \pm 9^\circ$. This indicates that the magnetic field orientation in this part of the source is close to the direction of the large-scale molecular bipolar outflow, which is thought to be oriented close to the plane of the sky at a position angle of 66° (Hunter et al. 1994). The other two H_2O maser groups VLA 1B and C show disordered linear polarization vectors, which cannot give information on the orientation of the magnetic field. The different orientation of the linear polarization vectors for these two groups might come from the different depths of the masers, i.e. high values of the ambient Faraday rotation, and therefore we can assume that the masers with angles far from -20° are located at higher depths than those with angles close to -20° (e.g. VLA1.14).

Since we cannot model the CH_3OH maser emission with the full radiative transfer method code (see Sect. 5.2.2), in order to estimate θ we have to solve the polarized radiative transfer using the equations from Nedoluha & Watson (1992). For this purpose we can consider an upper limit of the maser beaming angle $\Delta\Omega \leq 10^{-1}$ (Minier et al. 2002) and a brightness temperature given from Eq. 5.2, where now $\xi = \xi_{\rm CH_3OH} = 13.63 \cdot 10^9$ mas^2 Jy^{-1} K. As we find that all CH_3OH masers are marginally resolved we take a typical angular size value $\Sigma = 7$ mas. Most of the CH_3OH masers have $T_b \Delta\Omega < 10^9$ K sr and consequently we find that $\theta < \theta_{\rm crit} \sim 55^\circ$ is ruled out across the entire CH_3OH maser region (see Fig. 5.9). Consequently, also in this case the linear polarization vectors are perpendicular to the direction of the magnetic field. As indicated in Fig.5.9, considering

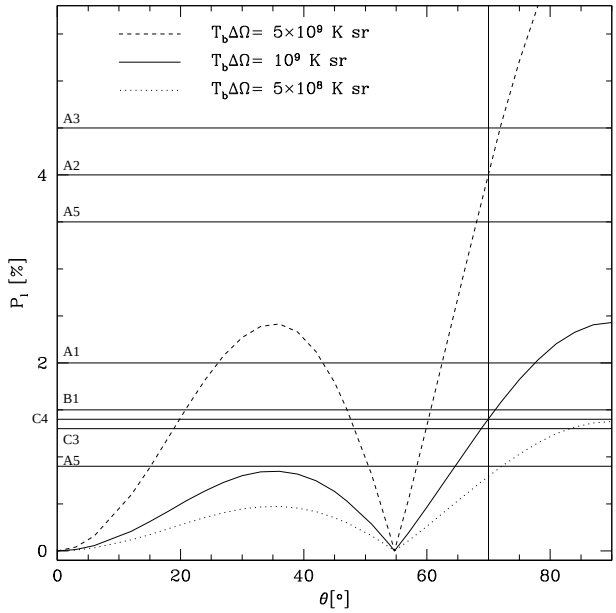

Figure 5.9: The angle θ between the CH_3OH maser propagation direction and the magnetic field vs. the fractional linear polarization P_l for different values of emerging maser brightness temperatures $T_b\Delta\Omega$. The dashed and dotted curves corresponds to the brightness temperature limits for our CH_3OH maser observations (assuming $\Delta\Omega = 10^{-1}$). The horizontal solid lines show the fractional linear polarization of CH_3OH masers as reported in Table 5.2. The vertical solid line shows the most likely value of θ for the W75N CH_3OH maser observations.

the observed brightness temperatures and assuming $\Delta\Omega = 10^{-1}$, we estimate the average angle between the magnetic field and the line-of-sight to be $\theta \sim 70°$. From the linear polarization of the CH_3OH masers the magnetic field orientation is $73° \pm 10°$, which is in good agreement with what we found from the H_2O maser observations. Following our argument the alignment of the magnetic field around VLA 1 with the large-scale molecular bipolar outflows indicates that VLA 1 is likely the driving source of the outflow.

The dust polarization of W75N(B) has been observed at three wavelengths (450, 800, 1100 μm; Greaves & Holland 1998). These observations indicate a change in the large-scale magnetic field position angle on the sky from 37° to –35° with increasing beam-size. This change is attributed to the twisted magnetic field lines around the massive protostar, a feature common to the models of low-mass star formation (e.g. Shu et al. 1995). In this case, the large beams are dominated by the dragged-in magnetic field lines, while the highest-resolution observations trace the components of the field that constrain the outflow (Greaves & Holland 1998). Our observations at mas resolution

of the masers related to VLA 1 are consistent with this model and suggest an outflow driving mechanism similar to that during low-mass star formation.

Although around VLA 2 some H_2O masers show the 90°-flip of the linear polarization angle (e.g., VLA2.15), which was also observed in some H_2O masers in Cepheus A (Vlemmings et al. 2006a), the magnetic field appears to be radial (see Fig. 5.5). Considering $\langle\chi_2\rangle_{H_2O} \approx -72°$, the magnetic field orientation is about 18° that indicates a misalignment with the large-scale molecular bipolar outflow and the magnetic field of VLA 1, even though the inclination of both ellipses ($\sim 60°$) is close to it.

The different orientation of the magnetic fields of the two sources again implies different local physical environments for VLA 1 and VLA 2, and suggests that VLA 1 rather than VLA 2 is the powering source of the large-scale molecular bipolar outflow.

5.4.3 J- or C-shocks?

As reported in previous papers, the H_2O masers are thought to be pumped by the transition of shocks generated in the two protostars (e.g., Torrelles et al. 1997). These shocks can be either C-shocks or J-shocks. In a H_2O masing region, *C-shocks* show $v \lesssim 50$ km s^{-1} and a post-shock $T < 4000$ K (Kaufam & Neufeld 1996), while *J-shocks* have velocities $v \gtrsim 45$ km s^{-1} and a post-shock plateau temperature that depends on the pre-shock density, the shock velocity, and the observed linewidth of the H_2O masers (Elitzur et al. 1989). Kylafis & Norman (1991) investigated the effects of the temperature on their J-shock model up to a temperature of about 1000 K, and they found that the brightness temperature starts to increase more slowly when a temperature $\sim$500 K is reached.

We first consider VLA 1. Assuming the proper motion of the H_2O masers reported by T03, i.e. 12 km s^{-1}, as the velocity of the shock and as pre-shock density, the density of the CH_3OH masers $n_{H_2} = 10^9$cm^{-3}, the equation reported in Elitzur et al. (1989) for a J-shock

$$T_{\rm plateau} \approx 400 \left(\frac{n_0}{10^7{\rm cm}^{-3}} \frac{v_{\rm s}}{100\,{\rm km\,s}^{-1}} \frac{\Delta v^{-1}}{1\,{\rm km\,s}^{-1}}\right)^{\frac{2}{9}} {\rm K}, \tag{5.4}$$

where here $\Delta v_{\rm VLA1} = 0.5$ km s^{-1}, gives us a most likely post-shock temperature $T^{\rm VLA1}_{\rm plateau} \approx 600$ K, which is higher than the temperature measured considering the weighted intrinsic velocity obtained from our fit ($T_{\rm VLA1} \approx 400$ K). Moreover, from the model of a C-shock described by Kaufam & Neufeld (1996), we are able to estimate the velocity of the shock by considering the temperature $T_{\rm VLA1}$. The model for a temperature of 400 K gives $v_{\rm s}^{\rm VLA1} \sim 15$ km s^{-1}, which is close to the

proper motion of the H_2O masers. Therefore, following our arguments, the shock in VLA 1 is most likely a C-shock.

In the case of VLA 2, the plateau temperature due to a J-shock is $T_{\rm plateau}^{\rm VLA2} \approx 800\,{\rm K}$ (where $\Delta v_{\rm VLA2} = 0.7\ {\rm km\,s^{-1}}$, and $v_{\rm VLA2} = 30\ {\rm km\,s^{-1}}$), which is less than the temperature that we measured ($T_{\rm VLA2} \approx 2500$ K). The difference of the two temperatures may be due to the turbulence velocity of the gas, which can be determined by considering $\Delta V_{\rm i}$. In fact, $\Delta V_{\rm i}$ is related to the thermal and turbulence velocities by the equation

$$\Delta V_{\rm i} = \sqrt{\Delta V_{\rm th}^2 + \Delta V_{\rm turb}^2}, \tag{5.5}$$

and considering the Eq. 5.1 we are able to estimate the turbulence velocity of the gas if a J-shock is present. The thermal velocity, which stems from the warming up of the gas by the compression due to the passage of a shock, for a temperature of 800 K is $\Delta V_{\rm th}^{\rm VLA\,2} \approx 1.4\ {\rm km\,s^{-1}}$, so we have $\Delta V_{\rm turb} \approx 2.1\ {\rm km\,s^{-1}}$. If instead we suppose that the shock is a C-shock from the model of Kaufam & Neufeld (1996) for $T_{\rm VLA2} \sim 2500$ K, we get $v_{\rm s}^{\rm VLA\,2} \sim 43\ {\rm km\,s^{-1}}$, which is close to the expansion velocity that we determined in the present paper ($v_{\rm VLA\,2} = 30\ {\rm km\,s^{-1}}$). Both velocities are also in good agreement with the velocity of 43 $\rm km\,s^{-1}$ measured by Slysh et al. (2010) for the OH masers near VLA 2 obtained by multiepoch observations. Moreover, since we obtain well-ordered high linear polarization fraction and linear polarization vectors, we have to suppose that the Faraday rotation is at most $\sim$20°; otherwise, the vectors no longer appear to be aligned with the large structure (i.e., ellipse 2). This condition is only met if the internal Faraday rotation is small; in other words, if the shock is a C-shock (Kaufam & Neufeld 1996). Therefore, we strongly suggest that there is a C-shock also in VLA 2 even if a J-shock cannot be completely ruled out.

From the equation

$$\frac{B_{\rm maser}}{[{\rm mG}]} \approx 80 \sqrt{\frac{n_{\rm H_2}}{[10^8\,{\rm cm^{-3}}]}} \cdot \frac{v_{\rm s}}{[10\,{\rm km\,s^{-1}}]}, \tag{5.6}$$

where $n_{\rm H_2}$ is the pre-shock density and $v_{\rm s}$ the velocity of the shock, we can verify our assumption about the pre-shock density and the rough estimation of $|B_{\rm VLA1}|$ and $|B_{\rm VLA2}|$. Equation 5.6 is valid for both types of shocks (Kaufam & Neufeld 1996). Considering $n_{\rm H_2} = 10^9\,{\rm cm^{-3}}$ as before, we get $|B_{\rm VLA1}| \approx 300$ mG and $|B_{\rm VLA2}| \approx 800$ mG, which are consistent with the rough values reported in Sect. 5.4.2, making the presence of a magnetic dynamo unnecessary. Finally, from our results we can strongly depict the following scenario for VLA 1: the hot gas in a C-shock pumps the H_2O masers and at the same time the warm dust associated with this shock emits infrared photons, which pumps the CH_3OH masers in the pre-shock region.

5.5 Conclusions

We observed the 22-GHz H_2O masers and the 6.7-GHz CH_3OH masers in full polarization mode in the massive star-forming region W75N with the VLBA and the EVN, respectively. We detected 124 and 10 H_2O and CH_3OH masers, respectively, around the two radio sources VLA 1 and VLA 2, which appear to be in two different evolutionary stages; i.e., VLA 1 is more evolved and a radio jet has not formed yet in VLA 2. All the CH_3OH masers are related to VLA 1. From our observations, we have shown that these two sources separated in the sky by $\sim 1''$ (1300 AU) have different local physical environments. In particular, the linear polarization indicates that the magnetic field around VLA 1 is aligned well with the large-scale molecular bipolar outflow, while the magnetic field is well-ordered around the shell-like expanding gas associated with VLA 2. The detection of Zeeman-splitting of the H_2O maser emission indicates an absolute weighted magnetic field strengths $|B_{\rm VLA1}| \sim 700$ mG and $|B_{\rm VLA2}| \sim 1700$ mG. While we have measured for the CH_3OH masers a Zeeman-splitting ranging from 0.53 $\mathrm{m\,s^{-1}}$ to 0.80 $\mathrm{m\,s^{-1}}$. We were also able to determine the type of shocks that pump the H_2O masers associated with both sources. They both are C-shocks. We suggest VLA 1 as the driving source of the large-scale molecular bipolar outflow.

Chapter 6

NGC7538-IRS1

NGC7538 is a complex massive star-forming region. The region is composed of several radio continuum sources one of which is IRS1, a high-mass protostar from which a 0.3 pc molecular bipolar outflow was detected. Several maser species have been detected around IRS1. The CH_3OH masers have been suggested to trace a Keplerian-disc while the H_2O masers are almost aligned to the outflow. More recent results suggested that the region hosts a torus and potentially a disc, however with a different inclination than the Keplerian-disc supposed to be traced by the CH_3OH masers. Tracing the magnetic field close to protostars is fundamental for determining the orientation of the disc/torus. The NRAO Very Long Baseline Array was used to measure the linear polarization and the Zeeman-splitting of the 22-GHz H_2O masers towards NGC7538-IRS 1. While the European VLBI Network and the MERLIN telescopes were used to measure the linear polarization and the Zeeman-splitting of the 6.7-GHz CH_3OH masers. We detected 17 H_2O masers and 49 CH_3OH masers at high angular resolution. We detected linear polarization emission towards two H_2O masers and towards twenty CH_3OH masers. The CH_3OH masers, most of which only show a core structure, seem to trace rotating and potentially infalling gas in the inner part of a torus. Significant Zeeman-splitting was measured in three CH_3OH masers. We also propose a new description of the structure of the NGC7538-IRS1 maser region.

6.1 The source

NGC7538 is a complex massive star-forming region located in the Perseus arm of our Galaxy at a distance of 2.65 kpc (Moscadelli et al. 2009). The region is composed of several clusters of infrared sources (Wynn-Williams et al. 1974) and radio continuum sources (Campbell 1984). The brightest source is NGC7538-IRS1, whose central star has been suggested to be an O6 star of about

30 $M_\odot$ with systemic local standard of rest velocity $V_{\rm lsr} = -58$ km s^{-1} (Campbell & Thompson 1984; Sandell et al. 2009; Puga et al. 2010). Several high-velocity molecular bipolar outflows were detected in NGC7538 and one of these is elongated 0.3 pc from IRS 1 (position angle PA=140°) with a velocity of 250 km s^{-1} and a mass of 82.8 $M_\odot$ (Kameya et al. 1989; Gaume et al. 1995; Davis et al. 1998; Qiu et al. 2011). VLA continuum observations by Campbell (1984) indicated that the PA of the outflow decreases away from IRS1; i.e., 180° at 0″.3 (0.004 pc) and 165° at 2″ (0.03 pc). Kameya et al. (1989) gave three possible interpretations of this rotation: disc precession, interaction of the flow with dense gas, and coupling of the gas with a large-scale magnetic field around IRS1. Since Sandell et al. (2009) found that the collimated free-free jet (opening angle $\lesssim 30°$) is approximately aligned with the outflow and that there is a strong accretion flow towards IRS1 (accretion rate $\sim 2 \times 10^{-4}$ $M_\odot$yr^{-1}), IRS1 must be surrounded by an accretion disc. The morphology of the free-free emission, which is optically thick up to 100 GHz (Franco-Hernández & Rodríguez 2004), suggests that the disc should be almost edge-on and oriented East-West (Sconville et al. 2008; Kameya et al. 1989; Sandell et al. 2009). A possible detection of this edge-on disc was made by Minier et al. (1998), who observed a linear distribution of the brightest CH_3OH masers with an inclination angle of about 112°. Pestalozzi et al. (2004) estimated that this disc is a Keplerian-disc with an outer radius of ∼750 AU and an inner radius of ∼290 AU by modeling the CH_3OH maser emissions at 6.7 and 12.2–GHz.

Recent results are in disagreement with the edge-on disc traced by the CH_3OH masers. The observations of the mid-infrared emission suggest that the radio continuum emission does not come from a free-free jet but that it traces the ionized gas wind from the disc surface that, in the new scenario, would be perpendicular to the CO-bipolar outflows with a disc inclination angle $i = 32°$ (De Buizer & Minier 2005). Klaassen et al. (2009) observed two warm gas tracers (SO_2 and OCS) towards NGC7538-IRS1 with the SMA. Although the region was unresolved, they found a velocity gradient consistent with the CH_3OH maser velocities and perpendicular to the large-scale molecular bipolar outflow. This rotating gas might indicate that there is a torus (with an angular size of about 2″; i.e., ∼5300 AU at 2.65 kpc) surrounding the smaller accretion disc proposed by De Buizer & Minier (2005).

In addition, Kraus et al. (2006) proposed two possible scenarios for NGC7538 by considering both the linear distribution of the 6.7-GHz CH_3OH masers detected previously (e.g., Pestalozzi et al. 2004; De Buizer & Minier 2005) and the asymmetry in the near infrared (NIR) images observed by them. In their most likely scenario, called “Scenario B”, the CH_3OH masers trace the edge-on

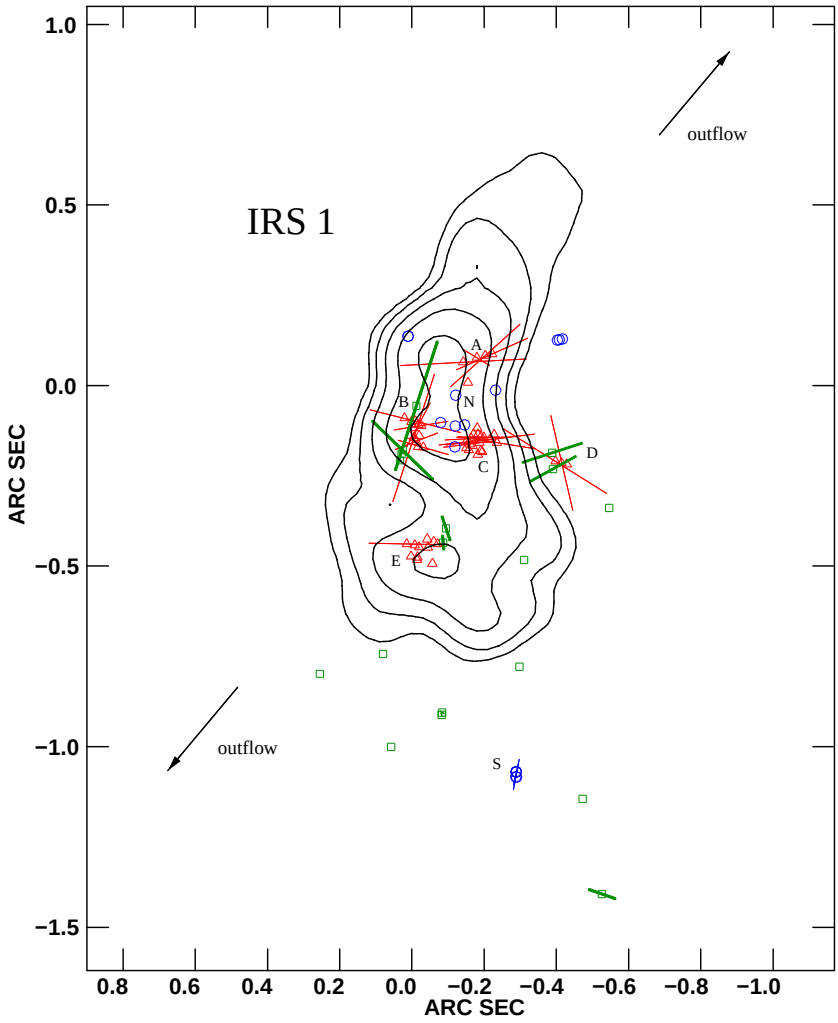

Figure 6.1: Positions of H_2O, CH_3OH, and OH maser features superimposed on the 2 cm continuum contour map of NGC7538-IRS1 observed with the VLA in 1986 (Franco-Hernández & Rodríguez 2004). Contours are 1, 2, 4, 8, 16 $\times$1.3 mJy beam^{-1}. The (0,0) position is $\alpha_{2000} = 23^{\rm h}13^{\rm m}45^{\rm s}.382$ and $\delta_{2000} = +61°28'10''.441$. Blue circles and red triangles indicate the positions of the H_2O and CH_3OH maser features, respectively, with their linear polarization vectors (60 mas correspond to a linear polarization fraction of 1%). Green boxes indicate the positions of the OH masers detected by Hutawarakorn & Cohen (2003) with their linear polarization vectors (thick lines, 6 mas correspond to 1%). The two arrows indicate the direction of the bipolar outflow ($\sim$140°).

disc as suggested by Pestalozzi et al. (2004) and the asymmetry might be due to the precession of the jet. In the "Scenario A" the CH_3OH masers do not trace a disc but an outflow cavity as proposed by De Buizer & Minier (2005) where the detected asymmetry might simply reflect the

innermost walls of this cavity.

Besides the CH_3OH masers, other maser species were detected around NGC7538-IRS1: OH, H_2O, NH_3 and H_2CO (e.g., Hutawarakorn & Cohen 2003; Galván-Madrid et al. 2010; Gaume et al. 1991; Hoffman et al. 2003). The OH masers are located southward and show no obvious disc structure or relation to the outflow direction (Hutawarakorn & Cohen 2003). H_2CO and H_2O masers are located near the centre of the continuum emission, and the H_2O masers are also almost aligned with the outflow (Galván-Madrid et al. 2010). The 6.7 and 12.2–GHz CH_3OH masers show a cone-shape that opens to the North-West (Minier et al. 2000).

So far, the magnetic field structure in NGC7538-IRS1 has been studied using submillimeter imaging polarimetry (Momose et al. 2001) and OH maser emission (Hutawarakorn & Cohen 2003). Although the polarization vectors are locally disturbed, at an angular resolution of $14''$ the magnetic field directions are in agreement with the direction of the outflow (Momose et al. 2001), while at milliarcsecond resolution the OH maser observations indicate a magnetic field oriented orthogonal to the outflow (Hutawarakorn & Cohen 2003). Since H_2O and CH_3OH masers were detected close to the centre of the continuum emission, i.e. to the protostar, it is worthwhile investigating their linear and circular polarization emissions. As shown in Chapter 5 for the massive star-forming region W75N, the polarization observations of the two maser species can depict a reasonable scenario for the magnetic field close to massive protostars. Moreover, the direction and strength of the magnetic field might help to disentangle the debate about the orientation of the disc.

Here we present VLBA observations of H_2O masers, MERLIN and EVN observations of CH_3OH masers in full polarization towards NGC7538-IRS1. In Sect. 6.3 we show our results obtained by studying the linear and circular polarization of H_2O and CH_3OH maser emissions in a similar way as done in Chapters 4 and 5. In Sect. 6.4 we discuss our results and we attempt to disentangle the complex morphology in NGC7538.

6.2 Observations and Analysis

6.2.1 22-GHz VLBA data

We observed the star-forming region NGC7538-IRS1 in the 6_{16}-5_{23} transition of H_2O (rest frequency: 22.23508 GHz) with the NRAO[1] VLBA on November 21, 2005. The observations were

[1]The National Radio Astronomy Observatory (NRAO) is a facility of the National Science Foundation operated under cooperative agreement by Associated Universities, Inc.

made in full polarization spectral mode using 4 overlapped baseband filters of 1 MHz in order to cover a total velocity range of ≈ 50 km s^{-1}. Two correlations were performed. One with 128 channels in order to generate all 4 polarization combinations (RR, LL, RL, LR) with a channel width of 7.8 kHz (0.1 km s^{-1}). The other one with high spectral resolution (512 channels; 1.96 kHz=0.027 km s^{-1}), which only contains the circular polarization combinations (LL, RR), to be able to detect Zeeman-splitting of the H_2O maser across the entire velocity range. Including the overheads, the total observation time was 8 h.

The data were edited and calibrated using AIPS following the method of Kemball et al. (1995). The bandpass, the delay, the phase and the polarization calibration were performed on the calibrator J0359+5057. The fringe-fitting and the self-calibration were performed on the brightest maser features (W06 in Table 6.1). All calibration steps were initially performed on the dataset with modest spectral resolution after which the solutions, with the exception of the bandpass solutions that were obtained separately, were copied and applied to the high spectral resolution dataset. Stokes I, Q and U data cubes (4 as $\times$ 4 as, rms ≈ 7 mJy beam^{-1}) were created using the AIPS task IMAGR (beam-size 1.0 mas $\times$ 0.4 mas) from the modest spectral resolution dataset, while the I and V cubes (rms ≈ 8 mJy beam^{-1}) where imaged from the high spectral resolution dataset and for the same fields. The Q and U cubes were combined to produce cubes of $POLI$ and $POLA$. Since these observations were obtained between two VLA polarization calibration observations[2], during which the linear polarization angle of J0359+5057 was constant at $-86\overset{\circ}{.}7$, we were able to estimate the polarization angles with a systemic error of no more than $\sim 3^\circ$.

We identified the H_2O maser features using the process described in Sect. 3.2.2. The two maser features that show linear polarization emission were fitted using the full radiative transfer method code for H_2O masers (Sect. 3.2.3). We modelled the observed linear polarized and total intensity maser spectra by gridding ΔV_i from 0.5 to 3.5 km s^{-1}, in steps of 0.025 km s^{-1}, by using a least square fitting routine. From the fit results we were able to determine the best values of the angle between the maser propagation direction and the magnetic field (θ). By considering the values of $T_\mathrm{b}\Delta\Omega$, ΔV_i, and θ we could also estimate the saturation state of the H_2O masers.

[2]http://www.aoc.nrao.edu/ smyers/calibration/

6.2.2 6.7-GHz MERLIN data

To detect the polarization of the CH_3OH maser emission at 6668.518 MHz ($5_1 - 6_0\,A^+$) we observed NGC7538-IRS1 with six of the MERLIN[3] telescopes in full polarization spectral mode on December 28, 2005. The observation time was $\sim$ 2 h, including overheads on the calibrators 2300+638, 3C84 and 3C286. We used a 250 kHz bandwidth ($\sim$ 11 km s^{-1}) with 256 channels (velocity resolution $\sim$ 0.04 km s^{-1}) centred on the source velocity $V_{\rm lsr} = -56.1$ km s^{-1}. For calibration purposes, the continuum calibrators were observed with the 16 MHz wide-band mode. Both 3C84 and 3C286 were also observed in the narrow-band spectral line configuration and were used to determine the flux and bandpass calibration solutions. The data were edited and calibrated using AIPS. The calibrator 3C84 was used to determine the phase offset between the wide- and narrow-band set-up. Instrumental feed polarization was determined using the unpolarized calibrator 3C84, and the polarization angle was calibrated using 3C286. Using one of the strongest isolated maser feature we were able to self-calibrate the data in right- and left-circular polarization separately. After calibration, the antenna contributions were re-weighed according to their sensitivity at 5 GHz and their individual efficiency. Stokes I, Q, U data cubes (5.12 as $\times$ 5.12 as, rms $\approx$ 10 mJy beam^{-1}) were created (beam-size 47 mas $\times$ 34 mas).

The CH_3OH maser features were also identified through the identification process mentioned above. If the program finds a group of maser spots that are not exactly spatially coincident but show a continuum linear distribution with a clear velocity gradient we report in the corresponding table only the brightest maser spot of the group (e.g., maser feature m06). We were unable to identify weak CH_3OH maser features ($<$ 1 Jy beam^{-1}) close to the brightest ones because of the dynamic range limits. To determine $T_{\rm b}\Delta\Omega$, $\Delta V_{\rm i}$, and θ, we adapted the code used for 22-GHz H_2O masers to model the 6.7-GHz CH_3OH masers, which has successfully been used in Chapter 4 for the CH_3OH masers in Cepheus A. We modelled the observed linear polarized and total intensity CH_3OH maser spectra by gridding $\Delta V_{\rm i}$ from 0.5 to 2.6 km s^{-1}, in steps of 0.05 km s^{-1}, by using a least square fitting routine.

[3]MERLIN is operated by the University of Manchester as a National Facility of the Science and Technology Facilities Council

6.2.3 6.7-GHz EVN data

NGC7538-IRS1 was also observed at 6.7-GHz in full polarization spectral mode with nine of the EVN[4] antennas (Jodrell2, Cambridge, Effelsberg, Onsala, Medicina, Torun, Noto, Westerbork, and the new joint antenna Yebes-40 m), for a total observation time of 5 h, on November 3, 2009 (program code ES063B). The bandwidth was 2 MHz, providing a velocity range of ~ 100 km s^{-1}. The data were correlated using 1024 channels in order to generate all 4 polarization combinations (RR, LL, RL, LR) with a spectral resolution of 1.9 kHz ($\sim$0.1 km s^{-1}).

The data were edited and calibrated using AIPS. The bandpass, the delay, the phase, and the polarization calibration were performed on the calibrator 3C286. Fringe-fitting and self-calibration were performed on the brightest maser feature (M26 in Table 6.3). Then we imaged the *I*, *Q*, *U*, *RR*, and *LL* cubes (2 as $\times$ 2 as, rms $\approx$ 8 mJy beam^{-1}) using the AIPS task IMAGR (beam-size 6.3 mas $\times$ 4.9 mas). The *Q* and *U* cubes were combined to produce cubes of *POLI* and *POLA*.

In this case, since the dynamic range of our EVN observations was better than that of MERLIN observations, we were able to identify with the "maser finder" program CH_3OH maser features with peak flux density less than 1 Jy beam^{-1}. The maser emission was fitted by using the adapted code for CH_3OH masers, but with a grid of $\Delta V_{\rm i}$ ranging from 0.5 to 1.95 km s^{-1}. We were able to determine the Zeeman-splitting from the cross-correlation between the RR and LL spectra, which was successfully used in Chapter 5 for the polarized CH_3OH maser emission detected in W75N. The dynamic range of the RR and LL cubes decreases close to the strongest maser emission of each group because of the residual calibration errors. As a result, we were not able to determine the Zeeman-splitting ($\Delta V_{\rm Z}$) for the maser features with a peak flux density less than 1.8 Jy beam^{-1}.

6.3 Results

In Fig. 6.1 we show the H_2O (blue circles) and CH_3OH maser features (red triangles) detected by us and superimposed on the 2 cm continuum contour map of NGC7538-IRS1 observed with the VLA in 1986 (Franco-Hernández & Rodríguez 2004). Since the continuum observations were made 20.3 yr before our observations, we have shifted the continuum map by -50 mas in both directions according to the proper motion, $\mu_\alpha = -2.45$ mas yr^{-1} and $\mu_\delta = -2.45$ mas yr^{-1}, measured by Moscadelli et al. (2009). The direction of the large-scale molecular bipolar outflow is also shown. Since we did not have absolute positions of the H_2O maser features, we estimated the offset of one

[4]The European VLBI Network is a joint facility of European, Chinese, South African and other radio astronomy institutes funded by their national research councils.

common H_2O maser feature detected both in the VLA observations of Galván-Madrid et al. (2010) and by us (features M3 and W01, respectively). All the positions of the H_2O maser features were shifted according to this offset. We indeed had absolute positions of the CH_3OH maser features at low angular resolution but not at high angular resolution. Hence, to overlay these features to the continuum, we matched the brightest CH_3OH maser feature detected with the EVN and the brightest one detected with MERLIN (m06, absolute position $\alpha_{2000} = 23^h13^m45^s.362$ and $\delta_{2000} = +61°28'10''.506$). All the CH_3OH maser features were shifted accordingly. Thus, based on the resolution of the VLA H_2O and MERLIN CH_3OH maser observations the uncertainties of H_2O and CH_3OH maser absolute positions are 50 mas (Galván-Madrid et al. 2010) and 10 mas, respectively.

6.3.1 H_2O masers

We detected 17 22-GHz H_2O maser features with the VLBA associated to NGC7538-IRS1 (named as W01-W17 in Table 6.1). No H_2O maser emission with a peak flux density (I) less than 0.13 Jy beam^{-1} is detected even though our channel rms is significantly less.

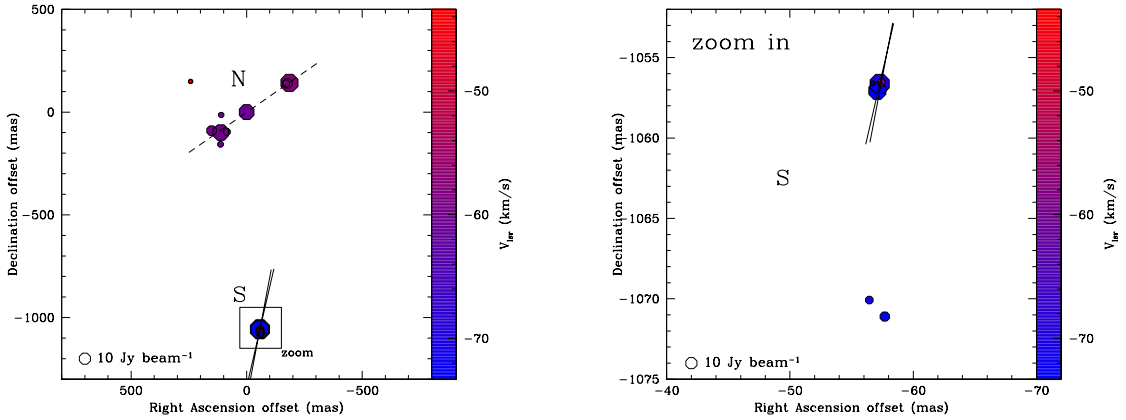

Figure 6.2: Left panel: a close-up view of the H_2O maser features around NGC7538-IRS1. Right panel: a zoom-in view of the boxed region of the left panel. The octagonal symbols are the identified H_2O maser features in present work scaled logarithmically according to their peak flux density. The maser LSR radial velocity is indicated by color. A 10 Jy beam^{-1} symbol is plotted for illustration in both panels. The linear polarization vectors, scaled logarithmically according to polarization fraction P_l (in Table 6.1), are overplotted. The dashed line (PA=$-52°$) is the results of the best linear fit of the H_2O masers of group N (features W16 and W17 were not included).The synthesized beam is 1.0 mas × 0.4 mas.

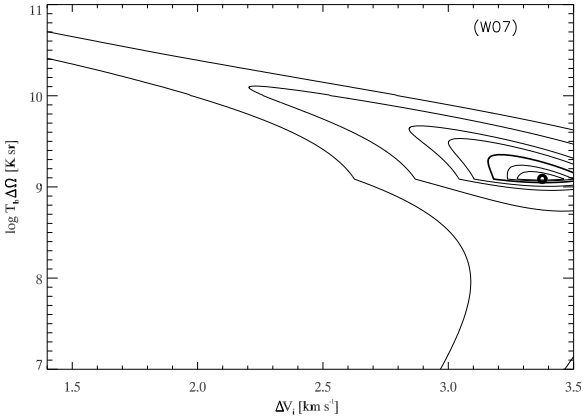

Figure 6.3: Results of the full radiative transfer χ^2-model fits, for the H_2O maser W07. The fit yields the emerging maser brightness temperature $T_b\Delta\Omega$ and the intrinsic maser thermal linewidth ΔV_i. Contours indicate the significance intervals $\Delta\chi^2$=0.25, 0.5, 1, 2, 3, 7, with the thick solid contours indicating 1σ and 3σ areas (see Vlemmings et al. 2006a and Chapter 5 for more details).

The H_2O maser features can be divided into two groups, N and S, that are composed of11 and 6 H_2O maser features, respectively. Group N is located at the centre of the continuum emission and it shows a linear distribution with a position angle of $-52°$ (see Fig. 6.2). The $V_{\rm lsr}$ of group N are between -60.2 km s^{-1} and -43.3 km s^{-1}. Excluding W16 and W17 the range is -60.2 km s^{-1}< $V_{\rm lsr}^{\rm N}$ < -58.3 km s^{-1}. Group S is located about $1''$ southward from group N and its velocity range is -73.3 km s^{-1}< $V_{\rm lsr}^{\rm S}$ < -57.3 km s^{-1}, thus more blue-shifted.

Linear polarization is detected in 2 H_2O maser features that belong to group S (W06 and W07). Their linear polarization fraction (column 7 of Table 6.1) is $P_{\rm l} \approx 1\%$ and the weighted linear polarization angles is $\langle\chi\rangle_{\rm H_2O}^{\rm S} \approx -11°$. The full radiative transfer method code for H_2O masers was able to fit the feature W07 and the results are given in column 10 and 11 of Table 6.1 and in Fig. 6.3. The emerging brightness temperature and the intrinsic thermal linewidth are 10^9 K sr and 3.4 km s^{-1}, respectively. By considering $T_b\Delta\Omega$ and the observed $P_{\rm l}$ we determined $\theta_{\rm H_2O}^{\rm B} = 81°$, indicating that the maser is operating in a regime where the magnetic field is close to perpendicular to the propagation of the maser radiation. No significant circular polarization emission is detected.

Table 6.1: All 22-GHz H_2O maser features detected in NGC7538-IRS1.

(1) Maser	(2) Group	(3) RA offset (mas)	(4) Dec offset (mas)	(5) Peak flux Density(I) (Jy/beam)	(6) $V_{\rm lsr}$ (km/s)	(7) $\Delta v_{\rm L}$ (km/s)	(8) $P_{\rm l}$ (%)	(9) χ (°)	(10) $\Delta V_{\rm i}^a$ (km/s)	(11) $T_{\rm b}\Delta\Omega^a$ (log K sr)	(12) $P_{\rm V}^b$ (m/s)	(13) θ^c (°)
W01	N	-185.2131	141.908	17.11 ± 0.07	-57.8	0.41	–	–	–	–	–	–
W02	N	-176.4676	139.422	1.00 ± 0.02	-58.3	0.32	–	–	–	–	–	–
W03	N	-170.9744	139.088	0.48 ± 0.02	-58.3	0.27	–	–	–	–	–	–
W04	S	-57.6929	-1071.104	0.90 ± 0.01	-72.2	0.59	–	–	–	–	–	–

Table 6.1: (continued)

(1) Maser	(2) Group	(3) RA offset (mas)	(4) Dec offset (mas)	(5) Peak flux Density(I) (Jy/beam)	(6) $V_{\rm lsr}$ (km/s)	(7) $\Delta v_{\rm L}$ (km/s)	(8) $P_{\rm l}$ (%)	(9) χ (°)	(10) $\Delta V_{\rm i}^{a}$ (km/s)	(11) $T_{\rm b}\Delta\Omega^{a}$ (log K sr)	(12) $P_{\rm V}^{b}$ (m/s)	(13) θ^{c} (°)
W05	S	-57.4470	-1056.554	0.48 ± 0.01	-57.3	0.47	–	–	–	–	–	–
W06	S	-57.3376	-1056.630	36.43 ± 0.02	-70.3	1.15	1.2 ± 0.1	-13.0 ± 1.3	–	–	–	–
W07	S	-57.1463	-1057.065	16.99 ± 0.01	-73.3	0.77	1.2 ± 0.1	-10.8 ± 0.5	$3.4^{+0.1}_{-0.3}$	$9.1^{+0.3}_{-0.1}$	0.4 ± 0.1	81^{+9}_{-13}
W08	S	-56.7637	-1056.586	0.15 ± 0.01	-67.3	1.46	–	–	–	–	–	–
W09	S	-56.4631	-1070.080	0.48 ± 0.01	-71.6	0.64	–	–	–	–	–	–
W10	N	0	0	7.34 ± 0.03	-60.6	0.56	–	–	–	–	–	–
W11	N	85.5692	-96.002	0.36 ± 0.02	-59.7	0.44	–	–	–	–	–	–
W12	N	110.0019	-13.538	0.20 ± 0.03	-60.2	0.83	–	–	–	–	–	–
W13	N	111.6690	-99.499	9.31 ± 0.03	-60.1	0.47	–	–	–	–	–	–
W14	N	112.8442	-156.492	0.25 ± 0.03	-60.1	0.42	–	–	–	–	–	–
W15	N	151.9803	-90.046	1.04 ± 0.03	-59.9	0.40	–	–	–	–	–	–
W16	N	242.0042	148.947	0.13 ± 0.01	-43.3	0.62	–	–	–	–	–	–
W17	N	242.7694	149.715	0.14 ± 0.01	-43.8	0.59	–	–	–	–	–	–

Notes. $^{(a)}$ The best-fitting results obtained by using a model based on the radiative transfer theory of H_2O masers for $\Gamma + \Gamma_\nu = 1{\rm s}^{-1}$ (Sect. 3.2.3). The errors were determined by analyzing the full probability distribution function. $^{(b)}$ The percentage of circular polarization is given by $P_{\rm V} = (V_{\rm max} - V_{\rm min})/I_{\rm max}$. $^{(c)}$The angle between the magnetic field and the maser propagation direction is determined by using the observed $P_{\rm l}$ and the fitted emerging brightness temperature. The errors were determined by analyzing the full probability distribution function.

6.3.2 CH_3OH masers

We detected 13 6.7-GHz CH_3OH maser features with the MERLIN telescope (named as m01-m13 in Table 6.2) that appear to be composed of 49 features when observed with the EVN resolution (named as M01-M49 in Table 6.3). Including the more sensitive EVN observations we detect no CH_3OH maser emission below 0.1 Jy beam^{-1}.

In the left panel of Fig. 6.4 we show the contours of the CH_3OH maser structures detected with MERLIN and in the right panel the distribution of the CH_3OH masers detected with the EVN. The CH_3OH maser features distribution at high angular resolution match the CH_3OH maser emission detected with MERLIN four years before perfectly. Following the naming convention adopted by Minier et al. (2000), they can be divided into five groups (from A to E). Group A, which is composed of 5 features (3 at MERLIN resolution) and hosts the brightest CH_3OH maser feature of the region (m06 and M26, respectively), shows a linear distribution. If we consider all the maser spots of the maser feature m06 (top-left panel of Fig. 6.5) we are able to measure a velocity gradient of about 0.02 km s^{-1} AU^{-1} from northwest to southeast, which is confirmed by considering the matching maser spots of M26 (EVN, top-right panel of Fig. 6.5).

Table 6.2: All 6.7-GHz methanol maser features detected in NGC7538-IRS1 with MERLIN.

(1) Maser	(2) Group	(3) RA[a] offset (mas)	(4) Dec[a] offset (mas)	(5) Peak flux Density(I) (Jy/beam)	(6) $V_{\rm lsr}$ (km/s)	(7) $\Delta v_{\rm L}$ (km/s)	(8) $P_{\rm l}$ (%)	(9) χ (°)	(10) $\Delta V_{\rm i}^{b}$ (km/s)	(11) $T_{\rm b}\Delta\Omega^{b}$ (log K sr)	(12) θ^{c} (°)
m01	D	-256	-275	22.91 ± 0.01	-60.68	0.86	7.1 ± 1.4	$+39 \pm 8$	$< 0.55^{d}$	$> 12^{d}$	–
m02	A	-115	47	1.70 ± 0.02	-55.94	0.45	–	–	–	–	–
m03	A	-74	22	23.53 ± 0.01	-57.30	0.36	1.3 ± 0.6	-47 ± 3	$1.20^{+0.08}_{-0.15}$	$8.7^{+0.1}_{-1.3}$	90^{+53}_{-53}
m04	C	-73	-215	51.32 ± 0.01	-61.38	0.37	1.3 ± 0.4	-42 ± 4	–	–	–
m05	C	-28	-222	50.53 ± 0.01	-60.81	0.85	0.7 ± 0.4	$+41 \pm 8$	$2.20^{+0.06}_{-0.13}$	$8.4^{+0.3}_{-1.0}$	76^{+11}_{-46}
m06	A	0	0	172.00 ± 0.02	-56.07	0.63	1.0 ± 0.4	$+45 \pm 60$	$< 0.95^{d}$	$> 12^{d}$	–
m07	B	59	-287	3.88 ± 0.01	-58.44	0.52	1.5 ± 0.9	-29 ± 7	–	–	–
m08	B	98	-186	1.11 ± 0.01	-58.70	0.54	–	–	–	–	–
m09	E	87	-559	3.54 ± 0.01	-59.05	0.31	1.6 ± 0.2	$+33 \pm 6$	$1.40^{+0.08}_{-0.12}$	$8.8^{+0.4}_{-0.3}$	87^{+4}_{-20}
m10	E	125	-546	1.08 ± 0.01	-58.83	0.42	–	–	–	–	–
m11	B	127	-207	24.41 ± 0.01	-57.61	0.70	0.5 ± 0.1	-23 ± 15	$< 0.90^{d}$	$> 12^{d}$	–
m12	E	154	-503	61.83 ± 0.01	-58.09	0.30	0.4 ± 0.1	$+10 \pm 5$	$1.65^{+0.05}_{-0.08}$	$8.2^{+0.7}_{-0.3}$	72^{+10}_{-44}
m13	B	159	-157	9.71 ± 0.02	-56.33	0.40	1.6 ± 1.3	$+18 \pm 13$	–	–	–

Notes.[a] The absolute reference position is $\alpha_{2000} = 23^{\rm h}13^{\rm m}45^{\rm s}.362$ and $\delta_{2000} = +61°28'10''.506$. [b] The best-fitting results obtained by using a model based on the radiative transfer theory of CH_3OH masers for $\Gamma + \Gamma_\nu = 1{\rm s}^{-1}$ (Sect. 3.2.3). The errors were determined by analyzing the full probability distribution function. [c] The angle between the magnetic field and the maser propagation direction is determined by using the observed $P_{\rm l}$ and the fitted emerging brightness temperature. The errors were determined by analyzing the full probability distribution function. [d] Because of the low angular resolution the code is able to give an upper limit for $\Delta V_{\rm i}$ and a lower limit for $T_{\rm b}\Delta\Omega$.

Group B is resolved into 12 CH_3OH maser features (4 at MERLIN resolution). The spots of the features M33 and M40 of this group show a velocity gradient similar to that of M26 but from southwest to northeast (bottom panels of Fig. 6.5). No CH_3OH maser features of group B detected with MERLIN show a velocity gradient. The CH_3OH maser groups C, D, and E are composed of 18, 3, and 11 features, respectively. While groups C and D are located close to the central peak of the continuum emission, the group E is located about 300 mas southward. The velocities of groups C and D are more blue-shifted ($-61.5\ {\rm km\,s^{-1}} < V_{\rm lsr} < -60.5\ {\rm km\,s^{-1}}$) than those of groups A, B and E ($-59\ {\rm km\,s^{-1}} < V_{\rm lsr} < -56\ {\rm km\,s^{-1}}$).

We detected linear polarization in 10 and 20 CH_3OH maser features with MERLIN and EVN, respectively. The features of group D show the highest linear polarization fraction of the region (column 8 of Tables 6.2 and 6.3), though the observations at higher angular resolution revealed M43 to be the feature with the highest linear polarization fraction (6.2%). Since the EVN provides an angular resolution eight times better than MERLIN and since we also have a higher dynamic range, we will, for the interpretation of the magnetic field, only use the linear polarization vectors of the CH_3OH maser features detected with the EVN. The groups A, C and E have weighted linear

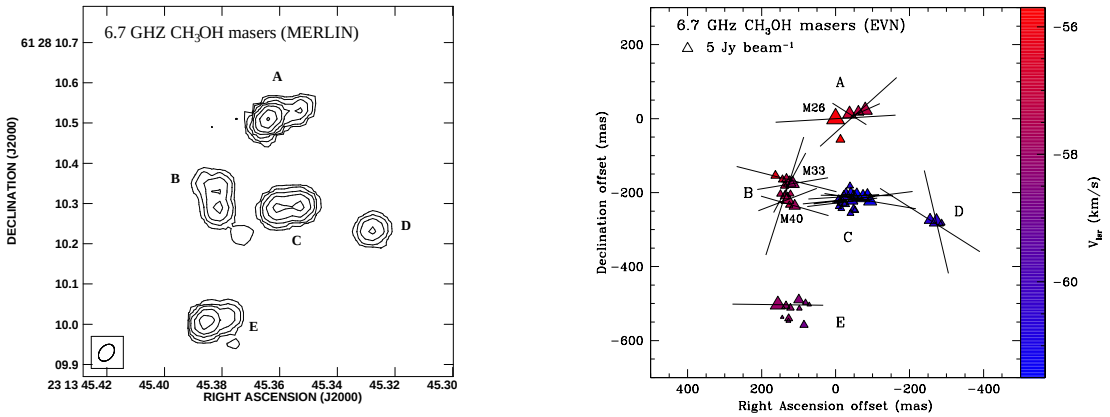

Figure 6.4: Left panel: CH_3OH maser structures detected with MERLIN around NGC7538-IRS1. Contours are 16, 32, 64, 128, 256, 512, 1024 × 0.15 Jy beam^{-1}. The synthesized beam is 47 mas × 34 mas. Right panel: a close-up view of the CH_3OH maser features detected with the EVN around NGC7538-IRS1. The synthesized beam is 6.3 mas × 4.9 mas. The triangle symbols are the identified maser features in present work scaled logarithmically according to their peak flux density. The maser LSR radial velocity is indicated by color. A 20 and 5 Jy beam^{-1} symbols are plotted for illustration in the left and right panels, respectively. The linear polarization vectors, scaled logarithmically according to the polarization fraction P_l (Tables 6.2 and 6.3), are overplotted.

polarization vectors almost oriented East-West, with angles $-86°\pm31°$, $-88°\pm6°$, and $+89°\pm44°$, respectively. The weighted linear polarization angles for the other two groups are $\langle\chi^{\rm B}_{\rm CH_3OH}\rangle = -60°\pm36°$ and $\langle\chi^{\rm D}_{\rm CH_3OH}\rangle = +48°\pm32°$.

The full radiative transfer method code for CH_3OH masers was able to fit 7 (MERLIN) and 20 (EVN) CH_3OH maser features, the results are given in columns 10 and 11 of Tables 6.2 and 6.3. Considering the high angular resolution observations, the weighted intrinsic maser linewidth and the weighted emerging brightness temperature are $\langle\Delta V_{\rm i}\rangle_{\rm CH_3OH} = 0.9$ km s^{-1} and $\langle T_{\rm b}\Delta\Omega\rangle_{\rm CH_3OH} \approx 10^9$ K sr. As an example, the χ^2-contours for feature M33 are reported in Fig. 6.6.

The fit for the CH_3OH maser features detected with MERLIN gives values both for $\Delta V_{\rm i}$ and for $T_{\rm b}\Delta\Omega$ consistent or larger than those detected with the EVN (see Table 6.4). However, due to the lower angular resolution of MERLIN, and the occurrence of strong velocity gradients, the fits are strongly affected by line blending. As we did for the H_2O maser features, we are able to determine the θ values (column 12 and 13 of Tables 6.2 and 6.3, respectively) from $T_{\rm b}\Delta\Omega$ and $P_{\rm l}$. The weighted value for the whole region is $\langle\theta\rangle^{\rm EVN}_{\rm CH_3OH} = 86^{\circ}{}^{+4^{\circ}}_{-43^{\circ}}$, which is almost constant in all groups. Only for the group E we determine a lower value; i.e., $\langle\theta^{\rm E}\rangle^{\rm EVN}_{\rm CH_3OH} = 75^{\circ}{}^{+15^{\circ}}_{-35^{\circ}}$.

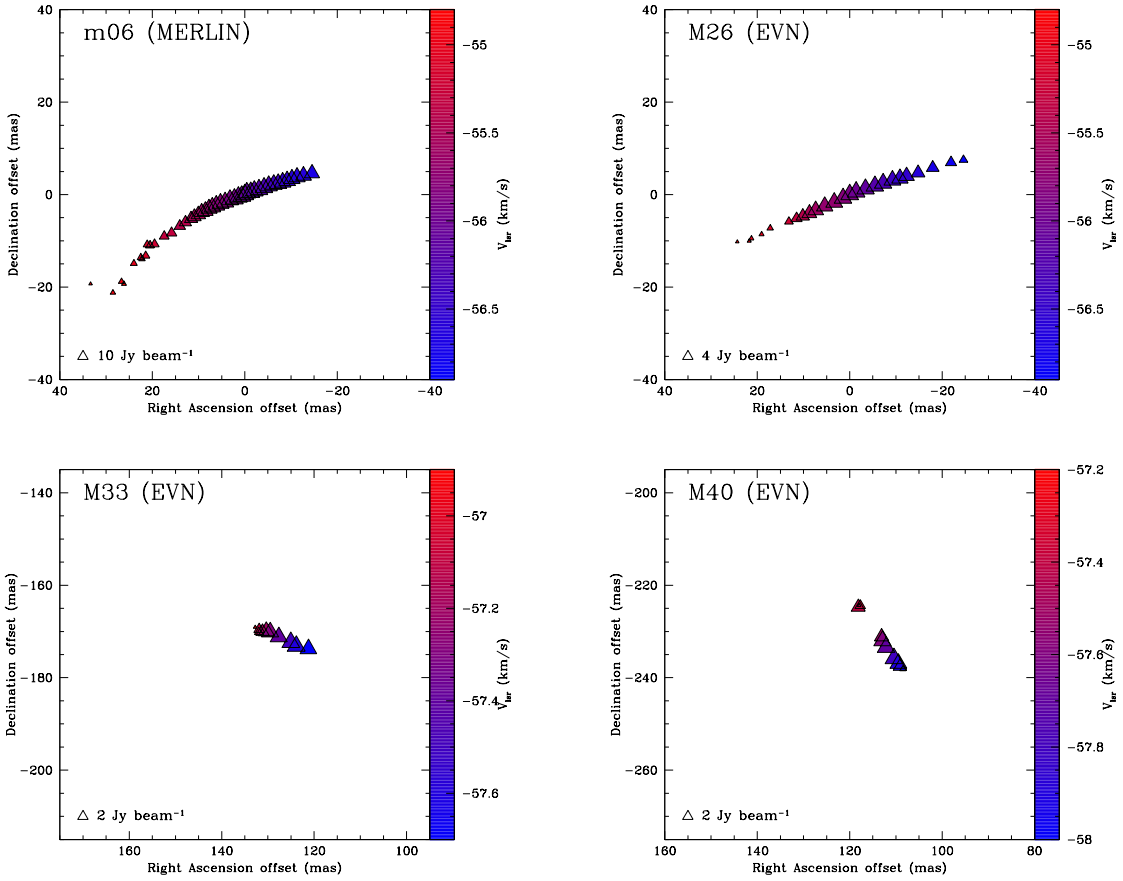

Figure 6.5: A zoom-in view of the CH_3OH maser spots of the features m06, which was detected with MERLIN, M26, M33, and M40, which were detected with the EVN. Features m06 and M26 are the same CH_3OH maser feature detected with the two instruments. The LSR radial velocity of the spots is indicated by color. A 10, 4, and 2 Jy beam^{-1} symbols are plotted for illustration in the panels.

The Zeeman-splitting (ΔV_Z) in m s^{-1} determined from the cross-correlation between the RR and LL spectra of the CH_3OH maser features detected with the EVN is reported in column 12 of Table 6.3. Note that the cross-correlation method is dynamic range sensitive, thus we are able to measure ΔV_Z only for those features that show a very high dynamic range. It has been impossible to obtain ΔV_Z measurements from MERLIN data because of the insufficient dynamic range.

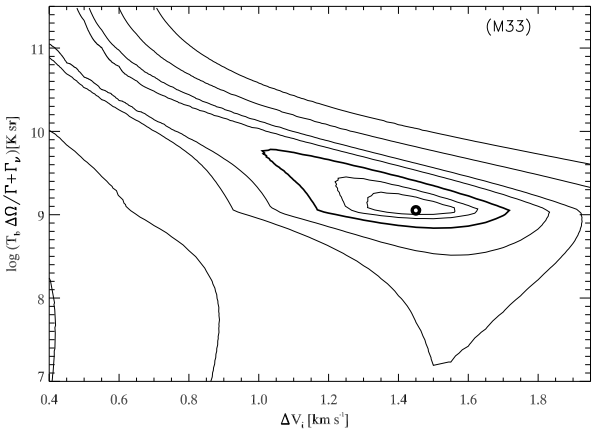

Figure 6.6: Result of the full radiative transfer χ^2-model fits for the CH_3OH maser feature M33 detected with the EVN. The fit yields the emerging maser brightness temperature $T_b\Delta\Omega$ and the intrinsic maser thermal linewidth ΔV_i. Contours indicate the significance intervals $\Delta\chi^2$=0.25, 0.5, 1, 2, 3, 7, with the thick solid contours indicating 1σ and 3σ areas.

Table 6.3: All 6.7-GHz methanol maser features detected in NGC7538-IRS1 with the EVN.

(1) Maser	(2) Group	(3) RA offset (mas)	(4) Dec offset (mas)	(5) Peak flux Density(I) (Jy/beam)	(6) V_{lsr} (km/s)	(7) Δv_L (km/s)	(8) P_l (%)	(9) χ (°)	(10) ΔV_i^a (km/s)	(11) $T_b\Delta\Omega^a$ (log K sr)	(12) ΔV_Z^b (m/s)	(13) θ^c (°)
M01	D	-286.910	-282.502	0.55 ± 0.02	-60.40	0.12	–	–	–	–	–	–
M02	D	-272.725	-279.037	16.82 ± 0.03	-60.49	0.21	4.5 ± 0.8	$+13 \pm 16$	$1.0^{+0.3}_{-0.3}$	$9.41^{+0.94}_{-0.39}$	$+2.7 \pm 0.3$	77^{+13}_{-11}
M03[d]	D	-255.344	-273.992	4.72 ± 0.03	-60.58	0.24	5.6 ± 0.9	$+58 \pm 5$	$0.9^{+0.5}_{-0.1}$	$9.58^{+0.81}_{-0.47}$	–	80^{+8}_{-10}
M04	C	-93.660	-222.357	10.39 ± 0.02	-61.28	0.24	3.6 ± 0.2	$+81 \pm 22$	$1.0^{+0.3}_{-0.2}$	$9.26^{+0.58}_{-0.14}$	–	83^{+7}_{-23}
M05	C	-86.171	-200.790	0.73 ± 0.02	-61.28	0.20	–	–	–	–	–	–
M06	A	-80.377	22.786	15.21 ± 0.03	-57.24	0.20	3.6 ± 0.2	-66 ± 10	$1.0^{+0.2}_{-0.2}$	$8.74^{+0.69}_{-0.11}$	–	87^{+8}_{-17}
M07	C	-74.392	-213.730	16.41 ± 0.03	-61.28	0.29	4.1 ± 0.5	-83 ± 20	$1.4^{+0.3}_{-0.5}$	$9.39^{+0.92}_{-0.25}$	–	77^{+8}_{-42}
M08	A	-61.547	18.163	4.08 ± 0.02	-57.15	0.23	4.3 ± 1.4	-48 ± 40	$0.8^{+0.2}_{-0.3}$	$9.37^{+0.61}_{-1.64}$	–	79^{+11}_{-22}
M09	C	-57.174	-207.658	9.48 ± 0.02	-61.46	0.27	2.5 ± 0.7	-90 ± 4	$1.3^{+0.3}_{-0.4}$	$9.10^{+0.94}_{-1.25}$	–	75^{+15}_{-36}
M10	C	-52.938	-248.180	0.73 ± 0.02	-60.84	0.31	–	–	–	–	–	–
M11	C	-49.085	-205.700	1.12 ± 0.03	-60.75	1.08	–	–	–	–	–	–
M12	C	-48.483	-245.093	1.21 ± 0.02	-60.67	0.28	–	–	–	–	–	–
M13	C	-44.930	-222.357	4.65 ± 0.02	-60.84	0.25	1.4 ± 0.4	-86 ± 83	$1.2^{+0.3}_{-0.3}$	$8.81^{+0.83}_{-1.00}$	–	76^{+14}_{-38}
M14	C	-41.350	-198.801	1.11 ± 0.01	-61.02	0.49	–	–	–	–	–	–
M15	C	-40.421	-255.891	0.59 ± 0.02	-60.84	0.33	–	–	–	–	–	–
M16	C	-39.082	-181.780	0.57 ± 0.03	-60.75	0.18	–	–	–	–	–	–
M17	A	-37.661	12.650	14.31 ± 0.02	-56.80	0.33	1.4 ± 0.2	$+58 \pm 12$	$1.6^{+0.3}_{-0.4}$	$8.77^{+0.75}_{-0.25}$	–	80^{+10}_{-40}
M18	C	-27.986	-199.362	0.80 ± 0.03	-60.75	0.19	–	–	–	–	–	–
M19	C	-25.963	-230.701	1.29 ± 0.02	-60.84	0.26	–	–	–	–	–	–
M20	C	-22.083	-211.354	3.19 ± 0.03	-60.58	0.27	2.4 ± 1.0	-87 ± 23	$1.0^{+0.3}_{-0.4}$	$9.05^{+0.39}_{-1.86}$	–	79^{+11}_{-42}
M21	C	-18.147	-226.401	2.53 ± 0.03	-60.75	0.22	2.41 ± 0.04	-83 ± 12	$1.0^{+0.3}_{-0.2}$	$9.05^{+0.56}_{-0.06}$	–	85^{+6}_{-41}
M22	C	-15.769	-242.950	0.51 ± 0.02	-60.84	0.25	–	–	–	–	–	–
M23	A	-13.091	-56.523	1.43 ± 0.05	-55.75	0.26	–	–	–	–	–	–
M24	C	-8.172	-220.826	1.83 ± 0.02	-60.67	0.29	2.5 ± 0.3	-84 ± 14	$1.3^{+0.3}_{-0.4}$	$9.09^{+0.67}_{-0.22}$	–	82^{+7}_{-39}
M25	C	-7.762	-238.071	0.42 ± 0.02	-60.84	0.32	–	–	–	–	–	–
M26[d]	A	0	0	95.15 ± 0.08	-55.92	0.33	5.83 ± 0.03	-87 ± 17	$0.5^{+0.4}_{-0.2}$	$11.39^{+0.75}_{-0.03}$	$+1.6 \pm 0.3$	86^{+5}_{-19}

Table 6.3: (continued)

(1) Maser	(2) Group	(3) RA offset (mas)	(4) Dec offset (mas)	(5) Peak flux Density(I) (Jy/beam)	(6) $V_{\rm lsr}$ (km/s)	(7) $\Delta v_{\rm L}$ (km/s)	(8) $P_{\rm l}$ (%)	(9) χ (°)	(10) $\Delta V_{\rm i}^{a}$ (km/s)	(11) $T_{\rm b}\Delta\Omega^{a}$ (log K sr)	(12) $\Delta V_{\rm Z}^{b}$ (m/s)	(13) θ^{c} (°)
M27	E	71.113	-503.039	0.19 ± 0.01	-58.56	0.12	–	–	–	–	–	–
M28	E	81.252	-497.234	0.37 ± 0.01	-58.56	0.27	–	–	–	–	–	–
M29	E	85.297	-557.914	1.06 ± 0.01	-58.91	0.27	–	–	–	–	–	–
M30	E	97.923	-513.329	0.30 ± 0.01	-58.38	0.18	–	–	–	–	–	–
M31	E	99.399	-489.943	2.26 ± 0.01	-58.38	0.21	–	–	–	–	–	–
M32	B	110.386	-235.856	4.37 ± 0.02	-57.77	0.31	2.4 ± 0.6	$+74 \pm 44$	$1.4^{+0.3}_{-0.4}$	$9.06^{+0.81}_{-1.33}$	–	89^{+10}_{-38}
M33	B	116.016	-175.760	10.11 ± 0.02	-57.86	0.30	2.5 ± 0.7	-81 ± 83	$1.5^{+0.4}_{-0.4}$	$9.05^{+0.94}_{-1.28}$	–	76^{+15}_{-36}
M34	B	121.782	-203.613	0.54 ± 0.02	-57.42	0.55	–	–	–	–	–	–
M35	E	122.083	-511.884	0.80 ± 0.02	-58.21	0.22	–	–	–	–	–	–
M36	B	123.859	-173.165	6.46 ± 0.02	-57.59	0.32	2.3 ± 0.6	-28 ± 42	$1.5^{+0.4}_{-0.4}$	$9.04^{+1.00}_{-1.08}$	–	89^{+12}_{-38}
M37	B	125.062	-233.976	0.68 ± 0.02	-57.07	0.28	–	–	–	–	–	–
M38	E	126.893	-540.110	0.93 ± 0.03	-58.12	0.21	–	–	–	–	–	–
M39	E	127.303	-546.631	0.21 ± 0.06	-58.73	0.26	–	–	–	–	–	–
M40	B	129.927	-218.961	8.98 ± 0.02	-57.51	0.37	2.1 ± 0.7	-69 ± 10	$1.8^{+0.1}_{-0.4}$	$8.99^{+1.00}_{-1.5}$	–	71^{+9}_{-44}
M41[d]	B	132.550	-163.392	1.81 ± 0.02	-57.24	0.34	4.3 ± 1.1	$+76 \pm 42$	$0.6^{+0.5}_{-0.1}$	$9.44^{+0.50}_{-1.72}$	–	85^{+5}_{-17}
M42	E	134.190	-506.261	1.10 ± 0.03	-58.12	0.20	–	–	–	–	–	–
M43[d]	B	137.196	-209.274	1.69 ± 0.03	-57.24	0.37	6.2 ± 2.0	-18 ± 17	$0.5^{+0.3}_{-0.3}$	$9.83^{+0.22}_{-1.94}$	–	90^{+20}_{-20}
M44	B	137.552	-181.682	1.05 ± 0.02	-57.33	0.24	–	–	–	–	–	–
M45	B	143.509	-164.852	0.98 ± 0.02	-56.72	0.32	–	–	–	–	–	–
M46	E	144.083	-537.047	0.12 ± 0.01	-58.73	0.28	–	–	–	–	–	–
M47	B	149.112	-203.584	0.71 ± 0.02	-57.42	0.27	–	–	–	–	–	–
M48	E	156.163	-503.223	23.68 ± 0.03	-58.03	0.24	3.5 ± 0.6	$+89 \pm 44$	$1.2^{+0.2}_{-0.4}$	$9.26^{+1.00}_{-0.31}$	-2.7 ± 0.3	75^{+15}_{-35}
M49	B	162.558	-154.095	1.50 ± 0.05	-56.19	0.16	–	–	–	–	–	–

Notes.[a] The best-fitting results obtained by using a model based on the radiative transfer theory of CH_3OH masers for $\Gamma + \Gamma_\nu = 1{\rm s}^{-1}$ (Sect. 3.2.3). The errors were determined by analyzing the full probability distribution function. For $\Gamma + \Gamma_\nu = 0.6{\rm s}^{-1}$ (Minier et al. 2002) $T_{\rm b}\Delta\Omega$ has to be adjusted by adding -0.22. [b] The Zeeman-splittings are determined from the cross-correlation between the RR and LL spectra. [c]The angle between the magnetic field and the maser propagation direction is determined by using the observed $P_{\rm l}$ and the fitted emerging brightness temperature. The errors were determined by analyzing the full probability distribution function. [d]Because of the degree of the saturation of these H_2O masers $T_{\rm b}\Delta\Omega$ is underestimated, $\Delta V_{\rm i}$ and θ are overestimated.

6.4 Discussion

6.4.1 Comparing CH_3OH spectra at different resolution

Vlemmings (2008) observed the CH_3OH masers with the Effelsberg 100-m telescope in November 2007, i.e. two year later than our MERLIN observations and two year before our EVN observations. A comparison between the single dish and MERLIN fluxes reveals only a difference $\lesssim 10\%$ across the whole spectra. This slight difference can be explained by the different resolution of the two instruments and flux calibration uncertainties in the Effelsberg observations ($\sim 10\%$,

Table 6.4: Weighted values of the linear polarization angles, the intrinsic thermal linewidths, the emerging brightness temperatures, and the angles between the line-of-sight and the magnetic field of the CH_3OH masers for feature in common.

Group	EVN				MERLIN			
	$\langle\chi\rangle$ (°)	$\langle\Delta V_i\rangle$ (km s^{-1})	$\langle T_b\Delta\Omega\rangle$ (K sr)	$\langle\theta\rangle$ (°)	$\langle\chi\rangle$ (°)	$\langle\Delta V_i\rangle$ (km s^{-1})	$\langle T_b\Delta\Omega\rangle$ (K sr)	$\langle\theta\rangle$ (°)
A	-86 ± 31	$0.9^{+0.4}_{-0.3}$	5×10^9	86^{+4}_{-42}	-51 ± 62	$<1.2^a$	$> 5 \times 10^{8\,b}$	90^{+53}_{-53}
B	-60 ± 36	$0.5^{+0.9}_{-0.1}$	1×10^9	87^{+4}_{-42}	-63 ± 76	$<0.9^a$	$> 1 \times 10^{12\,b}$	-
C	-88 ± 6	$1.0^{+0.3}_{-0.4}$	2×10^9	85^{+4}_{-46}	-74 ± 69	$2.2^{+0.1}_{-0.1}$	3×10^8	76^{+11}_{-46}
D	$+48 \pm 32$	$0.6^{+0.4}_{-0.1}$	2×10^{10}	79^{+8}_{-13}	$+39 \pm 8$	$<0.6^a$	$> 1 \times 10^{12\,b}$	-
E	$+89 \pm 44$	$1.2^{+0.2}_{-0.4}$	2×10^9	75^{+15}_{-35}	$+21 \pm 54$	$1.5^{+0.1}_{-0.1}$	6×10^8	86^{+5}_{-29}

Notes. $^{(a)}$ Only the highest value has been taken into account. $^{(b)}$ Only the lowest value has been taken into account.

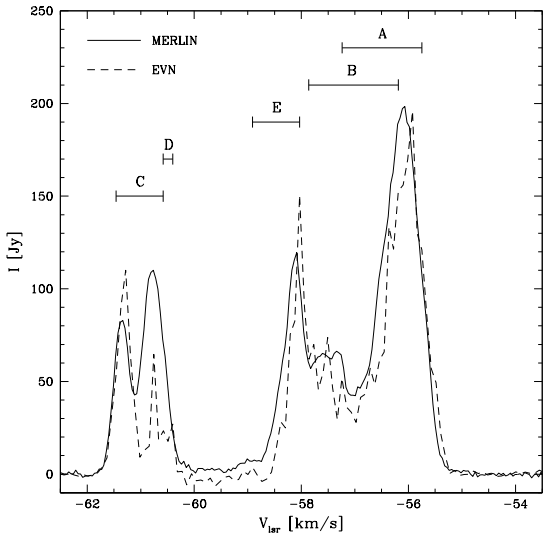

Figure 6.7: Profile of the flux spectra of the CH_3OH masers in NGC7538 detected with MERLIN (solid line, epoch 2005) and the EVN (dashed line, epoch 2009). The groups are also reported according to the velocity of Table 6.3.

Vlemmings 2008). Thus no significant changes occurred between the two epochs and there is no indication of a core/halo structure of the masers at scales of ∼100 AU such as described for a sample of CH_3OH maser sources by Pandian et al. (2011).

In Fig. 6.7 we show the total flux spectra of the CH_3OH maser features (or simply CH_3OH masers)

detected with MERLIN and the EVN in 2005 and 2009, respectively. Generally when 6.7-GHz CH_3OH masers are observed with both these instruments the EVN resolved out between 60 and 90% of the flux (e.g. Minier et al. 2002; Bartkiewicz et al. 2009; Torstensson et al. 2011). This indicates the presence of emission structures on scales that are resolved by the EVN, i.e. a halo structure that surrounds the core of the masers. Moreover, if the maser spots do not have a compact core, they would not be detected in the EVN observations (Pandian et al. 2011). Although in our observations the EVN resolves out about 50% of the flux of group C ($V_{\rm lsr} > -61$ km s^{-1}), the majority of the flux appears to be recovered across the entire CH_3OH maser spectrum. This suggests that the halo structure is absent, except in some masers of group C and likely in M26 of group A, and that the masers only contain a compact core. Moreover, the no detection of the maser m07 with the EVN might indicate the absence of the compact core in this maser.

Minier et al. (2002) observed the 6.7-GHz CH_3OH masers with 5 antennas of the EVN. They determined the size of the halo (d_1) and of the core (d_2) of the brightest CH_3OH masers of groups A and C by Gaussian fitting the visibility amplitudes. For the brightest maser of group A they determined $d_1 = 5$ mas ($\sim$13 AU at 2.65 kpc) and $d_2 = 3$ mas ($\sim$8 AU), and $d_1 = 17$ mas ($\sim$45 AU) and $d_2 = 5$ mas ($\sim$13 AU) were measured for the brightest maser of group C. The Gaussian fit of M26 and M07 gives a size of 5 mas and 6 mas respectively, indicating that the EVN resolves out the halo structure observed by Minier et al. (2002) and that we observe only the core of these two masers.

We suggest that the absence of a halo structure in most of the CH_3OH masers could be due to the amplification of the strong continuum emission shown in Fig. 6.1. This would argue that almost all the CH_3OH masers are on the front-side of this source. Similar arguments were used in the interpretation of the structure of Cepheus A (Torstensson et al. 2011).

6.4.2 H_2O and CH_3OH maser properties

Before discussing the polarization analysis of the masers in NGC7538-IRS1 we need to consider the degree of the maser saturation. As explained in details in Sect. 3.2.3, if the full radiative transfer method code is applied to a saturated maser the code gives a lower limit for $T_{\rm b}\Delta\Omega$ and an upper limit for $\Delta V_{\rm i}$. The masers are unsaturated when $R/(\Gamma + \Gamma_\nu) < 1$ and fully saturated when $R/(\Gamma + \Gamma_\nu) \sim 100$, where R is the stimulated emission rate given by

$$R \simeq \frac{A k_{\rm B} T_{\rm b} \Delta\Omega}{4\pi h\nu}. \tag{6.1}$$

Here A is the Einstein coefficient for the maser transition, which for H_2O masers is taken to be equal to 2×10^{-9} s^{-1} (Sect. 2.3.1) and for the CH_3OH masers is 0.1532×10^{-8} s^{-1} (Sect. 2.3.2), k_B and h are the Boltzmann and Planck constants, respectively, and ν the maser frequency. From $R/(\Gamma + \Gamma_\nu) < 1$ we can estimate an upper limit for the emerging brightness temperature below which the masers can be considered unsaturated. The limits are $(T_b \Delta\Omega)_{H_2O} < 6.7 \times 10^9$ K sr and $(T_b \Delta\Omega)_{CH_3OH} < 2.6 \times 10^9$ K sr for H_2O and CH_3OH masers, respectively. Consequently, only four CH_3OH masers are partly saturated; i.e., M03, M26, M41 and M43 (Table 6.3). Since the model emerging brightness temperature scale linearly with $\Gamma + \Gamma_\nu$ the ratio $R/(\Gamma + \Gamma_\nu)$ is independent on the value of $\Gamma + \Gamma_\nu$. The Δv_L of the saturated CH_3OH masers are close to ΔV_i implying that the maser lines are rebroadened as expected when the maser becomes saturated. Furthermore, these 4 CH_3OH masers do also show high linear polarization fraction, which again confirm their saturated state (Goldreich et al. 1973).

The intrinsic linewidth of the H_2O maser W07 is higher than the typical values measured in previous works, i.e. $\Delta V_i = 2.5$ km s^{-1} (Chapter 5). This difference might indicate the presence of a strong turbulent gas with a turbulence velocity of $\Delta V_{turb} = 2.3$ km s^{-1} or multiple components overlapping.

By comparing the brightness temperature T_b with $T_b \Delta\Omega$ obtained from the model, we can estimate the maser beaming angle ($\Delta\Omega$) for both maser species. We can estimate the brightness temperature (T_b) by considering the equation

$$\frac{T_b}{[\mathrm{K}]} = \frac{S(\nu)}{[\mathrm{Jy}]} \cdot \left(\frac{\Sigma^2}{[\mathrm{mas}^2]} \right)^{-1} \cdot \xi, \tag{6.2}$$

where $S(\nu)$ is the flux density, Σ the maser angular size and ξ is a constant factor that includes all constant values, such as the Boltzmann constant, the wavelength, and the proportionality factor obtained for a Gaussian shape by (Burns et al. 1979). The values of ξ for H_2O and CH_3OH masers, as already reported in Chapter 5, are

$$\xi_{H_2O} = 1.24 \cdot 10^9 \text{ mas}^2 \text{ Jy}^{-1} \text{ K}, \tag{6.3}$$

$$\xi_{CH_3OH} = 13.63 \cdot 10^9 \text{ mas}^2 \text{ Jy}^{-1} \text{ K}. \tag{6.4}$$

The H_2O maser W07 is unresolved and $\Delta\Omega_{H_2O} = 10^{-2}$. The Gaussian fit of CH_3OH masers detected with the EVN gives a size between 5 and 7 mas, which indicate that all the CH_3OH masers are marginally resolved.

In a tubular geometry $\Delta\Omega \approx (d/l)^2$, where d and l are the transverse size and length of the

tube, respectively. By assuming d approximately the size of the masers, the maser lengths are in the range 10^{13} cm $< l_{\rm H_2O} < 10^{14}$ cm and 10^{14} cm $< l_{\rm CH_3OH} < 10^{15}$ cm for W07 and the CH_3OH masers, respectively.

6.4.3 Magnetic field in NGC7538-IRS1

CH_3OH Zeeman-splitting and magnetic field

We measured 6.7-GHz CH_3OH maser Zeeman-splitting ranging from $-2.7\ \mathrm{m\,s^{-1}}$ to $+2.7\ \mathrm{m\,s^{-1}}$. This is 2–3 times larger than was measured with the Effelsberg telescope (Vlemmings 2008) as expected when resolving individual masers. As explained in Sect. 2.3.2 the Zeeman-splitting coefficient is still uncertain so we cannot give here any exact value for the magnetic field strength until careful laboratory measurements of the g-factor appropriate for the 6.7-GHz CH_3OH masers are made. Since there is a linear proportionality between $\Delta V_{\rm Z}$ and $B_{||}$, we can say that the negative value of the Zeeman-splitting indicates a magnetic field oriented towards the observer and positive away from the observer. However, we can speculatively give a possible range of values for $|B_{||}|$ by considering $0.005\ \mathrm{km\,s^{-1}\,G^{-1}} < \alpha_Z < 0.049\ \mathrm{km\,s^{-1}\,G^{-1}}$, thus $50\ \mathrm{mG} \lesssim |B_{||}| \lesssim 500\ \mathrm{mG}$.

Magnetic field orietation

Before discussing the orientation of the magnetic field we have to evaluate the foreground Faraday rotation (i.e., the rotation due to the medium between the source and the observer), which from Eq. 5.3 is given by

$$\Phi_{\rm f}[^\circ] = 4.22 \times 10^6 \left(\frac{D}{[\mathrm{kpc}]}\right) \left(\frac{n_e}{[\mathrm{cm^{-3}}]}\right) \left(\frac{B_{||}}{[\mathrm{mG}]}\right) \left(\frac{\nu}{[\mathrm{GHz}]}\right)^{-2}, \tag{6.5}$$

where now D is the length of the path over which the Faraday rotation occurs expressed in kpc, $n_{\rm e}$ and $B_{||}$ are respectively the average electron density and the magnetic field along this path and ν is the frequency. By assuming the interstellar electron density, the magnetic field, and the distance are $n_{\rm e} \approx 0.012\,\mathrm{cm^{-3}}$, $B_{||} \approx 2\,\mu$G (Sun et al. 2008), and $D = 2.65$ kpc, respectively, $\Phi_{\rm f}$ is estimated to be $0\overset{\circ}{.}5$ at 22-GHz and $6\overset{\circ}{.}0$ at 6.7-GHz. At both frequencies the foreground Faraday rotation is within the errors reported in Tables 6.1 and 6.3 thus it should not affect our conclusions.

Since all the θ values are greater than the Van Vleck angle $\theta_{\rm crit} \sim 55^\circ$ (Goldreich et al. 1973), the magnetic fields are inferred to be perpendicular to the linear polarization vectors. The magnetic field orientation derived from the H_2O masers is $\varphi_{\rm H_2O} = +79^\circ$, while the 5 groups of CH_3OH masers show orientation angles $\varphi^A_{\rm CH_3OH} = +4^\circ$, $\varphi^B_{\rm CH_3OH} = +30^\circ$, $\varphi^C_{\rm CH_3OH} = +2^\circ$, $\varphi^D_{\rm CH_3OH} = -42^\circ$, and

$\varphi^{D}_{\mathrm{CH_3OH}} = -1°$. However, considering the relatively large errors in column 13 of Table 6.3, we cannot rule out that the actual θ values are below 55°, in which case the magnetic field is parallel to the linear polarization vectors.

Since Hutawarakorn & Cohen (2003) measured the linear polarized emission of the 1.6 and 1.7-GHz OH masers, we can now compare the orientation of the magnetic field derived from the two maser species (Fig. 6.1). We have to consider that the Faraday rotation at the OH maser frequencies is, at the same conditions, larger than at 6.7-GHz. The linear polarization angles of group D show a 90° difference w.r.t those of the nearby 1.6-GHz OH masers. This might be due either to a 90°-flip phenomenon or to the Faraday rotation if the masers are deeply located in a strong ionized gas. In the case of OH masers, most of them are likely to be Zeeman σ-components, therefore the magnetic field is perpendicular to the linear polarization vectors. Considering the large errors of θ_{M48}, the orientation of the magnetic fields of group B and E are consistent with those derived from the nearby 1.6-GHz OH masers (Hutawarakorn & Cohen 2003). In particular, the linear polarization vector of M43, which shows the highest linear polarization fraction, is perfectly aligned with the feature 2 of the 1665-MHz OH maser (Hutawarakorn & Cohen 2003). Unless the Faraday rotation is 180°, the consistence of the magnetic field orientation indicates that the Faraday rotation at OH maser frequency is low.

The role of the magnetic field

The importance of the magnetic field in the region can be estimated by evaluating the ratio between thermal and magnetic energies (β). If $\beta < 1$ the magnetic field dominates the energies in the high-density protostellar environment. The β factor is given by

$$\beta = 2 \left(\frac{m_{\mathrm{a}}}{m_{\mathrm{s}}} \right)^2 , \tag{6.6}$$

where m_{a} is the Alfvénic Mach number and m_{s} is the sonic Mach number, which in formula are

$$m_{\mathrm{a}} = \frac{\sigma_{\mathrm{turb}}\ \sqrt{3}}{V_{\mathrm{A}}}, \qquad \text{and} \qquad m_{\mathrm{s}} = \frac{\sigma_{\mathrm{turb}}\ \sqrt{3}}{c_{\mathrm{s}}}. \tag{6.7}$$

Here V_{A} is the Alfvén velocity and c_{s} is the sound velocity, and σ_{turb}, the turbulence velocity, can be estimated using $\sigma_{\mathrm{turb}} = \Delta V_{\mathrm{turb}}/\sqrt{8\ \ln 2}$. By considering a mass $\mu_{\mathrm{H_2}} = 3.8 \times 10^{-24}$ g and the relation between the velocity and the temperature of a gas we can write V_{A} and c_{s} in terms of $|B|$, $n_{\mathrm{H_2}}$, and the kinetic temperature of the gas T_{k}

$$\frac{V_{\mathrm{A}}}{[\mathrm{km\ s^{-1}}]} = 1542 \left(\frac{|B|}{[\mathrm{mG}]} \right) \left(\frac{n_{\mathrm{H_2}}}{[\mathrm{cm^{-3}}]} \right)^{-\frac{1}{2}}, \tag{6.8}$$

$$\frac{c_{\rm s}}{[\rm km\ s^{-1}]} = 0.0603\ \left(\frac{T_{\rm k}}{[\rm K]}\right)^{-\frac{1}{2}}. \tag{6.9}$$

So we get

$$\beta = 3.058 \cdot 10^{-9}\ \left(\frac{|B|}{[\rm mG]}\right)^{-2}\ \left(\frac{n_{\rm H_2}}{[\rm cm^{-3}]}\right)\ \left(\frac{T_{\rm k}}{[\rm K]}\right), \tag{6.10}$$

that, considering

$$\Delta V_{\rm Z} = \alpha_{\rm Z} \cdot B_{||}, \tag{6.11}$$

and $|B| = |B_{||}|/cos\ \langle\theta\rangle$, can thus be written as

$$\beta = 3.058 \cdot 10^{-9}\ \alpha_Z^2\ cos\ \langle\theta\rangle\ \left(\frac{|\Delta V_{\rm Z}|}{[\rm ms^{-1}]}\right)^{-2}\ \left(\frac{n_{\rm H_2}}{[\rm cm^{-3}]}\right)\ \left(\frac{T_{\rm k}}{[\rm K]}\right). \tag{6.12}$$

By assuming $n_{\rm H_2} = 10^9$ cm^{-3}, $T \sim 200$ K, which are the typical values in the CH_3OH masing region, the weighted values for the unsaturated masers of the θ angle $\langle\theta\rangle$ =78°, and Zeeman-splittings $|\Delta V_{\rm Z}| = 2.7$ m s^{-1}, we obtain

$$\beta = 17.4 \cdot \alpha_Z^2. \tag{6.13}$$

Although the value of α_Z is still uncertain, we can expect that this must be neither larger than the old value ($\alpha_Z = 0.049$ km s^{-1} G^{-1}, Vlemmings 2008) nor smaller than the new value ($\alpha_Z = 0.005$ km s^{-1} G^{-1}, Vlemmings et al. 2011). Therefore, it is reasonable that β is between $4 \cdot 10^{-4}$ and $4 \cdot 10^{-2}$. Consequently the magnetic field is dynamically important in this massive star-forming region.

6.4.4 Structure of NGC7538-IRS1

Recently, large scale elliptical configurations have been detected in a significant CH_3OH masers around high-mass protostars. These masers are thought to trace molecular rings (e.g., Bartkiewicz et al. 2009). However, most of these rings do not show signs of rotation, but rather the radial motions dominate indicating that the masers are instead tracing infalling gas in the interface between the torus and the flow, e.g. Cepheus A HW2 (Chapter 4). In this light it is legitimate to reconsider whether the masers in NGC7538-IRS1 could trace similar gas.

In this source we have observed velocity gradients in three CH_3OH masers; i.e., M26, M33 and M40. Whereas the velocity gradient of M26 has already been observed by other authors (e.g., Minier et al. 1998; Pestalozzi et al. 2004), those of masers M33 and M40 have not been reported so far (Fig. 6.5). All the velocity gradients of M26, M33, and M40 are equal to 0.02 km s^{-1} AU^{-1}.

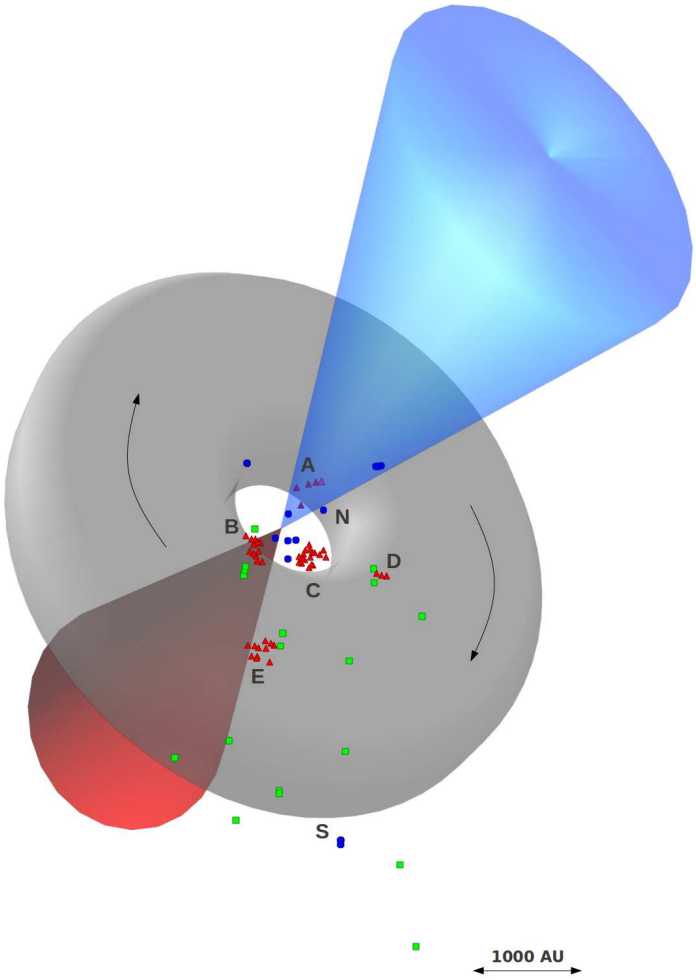

Figure 6.8: The 3-dimensional sketch of the massive star-forming region NGC7538-IRS1 as described in Sect. 6.4.4. The two cones are the red- and blue-shifted part of the large-scale molecular bipolar outflow (Kameya et al. 1989), the donut is the torus suggested by Klaassen et al. (2009) perpendicular to the outflow and with i=32° (De Buizer & Minier 2005), the triangles, the circles, and the boxes are the CH_3OH, H_2O masers (present Ph.D. work), and the OH masers (Hutawarakorn & Cohen 2003), respectively. The outflow and the torus are transparent to allow the reader to see behind them.

Considering the orientation of the linear distribution of the maser spots of M26, M33, and M40 we find that all of them seem to point towards a common center. This suggests that M26, M33, and M40 are likely tracing a gas with a radial motion, probably consistent with the interface of the torus and infalling gas. Consequently the maser spots of M26 are likely not tracing a Keplerian-disc

as proposed by Pestalozzi et al. (2004). The CH_3OH masers of groups A, B, C, and D show a cone-shape distribution that opens to the North-West. This seems to indicate that we are looking at a regular structure, for instance the inner part of a torus. Klaassen et al. (2009) detected an almost face-on 5300 AU-torus perpendicular to the outflow with a clockwise rotation motion. If this torus is on the same plane of the disc supposed by De Buizer & Minier (2005), then its inclination angle must be i=32°. By keeping in mind these new results we can suppose that the CH_3OH masers of groups A, B, and C are tracing the surface of the inner torus, possibly where the infall reaches the rotating structure. The masers of group D and E trace the gas sligthly further out on the torus. In particular group A is located to the opposite side of the torus w.r.t. the other three maser groups. In Fig. 6.8 a 3-dimensional sketch of the region as described above is shown. The outflow sketched here is a simplified representation of the chaotic and complex multi-outflows structure observed towards NGC7538 and in particular around IRS-1 (e.g., Qiu et al. 2011; Klaassen et al. 2011).

In this scenario the H_2O masers of group N are located parallel to the edges of the outflow, which show a blue-shifted part northwestern and a red-shifted part southeastern (e.g., Kameya et al. 1989; Hutawarakorn & Cohen 2003). In this case the H_2O masers can be pumped by a shock due to the interaction of the outflow with the infalling gas. The most southern H_2O masers, W06 and W07, might be associated either with the red-shifted part of the outflow or most likely with another source, as also suggested by the different orientation of the magnetic field in that region. Moreover, the OH masers located southward (Hutawarakorn & Cohen 2003) might be pumped by the red-shifted part of the high-velocity outflow and those located westward by the blue-shifted part.

This scenario is further supported by the similarity between the torus and outflow velocities and that of the three maser species. In Fig. 6.9 we plot the CH_3OH maser velocities as a function of the position angle (PA) along the torus. To determine the PA of each CH_3OH maser we consider that every maser lies on an own circle that has the same orientation and inclination angle of the torus with the centre located at the origin of the sketched outflow in Fig 6.8. Moreover in Fig. 6.9 we plot an empirical function (solid line) based on the orientation and the velocity field of the torus observed by Klaassen et al. (2009), i.e. the PA and velocity of all the points of a circle that has the same size, orientation, and inclination of the torus. The maser velocities perfectly match the non-Keplerian velocity profile of the torus that is rotating clockwise (Klaassen et al. 2009). This indicates that the CH_3OH masers are related to the torus structure. Groups A and E appear to be systematically blue- and red-shifted w.r.t the torus velocities respectively, supporting the

suggestion of infall motion (of order 1 km s^{-1}) along the line-of-sight.

The velocities of the blue- and red-shifted part of the outflow are $V_{\rm outf}^{\rm blue} = -76$ km s^{-1} and

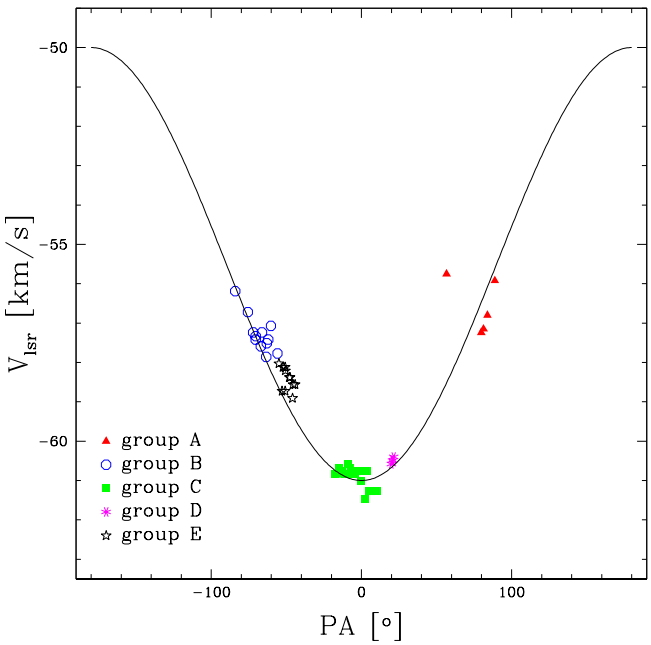

Figure 6.9: The measured velocities of the CH_3OH masers as a function of the position angle (PA) along the torus. The solid line shows the velocities of the torus reported by Klaassen et al. (2009) as function of their PA along the torus determined as described in Sect. 6.4.4.

$V_{\rm outf}^{\rm red} = -37$ km s^{-1} (Kameya et al. 1989). The mean velocities of the H_2O masers of group N and S are $V_{\rm H_2O}^{\rm N} = -59.4$ km s^{-1}, excluding the masers W16 and W17, and $V_{\rm H_2O}^{\rm S} = -68.7$ km s^{-1}. While $V_{\rm H_2O}^{\rm S}$ again suggests that these masers might be associated with another source, the difference between $V_{\rm H_2O}^{\rm N}$ and $V_{\rm outf}^{\rm blue}$ indicates that the H_2O masers are tracing the gas surrounding and being entrained by the outflow. The 1.6 and 1.7-GHz OH masers show a velocity ranges -61 km s^{-1}$< V_{\rm OH} < -51$ km s^{-1} in good agreement with $V_{\rm torus}$ and $V_{\rm lsr}^{\rm CH_3OH}$ that might indicate an association with the torus rather than with the CO-outflows. The presence of OH and CH_3OH masers in the same environments, also suggested by the linear polarization vectors of the two maser species (see Sect. 6.4.3), is in contrast with the excitation model of Cragg et al. (2002) that predicts the inhibition of the 6.7-GHz CH_3OH masers when 1.6-GHz OH masers arise.

The orientation of the magnetic field derived by the linear polarized emission of the CH_3OH

masers at high angular resolution matches the scenario we presented above. Most likely the magnetic field is perpendicular to the linear polarization vectors for most of the CH_3OH masers but for group E the magnetic field is instead parallel to the linear polarization vectors (see Sect. 6.4.3). This is also suggested by considering the linear polarization vectors of the OH masers (see Sect. 6.4.3). In this case the magnetic field is situated on the two surfaces of the torus, with a counterclockwise direction on the top surface. This interpretation is consistent with the signs of the magnetic field strengths determined from the Zeeman-splitting measurements of the CH_3OH masers and OH masers, which show negative strength ($B = -2.0$ mG, Hutawarakorn & Cohen 2003) towards the region where groups B and E arise and positive towards groups A and D.

Even if the CH_3OH masers are not tracing the Keplerian-disc reported by Pestalozzi et al. (2004), the presence of a smaller disc is not ruled out. In the scenario proposed here, it would be located within the torus. So we argue that a possible answer to the question about the morphology of NGC7538-IR 1 is that the CH_3OH masers are tracing a gas close to the torus that is falling towards the connection region between the torus and the disc as was observed in other protostars (e.g., Chapter 4).

The new scenario described in this chapter is determined by considering the entire CH_3OH maser region and not just the masers of group A. Consequently, this scenario is different both from "Scenario A" and from "Scenario B" suggested by Kraus et al. (2006), who considered the results obtained by De Buizer & Minier (2005) and by Pestalozzi et al. (2004) for the CH_3OH masers of group A, respectively. In "Scenario A" the CH_3OH masers of group A might resemble either clumps in the cavity of the outflow or recent ejecta from the outflow, while in "Scenario B" group A trace a disc and they proposed a jet precession model to explain the asymmetry of the NIR emission. However, in our scenario the asymmetry of the NIR emission might reflect the innermost walls of an outflow cavity as explained in "Scenario A" but with the CH_3OH masers that are tracing an infalling gas rather than the outflow cavity or a recent ejecta from the outflow.

Two questions remain: what is the radio continuum emission shown in Fig. 6.1? How can this scenario be consistent with the changing of the position angle of the outflows reported in Campbell (1984)? De Buizer & Minier (2005) argued that the radio continuum emission is consistent with radio emission arising from a photoevaporated disc wind and Kameya et al. (1989) suggested that the rotation of the outflows comes from a disc precession.

6.5 Conclusions

The massive star-forming region NGC7538-IRS 1 has been observed at 22-GHz in full polarization spectral mode with the VLBA and at 6.7-GHz with the EVN and MERLIN to detect linear and circular polarization emission from H_2O and CH_3OH masers, respectively. We detected 17 H_2O masers and 49 CH_3OH masers at high angular resolution. We have measured Zeeman-splitting for three CH_3OH masers ranging from -2.7 m s^{-1} to $+2.7$ m s^{-1}. No significant magnetic field strength has been measured from the H_2O masers. Furthermore, we have also shown that the masers of NGC7538 are all consistent with a torus-outflow scenario. Here the CH_3OH masers are tracing the interface between the infall and the large-scale torus, and the H_2O masers are related to the blue-shifted part of the outflow. The H_2O masers of the southern group are thought to be associated with another source. The magnetic field is situated on the two surfaces of the torus with a counterclockwise direction on the top surface.

Chapter 7

First EVN Sample

The first EVN sample consists of 4 massive star-forming complexes: W51, W48, IRAS 18556+0138, and W3(OH). These contain well-studied H II regions from some of which molecular bipolar outflows were detected (W51–e2, G35.20-0.74N). Several maser species, and specifically strong 6.7-GHz CH_3OH masers, have been detected towards these complexes. The polarization observations at milliarcsecond resolution of the CH_3OH masers at 6.7-GHz can give us fundamental information on the role of the magnetic field in driving outflows and in accreting matter via disc/torus structures onto the massive protostars. The European VLBI Network was used to measure the linear polarization and the Zeeman-splitting of the 6.7-GHz CH_3OH masers in the sample. We detected a total of 154 CH_3OH masers, one third towards W3(OH), and fractional linear polarization (1.2–11.5%) was detected towards 55 CH_3OH masers. The linear polarization vectors are well-ordered in all the massive star-forming regions. We were able to measure significant Zeeman-splitting in 3 massive star-forming regions (W51, W48, and W3(OH)) revealing a range $-3.5\ m\,s^{-1} < \Delta V_z < 3.8\ m\,s^{-1}$ with the smallest $|\Delta V_z| = 0.4\ m\,s^{-1}$. In some cases, we were able to compare our magnetic field results with those obtained at different frequencies (e.g., W51–e2).

7.1 The sample

We selected a sample of 4 massive star-forming regions among the northern hemisphere sources observed with the Effelsberg 100-m telescope where 6.7-GHz CH_3OH maser Zeeman-splitting was measured (Vlemmings 2008). A brief description of each source of the EVN sample is provided below.

7.1.1 W51

W51 complex is one of the most luminous star-forming regions in the first quadrant of the Galactic plane. The high luminosity comes from a large number of O-type stars that are within the molecular cloud (Bieging 1975; Carpenter & Sanders 1998). Kundu & Velusamy (1067) found that W51 is divided in four different regions: W51A, W51B, W51C, and W51D. Whereas W51C shows a non-thermal continuum spectrum indicating a supernova remnant (Subrahmanyan & Goss 1995; Koo & Moon 1997), W51A and W51B do show thermal spectra indicating compact H II regions (e.g., Mufson & Liszt 1979). These regions are composed of several sub-regions, for instance W51A consists of G49.4-0.3 and G49.5-0.4 (e.g., Mufson & Liszt 1979; Kang et al. 2010). Moreover, G49.5-0.4 comprises the sources W51-Main/South (it contains the UCH II regions W51–e1 and W51–e2; e.g., Ho et al. 1983; Gaume et al. 1993), W51–IRS1, and W51–IRS2 (it contains W51–d2; e.g., Ho et al. 1983; Lacy et al. 2007). W51–e1/e2 and W51–IRS2 are the two sources towards which we carried on polarization observations with the EVN and a more detailed description of these can be read below.

W51–e1/e2

W51–e1 and W51–e2 ($V_{\rm lsr}$ = 59 km s^{-1}) are the brightest molecular cores located at a distance of $5.41^{+0.31}_{-0.28}$ kpc (Sato et al. 2010) in the eastern edge of W51. Their masses are ∼150 $M_\odot$ and ∼110 $M_\odot$, respectively, which were derived from NH_3 observations (Zhang & Ho 1997). Observations of molecular lines showed evidence for infalling, or accreting, gas with a possible rotation around W51-e2 (e.g., Zhang & Ho 1997; Zhang et al. 1998; Sollins et al. 2004; Keto & Klaassen 2008). Keto & Klaassen (2008) suggested a possible bipolar outflow along the northwest and southeast direction from W51-e2 (PA≈ 150°), which appears to be along the rotation axis of the ionized disc. Evidences for infalling gas were also found around W51-e1 (Ho & Young 1996), which also contains two more UCH II regions (e3 and e4; Gaume et al. 1993) and a possible dust source (e8; Zhang & Ho 1997).

There is a maser concentration towards W51–e1/e2 known as W51 Main, where OH, H_2O, and 6.7-GHz CH_3OH masers were detected (Genzel et al. 1981; Benson et al. 1984; Argon et al. 2000; Phillips & van Langevelde 2005). Proper motions observations of H_2O masers revealed random motions that could indicate the presence of multiple outflows (Imai et al. 2002). OH maser polarization observations reveal a total of 46 Zeeman pairs with a predominantly positive magnetic field direction that reverses in the northern part of W51–e1 (Fish & Reid 2006). W51–e2 has two

Zeeman pairs implying a magnetic field strength of about −20 mG (Argon et al. 2002), with the rest of the OH masers indicating $B \sim 5$ mG. Vlemmings (2008) measured a Zeeman-splitting of the 6.7-GHz CH_3OH maser $\Delta V_Z = 0.72 \pm 0.04\ \mathrm{m\,s^{-1}}$. A large scale magnetic field, with an orientation varying smoothly from 23° (W51–e1) to 15° (W51–e2) was measured using the BIMA array (Lai et al. 2001). SMA observations revealed that the inferred $B_\perp$ morphology is hourglass-like near the collapsing core of W51–e2, with its pinched direction parallel to the direction of the ionized accretion, showing that the magnetic field plays a similar role as in low-mass star formation (Tang et al. 2009a).

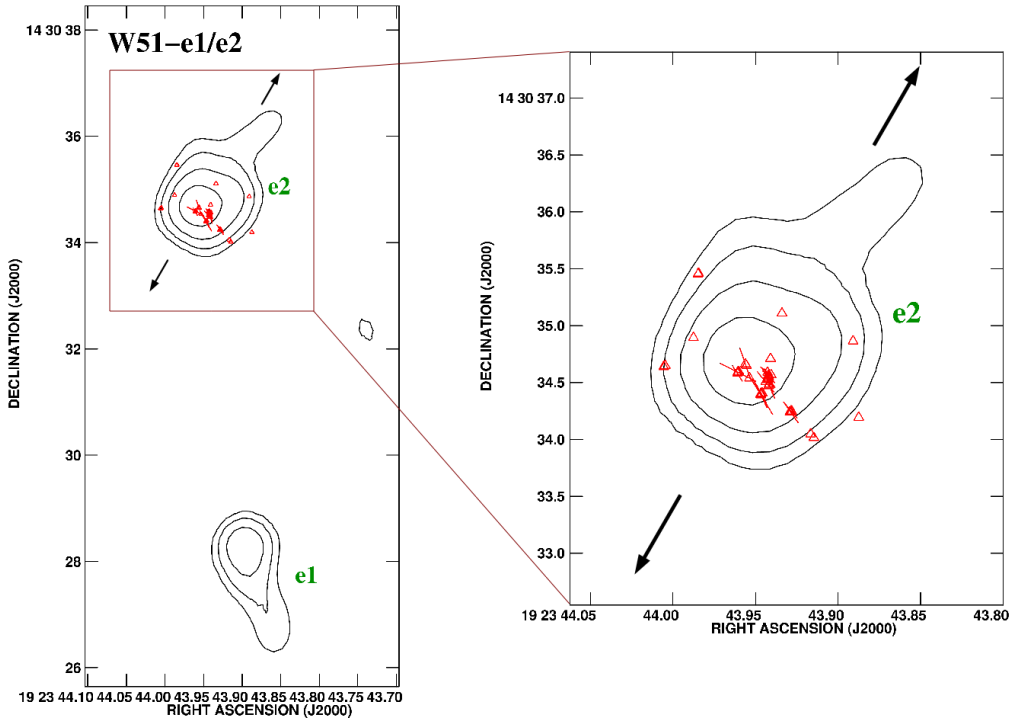

Figure 7.1: Positions of CH_3OH maser features (red triangles) superimposed on the 870 μm continuum contour map of W51–e1/e2 observed with the SMA in 2008 (Tang et al. 2009a). Contours are 2, 4, 8, 16 × 0.15 Jy beam^{-1}. The linear polarization vectors of CH_3OH maser features are also shown (100 mas correspond to a linear polarization fraction of 1%). The two arrows indicate the direction of the bipolar outflow (PA∼150°; Keto & Klaassen 2008).

W51–IRS2

W51–IRS2 is the most luminous massive star-forming region in the Milky Way (Erickson & Tokunaga 1980) and it is located at a distance of $5.1^{+2.9}_{-1.4}$ kpc (Xu et al. 2009a). The region around W51–IRS2 contains several O-type zero-aged main-sequence stars (ZAMS) with excess emission at the infrared and (sub)millimetre wavelengths (e.g., Barbosa et al. 2008). In addition the region hosts a young O5-type protostar (Zapata et al. 2008) and an UCH II region called W51–d2 (e.g., Gaume et al. 1993). The former contains an H_2O maser complex called W51–North whose proper motion observations revealed a compact ($\sim 1'' - 2''$) NW-SE outflow emanating from the protostar (Eisner et al. 2002; Imai et al. 2002). Eisner et al. (2002) proposed that the SiO masers detected in W51–North and close to the protostar trace the limbs of an accelerating bipolar outflow with $PA \sim 105°$, which is consistent with the angle of the outflow traced by H_2O masers. Moreover, a Keplerian molecular disc around the O5-type protostar has recently been observed

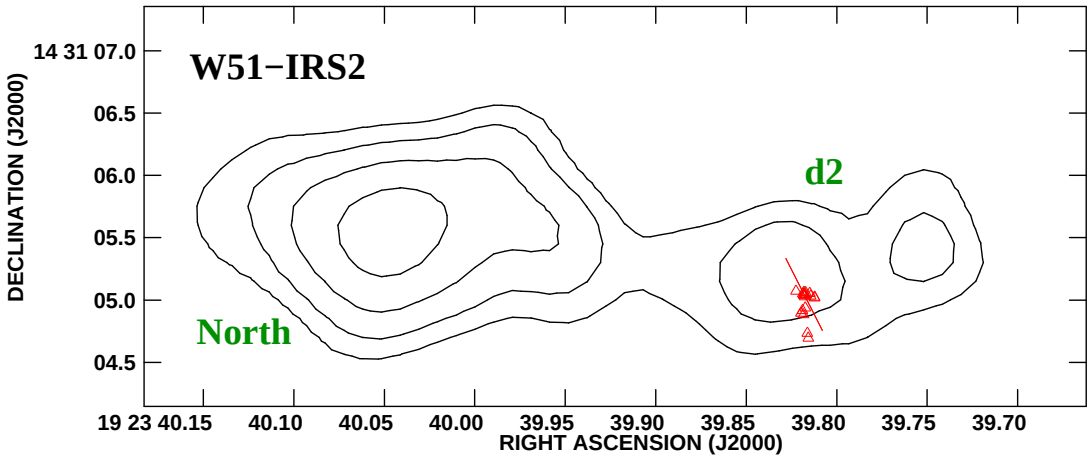

Figure 7.2: Positions of CH_3OH maser features (red triangles) superimposed on the 870 μm continuum contour map of W51–IRS2 observed with the SMA in 2008 (Tang et al. private communication). Contours are 2, 4, 8, 16 × 0.15 Jy beam^{-1}. The linear polarization vectors of CH_3OH maser features are also shown (500 mas correspond to a linear polarization fraction of 1%).

by Zapata et al. (2010), who also suggested that the accreting fresh gas to the protostar possibly quenches the formation of an HCH II region. Also OH masers and possibly 23.1-GHz and 44.1-GHz CH_3OH masers are associated to W51–North (Gaume & Mutel 1987; Cho et al. 2011). W51–d2 is located western w.r.t. W51–North at a distance of about 17000 AU. The source is associated with NH_3 and CH_3OH masers (Gaume et al. 1993; Minier et al. 2001; Phillips & van Langevelde 2005)

as well as H_2O masers (Eisner et al. 2002). The UCH II region has a spectral index 2.1, a physical size < 300 AU and its emission measure infers a central star of spectral type of B0.5 (Phillips & van Langevelde 2005).

7.1.2 W48

W48 complex is located in the Carina-Sagittarius spiral arm at a distance of $3.27^{+0.56}_{-0.42}$ kpc (Zhang et al. 2009). MacLeod et al. (1977) showed that W48 consists of three H II regions: G35.2–1.8, G35.1–1.5, and G35.4–1.8. Onello et al. (1994) renamed them as W48A, W48E, and W48D, respectively, and observed two more H II regions, W48B and W48C, with the VLA. W48A hosts a cometary UCH II region called G35.2–1.74 ($\alpha_{2000} = 19^{\rm h}01^{\rm m}46^{\rm s}.4$ and $\delta_{2000} = +01°13'23''.9$; Wood & Churchwell 1989; Roshi et al. 2005) that is believed to be a site of massive star formation, and two infrared sources IRS 1 and IRS 2 (Zeilik & Lada 1978).

CH_3OH masers are associated with G35.2–1.74, even if their absolute position, $\alpha_{2000} = 19^{\rm h}01^{\rm m}45^{\rm s}.5$ and $\delta_{2000} = +01°13'28''$, is not known within an accuracy better than few arcsec (Caswell et al. 1995; Minier et al. 2000). The CH_3OH maser region shows a ring-like structure of $\sim 200 \times 400$ mas along a direction North-South, the features at lower velocity are located southern and those at higher velocity northern (Minier et al. 2000; Sugiyama et al. 2008a). H_2O masers were first detected at $\sim 6'$ northern by Turner & Rubin (1971), while Hofner & Churchwell (1996) detected H_2O masers closer to the UCH II region at distances $> 10''$, where OH masers were also detected (Forster & Caswell 1989). Six mid-infrared sources were detected in this area (MIR 1-6, Persi et al. 1997), four of which were encompassed in De Buizer et al. (2005) observations. The source MIR 3 corresponds to G35.2–1.74 and it is quite predominant in the mid-infrared images of De Buizer et al. (2005). MIR 1 coincides with the OH and H_2O masers site (Fig. 7.3). De Buizer et al. (2005) argued that the OH and H_2O masers are tracing an outflow from MIR 1 in the North-East lobe, and the near-infrared emission is reflected light coming from the inner wall of the cavity produced by the South-West outflow lobe. Unfortunately, high resolution CO-maps are not available and consequently this is only a speculative scenario.

Vlemmings (2008) measured a Zeeman-splitting of the CH_3OH masers of 0.32 ± 0.02 m s^{-1}. Roshi et al. (2005) determined the magnetic field at the periphery of the UCH II region from carbon recombination line observations and they found $B = 2.9$ mG. Submillimeter polarimetry observations with Submillimetre Common User Bolometer Array (SCUBA) revealed two cores, the main and bright core in the East, W48main, and the small core in the West, W48W (Curran

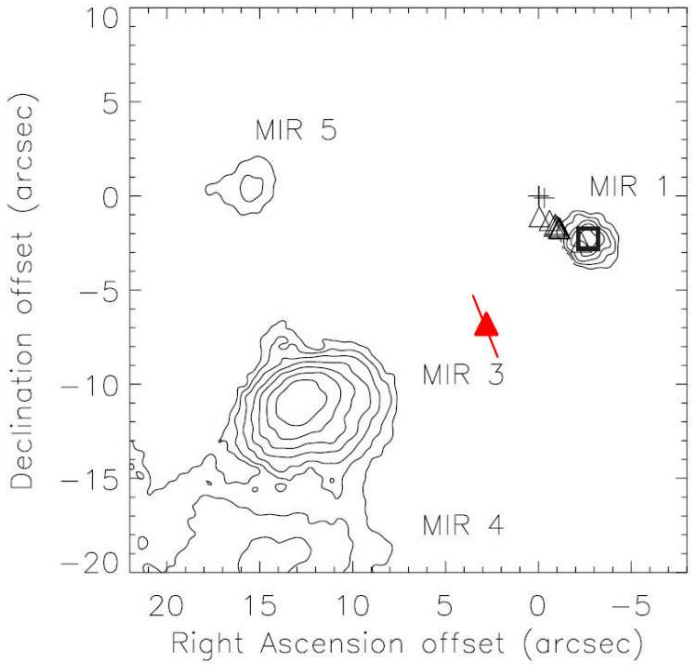

Figure 7.3: Position of CH_3OH masers region (red filled triangles) superimposed on the 11.7 μm continuum contour map of W48 (G35.20-1.74) observed with the Jet Propulsion Laboratory mid-infrared camera MIRLIN in 2002 and reported in De Buizer et al. (2005). Crosses represent the H_2O maser positions and the black open triangles represent the OH positions from Forster & Caswell (1989); the square represents the location of near-infrared source from Testi et al. (1994). The origin is $\alpha_{2000} = 19^{\rm h}01^{\rm m}45^{\rm s}.68$ and $\delta_{2000} = +01^\circ13'28''.0$. Mid-infrared source names are from Persi et al. (1997). The weighted linear polarization vector of CH_3OH maser features detected by us is also shown.

et al. 2004). The two cores appear to be connected by a ridge of dust and gas. The degree of polarization is lower (0.5%) towards the intensity peak of W48main, which is close to G35.2–1.74, and is higher towards the edges. Moreover, the magnetic field orientation is complicated and near the CH_3OH maser region, towards the centre of W48main, the magnetic field has a NW-SE orientation. Whereas, in W48W the magnetic field has an ordered orientation North-South. This changing in the orientation has been explained by twisting of the magnetic field towards the centre of W48main (Curran et al. 2004). Their estimation of the ratio $\lambda = (M/\Phi)_{\rm crit}/(M/\Phi)_{\rm crit}$ (Eq. 1.1) suggests that W48 is close to be critical.

7.1.3 IRAS 18556+0138

IRAS 18556+0138 is at a distance of $2.19^{+0.24}_{-0.20}$ kpc (Zhang et al. 2009) and has a systemic velocity $V_{\rm sys} \sim 34$ km s^{-1} (Matthews et al. 1984). This IRAS source is associated with the massive star-forming region G35.2–0.74N that contains an embedded B0.5 star with a luminosity of $\sim 10^4$ L$_\odot$ and a stellar mass of ~ 15 M$_\odot$ (Dent et al. 1985; Gibb et al. 2003). A collimated CO–molecular bipolar outflow (PA= 58°, Gibb et al. 2003) was detected from G35.2–0.74N (e.g., Little et al. 1983; Matthews et al. 1984; Dent et al. 1985). The outflow has a size of about 2 pc and its blue- (25.3 km s^{-1} $< V^{\rm blue}_{\rm outf-IRAS} < 30.3$ km s^{-1}) and red-shifted (37.8 km s^{-1} $< V^{\rm red}_{\rm outf-IRAS} < 43.8$ km s^{-1}) parts are oriented southwestern and northeastern (López–Sepulcre et al. 2009), respectively. Also a radio/infrared jet was detected at the same position of the bipolar outflow but with different position angle (PA$\sim$ 0°; Heaton & Little 1988; Fuller et al. 2001; De Buizer 2006) suggesting that the outflow is driven by the precessing jet (Heaton & Little 1988; Martí et al. 1993). However,

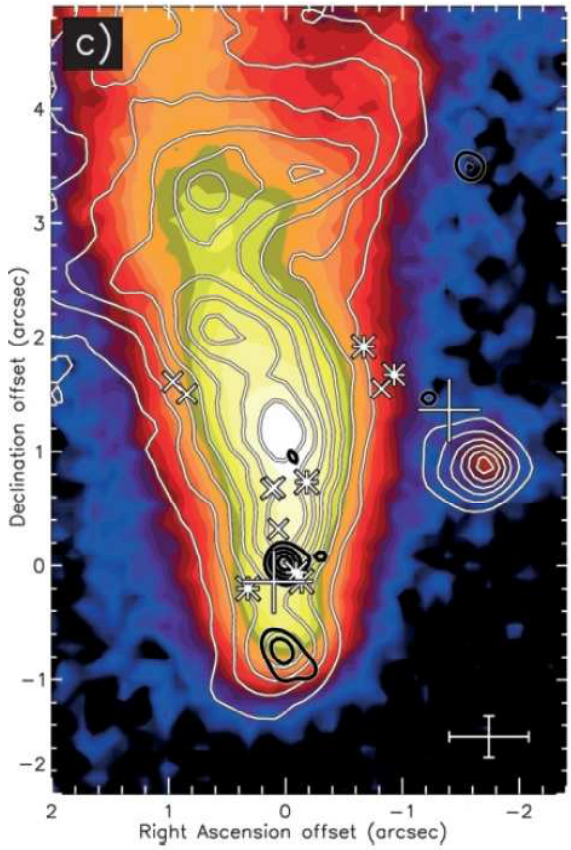

Figure 7.4: Image C of Fig. 2 of De Buizer (2006). The G35.20–0.74N (IRAS 18556+0138) jet at 11.7 μm in false color. The L' contours in white and the high-resolution radio continuum contours in black. The OH masers of Hutawarakorn & Cohen (1999) are shown as asterisks, H_2O masers of Forster & Caswell (1989) as crosses, and CH_3OH maser clusters as large plus signs. The bars at the lower right show the $\pm1\sigma$ relative astrometric uncertainty between the radio continuum and the NIR. The origin is the location of the radio continuum source G35.20–0.74, $\alpha_{2000} = 18^{\rm h}58^{\rm m}13^{\rm s}.033$ and $\delta_{2000} = +01°40'36''.14$.

Gibb et al. (2003) argued that the region contains four outflows and that the precession of the jet is unnecessary because the jet could be associated with another outflow. In addition a flattened structure rotating perpendicularly (PA= 148°) to the outflow axis was also observed using NH_3 and $C^{18}O$(2-1) emissions (Little et al. 1985; López–Sepulcre et al. 2009). López–Sepulcre et al. (2009) measured a velocity range of the rotating structure between 33.45 $\mathrm{km\,s^{-1}}$ (NW) and 34.75 $\mathrm{km\,s^{-1}}$ (SE), and a SE-NW size of $\sim 30''$, which at 2.19 kpc correspond to about 66000 AU (~ 0.3 pc).

As for most high-mass star-forming regions, G35.2–0.74N contains H_2O, OH, and CH_3OH masers (e.g., Forster & Caswell 1989; Hutawarakorn & Cohen 1999; Caswell et al. 1995). Hutawarakorn & Cohen (1999) suggested that the OH masers trace the inner edge of a possible molecular disc, which has a radius of 2800 AU and an inclination similar to the large rotating structure, while the H_2O masers seem to be aligned with the outflows (Forster & Caswell 1989). On the contrary De Buizer (2006) argued that the H_2O and OH masers are detected with a northern V-shape distribution with its apex close to the source G35.2–0.74N indicating that the masers are tracing the outflow cavity walls. For the first time Sugiyama et al. (2008a) made VLBI observations of the CH_3OH masers with the JVN. They detected two clusters, one located near G35.2–0.74N and the other northwestern at a distance of about 5000 AU. The two clusters seem to be at the ends of a linear structure with PA$\sim 140°$, which is close to the inclination of the large rotating structure. Xu et al. (2009b) reported an absolute position of the brightest CH_3OH maser $\alpha_{2000} = 18^{\mathrm{h}}58^{\mathrm{m}}13^{\mathrm{s}}.053$ and $\delta_{2000} = +01°40'35''.68$.

Hutawarakorn & Cohen (1999) measured magnetic field strengths between –2.5 mG, at North of G35.2–0.74N, and +5.2 mG, at South by studying the Zeeman-splitting of the OH masers. They also found an orientation of the magnetic field parallel to the outflow, even if Faraday rotation could play an important role. Using Effelsberg observations Vlemmings (2008) measured a Zeeman-splitting of the CH_3OH maser emission $\Delta V_{\mathrm{Z}} = 0.81 \pm 0.04$ $\mathrm{m\,s^{-1}}$.

7.1.4 W3(OH)

W3(OH) is the most studied UCH II region in our Galaxy. It is located in the Perseus spiral arm at a distance of 1.95±0.04 kpc (Xu et al. 2006). Infrared and radio continuum observations indicated that the central ionizing star is a O7 star with a mass of about 30 $M_\odot$ (Scott 1981; Campbell et al. 1989). An enigmatic source, named Turner–Welch object (TW; Turner & Welch 1984) is situated at $\sim 6''$ east of W3(OH) at a distance of 2.04±0.07 kpc (Hachisuka et al. 2006).

W3(OH) is the site of several CH_3OH and OH maser spots (e.g., Harvey–Smith & Cohen 2006; Fish & Sjouwerman 2007; Moscadelli et al. 2010), while H_2O masers have only been found towards the TW source (Reid et al. 1995).

Moscadelli et al. (1999, 2010) derived accurate proper motion of the 12-GHz CH_3OH masers

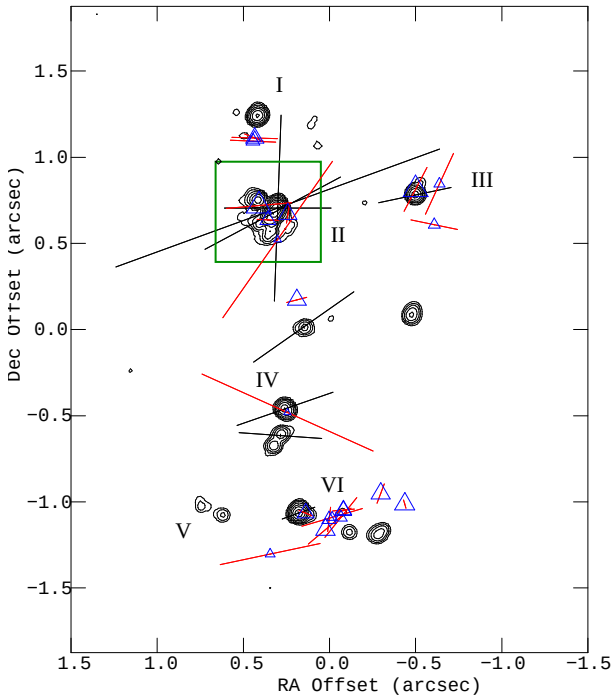

Figure 7.5: Modified version of Fig. 2 of Vlemmings et al. (2006b). The 6.7-GHz CH_3OH masers of W3(OH) (contours) including the polarization vectors (black) scaled linearly according the fractional linear polarization. The positions in the map are indicated with respect to $\alpha_{2000} = 02^{\rm h}27^{\rm m}03^{\rm s}.7743$ and $\delta_{2000} = +61°52'24''.549$. The linear structure correspond to group II. The blue triangles denote the main line OH masers from Wright et al. (2004) for which polarized intensity was detected and the red vectors are their linearly scaled polarization vectors. The main line OH maser polarization vectors lengths are scaled down by a factor of 5 with respect to the lengths of the CH_3OH maser polarization vectors.

of which the most intense concentrate in a small area towards the North (called the *northern clump*) of the UCH II region. A second clump is located southern, and between the two clumps an isolated single spot maser has been found. This North-South filamentary structure of 12-GHz CH_3OH masers is also shown by the 6.7-GHz CH_3OH and the OH masers (Harvey–Smith & Cohen 2006). The brightest 12-GHz CH_3OH masers of the northern clump are distributed along an axis at PA= 141° and show a regular trend of radial velocities with position, suggesting that they could trace a self-gravitating, low-mass ($M \approx 1.5$ $M_\odot$) circumstellar disk ($R \approx 270$ AU) in the phase of being photo-evaporated by the strong UV-radiation field escaping from the W3(OH) UCH II region (Moscadelli et al. 2010). 6.7-GHz CH_3OH masers were detected for the first time at high angular resolution by Menten et al. (1992) and they coincide with the masers at 12-GHz (Moscadelli et al. 1999). In particular some 6.7-GHz CH_3OH masers trace a similar linear structure as shown by the 12-GHz CH_3OH masers (PA= 130°; Harvey–Smith & Cohen 2006). Also part of the OH

masers detected towards the northern clump show a similar linear distribution (PA$\approx 130°-140°$) but with a more scattered pattern of velocities (Moscadelli et al. 2010). A comparison of the overall distribution of positions and velocities of the three maser emissions in the northern clump reveals that the two maser species complement each other, emerging from nearby but distinct cloudlets of masing gas (Harvey–Smith & Cohen 2006; Moscadelli et al. 2010).

Polarization observations of the CH_3OH masers with MERLIN showed that the magnetic field is parallel to the extended filament but with a complex structure in the dominating northern clump (Vlemmings et al. 2006b; Fig. 7.5). Wright et al. (2004) detected linear polarization from the 1.6-GHz OH maser emission (Fig. 7.5), showing a wider spread maser polarization angles, with the median polarization angle $\langle\chi^{\rm OH}_{\rm med}\rangle = 104 \pm 27°$, that has been attributed to Faraday rotation along the maser path. A Zeeman-splitting of the 6.7-GHz CH_3OH masers $\Delta V_{\rm Z} = 0.141 \pm 0.003\,{\rm m\,s^{-1}}$ was measured by Vlemmings (2008). EVN observations are uniquely suited to resolve the compact region (II) and determine the polarization structure of a probable disc suggested by the linear distribution of the CH_3OH and OH masers.

7.2 Observations and data reduction

The sample was observed at 6.7-GHz in full polarization spectral mode with nine of the EVN[1] antennas (Jodrell2, Cambridge, Effelsberg, Onsala, Medicina, Torun, Noto, Westerbork, and the new joint antenna Yebes-40 m), for a total observation time of 20 h, on November 2 (W48, IRAS 18556+0138, and W3(OH)) and 3 (W51), 2009 (program code ES063A and ES063B). The bandwidth was 2 MHz, providing a velocity range of $\sim$ 100 ${\rm km\,s^{-1}}$. The data were correlated using 1024 channels in order to generate all 4 polarization combinations (RR, LL, RL, LR) with a spectral resolution of 1.9 kHz ($\sim$0.1 ${\rm km\,s^{-1}}$). In order to detected CH_3OH maser towards both W51–e1/e2 and W51–IRS2 the data of W51 were correlated twice with two different correlator positions. The correlator position of W51–e1/e2 was the pointing position of the observations.

The data were edited and calibrated using AIPS by following the data reduction procedures described in Sect. 3.2.1. The bandpass, the delay, the phase, and the polarization calibration were performed on the calibrators J2202+4216 (W48 and W51) and 3C286 (IRAS 18556+0138 and W3(OH)). Fringe-fitting and self-calibration were performed on the brightest maser feature of each star-forming region. Then we imaged the *I*, *Q*, *U*, *RR*, and *LL* cubes (2 as $\times$ 2 as,

[1]The European VLBI Network is a joint facility of European, Chinese, South African and other radio astronomy institutes funded by their national research councils.

4 mJy beam^{-1}< rms < 50 mJy beam^{-1}) using the AIPS task IMAGR. The beam-sizes were 5.5 mas × 4.5 mas for W51, 6.8 mas × 5.4 mas for W48, 7.5 mas × 4.8 mas for IRAS 18556+0318, and 8.7 mas × 4.1 mas for W3(OH). The Q and U cubes were combined to produce cubes POLI and POLA. We were able to obtain the absolute position of the brightest features of W51–e2, W51–IRS2, and W3(OH) through fringe rate mapping using the AIPS task FRMAP. The absolute position errors were less than 30 mas.

We identified the CH_3OH maser features using the process described in Sect. 3.2.2 and we fitted the maser emission by using the adapted code for CH_3OH masers (Sect. 3.2.3) with a grid of ΔV_i ranging from 0.5 to 1.95 km s^{-1}. We determined the Zeeman-splitting from the cross-correlation between the RR and LL spectra, which was successfully used in Chapters 5 and 6 for the polarized CH_3OH maser emission detected in W75N and NGC 7538. The dynamic range of the RR and LL cubes decreases close to the strongest maser emission of each group because of the residual calibration errors. As a result, we were not able to determine ΔV_Z for any CH_3OH maser features of W3(OH) with a peak flux less than ∼15 Jy beam^{-1}.

7.3 Results

In Tables 7.1–7.5 we list all the 154 CH_3OH maser features detected towards the 4 massive star-forming regions observed with the EVN. The description of the maser distributions and the polarization results are reported for each source separately in Sects. 7.3.1–7.3.4.

7.3.1 W51

We detected 6.7-GHz CH_3OH maser emission in the star-forming region W51–e1/e2 and W51–IRS2. In particular, 37 features towards W51–e2 (named as WE01-WE37 in Table 7.1) and 18 towards W51–IRS2 (named as WN01-WN18 in Table 7.2), no CH_3OH maser emission (8σ = 0.1 Jy beam^{-1}) was detected around W51–e1 (Fig. 7.1).

W51–e2

In Fig. 7.6 we show the CH_3OH maser features with their LSR radial velocities indicated by color (50 km s^{-1}< V_{lsr} < 61 km s^{-1}). The maser features near the 870 μm continuum peak (Fig. 7.1) lie in an elongated structure (PA= 57°) perpendicular to the molecular bipolar outflow (PA∼ 150°; Keto & Klaassen 2008) and close to the ionized accreting flow direction (PA∼ 30°; Keto & Klaassen 2008). These CH_3OH maser features have also velocities consistent with the velocities at the centre

of the H53α emission, which traces the rotating flow (Keto & Klaassen 2008).

We detected linear polarization emission ($P_{\rm l}$ = 1.2% − 4.0%) in 16 CH_3OH maser features that are all located close to the centre of W51–e2. The error weighted linear polarization angle is $\langle\chi\rangle_{\rm W51-e2} = 33°\pm16°$. The full radiative transfer method code for CH_3OH masers was able to fit 14 features. The intrinsic thermal linewidths and the emerging brightness temperatures are given in column 9 and 10 of Table 7.1 and their weighted values are $\langle\Delta V_{\rm i}\rangle_{\rm W51-e2} = 0.7^{+0.6}_{-0.2}$ km s^{-1} and $\langle T_{\rm b}\Delta\Omega\rangle_{\rm W51-e2} \approx 10^9$ K sr, respectively. Considering $T_{\rm b}\Delta\Omega$ and $P_{\rm l}$ we determined the angles between the maser propagation direction and the magnetic field (θ), which are almost constant for all the CH_3OH maser features. The feature WE17 shows $\theta = 90°$ indicating that the feature could be partially saturated. Hence, excluding this feature, $\langle\theta\rangle_{\rm W51-e2} = 79^{\circ}{}^{+11^{\circ}}_{-40^{\circ}}$. Since $\theta > \theta_{\rm crit} = 55°$ the magnetic field is most likely perpendicular to the linear polarization vectors even though it might also be parallel because of the relatively large errors in column 12 of Table 7.1. We measured Zeeman-splitting (column 11) in 4 CH_3OH maser features. The weighted value is $\langle\Delta V_{\rm Z}\rangle_{\rm W51-e2} = -1.6 \pm 1.2$ m s^{-1} and in absolute value is twice larger than that measured by Vlemmings (2008).

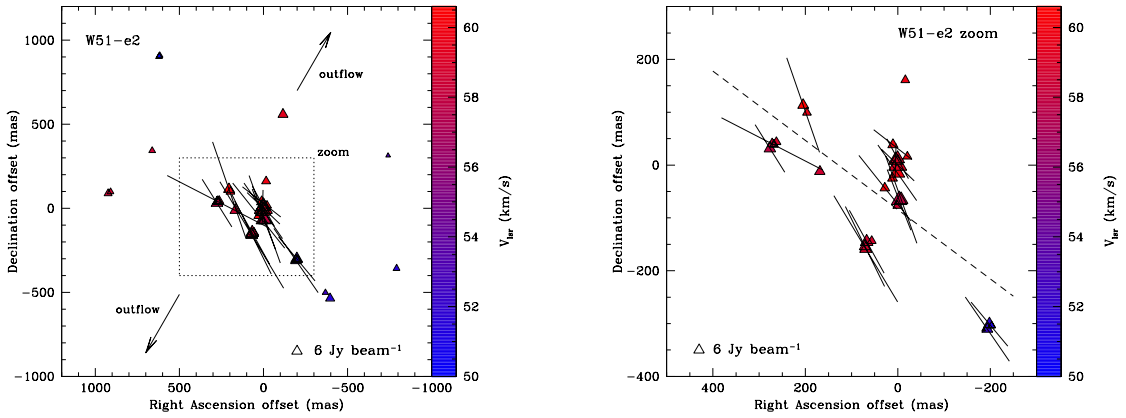

Figure 7.6: Left panel: a close-up view of the CH_3OH maser features detected around W51–e2. Right panel: a zoom-in view of the boxed region of the left panel. The triangles symbols are the identified maser features in present Ph.D. research scaled logarithmically according to their peak flux density (Table 7.1). The maser LSR radial velocity is indicated by color. A 6 Jy beam^{-1} symbol is plotted for illustration in both panels. The linear polarization vectors, scaled logarithmically according to polarization fraction $P_{\rm l}$, are overplotted. The two arrows indicate the direction of the bipolar outflow (PA$\sim$ 150°;Keto & Klaassen 2008). The dashed line is the best linear fit of the CH_3OH maser features in the right panel (PA= 57°)

Table 7.1: All 6.7-GHz methanol maser features detected in W51–e2.

(1) Maser	(2) RA[a] offset (mas)	(3) Dec[a] offset (mas)	(4) Peak flux Density(I) (Jy/beam)	(5) $V_{\rm lsr}$ (km/s)	(6) $\Delta v_{\rm L}$ (km/s)	(7) $P_{\rm l}$ (%)	(8) χ (°)	(9) $\Delta V_{\rm i}^{b}$ (km/s)	(10) $T_{\rm b}\Delta\Omega^{b}$ (log K sr)	(11) $\Delta V_{\rm Z}^{c}$ (m/s)	(12) θ^{d} (°)
WE01	-791.826	-357.414	0.78 ± 0.02	51.54	0.24	–	–	–	–	–	–
WE02	-741.361	313.950	0.24 ± 0.01	53.03	0.22	–	–	–	–	–	–
WE03	-396.633	-535.208	2.31 ± 0.02	51.45	0.42	–	–	–	–	–	–
WE04	-368.770	-501.720	0.47 ± 0.01	52.42	0.22	–	–	–	–	–	–
WE05	-202.860	-304.199	1.11 ± 0.04	51.10	0.33	–	–	–	–	–	–
WE06	-198.317	-300.964	9.73 ± 0.04	51.80	0.27	1.6 ± 0.2	40 ± 12	$1.3^{+0.1}_{-0.2}$	$8.9^{+0.6}_{-0.2}$	–	79^{+10}_{-40}
WE07	-193.719	-310.570	5.45 ± 0.03	52.15	0.27	2.2 ± 0.3	35 ± 49	$1.2^{+0.1}_{-0.2}$	$9.0^{+0.6}_{-0.2}$	–	80^{+10}_{-39}
WE08	-185.520	-311.840	0.13 ± 0.01	52.94	0.33	–	–	–	–	–	–
WE09	-116.608	558.552	3.84 ± 0.16	59.35	0.21	–	–	–	–	–	–
WE10	-20.773	16.247	2.05 ± 0.06	60.14	0.17	–	–	–	–	–	–
WE11	-16.176	160.938	2.02 ± 0.05	59.88	0.25	–	–	–	–	–	–
WE12	-7.368	-65.472	22.72 ± 0.03	58.30	0.27	2.6 ± 0.6	20 ± 6	$0.8^{+0.1}_{-0.1}$	$9.1^{+0.5}_{-0.6}$	–	79^{+11}_{-17}
WE13	-2.936	-65.970	65.78 ± 0.20	57.86	0.36	1.8 ± 0.4	21 ± 5	$1.7^{+0.1}_{-0.2}$	$8.9^{+0.7}_{-0.5}$	-0.4 ± 0.1	77^{+13}_{-37}
WE14	0	0	217.32 ± 0.23	59.26	0.33	1.4 ± 0.8	46 ± 9	$1.7^{+0.1}_{-0.2}$	$8.8^{+0.4}_{-1.3}$	-0.7 ± 0.1	67^{+11}_{-47}
WE15	0.443	12.135	26.63 ± 0.07	59.00	0.25	1.4 ± 0.4	29 ± 18	$1.2^{+0.1}_{-0.1}$	$8.8^{+0.6}_{-0.7}$	–	74^{+12}_{-41}
WE16	0.831	-76.960	2.28 ± 0.03	58.39	0.27	–	–	–	–	–	–
WE17	1.219	-14.587	50.54 ± 0.05	59.97	0.38	1.9 ± 0.4	35 ± 15	$1.7^{+0.6}_{-0.6}$	$8.9^{+0.1}_{-0.5}$	–	90^{+11}_{-11}
WE18	4.819	9.281	27.56 ± 0.16	59.35	0.28	1.2 ± 0.2	-2 ± 32	–	–	-2.4 ± 0.1	–
WE19	10.581	38.508	4.09 ± 0.05	59.97	0.27	1.5 ± 1.2	52 ± 17	$0.7^{+0.1}_{-0.1}$	$8.8^{+0.4}_{-1.0}$	–	68^{+12}_{-46}
WE20	11.412	-24.912	2.94 ± 0.05	60.05	0.25	–	–	–	–	–	–
WE21	27.975	-43.551	3.15 ± 0.01	60.32	0.23	2.3 ± 1.6	39 ± 46	–	–	–	–
WE22	56.393	-143.511	2.09 ± 0.04	58.91	0.19	–	–	–	–	–	–
WE23	67.250	-145.042	15.37 ± 0.05	58.74	0.28	2.0 ± 0.5	29 ± 11	$1.1^{+0.1}_{-0.1}$	$8.9^{+0.5}_{-0.7}$	–	78^{+12}_{-37}
WE24	69.300	-158.505	9.48 ± 0.07	59.00	0.30	4.0 ± 1.6	31 ± 6	$0.6^{+0.1}_{-0.1}$	$9.4^{+0.2}_{-1.3}$	–	84^{+6}_{-42}
WE25	70.851	-154.001	8.19 ± 0.03	58.82	0.26	2.5 ± 1.1	26 ± 8	$0.7^{+0.1}_{-0.1}$	$9.1^{+0.3}_{-1.1}$	–	76^{+14}_{-40}
WE26	168.514	-12.121	4.27 ± 0.03	58.56	0.51	–	–	–	–	–	–
WE27	196.655	99.159	1.82 ± 0.05	59.80	0.23	–	–	–	–	–	–
WE28	204.632	113.516	5.67 ± 0.02	60.58	0.34	2.9 ± 0.6	19 ± 8	–	–	–	–
WE29	262.520	43.556	2.26 ± 0.07	58.91	0.29	–	–	–	–	–	–
WE30	268.004	38.809	1.99 ± 0.03	58.82	0.27	–	–	–	–	–	–
WE31	271.716	40.205	3.30 ± 0.03	58.47	0.40	3.5 ± 1.1	63 ± 5	$1.4^{+0.1}_{-0.2}$	$9.3^{+0.2}_{-1.5}$	–	84^{+6}_{-40}
WE32	276.535	31.513	8.11 ± 0.06	57.86	0.48	1.6 ± 0.5	32 ± 23	$0.6^{+0.1}_{-0.1}$	$8.8^{+0.5}_{-0.6}$	-2.7 ± 0.1	75^{+14}_{-35}
WE33	616.831	909.365	0.57 ± 0.07	51.01	0.25	–	–	–	–	–	–
WE34	620.709	902.697	0.66 ± 0.02	50.04	0.40	–	–	–	–	–	–
WE35	661.979	343.477	0.62 ± 0.03	58.47	0.22	–	–	–	–	–	–
WE36	909.542	98.515	0.69 ± 0.03	58.82	0.28	–	–	–	–	–	–
WE37	923.834	88.762	1.29 ± 0.04	58.47	0.30	–	–	–	–	–	–

Notes. [a]The reference position is $\alpha_{2000} = 19^{\rm h}23^{\rm m}43^{\rm s}.942$ and $\delta_{2000} = +14°30'34''.550$. [b] The best-fitting results obtained by using a model based on the radiative transfer theory of methanol masers (Sect. 3.2) for $\Gamma + \Gamma_\nu = 1$. The errors were determined by analyzing the full probability distribution function. [c] The Zeeman-splittings are determined from the cross-correlation between the RR and LL spectra. [d] The angle between the magnetic field and the maser propagation direction is determined by using the observed $P_{\rm l}$ and the fitted emerging brightness temperature. The errors were determined by analyzing the full probability distribution function.

W51–IRS2

We detected 18 CH_3OH maser features with peak flux density between 0.16 mJy beam^{-1} and 12 mJy beam^{-1} and with velocities 54 km s^{-1}< $V_{\rm lsr}$ < 61 km s^{-1}. The CH_3OH maser features, all of which are associated with the UCH II region d2 (see Fig. 7.2), seem to lie in an arch structure oriented southwestern. We detected linear polarization emission only towards the brightest maser feature (WN11, $P_{\rm l}$ = 1.3% and $\chi_{\rm W51-IRS2}$ = 27°±13°). The intrinsic thermal linewidth and the emerging brightness temperature are in column 9 and 10 of Table 7.2 and the angle θ (column 13) indicates that the magnetic field is likely parallel to the linear polarization vector. Indeed, if we take into account the errors, the θ angle ranges between 10° and 71° that is less than the Van Vleck angle (Sect. 2.2). No Zeeman-splitting was measured.

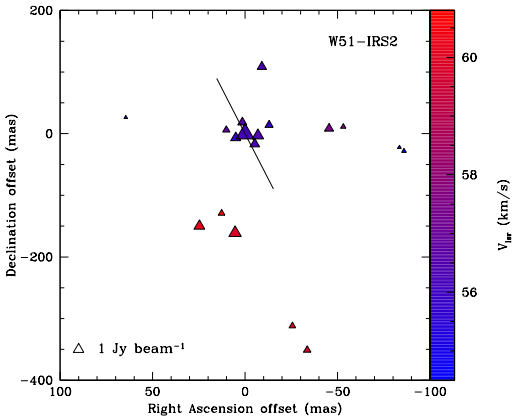

Figure 7.7: A close-up view of the CH_3OH maser features detected around W51–IRS2. The triangles symbols are the identified maser features in present Ph.D. research scaled logarithmically according to their peak flux density (Table 7.2). The maser LSR radial velocity is indicated by color. A 1 Jy beam^{-1} symbol is plotted for illustration. The linear polarization vectors, scaled logarithmically according to polarization fraction $P_{\rm l}$, are overplotted.

Table 7.2: All 6.7-GHz methanol maser features detected in W51–IRS2.

(1) Maser	(2) RA^a offset (mas)	(3) Dec^a offset (mas)	(4) Peak flux Density(I) (Jy/beam)	(5) $V_{\rm lsr}$ (km/s)	(6) $\Delta v_{\rm L}$ (km/s)	(7) $P_{\rm l}$ (%)	(8) χ (°)	(9) $\Delta V_{\rm i}^b$ (km/s)	(10) $T_{\rm b}\Delta\Omega^b$ (log K sr)	(11) $\Delta V_{\rm Z}^c$ (m/s)	(12) θ^d (°)
WN01	-85.860	-28.289	0.27 ± 0.01	54.52	0.31	–	–	–	–	–	–
WN02	-83.367	-22.108	0.20 ± 0.01	54.96	0.28	–	–	–	–	–	–
WN03	-53.067	-11.479	0.33 ± 0.04	57.94	0.28	–	–	–	–	–	–
WN04	-45.312	8.416	0.90 ± 0.02	57.51	0.25	–	–	–	–	–	–
WN05	-33.569	-351.122	0.61 ± 0.02	59.70	0.18	–	–	–	–	–	–
WN06	-25.536	-312.023	0.47 ± 0.03	59.88	0.28	–	–	–	–	–	–
WN07	-12.962	13.928	0.74 ± 0.02	55.84	0.25	–	–	–	–	–	–
WN08	-9.140	-108.629	1.02 ± 0.03	56.28	0.29	–	–	–	–	–	–
WN09	-6.813	-2.965	1.93 ± 0.01	56.45	0.21	–	–	–	–	–	–
WN10	-5.152	-16.856	1.12 ± 0.03	56.28	0.35	–	–	–	–	–	–

Table 7.2: (continued)

(1) Maser	(2) RA[a] offset (mas)	(3) Dec[a] offset (mas)	(4) Peak flux Density(I) (Jy/beam)	(5) $V_{\rm lsr}$ (km/s)	(6) $\Delta v_{\rm L}$ (km/s)	(7) $P_{\rm l}$ (%)	(8) χ (°)	(9) $\Delta V_{\rm i}^{b}$ (km/s)	(10) $T_{\rm b}\Delta\Omega^{b}$ (log K sr)	(11) $\Delta V_{\rm Z}^{c}$ (m/s)	(12) θ^{d} (°)
WN11	0	0	12.03 ± 0.07	56.19	0.35	1.3 ± 1.1	27 ± 13	$1.8^{+0.1}_{-0.1}$	$8.7^{+0.2}_{-1.4}$	–	61^{+11}_{-51}
WN12	1.496	18.406	0.95 ± 0.01	56.63	0.36	–	–	–	–	–	–
WN13	5.096	-6.713	1.25 ± 0.01	55.75	0.30	–	–	–	–	–	–
WN14	5.373	-161.138	2.42 ± 0.05	59.79	0.24	–	–	–	–	–	–
WN15	10.192	6.065	0.57 ± 0.01	56.98	0.31	–	–	–	–	–	–
WN16	12.630	-129.178	0.48 ± 0.02	60.84	0.26	–	–	–	–	–	–
WN17	24.761	-149.938	0.16 ± 0.01	60.23	0.26	–	–	–	–	–	–
WN18	64.644	26.281	0.20 ± 0.02	55.75	0.28	–	–	–	–	–	–

Notes. [a]The reference position is $\alpha_{2000} = 19^{\rm h}23^{\rm m}39^{\rm s}.818$ and $\delta_{2000} = +14^{\circ}31'5''.045$. [b] The best-fitting results obtained by using a model based on the radiative transfer theory of methanol masers (Sect. 3.2) for $\Gamma + \Gamma_{\nu} = 1$. The errors were determined by analyzing the full probability distribution function. [c] The Zeeman-splittings are determined from the cross-correlation between the RR and LL spectra. [d] The angle between the magnetic field and the maser propagation direction is determined by using the observed $P_{\rm l}$ and the fitted emerging brightness temperature. The errors were determined by analyzing the full probability distribution function.

7.3.2 W48

In Fig. 7.3 we show the position of the 6.7-GHz CH_3OH maser region detected by us, while in Fig. 7.8 all the 20 CH_3OH maser features are shown, named in Table 7.3 as W48-01–W48-20. The CH_3OH maser features appear to be symmetrically distributed, with the red-shifted features ($V_{\rm lsr} > 43$ km s^{-1}) located in the North-East and those blue-shifted ($V_{\rm lsr} < 43$ km s^{-1}) in the South-West.

Table 7.3: All 6.7-GHz methanol maser features detected in W48.

(1) Maser	(2) RA offset (mas)	(3) Dec offset (mas)	(4) Peak flux Density(I) (Jy/beam)	(5) $V_{\rm lsr}$ (km/s)	(6) $\Delta v_{\rm L}$ (km/s)	(7) $P_{\rm l}$ (%)	(8) χ (°)	(9) $\Delta V_{\rm i}^{a}$ (km/s)	(10) $T_{\rm b}\Delta\Omega^{a}$ (log K sr)	(11) $\Delta V_{\rm Z}^{b}$ (m/s)	(12) θ^{c} (°)
W48-01	-138.785	-87.692	19.00 ± 0.40	43.78	0.22	–	–	–	–	–	–
W48-02	-110.296	-57.672	6.84 ± 0.06	44.13	0.19	–	–	–	–	–	–
W48-03	-109.953	-128.784	14.07 ± 0.26	41.41	0.23	–	–	–	–	–	–
W48-04[d]	-101.143	-70.511	60.05 ± 1.46	42.91	0.29	5.1 ± 0.2	23 ± 8	$0.6^{+0.2}_{-0.1}$	$9.5^{+0.3}_{-0.1}$	–	87^{+3}_{-13}
W48-05	-99.026	-134.666	23.28 ± 0.95	40.89	0.29	–	–	–	–	–	–
W48-06	-94.621	-117.296	8.38 ± 0.14	42.03	0.24	–	–	–	–	–	–
W48-07	-90.502	-158.745	78.93 ± 1.40	41.50	0.22	–	–	–	–	–	–
W48-08	-89.072	-140.818	1.58 ± 0.02	40.18	0.35	–	–	–	–	–	–
W48-09	-82.093	-128.763	3.82 ± 0.09	40.18	0.35	–	–	–	–	–	–
W48-10	-81.635	-122.286	202.87 ± 6.56	42.47	0.26	4.4 ± 1.3	22 ± 6	$0.7^{+0.1}_{-0.1}$	$9.4^{+0.2}_{-1.4}$	–	84^{+6}_{-20}
W48-11	-81.235	-157.660	47.04 ± 0.08	40.97	0.31	–	–	–	–	–	–
W48-12	-77.974	-200.914	22.79 ± 0.18	41.76	0.37	–	–	–	–	–	–
W48-13	-75.171	-192.154	11.58 ± 0.26	41.41	0.17	–	–	–	–	–	–

Table 7.3: (continued)

(1) Maser	(2) RA offset (mas)	(3) Dec offset (mas)	(4) Peak flux Density(I) (Jy/beam)	(5) $V_{\rm lsr}$ (km/s)	(6) $\Delta v_{\rm L}$ (km/s)	(7) $P_{\rm l}$ (%)	(8) χ (°)	(9) $\Delta V_{\rm i}^{a}$ (km/s)	(10) $T_{\rm b}\Delta\Omega^{a}$ (log K sr)	(11) $\Delta V_{\rm Z}^{b}$ (m/s)	(12) θ^{c} (°)
W48-14[d]	0	0	294.68 ± 1.11	44.49	0.24	4.6 ± 1.5	12 ± 6	$1.0^{+0.1}_{-0.2}$	$9.5^{+0.6}_{-1.1}$	3.8 ± 0.4	73^{+16}_{-32}
W48-15	13.158	-65.594	2.48 ± 0.12	43.34	0.15	–	–	–	–	–	–
W48-16	27.631	-0.439	26.15 ± 0.41	44.57	0.26	–	–	–	–	–	–
W48-17	27.631	-29.171	22.64 ± 1.11	44.49	0.12	–	–	–	–	–	–
W48-18	34.267	-20.596	3.05 ± 0.17	45.36	0.24	–	–	–	–	–	–
W48-19[d]	47.082	-62.460	101.52 ± 1.30	43.70	0.25	5.4 ± 0.6	16 ± 4	$0.7^{+0.2}_{-0.1}$	$9.6^{+0.4}_{-0.2}$	–	84^{+4}_{-12}
W48-20[d]	58.352	6.796	32.74 ± 0.23	44.84	0.25	6.5 ± 0.6	27 ± 1	$0.6^{+0.2}_{-0.1}$	$9.7^{+0.3}_{-0.2}$	–	86^{+3}_{-10}

Notes.[(a)] The best-fitting results obtained by using a model based on the radiative transfer theory of methanol masers (Sect. 3.2) for $\Gamma + \Gamma_\nu = 1$. The errors were determined by analyzing the full probability distribution function. [(b)] The Zeeman-splittings are determined from the cross-correlation between the RR and LL spectra. [(c)] The angle between the magnetic field and the maser propagation direction is determined by using the observed $P_{\rm l}$ and the fitted emerging brightness temperature. The errors were determined by analyzing the full probability distribution function. [(d)]Because of the degree of the saturation of these H_2O masers $T_{\rm b}\Delta\Omega$ is underestimated, $\Delta V_{\rm i}$ and θ are overestimated.

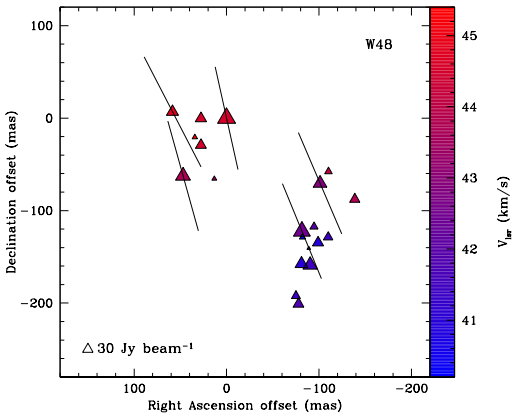

Figure 7.8: A close-up view of the CH_3OH maser features detected around W48 (G35.20–1.74). The triangles symbols are the identified maser features in present Ph.D. research scaled logarithmically according to their peak flux density (Table 7.3). The maser LSR radial velocity is indicated by color. A 30 Jy beam^{-1} symbol is plotted for illustration. The linear polarization vectors, scaled logarithmically according to polarization fraction $P_{\rm l}$, are overplotted.

Linear polarization emission was detected towards 5 CH_3OH maser features that show very high linear polarization fraction ($P_{\rm l} = 4.4\% - 6.5\%$). These high values of $P_{\rm l}$ suggest that the features might be partially saturated. Indeed the emerging brightness temperatures obtained by using the full radiative transfer method code are all but W48-10 greater than the limit for which CH_3OH maser features can be considered unsaturated, i.e. $T_{\rm b}\Delta\Omega = 2.6 \times 10^9$ K sr (see Sect. 6.4.2). As reported in Sect. 3.2.3, the intrinsic thermal linewidth for saturated masers is overestimated so the observed linewidths $\Delta v_{\rm L}$ might be equal to $\Delta V_{\rm i}$ (column 6 and 9 of Table 7.3, respectively). The θ angles (column 12) are all greater than 55° so the magnetic field is certainly perpendicular

to the linear polarization vectors. Zeeman-splitting was measured only for the brightest feature (W48-14) and its value is $\Delta V_{\rm Z} = 3.8 \pm 0.4$ m s^{-1}, which is 10 times larger than that measured by Vlemmings (2008).

7.3.3 IRAS 18556+0318

In Table 7.4, named as I-01–I-28, are reported all the 6.7-GHz CH_3OH maser features identified by using the identification process described in Sect. 3.2.2. In particular, they are associated with the source G35.20-0.74N and they can be divided in two groups (A and B) that appear to be at the ends of a linear structure with PA= 140°, which is almost perpendicular to the direction of the CO-outflow (PA= 58°; Gibb et al. 2003), see Fig. 7.9. Group A is composed of 20 CH_3OH maser features that seem to be along an arch structure (right panel of Fig. 7.10). Their velocities are between 27.60 km s^{-1} and 36.56 km s^{-1}. Group B is located about 2.3 as (∼5000 AU at 2.19 kpc) southeastern with respect to group A and close to the peak of the radio continuum emission shown in Fig 7.4. The 6.7-GHz CH_3OH maser features of group B have lower velocities (21 km s^{-1}< $V_{\rm lsr}$ < 27 km s^{-1}). The maser distribution described above coincides with that reported by Sugiyama et al. (2008a).

Table 7.4: All 6.7-GHz methanol maser features detected in IRAS 18556+0138 (G35.20–0.74N).

(1) Maser	(2) Group	(3) RA offset (mas)	(4) Dec offset (mas)	(5) Peak flux Density(I) (Jy/beam)	(6) $V_{\rm lsr}$ (km/s)	(7) $\Delta v_{\rm L}$ (km/s)	(8) $P_{\rm l}$ (%)	(9) χ (°)	(10) $\Delta V_{\rm i}^{a}$ (km/s)	(11) $T_{\rm b}\Delta\Omega^{a}$ (log K sr)	(12) $\Delta V_{\rm Z}^{b}$ (m/s)	(13) θ^{c} (°)
I-01^{d}	A	-1587.159	1817.554	14.71 ± 0.34	29.89	0.23	8.6 ± 1.3	−9 ± 3	< 0.5	$10.0^{+0.3}_{-0.9}$	–	90^{+14}_{-14}
I-02	A	-1563.866	1764.340	1.05 ± 0.10	28.57	0.42	–	–	–	–	–	–
I-03	A	-1561.521	1881.611	0.85 ± 0.03	33.22	0.30	–	–	–	–	–	–
I-04^{d}	A	-1558.818	1630.295	4.66 ± 0.03	36.56	0.26	9.1 ± 1.4	22 ± 28	< 0.5	$9.9^{+0.2}_{-1.2}$	–	90^{+11}_{-11}
I-05	A	-1559.276	1826.489	4.47 ± 0.03	27.95	0.24	–	–	–	–	–	–
I-06	A	-1553.628	1790.443	0.32 ± 0.03	27.95	0.26	–	–	–	–	–	–
I-07	A	-1551.154	1729.794	0.69 ± 0.02	27.60	0.28	–	–	–	–	–	–
I-08^{d}	A	-1550.882	1862.656	12.13 ± 0.08	29.36	0.29	6.5 ± 0.7	2 ± 3	$1.0^{+0.2}_{-0.1}$	$9.7^{+0.4}_{-0.2}$	–	84^{+4}_{-11}
I-09	A	-1549.567	1674.839	1.31 ± 0.02	30.41	0.30	–	–	–	–	–	–
I-10	A	-1548.166	1827.927	0.52 ± 0.02	27.25	0.22	–	–	–	–	–	–
I-11	A	-1548.080	1604.614	12.81 ± 0.11	35.42	0.30	4.8 ± 1.1	22 ± 18	$0.7^{+0.2}_{-0.1}$	$9.4^{+0.4}_{-1.2}$	–	84^{+6}_{-15}
I-12	A	-1538.571	1715.225	0.14 ± 0.01	33.49	0.30	–	–	–	–	–	–
I-13	A	-1535.311	1903.782	0.97 ± 0.03	33.22	0.20	–	–	–	–	–	–
I-14	A	-1527.890	1870.255	0.56 ± 0.02	33.40	0.14	–	–	–	–	–	–
I-15	A	-1519.568	1904.572	1.74 ± 0.01	26.90	0.43	–	–	–	–	–	–
I-16	A	-1513.805	1912.239	1.36 ± 0.01	26.20	0.31	–	–	–	–	–	–
I-17	A	-1501.437	1774.460	0.22 ± 0.01	30.94	0.21	–	–	–	–	–	–

Table 7.4: (continued)

(1) Maser	(2) Group	(3) RA offset (mas)	(4) Dec offset (mas)	(5) Peak flux Density(I) (Jy/beam)	(6) $V_{\rm lsr}$ (km/s)	(7) $\Delta v_{\rm L}$ (km/s)	(8) $P_{\rm l}$ (%)	(9) χ (°)	(10) $\Delta V_{\rm i}^{a}$ (km/s)	(11) $T_{\rm b}\Delta\Omega^{a}$ (log K sr)	(12) $\Delta V_{\rm Z}^{b}$ (m/s)	(13) θ^{c} (°)
I-18	A	-1466.290	1754.551	0.20 ± 0.01	32.34	0.37	–	–	–	–	–	–
I-19	A	-1454.021	1765.602	0.14 ± 0.01	31.73	0.27	–	–	–	–	–	–
I-20	A	-1293.200	1994.118	4.37 ± 0.19	29.10	0.21	–	–	–	–	–	–
I-21	B	-14.056	20.645	1.41 ± 0.02	27.95	0.40	–	–	–	–	–	–
I-22	B	-14.013	28.847	3.86 ± 0.05	28.31	0.23	–	–	–	–	–	–
I-23	B	-12.669	72.609	1.45 ± 0.05	28.31	0.65	–	–	–	–	–	–
I-24	B	-11.039	17.769	0.39 ± 0.01	27.43	0.25	–	–	–	–	–	–
I-25	B	-5.863	-4.211	0.31 ± 0.01	27.34	0.19	–	–	–	–	–	–
I-26	B	-3.117	-277.435	1.58 ± 0.05	28.39	0.21	–	–	–	–	–	–
I-27[d]	B	0	0	104.81 ± 1.05	28.57	0.26	11.5 ± 1.9	-10 ± 5	< 0.5	$10.8^{+0.5}_{-0.7}$	–	85^{+5}_{-7}
I-28	B	49.389	48.145	0.89 ± 0.03	27.69	0.18	–	–	–	–	–	–

Notes.[a] The best-fitting results obtained by using a model based on the radiative transfer theory of methanol masers (Sect. 3.2) for $\Gamma + \Gamma_\nu = 1$. The errors were determined by analyzing the full probability distribution function. [b] The Zeeman-splittings are determined from the cross-correlation between the RR and LL spectra. [c] The angle between the magnetic field and the maser propagation direction is determined by using the observed $P_{\rm l}$ and the fitted emerging brightness temperature. The errors were determined by analyzing the full probability distribution function. [d]Because of the degree of the saturation of these H_2O masers $T_{\rm b}\Delta\Omega$ is underestimated, $\Delta V_{\rm i}$ and θ are overestimated.

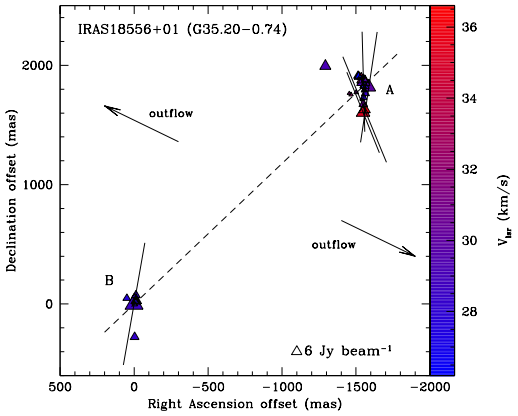

Figure 7.9: A close-up view of the CH_3OH maser features detected around IRAS 18556+0138 (G35.20–0.74N). The triangles symbols are the identified maser features in present Ph.D. research scaled logarithmically according to their peak flux density (Table 7.4). The maser LSR radial velocity is indicated by color. A 6 Jy beam^{-1} symbol is plotted for illustration. The linear polarization vectors, scaled logarithmically according to polarization fraction $P_{\rm l}$, are overplotted. The dashed line is the best linear fit of the CH_3OH masers (PA= 140°). The two arrows indicate the direction, but not the origin, of the collimated CO-molecular bipolar outflow (PA= 58°; Gibb et al. 2003).

We detected linear polarization in 5 CH_3OH maser features ($P_{\rm l} = 4.8\% - 11.5\%$) and the full radiative transfer method code was able to properly fit only two of them (I-08 and I-11). This is due to the likely high saturation degree of the CH_3OH maser features. For the features I-01, I-04, and I-27 the gridding of $\Delta V_{\rm i}$ used for fitting the linear polarized and total intensity spectra was insufficient and consequently the code provided only an upper limit for $\Delta V_{\rm i}$. All the emerging brightness temperatures obtained from the fit, except I-11, reveal that the features

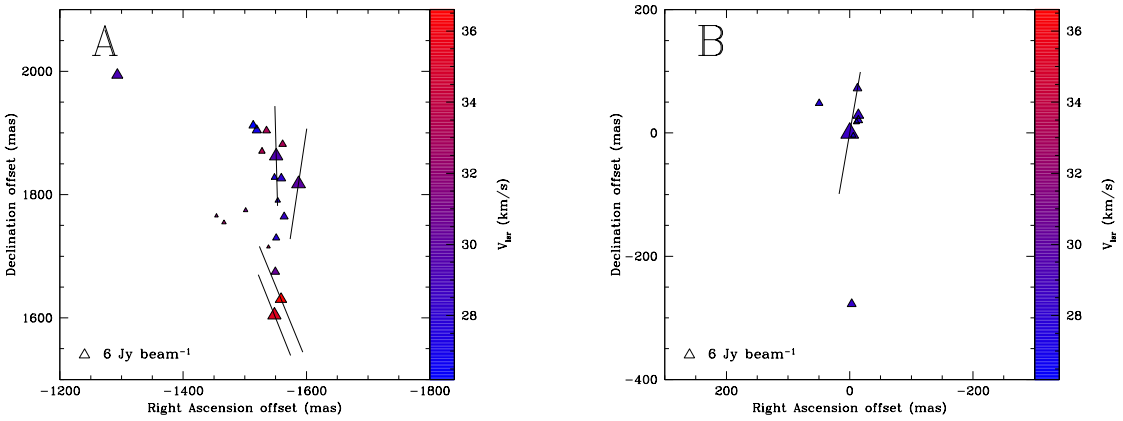

Figure 7.10: Zoom-in view of the two CH_3OH maser clusters of IRAS 18556+0138 (G35.20–0.74N).

have a high saturation degree. In particular, the reference maser feature I-27 shows the highest linear polarization fraction among all the 6.7-GHz CH_3OH maser features detected in the whole EVN sample ($P_l = 11.5\%$). The magnetic field is also in G35.20-0.74 perpendicular to the linear polarization vectors ($\theta > 55°$). No 6.7-GHz CH_3OH maser Zeeman-splitting was measured in this source.

7.3.4 W3(OH)

W3(OH) is the massive star-forming region towards which we detected one third of all the CH_3OH maser features of the EVN sample. They are listed in Table 7.5, where they are named as W3-01–W3-51, and plotted in Fig. 7.11. They can be divided in six groups (I–VI) and their zoom-in views are shown in Fig. 7.12. Morphologically the 6.7-GHz CH_3OH maser features detected with the EVN show the same filamentary structure observed with MERLIN by Harvey–Smith & Cohen (2006) and no new group of features was observed (Fig. 7.5). We do not detected the CH_3OH maser features located western w.r.t. the isolated feature W3-05 (features 22 and 23 in Harvey–Smith & Cohen 2006). The linear distribution of the central 6.7-GHz CH_3OH maser features of group II (PA= 121°) is similar to those of the 12-GHz CH_3OH masers (PA= 141°; Moscadelli et al. 2010) and of the OH masers (PA= 130°−140°; Moscadelli et al. 2010). Group IV seems to lie in an arch-like structure. The northern clump (groups I, II, and III) shows velocities in absolute value greater of $\sim 2-4$ km s^{-1} than the southern clump (groups IV, V, and VI), in particular group

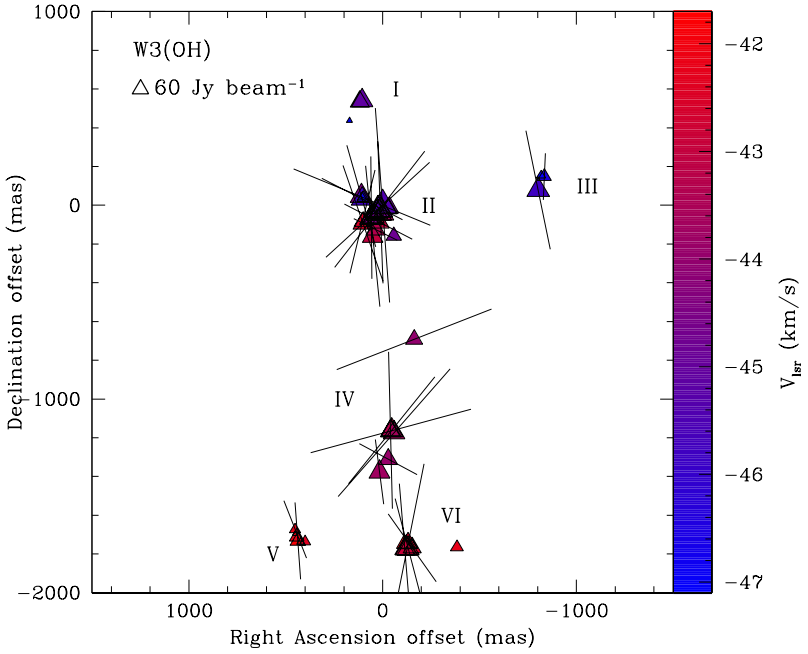

Figure 7.11: A close-up view of the CH_3OH maser features detected around W3(OH). The triangles symbols are the identified maser features in present Ph.D. research scaled logarithmically according to their peak flux density (Table 7.5). The maser LSR radial velocity is indicated by color. A 60 Jy beam^{-1} symbol is plotted for illustration. The linear polarization vectors, scaled logarithmically according to polarization fraction P_l, are overplotted. Compare with Fig. 7.5.

V has in absolute value the lowest velocity ($V_{\rm lsr} \approx -42$ km s^{-1}). Along the linear structure of group II the distribution of the maser velocities is well ordered, the most blue-shifted velocities are northwestern and the most red-shifted are southeastern. This velocity distribution coincides perfectly with that of the 12-GHz CH_3OH masers (Moscadelli et al. 2010).

We have detected linear polarization in more than 50% of the CH_3OH maser features (27/51) with linear polarization fraction ranging from 1.2% to 8.1%. The highest P_l corresponds to the brightest maser feature (W3-22) that also shows the highest emerging brightness temperature. This value indicates that the feature is partially saturated like other 5 features (W3-05, W3-10, W3-14, W3-17, and W3-18) that have $T_{\rm b}\Delta\Omega > 2.6 \times 10^9$ K sr. The weighted emerging brightness temperature and the weighted intrinsic thermal linewidth of the unsaturated features are $\langle T_{\rm b}\Delta\Omega\rangle_{\rm W3(OH)} \approx 2 \times 10^9$ K sr and $\langle \Delta V_{\rm i}\rangle_{\rm W3(OH)} = 0.9^{+0.4}_{-0.3}$ km s^{-1}, respectively. The error

weighted linear polarization angle is $\langle\chi\rangle_{\rm W3(OH)} = 3°\pm39°$, while considering only the unsaturated features $\langle\chi\rangle_{\rm W3(OH)} = 15°\pm31°$. The θ values reported in column 13 of Table 7.5 indicate that for some CH_3OH maser features (e.g., W3-35) the magnetic field is more likely perpendicular to the linear polarization vectors, while for other features it is parallel (e.g., W3-09). For 7 CH_3OH maser features was possible to measure the Zeeman-splitting of which values are in the range $-3.5\ {\rm m\,s^{-1}} < \Delta V_{\rm z} < 3.8\ {\rm m\,s^{-1}}$ (column 12 of Table 7.5).

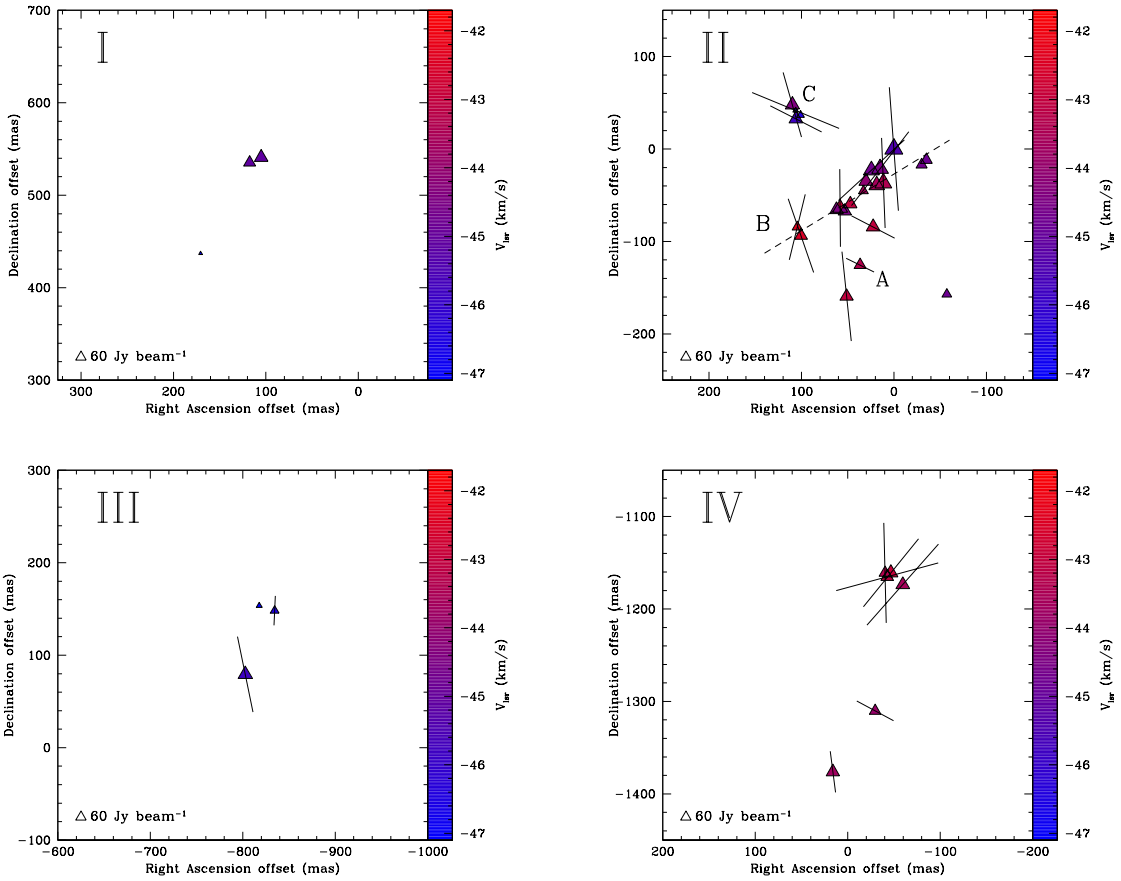

Figure 7.12: continue on next page

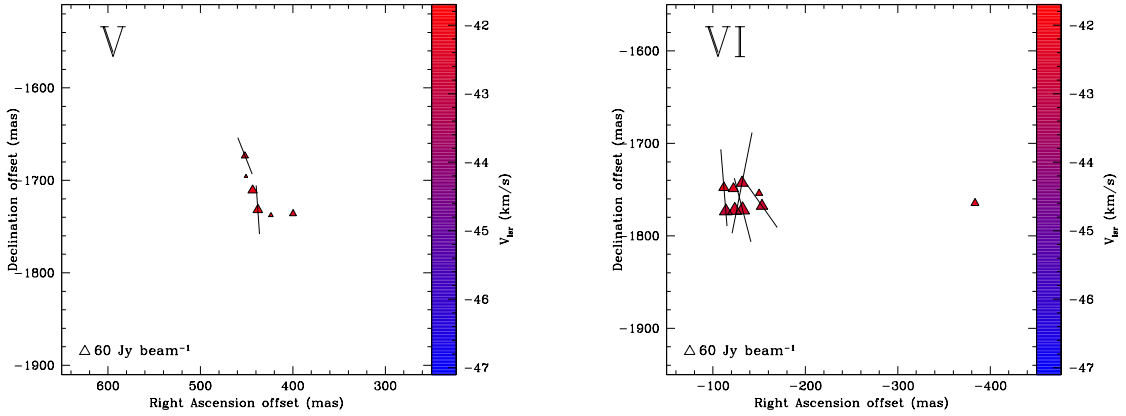

Figure 7.12: Zoom-in view of the six CH_3OH maser groups of W3(OH). The dashed line in panel II is the best linear fit of the central CH_3OH maser features (PA= 121°). A, B, and C are used to label three associations of 6.0-GHz OH, 12-GHz CH_3OH, and 6.7-GHz CH_3OH masers.

Table 7.5: All 6.7-GHz methanol maser features detected in W3(OH).

(1) Maser	(2) Group	(3) RA[a] offset (mas)	(4) Dec[a] offset (mas)	(5) Peak flux Density(I) (Jy/beam)	(6) $V_{\rm lsr}$ (km/s)	(7) $\Delta v_{\rm L}$ (km/s)	(8) $P_{\rm l}$ (%)	(9) χ (°)	(10) $\Delta V_{\rm i}^{b}$ (km/s)	(11) $T_{\rm b}\Delta\Omega^{b}$ (log K sr)	(12) $\Delta V_{\rm Z}^{c}$ (m/s)	(13) θ^{d} (°)
W3-01	III	-834.479	148.296	11.58 ± 0.02	-46.55	0.20	1.2 ± 0.4	-2 ± 10	$0.9^{+0.1}_{-0.1}$	$8.8^{+0.6}_{-0.5}$	–	71^{+10}_{-42}
W3-02	III	-817.800	153.654	2.26 ± 0.01	-47.07	0.18	–	–	–	–	–	–
W3-03	III	-802.674	79.334	27.78 ± 0.28	-45.76	0.22	3.2 ± 0.8	12 ± 69	$1.1^{+0.1}_{-0.2}$	$9.2^{+0.8}_{-0.4}$	–	69^{+9}_{-42}
W3-04	VI	-383.492	-1764.656	7.78 ± 0.04	-42.24	0.19	–	–	–	–	–	–
W3-05[e]	-	-162.497	-691.895	33.61 ± 0.55	-44.00	0.18	5.6 ± 1.7	-69 ± 5	$0.7^{+0.1}_{-0.1}$	$9.6^{+0.4}_{-1.2}$	–	83^{+7}_{-14}
W3-06	VI	-122.187	-1749.006	27.32 ± 0.05	-42.33	0.21	–	–	–	–	–	–
W3-07	VI	-153.206	-1767.649	54.81 ± 0.34	-42.60	0.20	1.9 ± 0.6	35 ± 14	$0.9^{+0.1}_{-0.1}$	$9.0^{+0.6}_{-0.7}$	–	72^{+18}_{-34}
W3-08	VI	-149.964	-1753.939	4.82 ± 0.04	-42.24	0.19	–	–	–	–	–	–
W3-09	VI	-132.122	-1771.915	235.45 ± 0.33	-42.60	0.19	2.5 ± 1.2	15 ± 33	$0.9^{+0.1}_{-0.1}$	$9.2^{+0.7}_{-0.9}$	–	67^{+16}_{-38}
W3-10[e]	VI	-131.591	-1742.706	60.79 ± 0.34	-42.60	0.18	5.3 ± 2.7	-11 ± 7	$0.8^{+0.1}_{-0.1}$	$9.6^{+0.4}_{-1.3}$	–	77^{+12}_{-42}
W3-11	VI	-123.541	-1772.516	212.03 ± 0.33	-42.60	0.22	–	–	–	–	-3.5 ± 0.2	–
W3-12	VI	-114.142	-1773.373	111.69 ± 0.37	-42.95	0.20	–	–	–	–	–	–
W3-13	VI	-111.926	-1747.892	22.93 ± 0.03	-42.07	0.20	3.1 ± 0.3	5 ± 38	$0.8^{+0.1}_{-0.1}$	$9.2^{+0.3}_{-0.1}$	–	81^{+8}_{-14}
W3-14[e]	IV	-59.565	-1173.670	182.60 ± 0.64	-43.65	0.26	5.9 ± 1.9	-41 ± 44	$1.1^{+0.1}_{-0.2}$	$9.6^{+0.5}_{-1.3}$	–	75^{+15}_{-29}
W3-15	II	-57.240	-157.034	20.812 ± 0.59	-44.79	0.33	–	–	–	–	–	–
W3-16	IV	-46.725	-1160.805	233.50 ± 0.38	-42.95	0.32	3.9 ± 0.5	-39 ± 86	$1.5^{+0.1}_{-0.3}$	$9.3^{+0.6}_{-0.2}$	–	74^{+11}_{-39}
W3-17[e]	IV	-42.741	-1165.085	110.50 ± 0.29	-43.12	0.25	5.6 ± 3.9	-75 ± 41	$1.1^{+0.2}_{-0.2}$	$9.6^{+0.1}_{-1.8}$	–	75^{+14}_{-45}
W3-18[e]	IV	-40.408	-1160.982	65.18 ± 0.49	-43.12	0.29	5.0 ± 2.6	2 ± 85	$1.2^{+0.1}_{-0.2}$	$9.5^{+0.2}_{-1.7}$	–	74^{+13}_{-43}
W3-19	II	-35.097	-11.770	69.09 ± 0.62	-44.79	0.25	–	–	–	–	–	–
W3-20	II	-30.011	-17.119	46.52 ± 0.72	-44.70	0.25	–	–	–	–	–	–
W3-21	IV	-29.630	-1310.143	57.91 ± 0.52	-43.91	0.31	1.5 ± 1.1	62 ± 49	$1.5^{+0.1}_{-0.2}$	$8.8^{+0.7}_{-0.4}$	–	77^{+13}_{-38}
W3-22[e]	II	0	0	2051.30 ± 1.42	-45.41	0.31	8.1 ± 0.7	4 ± 34	$1.0^{+0.1}_{-0.1}$	$10.0^{+0.5}_{-0.1}$	1.9 ± 0.1	73^{+10}_{-5}

Table 7.5: (continued)

(1) Maser	(2) Group	(3) RA[a] offset (mas)	(4) Dec[a] offset (mas)	(5) Peak flux Density(I) (Jy/beam)	(6) $V_{\rm lsr}$ (km/s)	(7) $\Delta v_{\rm L}$ (km/s)	(8) $P_{\rm l}$ (%)	(9) χ (°)	(10) $\Delta V_{\rm i}^{b}$ (km/s)	(11) $T_{\rm b}\Delta\Omega^{b}$ (log K sr)	(12) $\Delta V_{\rm Z}^{c}$ (m/s)	(13) θ^{d} (°)
W3-23	II	11.410	-36.799	1099.80 ± 0.81	-43.39	0.29	4.1 ± 1.2	2 ± 41	$1.2^{+0.1}_{-0.2}$	$9.4^{+0.6}_{-1.0}$	–	75^{+14}_{-36}
W3-24	II	14.956	-21.265	913.15 ± 0.92	-44.53	0.37	4.4 ± 2.0	-38 ± 41	$1.70^{+0.03}_{-0.25}$	$9.4^{+0.9}_{-1.0}$	–	68^{+9}_{-45}
W3-25	IV	15.969	-1376.160	156.18 ± 0.65	-43.74	0.21	1.5 ± 0.4	7 ± 23	$1.1^{+0.1}_{-0.1}$	$8.8^{+0.7}_{-0.4}$	3.8 ± 0.5	68^{+7}_{-45}
W3-26	II	18.653	-39.053	546.64 ± 0.63	-43.65	0.21	–	–	–	–	–	–
W3-27	II	22.492	-84.309	206.85 ± 0.36	-43.03	0.18	1.8 ± 0.2	63 ± 35	$0.9^{+0.1}_{-0.1}$	$9.0^{+0.5}_{-0.1}$	–	76^{+5}_{-46}
W3-28	II	24.383	-22.999	640.49 ± 0.70	-44.70	0.29	4.1 ± 1.6	-47 ± 19	$1.4^{+0.1}_{-0.2}$	$9.4^{+0.8}_{-1.0}$	–	68^{+12}_{-40}
W3-29	II	30.256	-34.817	239.84 ± 0.56	-44.09	0.27	–	–	–	–	–	–
W3-30	II	33.002	-45.343	20.09 ± 0.63	-43.56	0.26	–	–	–	–	–	–
W3-31	II	39.591	-125.509	74.16 ± 0.50	-43.30	0.19	1.2 ± 0.9	64 ± 29	$0.9^{+0.1}_{-0.1}$	$8.8^{+0.3}_{-1.2}$	–	65^{+7}_{-52}
W3-32	II	47.238	-59.534	155.18 ± 0.36	-43.03	0.18	–	–	–	–	–	–
W3-33	II	51.173	-159.398	146.66 ± 0.36	-43.03	0.26	4.1 ± 2.7	6 ± 42	$1.2^{+0.1}_{-0.2}$	$9.4^{+0.2}_{-1.6}$	–	70^{+13}_{-45}
W3-34	II	53.063	-67.207	140.91 ± 0.98	-44.53	0.40	–	–	–	–	–	–
W3-35	II	58.220	-63.723	347.43 ± 0.37	-42.86	0.19	3.2 ± 1.1	1 ± 37	$0.9^{+0.1}_{-0.1}$	$9.2^{+0.6}_{-0.9}$	-1.5 ± 0.1	71^{+18}_{-33}
W3-36	II	62.103	-65.691	180.85 ± 0.70	-44.35	0.37	–	–	–	–	–	–
W3-37	II	100.540	-93.575	110.11 ± 0.28	-42.51	0.31	3.2 ± 0.8	19 ± 53	$1.4^{+0.1}_{-0.2}$	$9.2^{+0.7}_{-0.8}$	-1.7 ± 0.4	76^{+13}_{-37}
W3-38	II	101.041	36.774	7.17 ± 0.02	-46.37	0.25	–	–	–	–	–	–
W3-39	II	104.515	-84.400	28.12 ± 0.05	-42.33	0.27	3.7 ± 1.0	-14 ± 6	$0.8^{+0.2}_{-0.1}$	$9.3^{+0.4}_{-1.1}$	–	81^{+9}_{-17}
W3-40	I	105.043	540.987	178.62 ± 0.45	-45.14	0.22	–	–	–	–	-3.4 ± 0.4	–
W3-41	II	106.053	32.572	19.21 ± 0.28	-45.76	0.31	2.1 ± 0.3	63 ± 80	$1.7^{+0.1}_{-0.2}$	$9.0^{+0.7}_{-0.2}$	–	69^{+6}_{-46}
W3-42	II	106.329	41.679	2.08 ± 0.01	-46.99	0.44	4.4 ± 0.5	68 ± 5	–	–	–	–
W3-43	II	109.883	47.815	254.77 ± 0.69	-44.35	0.24	2.6 ± 0.7	16 ± 27	$1.2^{+0.1}_{-0.1}$	$9.1^{+0.7}_{-0.7}$	–	73^{+11}_{-41}
W3-44	I	117.485	535.473	73.74 ± 0.44	-45.05	0.17	–	–	–	–	–	–
W3-45	I	170.642	437.187	0.72 ± 0.01	-47.07	0.18	–	–	–	–	–	–
W3-46	V	399.814	-1735.970	4.32 ± 0.11	-42.42	0.43	–	–	–	–	–	–
W3-47	V	423.769	-1737.766	1.25 ± 0.02	-41.89	0.28	–	–	–	–	–	–
W3-48	V	437.887	-1731.754	19.97 ± 0.02	-41.81	0.78	1.8 ± 0.3	4 ± 2	$1.0^{+0.1}_{-0.1}$	$9.0^{+0.5}_{-0.3}$	1.4 ± 0.2	76^{+11}_{-40}
W3-49	V	443.434	-1710.760	15.71 ± 0.04	-42.24	0.26	–	–	–	–	–	–
W3-50	V	450.607	-1695.734	0.62 ± 0.02	-41.72	0.27	–	–	–	–	–	–
W3-51	V	451.835	-1673.563	4.46 ± 0.04	-42.24	0.22	1.5 ± 0.2	22 ± 5	$0.55^{+0.09}_{-0.01}$	$8.8^{+0.4}_{-0.1}$	–	79^{+11}_{-35}

Notes. [a] The reference position is $\alpha_{2000} = 02^{\rm h}27^{\rm m}03^{\rm s}.833$ and $\delta_{2000} = +61°52'25''.288$. [b] The best-fitting results obtained by using a model based on the radiative transfer theory of methanol masers (Sect. 3.2) for $\Gamma + \Gamma_\nu = 1$. The errors were determined by analyzing the full probability distribution function. [c] The Zeeman-splittings are determined from the cross-correlation between the RR and LL spectra. [d] The angle between the magnetic field and the maser propagation direction is determined by using the observed $P_{\rm l}$ and the fitted emerging brightness temperature. The errors were determined by analyzing the full probability distribution function. [e] Because of the degree of the saturation of these H_2O masers $T_{\rm b}\Delta\Omega$ is underestimated, $\Delta V_{\rm i}$ and θ are overestimated.

7.4 Discussion

7.4.1 CH_3OH maser properties

Before discussing the magnetic fields in each source, it is worthwhile spending few lines on the properties of the CH_3OH maser features (or simply CH_3OH masers). As reported in Sect. 7.3

we observed a number of saturated CH_3OH masers in our EVN sample. If we consider all the 72 CH_3OH masers detected in this sample and in NGC7538 (Chapter 7) for which was possible to determine the emerging brightness temperature, we can estimate the upper limit of linear polarization fraction for unsaturated 6.7-GHz CH_3OH masers. In Fig 7.13 we report the emerging brightness temperature as function of the linear polarization fraction. From this plot we find that the 6.7-GHz CH_3OH masers with $P_l \lesssim 4.5\%$ are all unsaturated. Furthermore, from Sect. 2.1.2 we

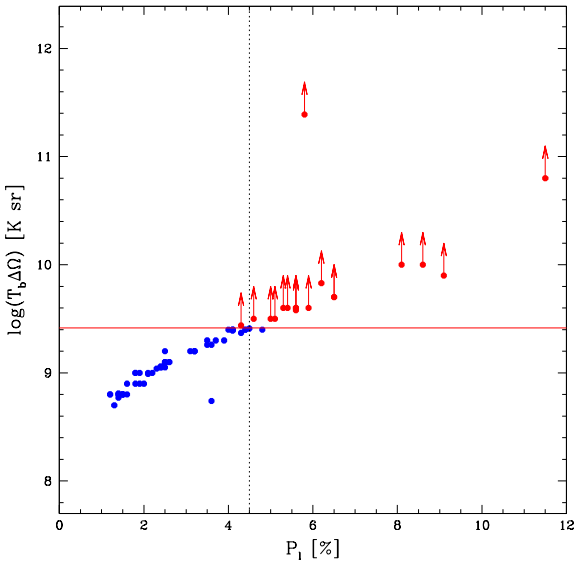

Figure 7.13: The emerging brightness temperatures ($T_b\Delta\Omega$) as function of the linear polarization fraction (P_l). The blue and red circles indicate the unsaturated and saturated masers, respectively, detected in NGC7538, W51, W48, IRAS 18556+0138, and W3(OH). The red arrows indicate that the $T_b\Delta\Omega$ values obtained from the radiative transfer method code are lower limits. The red full line is the limit of emerging brightness temperature from which the CH_3OH masers are considered saturated ($T_b\Delta\Omega > 2.6 \times 10^9$ K sr; Sect. 6.4.2), and the dotted line shows the lower linear polarization fraction for saturated masers ($P_l \approx 4.5\%$).

know that the beaming angle ($\Delta\Omega$) of unsaturated masers is roughly proportional to $|\tau_\nu|^{-1}$, which is proportional to the brightness temperature T_b. Consequently, if these masers are unsaturated $\Delta\Omega \propto (T_b)^{-1}$. As already done in Sects. 6.4.2, we can estimate $\Delta\Omega$ by comparing the brightness temperature T_b, which is given by

$$\frac{T_b}{[\mathrm{K}]} = \frac{S(\nu)}{[\mathrm{Jy}]} \cdot \left(\frac{\Sigma^2}{[\mathrm{mas}^2]}\right)^{-1} \cdot \xi_{CH_3OH}, \tag{7.1}$$

with $T_b\Delta\Omega$ obtained from the model. In Eq. 7.1 $S(\nu)$ is the flux density, Σ the maser angular size, which from the Gaussian fit of the masers is between 4 and 8 mas and almost all the CH_3OH masers appear resolved, and $\xi_{CH_3OH} = 13.63 \cdot 10^9$ mas^2 Jy^{-1} K. We obtain that $\Delta\Omega$ ranges from $3 \cdot 10^{-3}$ sr to $8 \cdot 10^{-2}$ sr. In Fig. 7.14all the values of $\Delta\Omega$ as function of T_b are reported, both in logarithmic scales. From a linear fit (blue line) we found that $\Delta\Omega \propto (T_b)^{-0.9}$ implying that the CH_3OH masers we have taken into account are indeed unsaturated.

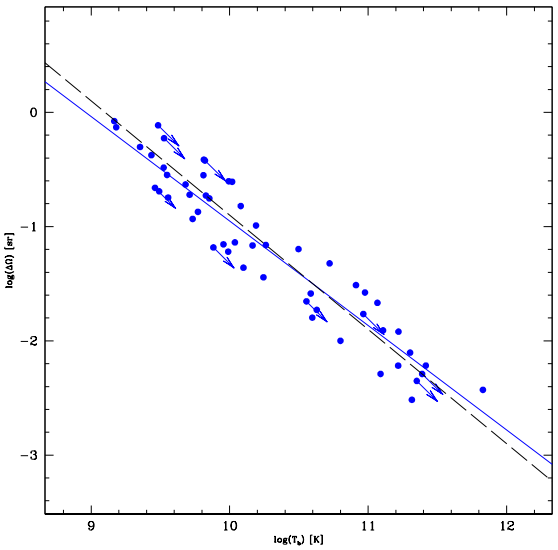

Figure 7.14: The beaming angle ($\Delta\Omega$) as function of the brightness temperatures (T_b) for all the unsaturated CH_3OH masers detected in NGC7538, W51, W48, IRAS 18556+0138, and W3(OH). The arrows indicate that the masers are unresolved, i.e. the maser angular size Σ is as large as the beam-size of the observations and consequently $\Delta\Omega$ is smaller and T_b is larger (Sect. 7.2). The blue line is the best linear fit of the resolved masers and the dashed black line is the theoretical proportionality.

In a tubular geometry we have that $\Delta\Omega \approx (d/l)^2$ where d is the transverse size of the tube, which we assume to be approximately the size of the maser spot, and l is the length of the tube, i.e. the size of the path through which the maser radiation is amplified. We found that l is between $3 \cdot 10^{14}$ cm ($\sim$ 20 AU) and $6 \cdot 10^{15}$ cm ($\sim$ 400 AU). Actually only for WE-14 we measured $l \approx 6 \cdot 10^{15}$ cm, while the other CH_3OH masers are well below this limit ($l < 3 \cdot 10^{15}$ cm $\approx$ 200 AU).

7.4.2 Individual sources and magnetic fields

We know that the measurements of the linear polarization angles (χ) might be disturbed by the rotation of the linear polarization vectors due to the medium between the source and the observer. This rotation is the foreground Faraday rotation that is given by Eq. 6.5. Assuming the interstellar electron density and the magnetic field are $n_\mathrm{e} \approx 0.012\,\mathrm{cm}^{-3}$ and $B_{||} \approx 2\,\mu$G (Chapter 6), Φ_f for the 6.7-GHz CH_3OH masers can be written as:

$$\Phi_\mathrm{f}[^\circ] = 2.26 \left(\frac{D}{[\mathrm{kpc}]}\right), \tag{7.2}$$

i.e. the farther the maser source is, the larger Φ_f is. This means that the foreground Faraday rotation ranges between $\Phi_\mathrm{f}^\mathrm{W51} \backsimeq 12^\circ$ and $\Phi_\mathrm{f}^\mathrm{W3(OH)} \backsimeq 4^\circ$. As we discuss below, from the orientation of the linear polarization vectors the Faraday rotation seems to be small and negligible.

We cannot determine the exact magnetic field strengths from our Zeeman-splitting measure-

ments because of the uncertain of α_Z. However, we can estimate the importance of the magnetic fields through Eq, 6.12. Assuming $n_{H_2} = 10^9$ cm^{-3} and $T \sim 200$ K, this equation can be written as

$$\beta = 611.6\ \alpha_Z^2\ cos\ \langle\theta\rangle\ \left(\frac{|\Delta V_Z|}{[\mathrm{ms}^{-1}]}\right)^{-2}. \tag{7.3}$$

We argued in Sect. 6.4.3 that a reasonable value for the Zeeman-splitting coefficient α_Z should be in the range $0.005\ \mathrm{km\,s^{-1}\,G^{-1}} < \alpha_Z < 0.05\ \mathrm{km\,s^{-1}\,G^{-1}}$, consequently from equation 7.3 we can estimate a range of β. The magnetic fields dominate the energies in the high-density protostellar environment if $\beta < 1$ (Sect. 1.2.2).

W51–e2

The linear distribution of the central 6.7-GHz CH_3OH masers (PA=57°) suggests that the masers likely trace a disc structure perpendicular to the bipolar outflow (PA∼150°; Keto & Klaassen 2008). But the good agreement between the ionized flow velocities and the maser velocities suggests that the CH_3OH masers might probe material that is being accreted onto the disc, like in NGC7538 and Cepheus A (Sects.4.4 and 6.4.4), rather than the disc material.

The quite perfect alignment of the linear polarization vectors implies that the foreground Faraday rotation is smaller than the value evaluated above. This probably indicates that the interstellar density and/or the interstellar magnetic fields are smaller than what we supposed. Because

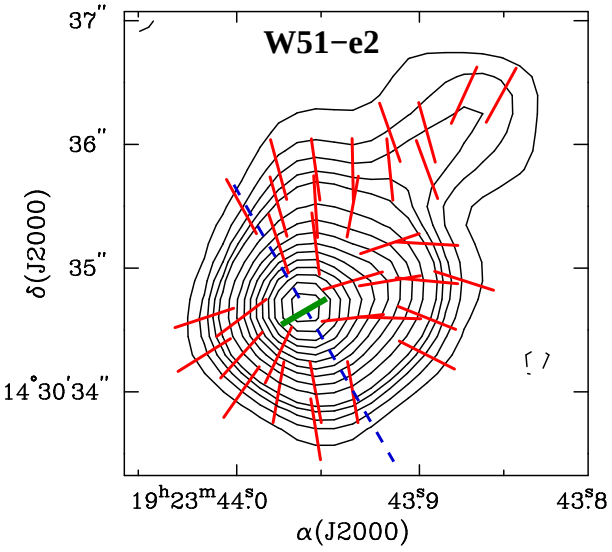

Figure 7.15: Modified version of Fig. 5a of Tang et al. (2009b). The magnetic field (red segments) detected with the SMA is superimposed on the 870 μm continuum contour map of W51–e2. The dashed blue line indicates the direction of the ionized accreting flow by Keto & Klaassen (2008). The green segment marks the direction of the magnetic field close to the 870 μm continuum peak as derived from the linear polarization emission of the CH_3OH masers.

$\langle\theta\rangle_{\rm W51-e2} = 79° > \theta_{\rm crit}$ the magnetic field is on the plane of the sky with a position angle of $\sim 120°$ that is perfectly perpendicular to the ionized accretion flow (PA$\sim$30°; Keto & Klaassen 2008) rather than to the linear distribution. The linear polarized emission has been detected close to the 870 μm continuum peak and so the CH_3OH masers are probing the magnetic field at the centre of the hourglass morphology mapped by Tang et al. (2009b) with the SMA. In Fig. 7.15 we superimposed the results obtained by Tang et al. (2009b) and by us. Here we can see that the magnetic field derived from the CH_3OH masers (green segment) is consistent with the hourglass morphology (red segments). This suggests that the massive protostar is formed in a similar way as low-mass protostar. In particular, the morphology of the magnetic field recalls that of Cepheus A HW2 (Fig. 4.6). The negative value of the Zeeman-splitting indicates that the magnetic field is orientated towards the observer and from Eq. 7.3, where $\langle|\Delta V_{\rm Z}|\rangle_{\rm W51-e2} = 1.6\ {\rm m\,s^{-1}}$, we get $10^{-3} < \beta < 10^{-1}$, i.e. the magnetic field plays a crucial role in the formation of the massive protostar.

W51–IRS2 (W51–d2)

In Fig. 7.16 the magnetic fields as derived from the SMA observations at 870 μm (red segments; Tang et al. private communication) and from our EVN observations at 6.7-GHz (green segment) are shown. Despite the different angular resolution of the two observations the two magnetic fields are in perfect agreement implying a well-ordered magnetic field.

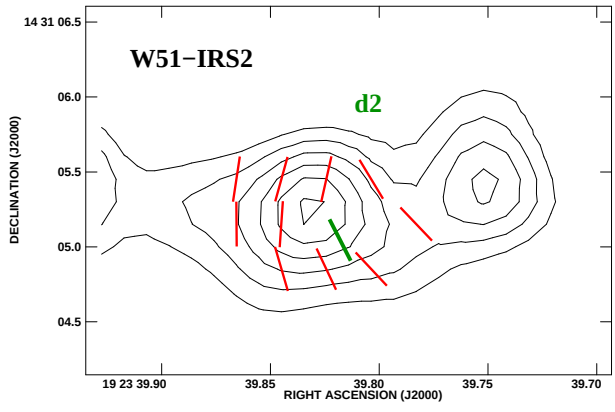

Figure 7.16: The magnetic field (red segments) detected with the SMA is superimposed on the 870 μm continuum contour map of W51–e2 (Tang et al. private communication). The green segment marks the direction of the magnetic field close to the 870 μm continuum peak as derived from the linear polarization emission of the CH_3OH masers.

W48 (G35.20–1.74)

The CH_3OH masers detected towards W48 are associated with the submillimetre–core W48main detected with SCUBA by Curran et al. (2004) and are closer to MIR3 than to MIR1 (Fig. 7.3).

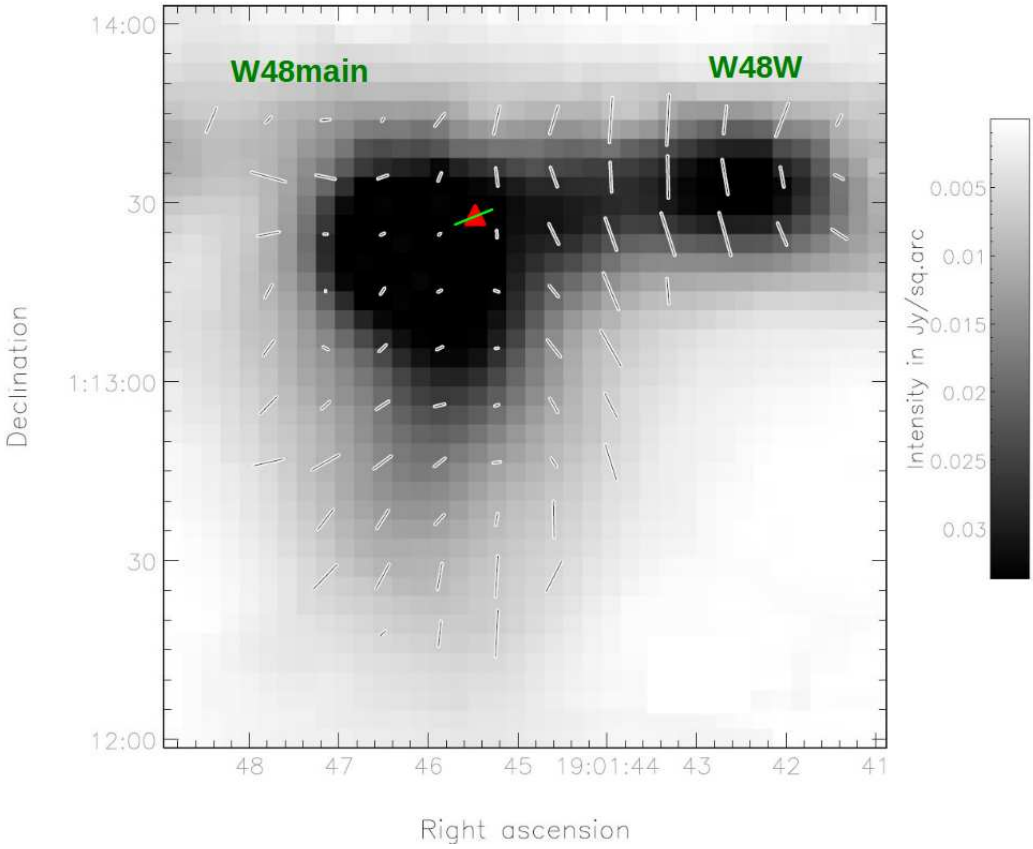

Figure 7.17: Position of CH_3OH maser region (red filled triangle) superimposed on the 850 μm continuum emission (grey scale) of W48 (G35.20-1.74) observed with SCUBA by Curran et al. (2004). The overlaid white vectors represent the direction of the magnetic field lines projected onto the plane of the sky (Curran et al. 2004). The green vector represents the direction of the magnetic field derived from the liner polarization observations of the CH_3OH masers made using the EVN.

This implies that the CH_3OH masers are not related to the other two maser species (H_2O and OH, Fig. 7.3).

Despite of the saturation state of the CH_3OH masers, the linear polarization vectors are well aligned, implying that either the saturation state of the masers does not affect the linear polariza-

tion emission or that the internal Faraday rotation plays a crucial role in saturated masers. As Fish & Reid (2006) showed, the internal Faraday rotation can destroy the linear polarization. Since we measured a quite high linear polarization fraction (∼5%) in all the polarized CH_3OH masers, the contribution of the internal Faraday rotation must be negligible. Hence, the linear polarization emission is not affected by the saturation degree of the CH_3OH masers, otherwise it would be impossible to have a perfect alignment of the vectors. A comparison between the magnetic fields derived from the 6.7-GHz CH_3OH maser observations and from the 850 μm observations (Fig 7.17; Curran et al. 2004) shows that, like in W51–d2, the magnetic fields are consistent towards the core at different angular resolution. Furthermore, the positive Zeeman-splitting ($|\Delta V_Z|_{W48} = 3.8\ m\,s^{-1}$) indicates that the magnetic field is oriented away from the observer and that the magnetic field is important in the region ($10^{-4} < \beta < 10^{-2}$).

IRAS 18556+0318 (G32.20–0.74N)

The two groups of CH_3OH masers seem to trace a linear structure probably symmetric w.r.t. the protostar, i.e. where the group B arises, with a radius of about 5000 AU. This is suggested by the position angle of this linear structure that agrees with the inclinations obtained both from the OH maser emission (Hutawarakorn & Cohen 1999) and from the $CO^{18}O(2-1)$ emission (López–Sepulcre et al. 2009). If we consider the velocities of the CH_3OH and OH masers, of the large flattened structure, of the outflows, and of the source itself we find that the whole picture is quite different. The velocities of the two maser species are in good agreement, both are in the range 21 $km\,s^{-1} < V_{masers} < 37\ km\,s^{-1}$, and probably they are tracing the same gas, but they are totally in disagreement with the velocities of the large flattened structure. Moreover, while the mean radial velocity of the large flattened structure is identical to the LSR velocity of the source ($V_{lsr}^{G35.20} = 34\ km\,s^{-1}$, Hutawarakorn & Cohen 1999), the velocities of group B, that should be at the centre of the linear structure, are about 10 $km\,s^{-1}$ lower than $V_{lsr}^{G35.20}$. The velocities of group B are instead in the velocity range of the blue-shifted part of the outflow suggesting an association with it. Also the velocities of group A seem to be in agreement with the outflow even if the arch-like distribution of the group seems to imply an association with a torus structure. This torus structure might not be related to the large flattened structure.

As we observed in W48, also in G32.20–0.74N the saturation state of the masers does not influence the orientation of the linear polarization vectors, that appear to be well ordered, and the magnetic field is parallel to them. Considering all the four masers of group A that show linear

polarization emission the magnetic field has PA=90°. Since features I-04 and I-11 have velocities 7 $\mathrm{km\,s^{-1}}$ greater than features I-01 and I-08 we can determine the orientation of the magnetic field separately, i.e. PA=112° and PA=83° respectively. From group B we get PA=80°. In all cases the magnetic field derived from the 6.7-GHz CH_3OH masers is not aligned neither with the outflow nor with the linear structure, but is almost perpendicular to the radio/infrared jet.

W3(OH)

In the top-right panel of Fig. 7.12 are reported the three associations A, B, and C of 6.0-GHz OH, 12-GHz CH_3OH, and 6.7-GHz CH_3OH masers. The perfect agreement of the positions and velocities of the 6.7-GHz CH_3OH masers with the OH and 12-GHz CH_3OH masers confirms that all the masers complement each other as argued by Moscadelli et al. (2010).

Since we observed at higher angular resolution than Vlemmings et al. (2006b) we are able to better determine the magnetic field morphology in group II. Comparing Figs. 7.5 and 7.11 we see that the linear polarization vectors of the 6.7-GHz CH_3OH masers are not as similar through the whole filamentary structure as observed with the MERLIN, probably because of the 90°-flip phenomenon. However, they appear well ordered within each group (Fig. 7.12) and this again indicate that the saturation state of the masers does not influence the linear polarization emission. Groups III, V, and VI show error weighted linear polarization angles ($\langle\chi\rangle$) close to 0°. A comparison with the results obtained by Vlemmings et al. (2006b), who did not detect any linear polarization emission from group V, indicates that the orientation of the linear polarization vectors in these groups are likely influenced by the 90°-flip phenomenon. This 90°-flip is also confirmed from the θ angles measured by us (column 14 of Table 7.5), or better the magnetic field is more likely parallel to the vectors, i.e. with orientation North-South. In group IV we see that all the features but W3-18 and W3-25 show a linear polarization angle similar to that measured by Vlemmings et al. (2006b). The different angles of W3-18 and W3-25 could also be do to the 90°-flip and consequently we find that also here the magnetic field is oriented almost North-South. This orientation of the magnetic field is also determined from the isolated feature W3-05 of which linear polarization angle agrees quite perfectly with that measured with MERLIN. While the magnetic fields in all these groups (III, IV, V, VI) has an orientation along the filamentary structure, the magnetic field morphology in group II is completely different. For all the CH_3OH maser features that have χ angles close to 0° (W3-22, W3-23, W3-33, W3-35, W3-37, and W3-37) we find, considering the errors, that their θ_{min} angles are greater than 55°, indicating that the magnetic field is perpendicular to the

filamentary structure and aligned with the linear distribution. This orientation of the magnetic field is also suggested by the features that have linear polarization vectors parallel to the linear structure (W3-24 and W3-28) that show $\theta_{\rm min} < 55^\circ$, i.e. magnetic field is likely parallel to them. The other maser features of group II (W3-27, W3-31, W3-41, W3-42, and W3-43) show magnetic field more consistent with this morphology than with the North-South orientation.

From the Zeeman-splitting measurements we can determine the pointing direction of the magnetic fields. Let consider first group II. Since we measured both positive (W3-22) and negative (W3-35 and W3-37) Zeeman-splittings at the North-West end and at the South-East end of the linear distribution respectively, the magnetic field must have a counterclockwise direction. This direction is opposite to the rotation of the linear distribution, which is clockwise as derived from the OH and CH_3OH masers velocities. If the masers along the linear distribution trace a disc that is rotating clockwise ($M \approx 1.5$ M$_\odot$ and $R \approx 270$ AU; Moscadelli et al. 2010), we have in W3(OH) a scenario similar to that of NGC7538. The magnetic field is on the disc (in NGC7538 on the torus) rotating in opposite direction to the disc. The Zeeman-splitting measurements of the other groups suggest that the magnetic field is twisted along the filamentary structure. Since for all the groups the error weighted value of θ is about 74° and considering that $\langle|\Delta V_{\rm Z}|\rangle_{\rm II} = 1.84$ m s^{-1} and $\langle|\Delta V_{\rm Z}|\rangle_{-\rm II} = 2.13$ m s^{-1} are the error weighted Zeeman-splittings of group II and of all the other groups respectively, from Eq. 7.3 we find that in both cases $10^{-3} < \beta < 10^{-1}$. The magnetic field is important in the whole massive star-forming region W3(OH).

7.5 Conclusions

We observed a sample of 4 massive star-forming regions at 6.7-GHz in full polarization spectral mode with the EVN to detect linear and circular polarization emission from the CH_3OH masers. We detected a total of 154 6.7-GHz CH_3OH masers one third of which only towards W3(OH). We detected linear polarization emission in all the regions of the EVN sample, and in 3 of them we also measured Zeeman-splitting. From our observations we have found that the magnetic field is well ordered in W51–e2 and W3(OH). In the former the magnetic field derived from the CH_3OH masers is at the centre and along the axis of symmetry of the hourglass morphology observed with the SMA at 870 μm. In W3(OH) we determined two different magnetic fields, one twisted along the filamentary structure and the other one in the northern clump on the likely low-mass rotating disc probed by the linear distribution of the CH_3OH and OH masers with a counterclockwise orientation. In the case of IRAS18556+0318 (G32.20–0.74N) the magnetic field seems to be perpendicular to the

radio/infrared jet rather than along the outflow or along a possible torus structure. The magnetic fields are in perfect agreement with their morphology at lower angular resolution determined with the SMA and SCUBA (W51–e2, W51–d2, and W48) and they play an important role in all the massive star-forming regions of the EVN sample.

In addition, we have also estimated a limit of linear polarization fraction of 4.5% below which the 6.7-GHz CH_3OH masers are unsaturated.

EPILOGUE

Chapter 8

General summary

During the formation of low-mass stars the magnetic field is thought to slow the collapse, to transfer the angular momentum, and to power the outflows, but its role during the formation of high-mass stars is still under debate. Several questions remain unanswered because massive star-forming regions are rare, distant and often consist of large number of protostars, consequently it is difficult to observe magnetic fields during their protostellar phase. The best probes of the magnetic field on the smallest scales in the high-mass star-forming environments are maser lines. Their bright and narrow spectral line emission is ideal for detecting both the Zeeman-splitting and the direction of the magnetic field. During this Ph.D. work 22-GHz H_2O and 6.7-GHz CH_3OH maser emissions towards several massive star-forming regions have been observed and analyzed using VLBA, EVN, and MERLIN data. In this last chapter the main conclusions of this Ph.D. thesis are summarized. The last section is focused on the future of this Ph.D. research.

8.1 Main conclusions

The interferometric observations of H_2O and CH_3OH masers allowed us to investigate the magnetic fields in 7 massive star-forming regions yielding the following main conclusions:

- We have demonstrated the *power of maser polarization observations*, and in particular for the first time those using 6.7-GHz CH_3OH masers, in deducing the magnetic field morphology around massive protostars. The detection of coherent magnetic field direction in CH_3OH masers suggests that these masers do not probe isolated pockets of a shock compressed magnetic fields but they *probe the actual large-scale magnetic fields.*

- The detection of large-scale magnetic fields is further confirmed both by the *perfect agreement* of the field directions with those determined using *dust polarization observations* (Cepheus A, W51–e2, W51–d2, and W48), and by the comparison of the magnetic field directions obtained using the H_2O and the CH_3OH masers, which have two different pumping mechanisms, around the same protostar, i.e. VLA 1 in W75N(B).

- For the first time we were able to determine the *full 3-dimensional magnetic field geometry around a massive protostar*, i.e. Cepheus A HW2. Here, the magnetic field is perpendicular to the molecular and dust discs and parallel to the radio outflows implying an *hourglass morphology*. Hence, the magnetic field regulates the infall and outflow close to massive protostars in a similar way as during the low-mass star formation.

- An *hourglass morphology* was also detected with the SMA around W51–e2 and the magnetic field derived from the 6.7-GHz CH_3OH maser emission is consistent with this morphology suggesting a similar magnetic field as in Cepheus A HW2.

- In the star-forming region W75N(B) we showed that it is possible to measure the *magnetic fields around two massive protostars at different evolutionary stages separated by only 1300 AU*. In particular, the magnetic field around VLA 1, which is the most evolved protostar, is aligned well with the *large-scale molecular bipolar outflow*, while the magnetic field is well-ordered around the *shell-like expanding gas* associated with VLA 2. Thanks to the H_2O masers we were also able to measure magnetic field strengths of $|B_{\rm VLA1}| \sim 700$ mG and $|B_{\rm VLA2}| \sim 1700$ mG around VLA 1 and VLA 2, respectively.

- In NGC7538 we showed that the H_2O and CH_3OH masers are consistent with a *torus-outflow scenario*. Here the CH_3OH masers are tracing the interface between the infall and the large-scale torus, while the H_2O masers are related to the blue-shifted part of the outflow. In this source the magnetic field appears to be *on the two surfaces of the torus with a counterclockwise direction* on the top surface, which is opposite to the clockwise rotation of the torus.

- A similar morphology of the magnetic field was also determined in the northern CH_3OH maser clump of W3(OH). The magnetic field is indeed *on the likely clockwise-rotating disc*, which is probed by the 12-GHz and 6.7-GHz CH_3OH and 1.6-GHz OH masers, but with a counterclockwise orientation. Moreover, we also determined a *twisted magnetic field along the filamentary structure* described by the CH_3OH masers.

- Towards IRAS 18556+0138, or better G32.20-0.74N, we measured a magnetic field *perpendicular to the radio/infrared jet*. This is the only case in all the star-forming regions investigated in this Ph.D. work where the magnetic field is neither along the outflow nor on the surface of a possible torus structure that is probably traced by the CH_3OH masers.

- Thanks to the Zeeman-splitting measurements of the 6.7-GHz CH_3OH masers we found that the *magnetic field is crucially important in all the massive star-forming regions* that we observed. Because of the number of sources observed, we cannot conclude that this fact is only a coincidence but we can start to consider the magnetic fields really important also in the formation of high-mass stars.

In conclusion we have found that the magnetic field in massive star-forming regions plays a role as important as in the formation of low-mass stars. All our results are in perfect agreement with the theoretical simulations of Banerjee & Pudritz (2007), who demonstrated that the formation of an early outflow driven by the magnetic field is necessary in order to form the observed disc-outflow systems. From our measurements the magnetic fields seem to be oriented along the outflow with an hourglass morphology at large-scales and when we observe closer to the protostar the magnetic fields appear to be on the surfaces of a torus/disc structure from which the matter accreates onto the protostar along the magnetic field lines.

In addition we determine some important properties of the polarized CH_3OH maser emission. We found that:

- All the masers with a linear polarization fraction greater than 4.5% are all saturated with an emerging brightness temperature $T_b \Delta\Omega > 2.6 \times 10^9$ K and the saturation state does not influence the orientation of the linear polarization vectors.

- In unsaturated CH_3OH masers the beaming angle is roughly proportional to $|\tau_\nu|^{-0.9}$ that is close to the theoretical proportionality (Chapter 2).

- The measured brightness temperatures for the H_2O and CH_3OH masers are $T_b < 10^{12}$ K and the beaming angles are in the range 10^{-1} sr $< \Delta\Omega < 10^{-3}$ sr for the CH_3OH masers and $\Delta\Omega < 10^{-3}$ sr for the H_2O masers. From the beaming angles we estimated amplification paths of 10^{14} cm $< l < 10^{16}$ cm for the CH_3OH masers and 10^{12} cm $< l < 10^{15}$ cm for the H_2O masers.

- From the analysis of the linearly polarized H_2O maser emission we were able to determine gas temperatures of ∼400 K and ∼2500 K into the H_2O masing regions around the protostars VLA 1 and VLA 2 (W75N), respectively. Moreover, we also showed that from the polarized H_2O masers is also possible to determine the type of shocks that pump the H_2O masers.

8.2 The near future

8.2.1 Follow-ups

In order to bring our total sample up to 12 massive star-forming regions we proposed further EVN observations in full polarization at 6.7-GHz towards 5 massive star-forming regions (S231, S255, IRAS 0658+2138, IRAS 20126+4104, and IRAS 22272+6358). For this second EVN sample we choose sources that host 6.7-GHz CH_3OH masers that either show linear structures with a clear velocity gradient (infalling gas or disc?) or that are likely associated with outflows. All these sources were observed with the 100 m-Effelsberg telescope by Vlemmings (2008) and Vlemmings et al. (2011) who measured 6.7-GHz CH_3OH maser Zeeman-splitting. These observations will allow the start of a statistical approach in defining the relation between field morphology and the occurrence of the masers in outflows and torus/disc structures. The proposal was accepted in March 2011 and scheduled and observed in May 2011.

In February 2011 VLBA polarization observations of H_2O masers at 22-GHz towards three massive star-forming regions were proposed and accepted in May 2011. To better understand the magnetic field morphology of IRAS 18556+0138, which was observed at 6.7-GHz in this Ph.D. work (Chapter 7), and to follow the H_2O masers dynamics in W75N–VLA 2 we included these two regions in this VLBA proposal. The third region is IRAS 20126+4104 that is also included in the second EVN sample. The observations of IRAS 20126+4104 at both frequencies will give us the opportunity to investigate the magnetic field morphology in the interface between the disc and the outflow, in particular we could see how the magnetic field changes its orientation when it passes from the disc to the outflow.

Finally we propose for the first time full polarization observations of 6.7-GHz CH_3OH masers with the Expanded Very Large Array (EVLA) in February 2011, which were accepted in May 2011. With the new C-band receivers, the EVLA has the potential to play a major role in magnetic field measurements of CH_3OH masers, providing both linear and circular polarization measurements of somewhat weaker masers then is currently possible with single dish telescopes. For instance, the

EVLA is able, in 2 hr on source, to expand the total sample of EVN candidates to masers down to ~ 25 Jy beam^{-1}. The sample is composed of 7 massive star-forming regions and five of which are proposed to test the instrument, among these are Cepheus A, W75N and IRAS 20126+4104.

8.2.2 The new golden age

Thanks to the improved "old" instruments, such as the EVLA or the e-MERLIN, and the coming on-line of new instruments, such as the Atacama Large Millimeter/submillimeter Array (ALMA), the Low Frequency Array (LOFAR) or the Square Kilometre Array (SKA), in the next years the Radio Astronomy will enter in its *golden age*. All these instruments will give an acceleration to the study and understanding of the formation of high-mass stars including the role of magnetic fields. Below three examples are reported.

1. By observing in continuum at 6-GHz with the e-MERLIN all the massive star-forming regions within a distance of 7 kpc the astronomers will be able (1) to determine at which evolutionary stage and luminosity the MHD jets turn on and how the jet parameters vary during the jets evolution, (2) to determine at what evolutionary stage the switch from magnetically driven jets to radiatively driven disc winds occurs. Moreover, the polarization observations of 6.7-GHz CH_3OH maser emission will allow to determine the 3-dimensional magnetic field morphology, as done in Cepheus A HW2 (Chapter 4) but with more sensitivity, and directly relate the continuum morphology, i.e. jet and outflows, to the magnetic field geometry (see Sect. 4.5.2). The determination of the 3-dimensional magnetic field morphology is a fundamental input to MHD modelling. This research is part of the e-MERLIN legacy project called "Feedback during massive star formation" that will start by the end of 2011. I am part of the investigator team.

2. The ALMA telescope will allow the astronomers to map the gas motions in collapsing clouds with high velocity and angular resolutions, and with high sensitivity that none current and planned instruments can or could provide at millimitre and submillimitre wavelengths (from ∼80-GHz to ∼800-GHz). Moreover the smaller structures of massive protostars (but also of low-mass protostars), such as disc and early jet/outflow, could also be observed, revealing details that now cannot be observed in the millimetre and submillimetre wavelength range. In addition, with ALMA the thermal methanol emission towards CH_3OH maser regions could be investigated. The thermal methanol can provide information on the density and temperature on the same scale of the magnetic field measurements made in this Ph.D. work,

allowing to link the magnetic fields to infall, accretion or outflow components present in massive protostars.

3. How does the matter accumulate along the magnetic field lines from the ISM to H II regions? Does the formation of massive stars depend on the Galactic Magnetism? LOFAR, and afterwards the SKA, is able to contribute in answering these questions. By investigating the polarized emission emitted from background sources and by detecting more precise Rotation Measure (RM) the astronomers could understand how the magnetic field influences the formation of massive stars. Comparing the polarized emission from several sources behind and close to H II regions the astronomers will be able to probe and measure the magnetic fields and the densities along many separate sightlines in the H II regions. Since LOFAR is a very sensitive instrument and because its working frequency range has been unobserved so far, it is now possible to observe more background sources than with the current instruments. The same observations could also be made with the SKA at high frequencies and, at that point, by combining the information from the two instruments and knowing the RM contribution from the Galactic foreground the astronomer could answer those questions.

These are only a small part of the potential observations that could be carried on with some of these new instruments. The future years will be very important for astronomy and astrophysics, and in particular for the study of massive star formation. The new observational results with the new powerful computers will also improve the modelling simulations allowing the astronomers to depict a more and more precise scenario for the formation of stars with masses greater about 8 $M_{\odot}$.

Bibliography

Alakov A.V., Slysh V.I., Popov M.V. et al. 2005, Astron.Lett., 31, 375

Anderson, N., & Watson, W.D., 1993, ApJ, 407, 620

Argon, A.L., Reid, M.J. & Menten, K.M. 2000, ApJ, 129, 159

Argon, A.L., Reid, M.J. & Menten, K.M. 2002, IAU Symp., 206, 367

Baart, E.E., Cohen, R.J., Davies, R.D. et al. 1986, MNRAS, 219, 145

Bally, J. & Zinnecker, H. 2005, AJ, 129, 2281

Banerjee, R. & Pudritz, R.E. 2007, ApJ, 660, 479

Barbosa, C.L., Blum, R.D., Conti, P.S. et al. 2008, ApJ, 678, L55

Bartkiewicz, A., Szymczak, M., Cohen, R.J. et al. 2005, MNRAS, 361, 623

Bartkiewicz, A., Szymczak, M. & van Langevelde, H.J. 2006, Proceedings of the 8th European VLBI Network Symposium, 39B

Bartkiewicz, A., Szymczak, M., van Langevelde, H.J. et al. 2009, A&A, 502, 155

Bate, M.R. & Bonnell, I.A. 2005, MNRAS, 356,1201

Benson, J.M., Mutel, R.L. & Gaume, R.A. 1984, AJ, 89, 9

Bieging, J. 1975, in Lecture Notes in Physics, Vol. 42, 443

Beuther, H., Churchwell, E.B., McKee, C.F. et al. 2007, Protostars and Planets V, 165

Bonnell, I.A., Bate, M.R., Clarke, C.J. et al. 2001, MNRAS, 323, 785

Bonnell, I.A., Vine, S.G., & Bate, M.R. 2004, MNRAS, 349, 735

Bonnell, I.A., Larson, R.B. & Zinnecker, H. 2007, Protostars and Planets V, 149

Bonnell, I.A. 2008, ASP Conference Series, 390, 26

Burns, J.O., Owen, F.N., & Rudinick, L. 1979, AJ, 84, 1683

Campbell, B. 1984, ApJ, 282, L27

Campbell, B. & Thompson, R. 1984, ApJ, 279, 650

Campbell, M.F., Lester, D.F., Harvey, P.M. et al. 1989, ApJ, 345, 298

Carpenter, J.M. & Sanders, D.B. 1998, AJ, 116, 1856

Carrasco-González, C., Rodríguez, L.F., Anglada, G., et al. 2010, Science, 330, 1209

Caswell, J.L., Vaile, R.A., Ellingsen, S.P. et al. 1995, MNRAS, 272, 96

Chansrasekhar, S. & Fermi, E. 1953, ApJ, 118, 113

Cheung, A.C., Rank, D.M., Townes, C.H. et al. 1969, Nature, 221, 626

Chini, R., Hoffmeister, V., Kimeswenger, S., et al. 2004, Nature, 429, 155

Chini, R., Hoffmeister, V., Nielbock, M., et al. 2006, ApJ, 645, L61

Cho, S.-H., Kim, J. & Byun, D.-Y. 2011, ApJ, 727, 99

Comito, C., Schilke, P., Endesfelder U. et al. 2007, A&A, 469, 207

Cotton, W.D. 1999, ASPC, 180, 111

Cragg, D.M., Sobolev, A.M., & Godfrey, P.D. 2002, MNRAS, 331, 521

Cragg, D.M., Sobolev, A.M. & Godfrey, P.D. 2005, MNRAS, 360, 533

Crutcher, R.M. 2005, IAU Symposium, 227, 98

Crutcher, R.M., 1999, ApJ, 520, 706

Curiel, S., Ho, P.T.P., Patel, N.A. et al. 2006, ApJ, 638, 878

Curran, R.L., Chrysostomou, A., Collett, J.L. et al. 2004, A&A, 421, 195

Curran, R.L. & Chrysostomou, A. 2007, MNRAS, 382, 699

Dale, J.E. & Bonnell, I.A. 2008, MNRAS, 391, 2

Davis, C.J., Moriarty-Schieven, G., Eislöffel, J. et al. 1998, AJ, 115, 1118

de Jong, T. 1973, A&A, 26, 297

De Buizer, J.M. 2006, ApJ, 642, L57

De Buizer, J.M. & Minier, V. 2005, ApJ, 628, L151

De Buizer, J.M., Radomski, J.T., Telesco, C.M. et al. 2005, ApJSS, 156, 179

Deguchi, A. & Watson, W.D. 1990, ApJ, 354, 649

Dent, W.R.F., Little, L.T., Kaifu, N. et al. 1985, A&A, 146, 375

Dickel, J.R., Dickel H.R. & Wilson, W.J. 1978, ApJ, 223, 840

Dobbs, C.L., Bonnell, I.A., & Clark, P.C. 2005, MNRAS, 360, 2

Dodson, R. 2008, A&A, 480, 767

Donati, J.-F., Howarth, , I.D., Bouret, J.-C. et al. 2006, MNRAS, 365, L6

Edgar, R. & Clarke, C.J. 2004, MNRAS, 349, 678

Eisner, J.A., Greenhill, L.J., Herrnstein, J.R. et al. 2002, ApJ, 569, 334

Elitzur, M., Hollenbach, D.J. & McKee, C.F. 1989, ApJ, 346, 983

Elitzur, M. 1992, *Astronomical masers*, Kluwer Academic Publishers (Astrophysics and Space Science Library Vol.170), 365 p.

Erickson, E.F. & Tokunaga, A.T. 1980, ApJ, 238, 596

Fiebig, D. & Güsten, R. 1989, A&A, 214, 333

Fish, V.L., Reid, M.J. & Menten, K.M. 2005, ApJ, 623, 269

Fish, V.L. & Reid, M.J. 2006, ApJS, 164, 99

Fish, V.L. & Reid, M.J. 2007, ApJ, 656, 952

Fish, V.L., & Sjouwerman, L.O. 2007, ApJ, 668, 331

Forster, J.R. & Caswell, J.L. 1989, A&A, 213, 339

Franco-Hernández, R. & Rodríguez , L.F. 2004, ApJ, 604, 105

Fuller, G.A., Zijlstra, A.A. & Williams, S.J. 2001, ApJ, 555, L125

Galván-Madrid, R., Montes, G., Ramírez, E.A. et al. 2010, ApJ, 713, 423

Garrington, S.T., Anderson, B., Baines, C. et al., 2004, in Oschmann, Jr. J.M., ed., Society of Photo-Optical Instrumentation Engineers (SPIE) Conference Series Vol. 5489 of Society of Photo-Optical Instrumentation Engineers (SPIE) Conference Series, e-MERLIN. pp 332–343

Gaume, R.A. & Mutel, R.L. 1987, ApJS, 65, 193

Gaume, R.A., Johnston, K.J., Nguyen, H.A. et al. 1991, ApJ, 376, 608

Gaume, R.A., Johnston, k.J. & Wilson, T.L. 1993, ApJ, 417, 645

Gaume, R.A., Goss, W.M., Dickel H.R. et al. 1995, ApJ, 438, 776

Genzel, R., Downes, D., Schneps, M.H. et al. 1981, ApJ, 247, 1039

Gibb, A.G., Hoare, M.G., Little, L.T. et al. 2003, MNRAS, 339, 1011

Goldreich. P., Keeley, D.A., & Kwan, J.Y., 1973, ApJ, 179, 111

Goldreich, P. & Kwan, J. 1974, ApJ, 190, 27

Greaves, J.S. & Holland, W.S. 1998, A&A, 333, L23

Green, J.A., Richards, A.M.S., Vlemmings, W.H.T. et al. 2007, MNRAS, 382, 770

Hachisuka, K., Brunthaler, A., Menten, K.M. et al. 2006, ApJ, 645, 337

Harvey–Smith, L. & Cohen, R.J. 2006, MNRAS, 371, 1550

Haschick, A.D., Reid, M.J., Burke, B.F., et al. 1981, ApJ, 244, 76

Heaton, , B.D., & Little, , L.T. 1988, A&A, 195, 193

Hillenbrand, L.A. & Hartmann, L.W. 1998, ApJ, 492, 540

Ho, P.T.P., Genzel, R. & Das, A. 1983, ApJ, 266, 596

Ho, P.T.P. & Young, L.M. 1996, ApJ, 472, 742

Hoffman, I.M., Goss, W.M., Palmer, P. et al. 2003, ApJ, 598, 1061

Hofner, P. & Churchwell, E. 1996, A&ASS, 120, 283

Hughes, V.A. & Wouterloot, J.G.A. 1984, ApJ, 276, 204

Hunter, T.R., Taylor, G.B., Felli. M. et al. 1994, A&A, 284, 215

Hutawarakorn, B. & Cohen, R.J. 1996, ASPC, 97, 532

Hutawarakorn, B. & Cohen, R.J. 1999, MNRAS, 303, 845

Hutawarakorn, B., Cohen, R.J. & Brebner, G.C., 2002, MNRAS, 330, 349

Hutawarakorn, B. & Cohen, R.J. 2003, MNRAS, 345, 175

Imai, H., Watanabe, T., Omodaka, T. et al. 2002, PASJ, 54, 741

Jiménez-Serra, I., Martín-Pintado, J., Rodríguez-Franco, A. et al. 2007, ApJ, 661, L187

Jiménez-Serra, I., Martín-Pintado, J., Caselli, P. et al. 2009, ApJl, 703, L157

Johansen, A. & Klahr, H. 2005, ApJ, 634, 1353

Johansen, A. & Levin, Y. 2008, A&A, 490, 501

Kameya, O., Tatsuhiko, I.H., Hirano, N. et al. 1989, ApJ, 339, 222

Kang, M., Bieging, J.H., Kulesa, C.A. et al. 2010, ApJSS, 190, 58

Kaufman, M.J. & Neufeld, D.A., 1996, ApJ, 456, 250

Kemball, A.J., Diamond, P.J. and Cotton, W.D. 1995, A&AS, 110, 383

Keto, E. 2007, ApJ, 666, 976

Keto, E. & Klaassen, P. 2008, ApJ, 678, L109

Klaassen, P.D., Wilson, C.D., Keto, E.R. et al. 2009, ApJ, 703, 1308

Klaassen, P.D., Wilson, C.D., Keto, E.R. et al. 2011, arXiv1103.5706K

Koo, B.-C. & Moon, D.-S. 1997, ApJ, 475, 194

Kraus, S., Balega, Y., Elitzur, M. et al. 2006, A&A, 455, 521

Kylafis, N.D. & Norman, C.A., 1987, ApJ, 323, 346

Kylafis, N.D. & Norman, C.A., 1991, ApJ, 373, 525

Kundu, M.R. & Velusamy, T. 1967, Ann.Astrophys., 30, 59

Kurtz, S. 2005, IAUS, 227, 111

Krumholz, M.R., McKee, C.F. & Klein, R.I 2005, ApJ, 618, L33

Krumholz, M.R., Klein, R.I & McKee, C.F., 2007, ApJ, 656, 959

Krumholz, M.R., Keiln, R.I., McKeee, C.F. et al. 2009, Science, 323, 754

Lacy, J.H., Jaffe, D.T., Zhu, Q. et al. 2007, ApJ, 658, L45

Lai, S.-P., Crutcher, R.M., Girart, J.M. et al. 2001, ApJ, 561, 864

Larson, R.B. 2003, Rep. Prog. Phys., 66, 1651

Little, L.T., Brown, A.T., Riley, P.W. et al. 1983, MNRAS, 203, 409

Little, L.T., Dent, W.R.F., Heaton, B. et al. 1985, MNRAS, 217, 227

López-Sepulcre, A., Codella, C., Cesaroni, R. et al. 2009, A&A, 499, 811

McKee, C.F. & Tan, J.C. 2003, ApJ, 585, 850

McKee, C.F. & Ostriker, E.C. 2007, Annu. Rev. Astro. Astrophys., 45, 565

MacLeod, J.M., Doherty, L.H. & Higgs, L.A. 1977, JRASC, 71, 377

Martí, J., Rodríguez, L.F., Reipurth, B. 1993, ApJ, 416, 208

Matthews, N., Little, L.T., Nyman, L.A. et al. 1984, A&A, 136, 282

Menten, K.M., Reid, M.J., Pratap, P. et al. 1992, ApJ, 401, L39

Minh, Y.C., Su, Y.-N., Chen, H.-R. et al. 2010, ApJ, 723, 1231

Minier, V., Booth, R.S., and Conway, J.E. 1998, A&A, 336, L5

Minier, V., Booth, R.S. & Conway, J.E. 2000, A&A, 362, 1093

Minier, V., Conway, J.E. & Booth, R.S. 2001, A&A, 369, 278

Minier, V., Booth, R.S. & Conway, J.E. 2002, A&A, 383, 614

Momose, M., Tamura, M., Kameya, O. et al. 2001, ApJ, 555, 855

Moscadelli, L., Menten, K.M., Walmsley, C.M. et al. 1999, ApJ, 519, 244

Moscadelli, L., Reid, M.J., Menten, K.M. et al. 2009, ApJ, 693, 406

Moscadelli, L., Xu, Y. & Chen, X. 2010, ApJ, 716, 1356

Mufson, S.L. & Liszt, H.S. 1979, ApJ, 232, 451

Nedoluha, G.E. & Watson, W.D. 1990, ApJ, 354, 660

Nedoluha, G.E. & Watson, W.D. 1992, ApJ, 384, 185

Onello, J.S., Phillips, J.A., Benaglia, P. et al. 1994, ApJ, 426, 249

Pandian, J.D., Momjian, E., Xu, Y. et al. 2011, ApJ, 730, 55

Patel, N.A., Curiel, S., Sridharan, T.K. et al. 2005, Nature, 437, 109

Persi, P., Felli, M., Lagage, P/O/ et al. 1997, A&A, 327. 299

Persi, P., Tapia, M., and Smith, H.A. 2006, A&A, 445, 971

Pestalozzi, M.R., Elitzur, M., Conway, J.E. et al. 2004, ApJ, 603, L113

Peters, T., Banerjee, R., Klessen, R.S., et al. 2011, ApJ, 729, 72

Phillips, C. & van Langevelde, H.J. 2005, ASPCS, 340, 342

Puga, E., Marín-Franch, A., Najarro, F. et al. 2010, A&A, 517, 2

Qiu, Keping; Zhang, Qizhou; Menten, Karl M. 2011, ApJ, 728, 6

Reid, M.J. & Moran, J.M. 1981, ARA&A, 19, 231

Reid, M.J., Argon, A.L., Masson, C.R. et al. 1995, ApJ, 443, 238

Roshi, D.A., Goss, W.M., Anantharamaiah, K.R. et al. 2005, ApJ, 626, 253

Rygl, K.L.J., Brunthaler, A., Menten, K.M. et al. 2010, PoS (IX EVN Symposium), arXiv1011.5042

Sandell, G. Goss, W.M., Wright, M. et al. 2009, ApJ, 699, L31

Sarma, A.P., Troland, T.H. & Romney, J.D. 2001, ApJ, 554, L217

Sato, M., Reid, M.J., Brunthaler, A. et al. 2010, ApJ, 720, 1055

Scappaticci, G.A. & Watson, W.D. 1992, 1992, ApJ, 387, L73

Scott, P.F. 1981, MNRAS, 194, 25

Scoville, N.Z., Sargent, A.I., Sanders, D.B. et al. 1986, ApJ, 303, 416

Shepherd, D.S., Testi, L. & Stark, D.P. 2003, ApJ, 584, 882

Shu, F.H., Najita, J., Ostriker, E.C. et al. 1995, A&A, 455, 155

Slysh, V.I., Migenes, V., Val'tts, I.E. et al. 2002 ApJ, 564, 317

Slysh, V.I. & Migenes, V. 2006, MNRAS, 369, 1497

Slysh, V.I., Alakov, A.V. & Migenes, V. 2010, MNRAS, 404, 1128

Sobolev, A.M., Cragg, D.M. & Godfrey, P.D. 1997, A&A, 324, 211

Sollins, P.K., Zhang, Q. & Ho, P.T.P. 2004, ApJ, 606, 943

Sollins, P.K., Zhang, Q., Keto, E. et al. 2005, ApJ, 624, L49

Stahler, S.W., Palla, F., & Ho, P.T.P. 2000, Protostars and Planets IV, 327

Stahler, S.W. & Palla, F., *The Formation of Stars*, ed. 2004, WILEY-VCH

Subrahmanyan, R. & Goss, W.M. 1995, MNRAS, 275, 755

Sugiyama, K., Fujisawa, K., Doi, A. et al. 2008, PASJ, 60, 23

Sugiyama, K., Fujisawa, K., Doi, A. et al. 2008, PASJ, 60, 1001

Sun, X. H., Reich, W., Waelkens, A. et al. 2008, A&A, 477, 573

Tan, J.C. & McKee, C.F. 2003, IAU Symp, 221, 274

Tang, Y.-W., Ho, P.T.P., Girart, J.M., et al. 2009, ApJ, 695, 1399

Tang, Y.-W., Ho, P.T.P., Koch, P.M. et al. 2009, ApJ, 700, 251

Testi, L., Felli, M., Persi, P. et al. 1994, A&A, 288, 634

Thompson, A.R. 1999, ASPC, 180, 11

Tomisaka, K., Ikeuchi, S. & Nakamura, T. 1988, ApJ, 335, 239

Torrelles, J.M., Gómez, J.F., Rodríguez, L.F. et al. 1997, ApJ, 489, 744

Torrelles, J.M., Patel, N.A. Anglada, G. et al. 2003, ApJ, 598, L115 (T03)

Torrelles, J.M., Patel, N.A., Curiel, S. et al. 2007, ApJl, 666, L37

Torstensson, K.J.E., van Langevelde, H.J., Vlemmings, W.H.T. et al. 2011, A&A, 526, 38

Turner, B.E. & Rubin, R.H. 1971, ApJ, 170, 113

Turner, J.L., & Welch, W.J. 1984, ApJ, 287, L81

van der Walt, J. 2005, MNRAS, 360, 153

Vlemmings, W.H.T., Diamond, P.J., van Langevelde, H.J. et al. 2006a, A&A, 448, 597

Vlemmings, W.H.T., Harvey-Smith, L. & Cohen, R.J. 2006b, MNRAS, 371, L26

Vlemmings, W.H.T. 2007, IAUS, 242, 37

Vlemmings, W.H.T. 2008, A&A, 484, 773

Vlemmings, W.H.T., Torres, R.M. & Dodson, R. 2011, A&A, 529, 95

Walker, R.C. 1984, ApJ, 280, 618

Wardle, M. 2007, Ap&SS, 311, 35

Watson, W.D. 2002, IAUS, 206, 464

Wood, D.O.S. & Churchwell, E. 1989, ApJS, 69, 831

Wright, M.M., Gray, M.D. & Diamond, P.J., 2004, MNRAS, 250, 1272

Wynn-Williams, C.G., Becklin, E.E., & Neugebauer, G. 1974, ApJ, 187, 473

Xu, Y., Reid, M.J., Zheng, X.W. et al. 2006, Science, 311, 54

Xu, Y., Reid, M.J., Menten, K.M. et al. 2009a, ApJ, 693, 413

Xu, Y., Voronkov, M.A., Pandian, J.D. et al. 2009b, A&A, 507, 1117

Yorke, H.W. & Sonnhalter, C. 2002, ApJ, 569, 846

Zapata, L.A., Ho, P.T.P., Schilke, P. et al. 2008, ApJ, 698, 1422

Zapata, L.A., Tang, Y.-W. & Leurini, S. 2010, ApJ, 725, 1091

Zeilik II, M. & Lada, C.J. 1978, ApJ, 222, 896

Zhang, Q. & Ho, P.T.P. 1997, ApJ, 488, 241

Zhang, Q., Ho, P.T.P. & Ohashi, N. 1998, ApJ, 494, 636

Zhang, B., Zheng, X.W., Reid, M.J. et al. 2009, ApJ, 693, 419

Zinnecker, H. & Yorke, H.W. 2007, Ann. Rev. Astro. Astrophys., 45, 481

Abbreviations

AIPS = Astronomical Image Processing System

ALMA = Atacama Large Millimeter/submillimeter Array

BIMA = Berkeley Illinois Maryland Association

CH_3OH = Methanol

EVN = European VLBI Network

EVLA = Expanded Very Large Array

FWHM = Full Width Half-Maximum

GMC = Giant Molecular Cloud

HCH II = Hypercompact H II regions

H_2O = Water

IMF = Initial Mass Function

ISM = Interstellar Medium

JIVE = Joint Institute for VLBI in Europe

JVN = Japanese VLBI Network

LOFAR = Low Frequency Array

LSR = Local Standard of Rest

MERLIN = Multi-Telescope Radio Linked Interferometer

MHD = Magnetohydrodynamics

NIR = Near Infrared

NRAO = National Radio Astronomy Observatory

OH = Hydroxyl radical

POLA = Polarization angle

POLI = Polarization intensity

RM = Rotation Measure

SCUBA = Submillimetre Common User Bolometer Array

SiO = Silicon monoxide

SKA = Square Kilometre Array

SMA = Submillimeter Array

UCH II = Ultracompact H II regions

UV = Ultraviolet

VLBA = Very Long Baseline Array

VLBI = Very Long Baseline Interferometry

ZAMS = Zero-Aged Main-Sequence Stars

Acknowledgements

This Ph.D. work could not be what it was without the constant and patient support of Dr. Wouter Vlemmings. I am very glad and proud to have had the chance to work side by side with him. I acknowledge support by the International Max Planck Research School (IMPRS) for Astronomy and Astrophysics at the Universities of Bonn and Cologne and by the Deutsche Forschungsgemeinschaft (DFG) through the Emmy Noether Research grant VL 61/3-1.

I would like to say thank you to all my collaborators who supported me in this intensive adventure. They are alphabetically: S. Curiel, R. Dodson, B. Hutawarakorn Kramer, H.J. van Langevelde, A.P. Sarma, J.M. Torrelles, R.M. Torres, and K.J.E. Torstensson. A particular thanks to my IMPRS Thesis Committee composed of Prof. Dr. F. Bertoldi, Prof. Dr. K. Menten, Dr. W. Vlemmings, and Dr. B. Hutawarakorn Kramer. Their suggestions were fundamental for my research and their support motivated me to work more and more.

A technical thanks to J.M. Torrelles and V. Minier for kindly providing the VLA continuum image of W75N and the methanol masers positions in W75N respectively, R. Franco-Hernández for friendly providing the VLA continuum map of NGC7538. Also thanks to Y.-W. Tang for providing the SMA continuum and polarization maps of W51–e1/e2 and W51–North.

The last thanks, but not the least important, is for my whole great family. To my lovely wife who makes every day worth to be lived. To my parents and parents-in-law for their support during the last tree years. To my brothers and to my sister (with the whole crazy crew) who are always ready to make me laughing even at large distances.